Analysis of Fluctuating Static Pressure Measurements in a Large High Reynolds Number Transonic Cryogenic Wind Tunnel

By

William B. Igoe

A Dissertation submitted to
The Faculty of
The School of Engineering and Applied Science
of The George Washington University in partial fulfillment
of the requirements for the degree of Doctor of Science

Dissertation directed by
Dr. John L. Whitesides
Professor of Engineering and Applied Science

ABSTRACT

Dynamic measurements of fluctuating static pressure levels were made using flush mounted high frequency response pressure transducers at eleven locations in the circuit of the National Transonic Facility (NTF) over the complete operating range of this wind tunnel. Measurements were made at test section Mach numbers from 0.2 to 1.2, at pressure from 1 to 8.6 atmospheres and at temperatures from ambient to $-250°F$, resulting in dynamic flow disturbance measurements at the highest Reynolds numbers available in a transonic ground test facility. Tests were also made independently at variable Mach number, variable Reynolds number and variable drivepower, each time keeping the other two variables constant thus allowing for the first time, a distinct separation of these three important variables.

This report contains a description of the NTF emphasizing its flow quality features, details on the calibration of the instrumentation, results of measurements with the test section slots covered, downstream choke, effects of liquid nitrogen injection and gaseous nitrogen venting, comparisons between air and nitrogen, isolation of the effects of Mach number, Reynolds number and fan drive power, and identification of the sources of significant flow disturbances. The results indicate that primary sources of flow disturbance in the NTF may be edge-tones generated by test section sidewall re- entry flaps and the venting of nitrogen gas from the return leg of the tunnel circuit between turns 3 and 4 in the cryogenic mode of operation. The tests to isolate the effects of Mach number, Reynolds number and drive power indicate that Mach number effects predominate. A comparison with other transonic wind tunnels shows that the NTF has low levels of test section fluctuating static pressure especially in the high subsonic Mach number range from 0.7 to 0.9.

ACKNOWLEDGMENTS

First and foremost, the author takes pleasure in acknowledging the wisdom, guidance, and patience of his dissertation research advisor, Dr. John L. Whitesides. Acknowledgment is also due to Dr. Richard W. Barnwell who initially recommended the topic. Special thanks are also due to Dr. N. Sam Dougherty (formerly of AEDC) currently with Rockwell International, and Prof. Dennis G. Mabey (formerly of RAE, Bedford) currently with the Imperial College, London for their enlightening and stimulating discussions of the subject. Thanks are also due to Mr. Walter E. Bruce, the authors former branch head, and Mr. Lawrence E. Putnam, current branch head for their constant support and willing commitment of resources toward the completion of the experimental measurements.

As in any experimental investigation of this magnitude, the expert assistance of a large number of very talented people was absolutely essential. The author takes special pleasure in acknowledging the help of Jim Richardson and Roy Skeen for their expert assistance in installing and maintaining the electronic dynamic data acquisition instrumentation, Lewis Horsley and Chris Alexander for the delicate and precise work of mounting and installing the dynamic pressure transducers, thermocouples, and related instrumentation, Dennis Fuller and Jeff Hill for expert supervision of the operation of the NTF safely and efficiently, Julio Chu, Bill Johnson, Lewis Owens and Susan Williams for their dedicated test direction efforts, Bill Tomek for his invaluable assistance in acquiring the dynamic test data, Jean Foster for her timely and efficient computing of the NTF steady state test conditions, and Bill Wood for his yeoman service in the phase matching of all the signal conditioners.

Special thanks are due to Tom Norum, Tony Parrott, and Jay Hardin for their generous consultation on the subject of edge-tones.

A final word of thanks is due to Jack Peterson and Jerry Adcock who were veritable fountains of information on the many related subjects which were necessary to contend with during the course of the investigation and who generously shared their time,

experience, and know-how, and to Tammie Bonser and Jamie Carter for their superb job of typing.

TABLE OF CONTENTS

LIST OF FIGURES

LIST OF TABLES

SYMBOLS

(U.S. standard units are used throughout)

A_x	cross sectional area of model, square ft.
$A_{\max}$	maximum cross sectional area of model, square ft.
A_T	cross sectional area of test section at throat, square ft. (66.77 sq. ft. for NTF)
a	slope of least squares straight line
BPF	fan blade passage frequency, Hz
b	intercept of least squares straight line
C_x	longitudinal buoyancy force coefficient, F_x/qS
c	speed of sound, fps
c_t	stagnation speed of sound, fps
$\bar{c}$	wing mean aerodynamic chord
D	diameter, in.
$d_1,\ d_2$	cavity depth of outer and inner chamber respectively of dual Helmholtz resonator (see figure A13), in.
e	base of Naperian logarithms (2.71828...)
F_x	longitudinal buoyancy force, lb.
f	frequency, Hz
f_p	fundamental frequency of slotted wall-plenum resonance, calculated, Hz
f_s	characteristic slot frequency, Hz
g	gravitational acceleration
h	test section height at throat, ft. (8.202 ft. for NTF)
i	subscript designating ith data point
J	highest order exponent in polynomial fit to area distribution
j	upper limit of summation for least squares straight line fit
k_1	model blockage area ratio, $A_{\max}/A_T$
k_2	wing area to test section area ratio, S/A_T
k_3	model length to test section height ratio l/h
L	lip-to-wedge gap distance for edge-tone geometry
l	length of model, ft.
M	test section free stream Mach number, V/c
M_L	local Mach number
m	stage number for edge-tone frequencies

N	amplification factor, logarithmic exponent of disturbance growth ratio
n	exponent in polynomial fit to area distribution
OA_1, OA_2	open area ratio of perforated liner for outer and inner chamber respectively of dual Helmholtz resonator (see figure A13)
OD	outer diameter, in.
P	static pressure measurement reading, psi
P_i	static pressure measurement reading at ith point, psi
p	static pressure with the mean subtracted
p_i	true static pressure at ith point, psi
$p_{\max}$	maximum pressure amplitude range of pressure sensor, psi
p_t	free stream stagnation pressure, psi
$\tilde{p}$	root mean square value of fluctuating component of static pressure, psi
$(\tilde{p}/q)^2$ per Hz	power spectral density function of the fluctuating static pressure coefficient
q	test section free stream dynamic pressure, one half of the product of the gas mass density times the square of the free stream velocity, psf
q_{sc}	dynamic pressure in settling chamber, psf
R	Reynolds number, product of a reference length times velocity times the gas mass density divided by the absolute viscosity
$R_{\bar{c}}$	Reynolds number based on wing mean aerodynamic chord
r	radius, in.
S	model wing area or other reference area, square ft.
St	Strouhal number
T_{aw}	adiabatic wall temperature, °F
T_t	free stream stagnation temperature, °F
T_w	wall temperature, °F
T_∞	free stream static temperature, °F
$u_c(x)$	overall streamwise convection velocity, fps
V	free stream velocity, fps
x	longitudinal distance, positive downstream, ft.
α_{rf}	reentry flap angle, positive away from flow, deg.
Δ	increment or change in a quantity or variable

Δa	error in least squares straight line slope, a
γ	lag factor in edge-tone feedback emittance
δ	root sum squares of δ_i
δ_i	increment between pressure reading, P_i, and least squares straight line fit at ith point
δ_{msw}	model support wall angle, positive away from flow, deg.
ϵ_i	error in pressure reading, P_i
θ_{tsw}	test section wall divergence angle, positive away from flow, deg.
ϕ	phase angle, deg.

ABBREVIATIONS

AEDC	Arnold Engineering and Development Center
AIAA	American Institute of Aeronautics and Astronautics
arb	arbitrary
atm	atmospheres (14.7 psi)
BPF	blade passage frequency
calc	calculated
cryo	cryogenic
cu	cubic
dB	decibel
diam	diameter
E	exponent power of 10
ESP	electronically scanned pressure
F	Fahrenheit temperature scale
FM	frequency modulation
fps	feet per second
freq	frequency
ft	foot
GN_2	gaseous nitrogen
Hz	Hertz, frequency, cycles per second
hp	horsepower
IGV	inlet guide vane
IRIG	Inter-Range Instrumentation Group
in	inch
ips	inches per second
LHS	left hand side
LN_2	liquid nitrogen
LaRC	Langley Research Center
lb	pound
MW	megawatts
max	maximum
meas	measured
min	minimum or minute
mv	millivolt

NACA	National Advisory Committee for Aeronautics
NASA	National Aeronautics and Space Administration
NBS	National Bureau of Standards
NIST	National Institute of Standards and Technology (formerly NBS)
NLR-HST	National Aerospace Laboratory—High Speed Tunnel
NTF	National Transonic Facility
psf	pounds per square foot
psi	pounds per square inch
R	Rankine temperature scale
RAE	Royal Aerospace Establishment
RHS	right hand side
rms	root mean square
rpm	revolutions per minute
rss	root sum square
sec	second
sta	tunnel station (measured from start of test section, positive downstream, ft.)
TPT	Transonic Pressure Tunnel
temp	temperature
v	volt
vol	volume
w/	with

1.0 INTRODUCTION

A wind tunnel is primarily a means of creating a flow over a model or body with the object of determining the influence of one on the other. With the exception of specialized wind tunnels for studying specific fluid dynamic problems, the principal objective of the wind tunnel is to study the flow about configurations duplicating full-scale, free flight conditions to the fullest extent possible. Wind tunnels such as the National Transonic Facility (NTF) fulfill the first condition by achieving full-scale Reynolds numbers. In general, the second condition is addressed in a variety of ways. The interference created by the test section walls is alleviated by wall ventilation such as slots or perforations, and adaptive walls are resorted to in an attempt to remove the interference more completely. The interference created by the model supports is minimized by supporting the model from the rear by stings or blades and again, is removed more completely by resorting to magnetic suspension. It is in the area of the uniformity and steadiness of the flow that there is, as yet, no complete resolution. Few, if any wind tunnels, especially transonic wind tunnels, can approach the relatively quiescent conditions of free air. It is therefore desirable to examine the disturbance level of wind tunnels in order to assess their capability to perform their diverse research roles.

1.1 Background

The influence of flow disturbances such as velocity turbulence and noise on aerodynamic phenomena has long been widely recognized, and in recent years, the dynamic flow quality of wind tunnels has received close attention. Lately, the efforts to develop natural laminar flow, or laminar flow control airfoils and other aerodynamic surfaces for use on commercial aircraft have increased the interest in the magnitude and the frequency characteristics of flow disturbances in wind tunnels.

An early example of the effect of dynamic flow quality on wind tunnel measurements involved the discrepancy in the drag of a sphere measured under comparable test conditions in the wind tunnels of Prandtl and Eiffel in the early 1900's. Here of course, the discrepancy was resolved by Prandtl (1914) when it was recognized that higher velocity turbulence levels in the Eiffel wind tunnel had caused an earlier transition of the sphere boundary layer which was then more resistant to separation and gave lower drag. An important byproduct of the discovery of the cause of the sphere drag discrepancy was to alert wind tunnel investigators to the need for caution in applying the results of measurements made in turbulent wind tunnel airstreams to aircraft in nominally quiescent free air.

As used by Mabey (1976), the term wind tunnel unsteadiness is a general one which refers to fluctuations in velocity, pressure, and temperature. Timme (1973) distinguished between those disturbances whose pattern showed a wave form, with a phase velocity corresponding to the speed of sound, calling this noise or acoustic disturbances, and those disturbances whose fluctuations are stochastic in nature, with a phase velocity that is some fraction of the flow velocity, calling this turbulence. However, the difference between the two may not always be distinct. Figure 1, adapted from Mabey (1971), shows many of the sources of flow unsteadiness identified by Mabey in transonic wind tunnels.

Although flow disturbance levels may to some extent have some effect on all measurements made in wind tunnels, there are instances where the effects are more pronounced. As indicated by Timme (1973) and by Mabey (1976), those research areas which can be most affected by wind tunnel unsteadiness include boundary layer transition from laminar to turbulent flow, the development and characteristics of turbulent boundary layers, shock wave-boundary layer interaction, separated flows and wakes, reattachment, inlet and control surface buzz, buffeting, and flutter.

Commonly in wind tunnels, fluctuations in velocity have been considered the most important from a dynamic flow quality aspect. In early wind tunnels, as proposed by Prandtl (1914), the abrupt change with Reynolds number in the drag coefficient of a sphere was used to indicate a measure of the velocity turbulence. However, as discussed by Dryden and Abbott (1948), spheres were not reliable indicators for low-turbulence wind tunnels at turbulence levels below about 0.5 percent. Also, due to the effects of compressibility, spheres were not suitable for high-speed wind tunnels at Mach numbers above about 0.35, as shown by Robinson (1937). Because of these limitations, the sphere drag test became less useful as a turbulence indicator.

As described by Dryden and Abbott (1948), the hot-wire anemometer became the standard instrument for the measurement of the components of velocity turbulence. Kovasznay (1950, 1953) developed the application of hot-wire measurement techniques to supersonic flows. Spangenberg (1954) showed that the hot-wire sensitivities were a function of both Mach number and Knudsen number. Morkovin (1956) improved and extended Kovasznay's techniques, but the area of high subsonic compressible flow and transonic flow remained in question. Horstman and Rose (1975) and Rose and McDaid (1976) applied the supersonic flow hot-wire techniques to transonic flows under the condition that the hot-wire sensitivities for velocity and for density changes were equal. However, using a 3-wire technique, Stainback, Johnson, and Basnett (1983), and Jones (1991) have shown that the velocity and density sensitivities for hot-wires are not equal. The 3-wire technique of Stainback, and of Jones, to separate the effects of velocity, density, and temperature changes has not yet received universal acceptance. The velocity and density fluctuations measured using this technique appear unusually large, and the reasons for these results have not been resolved.

Laser velocimeters have been used to measure velocity turbulence, as shown for example by Meyers and Wilkinson (1982), and have indicated reasonable comparisons with hot-wire results for the streamwise component of turbulence. However, the high

speed burst counter technique such as used by Meyers and Wilkinson has a high amplitude threshold of detection of about 0.5 percent. This threshold of detection can be lowered to about 0.2 percent by using a frequency domain signal processor, as indicated by Meyers and Clemmons (1987), but even this amplitude threshold is not sufficiently sensitive for low-turbulence wind tunnel measurements.

The length of laminar boundary layer run before transition to turbulence occurs is considered a sensitive measure of flow quality. In a review article, Michel (1988) has indicated that although the boundary layer transition process is primarily sensitive to velocity turbulence, below a minimum threshold value of about 0.2 percent, aerodynamic sound can control the transition process. Dougherty (1980) has used the boundary layer transition sensitivity to evaluate wind tunnel flow quality in a large number of wind tunnels using a 10° included angle cone of revolution. The AEDC 10° transition cone was instrumented with a traversing surface probe to detect the location of transition, and with surface mounted microphones or pressure transducers, to measure the fluctuating static pressure on the cone surface. This cone has been used to determine the dynamic flow quality in 23 different wind tunnels in this country and in Europe. In addition to wind tunnel tests, the cone was also tested in flight on the nose of an F-15 fighter airplane as described by Dougherty and Fisher (1980). With so much testing history in so many different research environments, the cone has gained the status of a calibration standard. The distinct advantage of the 10° cone tests was the ability to obtain dynamic flow quality information in a large number of different test facilities using identical hardware and instrumentation, thus assuring comparability in all the measurements. Unfortunately the AEDC 10° cone is not compatible with a cryogenic environment either in materials or in operational capability so it could not be tested at the cryogenic test conditions of the NTF.

The initial analysis of the variation of the transition Reynolds number with the measured fluctuating static pressure coefficient of the AEDC 10° cone by Dougherty

(1980) showed a substantial correlation between the fluctuating pressure coefficient and the transition Reynolds number based on either the start or the end of transition. The transition data however show a considerable scatter when compared from one facility to another. Spangler and Wells (1968) have further shown that the effectiveness of sound in promoting transition is highly dependent on the frequency of the excitation. The correlation between the rms noise level and the location of transition will not be a simple one since the frequency spectrum of the noise and the receptivity of the boundary layer will be involved. The apparent correlation in the AEDC 10° cone data due to Dougherty has been called into further question in an analysis of the data by Murthy and Steinle (1985, 1986) where they attempted to account for the effects of Mach number in the correlation. Their conclusion was that there was no acceptable correlation in the AEDC 10° cone data between the transition Reynolds number and the fluctuating pressure coefficient, at least at low noise levels.

The sensitivity of an initially laminar boundary layer to flow disturbances which cause transition to turbulence has been used by Elsenaar (1990) as a measure of dynamic flow quality by comparing the boundary layer transition locations calculated by the e^N method using linear compressible stability theory to those locations actually measured in a wind tunnel. The comparison yielded representative N factors which are characteristic of the flow for specific configuration examples. In the NLR-HST, on a two-dimensional laminar flow airfoil, Elsenaar obtained N factors from 6 to 12, depending on Mach number and Reynolds number, where high N factor values close to free flight values were associated with good dynamic flow quality.

Both Timme (1973) and Mabey (1976) have described the difficulties of measuring velocity turbulence at transonic speeds, and have indicated that flow unsteadiness in transonic wind tunnels is usually assessed by measurement of the fluctuating static pressure. Elsenaar (1990) has reiterated that the measurement of the fluctuating static

pressure in the test section provides a first indication of the dynamic flow quality in a wind tunnel.

By comparing the static pressure fluctuation measured on a body of revolution on the tunnel centerline with that on a sidewall, Mabey (1971) concluded that the pressure fluctuations were almost the same, and that the pressure fluctuation field was approximately one-dimensional. Dolling and Dussauge (1989) also indicated that fluctuating pressures measured on a wall, being dependent on the surrounding flow, reflect the salient features of that flow, and have the additional advantage of being non-intrusive measurements.

For measurements in the free stream, Siddon (1969) has cautioned that fluctuating static pressure measurements using probes can be seriously in error. The interaction between the probe and the fluctuating flow can cause errors which can be either positive or negative depending on whether the scale of a typical eddy size in the flow is smaller or larger than the dimensions of the probe. Eckelman (1988) has confirmed that pressure probe measurements within turbulent flows are not reliable since velocity fluctuations in the flow produce random pressure fluctuations on the probe which would not occur if the probe were not present.

In addition to receiving the fluctuations occurring in the free stream, wall pressure measurements receive additional contribution from disturbance levels generated within the turbulent boundary layer itself. Within the turbulent boundary layer there is an interaction of the turbulence with the mean shear, and an interaction of the turbulence with itself. However, Mabey (1971) has indicated that this contribution which wall pressure measurements receive represents a small correction at high frequency which is frequently approximated as a constant.

In view of the difficulties associated with other means of determining wind tunnel dynamic flow quality, and because of the advantages associated with the wall measurement of fluctuating static pressures as cited above, this approach was adopted for the preliminary assessment of dynamic flow quality in the NTF.

1.2 Dynamic Measurements in the NTF

Since the NTF is a wind tunnel which operates at high Reynolds numbers, it was considered necessary to determine the acceptability of the dynamic flow quality and to gain perspective on the suitability of the NTF for laminar flow research and for dynamic aeroelastic research such as flutter and buffet testing. The cryogenic features of this wind tunnel, which contribute so importantly to its high Reynolds number capability, also introduce additional factors which affect the flow quality and complicate its measurement. To accomplish this task, high-frequency response pressure transducers were installed flush with the surface at 11 locations in the NTF circuit. Dynamic measurements were made of the fluctuating static pressure levels over the complete operating range of the NTF at test section Mach numbers from 0.2 to 1.2, at pressures from 1 to 8.6 atmospheres and at temperatures from ambient to $-250°F$. This combination of test conditions has resulted in data at the highest Reynolds numbers available in a transonic ground test facility.

The capability to test over a wide range of temperatures allowed measurements of fluctuating static pressures to be made at variable Mach number keeping Reynolds number and drive power constant by appropriate variation of temperature and pressure. Similarly, additional tests were made at variable Reynolds number keeping Mach number and drive power constant, and at variable drive power keeping Mach number and Reynolds number constant thus allowing for the first time a distinct separation of the effect of these important variables.

The importance of the fan drive system as a source of wind tunnel noise has been described in several papers including Williams (1977), Michel and Froebel (1988), and Chiu and Lauchle (1989). As indicated by Williams (1977), the wind tunnel drive

system represents one of the primary sources of background noise in the test section. According to Chiu and Lauchle (1989), the fan aerodynamic noise has a broadband spectrum, sometimes with a series of discrete frequency peaks associated with the fan blade passage frequency and its harmonics. The major broadband noise sources include blade vortex shedding from the blade trailing edge, blade to blade vortex interaction, flow separation from the blade upper surface, and random fluctuating blade forces caused by the blade boundary layer, and by blade interaction with inflow turbulence. The discrete frequency peaks are primarily due to inflow distortion where the blades interact with wakes from upstream obstructions. This unsteady interaction causes fluctuating pressure fields which, in a compressible medium, radiate as dipole sound sources.

Williams (1977) indicated that when comparing broadband dipole fan noise under similar operating conditions a useful working approximation is that the fan overall sound power is proportional to the cube of the fan tip speed times the fan aerodynamic shaft power times one minus the fan aerodynamic efficiency. To help isolate the effects of blade tip speed from those of fan drive power, the NTF was operated over the same speed range using either fan rpm change or inlet guide vane change to load the fan and change tunnel speed.

2.0 TEST APPARATUS

Before beginning a description of the NTF, it may be worthwhile to review briefly the cryogenic concept. Historically, the use of modest cooling to increase Reynolds number was first proposed by Margoulis (1920), and the potential benefits of further temperature reduction were later pointed out by Smelt (1945). It was not until much later that the cryogenic concept was successfully demonstrated at LaRC by Kilgore (1974) [see also Goodyer and Kilgore (1973)].

2.1 Benefits of the Cryogenic Concept

The benefits of the cryogenic approach can best be illustrated by reference to figure 2, [taken from Kilgore, Adcock, and Ray (1974)] which is shown for a Mach number of one. On the left hand side of this figure, the variation with temperature of the gas properties is shown referred to the properties at 120°F. As can be seen in the figure, the density increases and both the viscosity and speed of sound decrease with decreasing temperature. Since the Reynolds number depends on density in the numerator and viscosity in the denominator, the change with temperature produces the variation of Reynolds number with temperature shown on the right hand side of the figure, again in relative terms. In the extreme, an increase of six-fold or more in Reynolds number can be obtained, although in actual testing the temperature is rarely taken this low. The difficulty arises in approaching the gas condensation boundary too closely. A more realistic factor for increase of Reynolds number with temperature reduction would be four to five. Because the speed of sound is reduced with reduced temperature, the velocity to achieve a given Mach number is also reduced so the required drive power is reduced. All this is obtained with no change in dynamic pressure. From this, it is readily apparent why the cryogenic concept is an attractive way to obtain high Reynolds numbers. Any further increase of Reynolds numbers would normally be obtained by increasing the stagnation pressure with the accompanying increase in dynamic pressure and drive power.

Some additional benefits of the cryogenic concept were pointed out by Kilgore et al. (1974) and are shown in figures 3, 4, and 5. These figures are conceptual and do not represent actual performance for the NTF. Figure 3 shows that at a constant Mach number it is possible to hold dynamic pressure and hence model loads and deflections constant while varying Reynolds number, or conversely to hold Reynolds number constant while varying dynamic pressure for pure aeroelastic studies. Figure 4 shows that at a constant Reynolds number, Mach number can be varied while holding dynamic pressure constant. Figure 5 shows that at a constant dynamic pressure, either Mach number or Reynolds number can be varied. This feature of the cryogenic concept thus allows pure Mach number, pure Reynolds number or pure aeroelastic studies to be made holding the other parameters constant. Later in this paper, some further benefits of the cryogenic concept for dynamic flow quality testing will be presented showing that it is also possible to separate the effects of drive power from those of Mach number and Reynolds number.

2.2 Description of the National Transonic Facility

The NTF has been amply described as its characteristics have evolved during the planning, design, construction and initial operation of the wind tunnel. Howell and McKinney (1976), Igoe (1980), and Bruce (1985) are typical sources of information on the NTF, and contain many more cited references. A brief description of the NTF is presented here. A more detailed description including those components which influence the dynamic flow quality is presented in Appendix A. These descriptions are essentially a review of the above mentioned sources, borrowing material freely from them and the cited references.

In most respects, the NTF is a rather conventional wind tunnel with only a few unconventional features. The circuit lines and over-all dimensions of the wind tunnel are shown in figure 6. The tunnel circuit is about 200 ft. long and about 48.6 ft. wide between centerlines, giving an internal circuit length of about 497 ft. and an enclosed volume of about 230,000 cubic ft. It was constructed on the site of the deactivated 4-foot Supersonic

Pressure Tunnel, and used some of the equipment from that tunnel including induction drive motors. The plane of the tunnel circuit is tilted about 9° with the centerline of the fan being at a lower elevation than the centerline of the test section. The fan and test section centerlines lie in horizontal planes, and the walls of the test section are oriented horizontally and vertically. The reason for the tilt was to accommodate the fan driveshaft centerline positioning with respect to the existing induction drive motors, and to minimize large below-grade excavation requirements in the test section-plenum region.

The wind tunnel has two basic modes of operation; one at near-ambient temperatures using air as the test gas and the other at cryogenic temperatures using nitrogen as the test gas. In the air mode of operation, cooling is accomplished by a conventional water-cooled heat exchanger inside the tunnel circuit. For cryogenic operation, cooling is accomplished by spraying liquid nitrogen directly into the tunnel circuit. It is, of course, possible to use nitrogen as the test gas and to use the heat exchanger for cooling, but this is not done.

2.3 Instrumentation

2.3.1 Pressure Transducer Characteristics

The fluctuating pressures were measured using Endevco 8507-10M16 miniature electrical pressure transducers. The transducer casing was 0.092 in. diam. and 0.5 in. long, and had a pressure range of ± 10 psi differential. They had an anisotropically etched silicon diaphragm 0.05 in. diam. with an active 4-arm piezoresistive bridge diffused into the diaphragm. The diaphragm was recessed below the surface of the transducer beneath a 0.03 in. diam. orifice with a dead volume of 15 E-6 cu. in. The specified resonant frequency of the diaphragm was 130 kHz. The sensitivity to acceleration was 1.5 E-4 psi per g. Temperature compensation to account for bridge resistance change with temperature is accomplished with integral hybrid electrical circuitry. The transducers were temperature compensated over a temperature range of about -280°F to 150°F. The

excitation voltage for both the data measurement and the bench calibration was 10v and was continuously monitored during the measurements.

2.3.2 Pressure Transducer Calibration

The primary calibration of the pressure transducers was done in a laboratory environment using calibration standards traceable to the NIST (formerly NBS). The calibrations were performed both statically and dynamically. All calibrations were done at an excitation voltage of 10v.

2.3.2.1 Static Calibrations. The pressure transducers were calibrated statically over their full pressure range of ± 10 psi at 2 psi pressure increments at temperatures from 135°F to −280°F to span the expected range of temperature operation in the NTF of 120°F to −250°F. The individual calibration data at each temperature were fitted with a least-squares straight line. The slopes of the straight line fits for one of the pressure transducers (64RY) which was used in the NTF test section sidewall at station 13 on the right hand side are shown in figure 7(a). The dashed line through the data points is a least-squares straight line versus temperature. The variation of calibration sensitivity with temperature was fitted this way for all the pressure transducers used in this investigation. The static calibration sensitivities were used to reduce the data from the dynamic pressure transducers.

2.3.2.2 Dynamic Check-Calibrations. The pressure transducers were dynamically check-calibrated using a Photocon Research Products PC-120 microphone calibrator. The output of the calibrator itself was verified using a Br el and Kjaer 4134 1/2 in. microphone as a standard. The pressure transducers were check-calibrated at a constant frequency of 1 kHz with input amplitude varying from 0.001 psi to 0.1 psi, and at a constant input amplitude of 0.05 psi at frequencies ranging from 50 Hz to 2 kHz. These dynamic calibrations were only performed at room temperature. The results of the constant frequency and constant amplitude dynamic calibrations for transducer 64RY are shown in figures 7(b) and (c). The variation in sensitivity with either amplitude or

frequency variation was within the ±1/2 dB band normally expected in these types of calibrations for all of the pressure transducers. In addition to the laboratory calibration, all the transducer outputs were verified in place in the wind tunnel with a portable calibrator at a signal amplitude of 0.0015 psi and a frequency of 2 kHz.

2.3.2.3 Resonant Frequency. Because of the high resonant frequency (130 kHz) of the pressure transducers which were used in this investigation and because of the frequency limitations on the spectral analyzer which was used (100 kHz due to the maximum digital sampling rate of 256 kHz in the single channel mode of operation), it was not possible to show the resonant peak of these transducers in a power spectrum. However, frequency counting on an oscilloscope trace yielded a frequency of about 137 kHz which because of its proximity to the 130 kHz resonant frequency specified for the transducers, can probably be identified as the actual resonant frequency.

2.3.3 Pressure Transducer Installation

Before the pressure transducers were installed in the tunnel circuit, they were first mounted in brass instrument plugs as shown in figure 8. Brass was chosen as the material for the plug because of its ease of machining and brazing or soldering, and because its thermal coefficient of expansion is not too different from that of the aluminum structure of the wind tunnel to which they were attached. This method of installation was utilized for all the transducers except for two of them as will be indicated later. With guidance from the results of Coe (1969) and following the recommendations of Hanly (1975), the pressure transducers were mounted either flush or slightly below (0.001 in.) the surface of the brass plug to minimize disturbances caused by transducer mounting non-flushness. A static pressure orifice and a copper-constantan thermocouple were included in the instrument plug. The static pressure orifice was connected to the reference pressure side of the pressure transducer through a 100 ft. coil of flexible pressure tubing to provide damping to the reference pressure. The thermocouple was used to monitor the temperature of the pressure transducer environment. The pressure transducers were

potted in place in the plugs using an instrument-grade silicone rubber compound. Prior to cryogenic operation, the reference lines were purged with dry nitrogen gas.

Eight instrumented brass plugs were installed in the NTF circuit, flush with the local surface and at mid-height. The locations are shown in figure 9 and are as follows: one on the left hand side (LHS) (looking upstream) at sta 6.5 and another opposite it on the RHS, three closely spaced (2.25 in. apart streamwise) on the RHS at station 13, one on the RHS at sta 16, one on the LHS in the high speed diffuser (station 68), and one on the RHS just downstream of turn 1 and adjacent to the liquid nitrogen injectors. An additional instrumented brass plug was installed in the plenum on the RHS at sta 0, near the plenum wall and at the same height as the test section top wall.

Because of space limitations, the pressure transducer installed in the settling chamber was first potted into a drilled-out 1/4–20 stainless steel bolt and then installed flush in the settling chamber wall on the RHS, 1 ft. downstream of the last screen and about 30° up the wall from bottom center. The reference pressure for the transducer was supplied from an adjacent static pressure orifice, and again damped through a 100 ft. coil of flexible pressure tubing. The temperature environment for this transducer was taken to be equal to the tunnel stagnation temperature. A conventional pitot-static pressure probe was installed downstream of the heat exchanger to measure the local flow conditions in the settling chamber.

During this investigation, the test section was nominally empty, that is, there was no test model installed in the test section. In order to cover up the blunt centerbody on the model support arc-sector strut, a 10.6° included angle conical fairing was installed as shown in the photograph of figure 10. Most of the rearward section of the fairing was made of fiber glass reinforced plastic. The front section of the fairing was made of stainless steel and is shown in the photograph of figure 11 and the sketch of figure 12. The apex of the cone was blunted with a 0.06 in. radius tip. The machined surface of the cone front section was estimated to have a 32 microinch finish.

A dynamic pressure transducer was installed flush-mounted on the cone surface 10.4 in. rearward from the blunted cone tip. Since the transducer had a flat 0.092 in. diameter face, and was mounted in a conical surface whose radius at that point was 1.03 in., the so-called flush-mount was not really flush. The philosophy which was followed in mounting the pressure transducer in the cone was to avoid any forward facing surfaces or other protrusions by the transducer. So although the installation was as clean as could be done under the circumstances, it still represented some discontinuity in the cone surface. When installed in the tunnel, the cone tip was on the test section centerline at station 16.74. The transducer was on the RHS, facing the RHS test section wall and was at station 17.60. A copper constantan thermocouple was installed in the cone on the opposite side from the pressure transducer. The reference pressure for the transducer was the plenum static pressure, and was supplied to the transducer through a 100 ft. coil of flexible pressure tubing.

2.3.4 Signal Conditioners

The Neff 130 signal conditioners used for the dynamic pressure transducer signals were all silicon, solid state, feedback amplifiers with gain settings on a dB scale from 0 to 60 (linear scale equivalent of 1 to 1000). The filter settings ranged from 10 Hz to wide band with a 12 dB per octave Bessel filter characteristic. The input impedance was 100 megohms.

Before the signal conditioners were used in this investigation, they were carefully matched with regard to phase shift characteristics so that for signal pairs that were to be analyzed with respect to phase shift, cross correlation, etc., the phase shift characteristics of the respective amplifiers were compatible.

The amplifiers were operated in the manual gain setting mode but the gain settings were acquired automatically on the NTF steady state data acquisition system. During the entire investigation, all of the filters were set at the wideband setting so the upper limit on frequency response was ultimately encountered in the data recording on FM tape.

2.3.5 Dynamic Data Acquisition

All of the dynamic pressure transducer data signals were recorded on magnetic tape on a 28 track Honeywell 96 FM tape recorder. The tape recorder was operated in the wide band 1 mode so that at the tape recording speed of 60 ips, the frequency fidelity was up to 40 kHz. The data signals were continuously monitored on-line using four Data Check Scan Scopes, and the amplifier gain settings were manually adjusted to keep the signal amplitude (recorded on tape) as high as possible but not exceeding $\pm$ 1v peak-to-peak. A Systron Donner 8154 time code generator signal was synchronized with the NTF steady state data acquisition system clock and was also recorded on the FM tape.

Some selected data signals were also simultaneously acquired on-line using a Spectral Dynamics 380Z four-channel spectral analyzer. The analyzer digitized the input data, performed a fast Fourier transform on the digital data, and computed power spectra or other frequency domain or time domain statistical quantities which were then stored on a disk. A photograph of the dynamic data acquisition instrumentation in the NTF control room and a simplified block wiring diagram of the system are shown in figures 13 and 14, respectively.

2.3.6 NTF Steady State Data System

The current configuration of the NTF steady state data system utilizes four Modcomp Classic 16 bit, serial processor, digital computers each with 2 megabytes of memory and a 167 megabyte hard disk drive. The computers are linked together and share four magnetic tape drives. Each computer supports specific functions for the NTF operation. One computer is dedicated to research data acquisition and processing, another supports data management and communication, a third serves as a process monitor for operation of the NTF and a fourth is dedicated to tunnel control. Descriptions of the data system are given by Fuller (1981), Boyles (1986), and Foster and Adcock (1987).

Since the NTF operates at high pressures in air, and at high pressures and low temperatures in nitrogen, the test gas can depart significantly from perfect gas behavior.

It has been shown by Adcock (1976), Adcock and Johnson (1980), and Hall and Adcock (1981) that imperfect gas effects can be adequately accounted for by using Beattie-Bridgeman type equations of state and computing iteratively for the appropriate gas flow parameters. It may be noted that the most serious departures from perfect gas behavior occur at low temperatures as the gas condensation boundary is approached.

All of the steady state gas flow parameters for this investigation were computed with imperfect gas effects taken into account as indicated by Foster and Adcock (1987). As noted earlier, the amplifier gain settings from the signal conditioners for the dynamic pressure transducer signals were acquired on the steady state data acquisition system. In addition, the outputs of the thermocouples, and the monitor signals on the excitation voltage of the dynamic pressure transducers were also acquired on that system along with all the usual steady state flow parameter measurements for the tunnel.

2.4 Data Accuracy

The uncertainty expected in the fluctuating static pressure data will be considered in three categories. The first category concerns the free stream quantities and other tunnel related data. The second category concerns the actual measurement of the fluctuating static pressure. The third category concerns the statistical reliability of the spectral data derived from statistical analysis of the fluctuating static pressure measurements.

2.4.1 Free Stream Quantities

Based on information presented on the NTF instrumentation by Kern, Knight, and Zasimowich (1986), on the NTF data system by Foster and Adcock (1987), and on the NTF static wind tunnel calibration by Williams and Adcock (1993), the estimated uncertainty for the free stream quantities for the present investigation is:

Mach number (M)	±0.002
Reynolds number (R)	±0.2 million per ft.
dynamic pressure (q)	±0.1% of value
velocity (V)	±2 fps

stagnation pressure (p_t)	±0.025% of value
stagnation temperature (T_t)	±0.1°F
fan rotational speed	±2 rpm
dynamic pressure in settling chamber (q_{sc})	±5% of value

2.4.2 Fluctuating Static Pressure

The static calibration of the pressure transducers yielded least square straight line slopes (sensitivities) with a maximum deviation of less than 1% of full scale and generally less than 0.5% indicating good linearity and very small hysteresis. The variations of sensitivity with temperature were fitted with least squares straight lines with a maximum deviation of less than 1% for all the pressure transducers.

The dynamic check-calibrations show basically that there are no significant anomalies in the dynamic performance of the pressure transducers, at least over the range covered by the dynamic check-calibrations. The variations in performance which were indicated by the dynamic check-calibrations are primarily a characteristic of the dynamic calibrator system which was used, and are not a characteristic of the pressure transducers.

Dolling and Dussauge (1989) list several sources of error for fluctuating static pressure measurements using wall-mounted pressure transducers. For transducers with diaphragm sensors mounted in cavities beneath orifices, there are diaphragm and cavity resonances to be avoided. For the pressure transducers used in the present investigation, the diaphragm resonance was about 137 kHz and the cavity Helmholtz resonance was estimated to be about 75 kHz under no-flow conditions. Both of these frequencies are well above the 20 kHz upper cut-off frequency used for the analysis of the rms fluctuating static pressure coefficient data.

For turbulent boundary layers, Dolling and Dussauge (1989) indicated that a typical frequency for energy containing eddies is of the order of the velocity at the outer edge of the boundary layer divided by the thickness of the boundary layer. They stated that a safe upper cut-off frequency would be on the order of five times this typical frequency

for energy containing eddies. This criterion was developed for velocity fluctuations, but it was assumed that it would also apply to pressure fluctuations. For an assumed wall boundary layer thickness of about 3 in. on the NTF test section sidewall, the upper frequency cut-off criterion for the flow conditions of the present investigation is about 20 kHz.

Another source of error discussed by Dolling and Dussauge (1989) involves the effect of orifice size on the spatial resolution of the measurement. Disturbances whose scales are small compared to the orifice diameter tend to be averaged out, and the spectrum is therefore under-estimated at the higher frequencies. Using the above-noted upper frequency cut-off criterion, these authors concluded that an orifice less than 0.04 times the boundary layer thickness should be adequate. Again for an assumed 3 in. thick boundary layer the orifice diameter criterion would be about 0.12 in. which is large compared to the actual diameter of 0.03 in. for the NTF transducers.

Using empirically determined relationships for the one-dimensional longitudinal and lateral cross-spectral density for the turbulent wall boundary layer, Corcos (1963, 1967) developed a correction procedure for the power spectral density as a function of a non-dimensional (similarity) reduced frequency. The correction gives the ratio of the measured to actual power spectral density at a given reduced frequency caused by the averaging effect of the finite size of the transducer orifice. However, both Willwarth and Roos (1965) and Schewe (1983) indicate that the Corcos correction may not be adequate at high frequencies.

Schewe (1983) measured the fluctuating wall static pressures beneath turbulent boundary layers with pressure transducers of different sizes. Schewe's results showed increased spatial resolution as a function of the reduced diameter of the pressure transducer diaphragm expressed in terms of wall coordinates (essentially the Reynolds number of the diaphragm diameter based on the friction velocity). Schewe concluded that a diaphragm diameter of about 20 in wall coordinates was adequate to resolve the pressure

structures in a turbulent boundary layer. For the NTF, Schewe's criterion for transducer diameter would pose an unusually stringent requirement on the pressure transducers. For the NTF sidewall installation, the orifice diameter in wall coordinates was estimated to vary from about 50 to over 6000. Only for the pressure transducer in the settling chamber, and only for the lowest free-stream Reynolds number, with an estimated orifice diameter in wall coordinates of about 13, did the orifice size even approach Schewe's criterion. It was concluded that no realistic size of orifice diameter for the NTF pressure transducers could have satisfied Schewe's criterion at the NTF test conditions. For the NTF data, no corrections have been made to the spectra for the turbulent boundary layer fluctuations or for the size of the transducer relative to the boundary layer.

The data channels for the RHS sta 13 test section sidewall location and for the 10.6° cone were two of the four channels analyzed on-line with the spectral analyzer. The mean square data and the 20 kHz bandwidth spectra for these two channels on the spectral analyzer had a maximum dynamic range of 76 dB. All other data were analyzed off-line and were limited to the maximum signal-to-noise ratio of 47 dB characteristic of the playback performance of the 28 track FM tape recorder.

2.4.3 Statistical Reliability

Bendat and Piersol (1980) list several factors affecting errors in the statistical analysis of random data. Among these factors are measurement transducers, signal conditioners, magnetic tape recording, analog-to-digital conversion, pre-analysis data conditioning, stationarity (ergodicity), finite sample length, random error and bias (systematic) error. The last few factors are the ones involved in statistical analysis errors. For the NTF data, stationarity is obtained by holding all of the test conditions which are subject to control as nearly constant as possible over the time interval of the data sample. A long sample length, generally on the order of 30 seconds was used for most of the data analyses, although sometimes even longer samples were used where it was advantageous to do so, for example, on the cross-correlation analyses.

With certain simplifying asssumptions, Bendat and Piersol (1980) show that the normalized random error for a power spectral density estimate is inversely proportional to the square root of the number of distinct averages used in the computation. For most of the NTF power spectral density data, 100 averages were used so the normalized random error was on the order of 10%, and the same error for the rms data was on the order of 5%. A Hanning window was used for all the spectral analyses. For the type of random data analyzed herein, the normalized bias error is expected to be small compared to the random error, and being frequency specific, cannot be quoted in general terms.

2.4.4 Data Repeatability

During the cryogenic phase of testing, a single test condition nominally at a Mach number of 0.8 and a Reynolds number of 40 million per foot was repeated to give a total of five data points all at the same nominal test condition except for the wall-to-gas temperature ratio. The repeatability of these test conditions and of the rms fluctuating pressure coefficient at the RHS sta 13 on the test section sidewall was as follows:

Mach number (M)	±0.001
Reynolds number (R)	±0.5 million per ft.
dynamic pressure (q)	±0.3%
velocity (V)	±3 fps
stagnation pressure (p_t)	±0.1%
stagnation temperature (T_t)	±1.5°F
rms fluctuating pressure coefficient ($\tilde{p}/q$)	±2%

3.0 TESTS

With the exception of some preliminary tests which were performed during the steady state calibration with a centerline calibration probe in the test section, all of the dynamic investigation was performed with the test section empty and as noted earlier a 10.6° cone fairing covered the model support strut centerbody. The NTF steady state calibration, reported by Williams and Adcock (1993), was done only with the test section slots open and used the plenum static pressure as the calibration reference pressure. For the dynamic measurements, with a couple of exceptions, the test section geometry variables of test section wall divergence, reentry flap angle and model support wall angle were positioned at the wall settings developed during the NTF steady state calibration to obtain minimum longitudinal static pressure gradients. The exceptions were when the effects of variation in wall divergence, flap angle and model support wall angle were being investigated, and when the slots were covered. The presence of the slot covers changed the test section static pressure gradient and also rendered the plenum pressure unusable as a reference. For the latter case, that is slots covered, it was necessary to take special steps, not only to obtain a satisfactory reference pressure, but also to ascertain the effects of the slot covers on the static pressure gradient.

3.1 Static Pressure Gradient

The reason for interest in longitudinal static pressure gradients in the test section is that gradients tend to promote interaction between the turbulent fields of fluctuations in velocity, pressure, and temperature, and can distort the spectra at high frequencies. In order for the dynamic measurements to be representative for aerodynamic research conditions, it is necessary to make these measurements under the same flow conditions as are encountered in the aerodynamic research.

Generally, for aerodynamic research purposes, it is desirable to have as small a gradient as possible as a means of more closely duplicating free air conditions. When longitudinal static pressure gradients are encountered in aerodynamic research, for

example on force test models, the gradients are usually accounted for by introducing longitudinal buoyancy corrections to the force data. Since the NTF is capable of variable wall divergence, it is at least hypothetically possible to reduce the longitudinal buoyancy in the NTF to a vanishingly small amount, but in reality this is seldom actually accomplished. One of the objectives in the NTF steady state calibration was to determine the sensitivity of the longitudinal static pressure gradient to wall divergence angle. In a solid wall test section, the sensitivity is high and only small wall angle changes are needed to cancel gradients. However, in a ventilated wall test section, the flow is in intimate communication with the plenum which is a uniform pressure reservoir. As a consequence, the longitudinal gradients are automatically very small, but are also less sensitive to change in wall angle.

If consideration is restricted to a linear change of static pressure with longitudinal distance, and if some further simplifying assumptions are invoked, it is possible to obtain some general results on buoyancy effects as indicated in Appendix B. These results are based on the maximum recommended size limits for models in transonic testing as indicated by Baals and Stokes (1971), and Monti (1971). The results are shown in figure 15 as a test section longitudinal static pressure gradient which would cause one count (defined as 0.0001) of buoyancy-induced incremental drag coefficient on a large model. Other gradients are obtained by scaling linearly up or down according to the chosen allowable level of buoyancy drag. Figure 16 shows the same gradient expressed in terms of Mach number.

For the steady state calibration, an extensive distribution of static pressure orifices (25) was available in the centerline calibration probe. The individual pressures for each orifice were determined using an electronically scanned pressure (ESP) unit with a maximum pressure range of ± 2.5 psi and a specified error of no more than 0.15 percent of full range. Appendix C shows that a least squares straight line fit to the longitudinal static pressure variation can be determined from the above instrumentation as accurately

as shown by the lower dashed line in figure 15 for the gradients determined using the centerline calibration probe. In order to determine the static pressure gradients with the slots covered, static pressure orifices in the walls were used. The same ESP unit was used but far fewer orifices (13) were available resulting in the somewhat degraded accuracy levels shown in figure 15 by the upper dashed line. The same gradient error information is shown is figure 16 in terms of Mach number.

3.2 Air Mode Tests

The NTF performance envelope for air mode operation [due to Adcock (1992)] is shown in figure 17. The boundaries are formed on the bottom by the minimum operating pressure of about 1 atm, on the LHS by the minimum Mach number of about 0.1, on the RHS by the maximum fan rpm, on the top left by the maximum pressure limit of the shell of 130 psi, and on the top right by the cooling capacity of the water-cooled heat exchanger. The symbols shown on this figure indicate the test conditions at which dynamic data were obtained. These conditions include Mach number variations along the minimum pressure boundary, along the maximum performance boundary, at a constant Reynolds number of 6 million per ft, and a Reynolds number variation at a constant Mach number of 0.5.

At a constant Reynolds number of 6 million per ft., the effect of changing Mach number using the inlet guide vanes with the fan rotational speed constant at 550 rpm was investigated at Mach numbers from 0.6 to 1.0. A comparison was made at the same Reynolds number, changing Mach number by varying the fan rotational speed and keeping the inlet guide vanes fixed at 0°. In addition, also at the same Reynolds number, and at a Mach number of 0.8, the effects of variable test section wall geometry, test section wall divergence from 0.3° converged to 0.3° diverged, reentry flap deflection from −1.5° (toward flow) to 2° (away from flow), and of test section wall to model support wall step height from 4.0 in. to 6.2 in. (0.08 to 0.13 as a fraction of test section semi-height) were investigated.

Along the minimum pressure boundary, the effect of slot covers was investigated at Mach numbers from 0.2 to 0.9. The slot covers are shown in place in the photograph of figure 18. The effect of a downstream choke was investigated both with slots open and slots covered at a Mach number of 0.8. On the 10.6° cone, the effect of free transition was investigated at Mach numbers from 0.1 to 0.8.

At a constant Mach number of 0.5, the effect of varying Reynolds number from 2.9 million to 19 million per ft. by variation in total pressure was investigated, with transition both fixed and free on the 10.6° cone. For all other tests, the transition on the cone was fixed near the tip. The transition strip consisted of number 80 (0.007 in.) grit sparsely distributed in a 0.1 in. wide band 2 in. downstream from the tip. The choice of grit size and location was guided by the criteria given by Braslow and Knox (1958) and by Braslow, Hicks, and Harris (1966).

3.3 Cryogenic Mode Tests

The NTF performance envelope in the cryogenic mode of operation [due to Fuller (1980)] is shown in figure 19 for a stagnation temperature chosen so as to avoid local condensation of nitrogen over the surface of a test model assuming an arbitrary local Mach number of 1.4. As a consequence, the minimum temperature assumed in figure 19 varies as a function of the free stream Mach number and the stagnation pressure. For general purposes, a nominal temperature of $-250°$F may be used as a minimum operating temperature.

The boundaries of the NTF performance envelope are encountered at the bottom by a minimum operating pressure of about 20 psi, on the LHS by a minimum Mach number of about 0.2, on the top left by the maximum pressure of 130 psi, on the top right by the maximum power of 126,000 hp and on the RHS by the maximum Mach number of 1.2. The maximum Reynolds number available in the NTF is about 146 million per ft. and occurs at a Mach number of one. At this test condition, the maximum dynamic pressure is about 7,000 psf.

The symbols shown in figure 19 indicate the test conditions at which dynamic measurements were obtained in the cryogenic mode of operation. As shown at the bottom of the figure, Mach number was varied from 0.2 to 1.05 at a constant Reynolds number of 6 million per ft. This test was done in warm nitrogen to correspond to the similar test in air and provide a direct comparison between results in air and in nitrogen. The test points in nitrogen were taken at the same temperature as those in air, and the pressure was adjusted to give the same Reynolds number for each Mach number. In retrospect, it might have been better to have adjusted the temperature to give the same stagnation speed of sound and then adjusted the pressure to match Reynolds number. This point will be examined further when the results are discussed (section 4.3).

The other test points shown in figure 19 were chosen to give as complete coverage of the operating envelope as possible under the circumstances of limited resources of liquid nitrogen. At a pressure of 43.2 psi and a temperature of $-250°F$, the Mach number was varied from 0.2 to 1.0. A single point was taken at a Mach number of 0.8 and a pressure of 80 psi at the same $-250°F$ temperature. The points near the upper boundary were taken at near maximum pressure and at the same temperature. A single point was taken at a Mach number of 1.2 at a pressure of 20 psi and a temperature of $-158°F$.

As mentioned earlier, the special cryogenic features of the NTF made it possible to isolate effects such as variations in Mach number, Reynolds number, and drive power. In a conventional wind tunnel, the operating temperature is usually fixed within narrow limits, and Reynolds number changes are obtained by pressure changes with an accompanying change in drive power. Generally speaking, the same is true for Mach number variations. However, in a cryogenic tunnel such as the NTF, it is possible to vary Mach number holding Reynolds number and drive power constant by appropriate variation of the pressure and temperature. Similarly, it is possible to vary Reynolds number holding Mach number and drive power constant. It is also possible to vary drive power, holding Mach number and Reynolds number constant. These latter two

variations are indicated in figure 20 which shows an operating envelope (due to Adcock (1992)) for a Mach number of 0.8. The Reynolds number variation at constant power is shown along a constant power line of 30 MW. The drive power variation at constant Reynolds number is shown at 40 million per ft. The Mach number variation at constant Reynolds number and drive power can be visualized as occurring normal to the page, going through successive points at different Mach numbers, all at a Reynolds number of 40 million per ft. and a drive power of 30 MW. Figure 20 also shows a variation of Reynolds number by varying pressure holding temperature constant at $-230°F$, and by varying temperature, holding pressure constant at 43.2 psi. It may be noted that all of these variations pass through a common point at a Mach number of 0.8, Reynolds number of 40 million per ft., drive power of 30 MW, pressure of 43.2 psi and temperature of $-230°F$. This point was repeated each time but was usually approached from different previous conditions such that the wall temperatures were not in thermal equilibrium with the gas temperature thus permitting a limited study of the effect of hot wall or cold wall on the measured wall pressure fluctuations.

The effect of hot wall and cold wall was studied further during the initial cool-down of the NTF from near ambient temperature to cryogenic temperatures during this investigation. One of the design conditions for the structure of the NTF was that it be able to withstand the thermal effects of a rapid cool-down or warm-up of 80°F. This rapid change of temperature was done at a Mach number of 0.8 and a stagnation pressure of 25 psi, producing fairly large differences in wall temperature compared to adiabatic wall temperature. For these hot wall/cold wall tests, the adiabatic wall temperature was calculated assuming a recovery factor equal to the cube root of the Prandtl number.

During the steady state calibration of the NTF, an attempt was made to obtain some preliminary dynamic measurements. If the requirements for both the steady state and the dynamic measurements could have been satisfied at the same time, it would have been

an efficient use of tunnel test time and of liquid nitrogen resources. The consequences of these preliminary simultaneous measurements are discussed in Appendix D.

4.0 DISCUSSION OF RESULTS

The dynamic data are presented in the form of a dynamic pressure coefficient $\tilde{p}/q$ where $\tilde{p}$ is the root-mean-square (rms) value of the fluctuating static pressure readings with the mean subtracted. The fluctuating pressure coefficients were computed for all the pressure transducer outputs using the dynamic pressure in the test section except for the transducer in the settling chamber where the local flow conditions were measured using a pitot-static probe. For this pressure transducer, the dynamic pressure in the settling chamber was used.

The fluctuating components were recorded in analog form on FM magnetic tape and were played back into a spectral analyzer, four channels at a time. The analyzer which was used had an upper frequency limit of 20 kHz per channel when four channels were analyzed simultaneously because the maximum digital sampling rate was 51.2 kHz per channel in this mode of operation. The mean-square values were obtained by integration of the power spectra from 0 to 20 kHz. The power spectra presented in figure 21 show some of the consequences of terminating the integration of the spectra at 20 kHz. One of the spectra is for the transducer in the test section sidewall at station 13. The other is for the transducer in the 10.6° cone. Both spectra are from ambient temperature air mode tests at a Mach number of 0.8 and a Reynolds number of 3.8 million per ft. which corresponds to the minimum pressure boundary in air. The numbers at the top of the grid in figure 21 are the rms fluctuating pressure coefficients corresponding to the integrated mean-square values when the integration is terminated at that frequency. There is a 1 to 1.5 percent reduction in the coefficient as the integration range is shortened from 40 kHz to 20 kHz.

As indicated by Mabey (1971), disturbances propagating upstream from the extraction region and the high speed diffuser are major sources of high levels of fluctuating static pressure in slotted transonic test sections at high subsonic speeds. Measurements presented by Mabey show that the disturbance levels are a strong function of the

longitudinal location of the measurement, being highest near the downstream end of the test section, and diminishing sharply in strength toward the upstream end. A similar though not so pronounced variation occurred in the NTF test section as shown in figure 22 where RHS sidewall data at stations 6.5, 13, and 16 are shown with data from the 10.6° cone at station 17.6 for a Mach number of 0.8. Because of the variation of disturbance level with location in the test section and since station 13 corresponds with the center of the calibrated region of the test section, and is the center of pitch rotation for models tested at angle of attack, data for this station are used to represent the test section disturbance levels for the NTF.

4.1 Effect of Hot Wall and Cold Wall

Whenever the test gas temperature is changed, there is a thermal lag of the temperature of the tunnel structure; the larger and more rapid the temperature change, the larger the lag. When the NTF is cooled from ambient temperature down to cryogenic temperatures, the cooling process can take 4 to 5 hours to avoid large temperature differences in the structure and the thermal strains which accompany them. During this cooling process, the tunnel flow conditions are only high enough to promote satisfactory heat transfer, and not much liquid nitrogen is consumed in the process. However, when gas temperature changes are made at research conditions, the liquid nitrogen flow rates can be much higher, and any delays in reaching stabilized test conditions can be very costly in terms of nitrogen consumption. During the dynamic investigation, the concern was whether or not differences in wall temperature compared to gas temperature would have a significant effect on the measured fluctuating pressures. These temperature differences affect the wall shear stress and the thickness and stability of the boundary layer, so the question was to what extent the fluctuating pressures would be similarly affected.

Fluctuating pressure data obtained on the RHS test section wall at station 13 during the initial cooldown of the NTF for this investigation are shown by the square symbols

in figure 23. There is a tendency for the cold wall data to have a higher level than the hot wall data but the differences are slight except for the point on the extreme right of the figure. The temperature differences obtained during the cooldown were greater than those encountered during the normal research test conditions. The data point shown in figure 20, which was repeated several times, resulted in the pressure fluctuation data shown by the circles in figure 23. The temperature differences encountered for these data are more nearly typical of what occurred during the dynamic investigation. Over this more limited range, the effects appear quite small and indicate that wall temperature differences can be ignored in the dynamic data.

4.2 Effect of Fixing Boundary Layer Transition on 10.6° Cone

The fluctuating pressure coefficient measured on the 10.6° cone with fixed and free boundary layer transition is shown in figure 24(a). These data were taken along the minimum Reynolds number boundary in the air mode of operation at ambient temperature and a stagnation pressure of 15 psi. As described earlier, the transition strip consisted of No. 80 grit sparsely distributed in a 0.1 in. wide band 2 in. downstream of the tip of the cone. With free transition, at low Mach numbers, from 0.1 to 0.4, the cone apparently had a laminar boundary layer extending past the location of the cone pressure transducer at 10.4 in. from the tip. Boundary layer transition from laminar to turbulent flow was detected in time history traces of the 10.6° cone pressure transducer signal on an oscilloscope by observation of the occurrence of intermittent pressure spikes in the time history signal. At a Mach number of 0.5, the boundary layer was transitional at the pressure transducer and continued so up to a Mach number of 0.7, at which point the boundary layer was fully turbulent and developed trends similar to the results for fixed transition. For the free transition case, very low levels of fluctuating pressure coefficient (as low as 0.001) were measured beneath the laminar boundary layer and very high levels (as high as 0.023) were measured beneath the transitional boundary layer.

Further effects of fixing boundary layer transition on the 10.6° cone are shown in figure 24(b) for a Mach number of 0.5 at Reynolds numbers from about 3 million per ft. to 20 million per ft. For Reynolds numbers above 6 million per ft., the results for free transition are very close to those for fixed transition indicating that the boundary layer is fully turbulent in this range. However, at a Reynolds number of 3 million per ft., the results for free transition are influenced by a transitional boundary layer. The lack of agreement for the repeat points here and in figure 24(a) is indicative of how sensitive the transitional boundary layer is to minor variations in test conditions. In order to avoid this sensitivity and to avoid such wide and abrupt variations in transducer response as shown in figure 24, most of the dynamic investigation was performed with the boundary layer transition fixed on the 10.6° cone.

Measurements beneath a laminar boundary layer would ordinarily be preferrable because they would be uncontaminated by the higher pressure fluctuation levels associated with a turbulent boundary layer, and would thereby more closely represent the fluctuation levels occurring in the freestream. However such measurements were not possible over most of the operating range of the NTF due both to the limitations on instrumentation, and to the high unit Reynolds number of the wind tunnel flow.

4.3 Comparison Between Air and Gaseous Nitrogen Results

Since air at standard conditions is roughly 78 percent nitrogen, and since both gases behave as diatomic perfect gases at these conditions, it can reasonably be expected that measurements in the two media would compare well. Results for air and gaseous nitrogen, measured on the RHS test section sidewall at station 13, are shown in figure 25 for a Reynolds number of 6 million per ft. Wide bandwidth (0–20 kHz) spectra for the rms data of figure 25 are shown in figure 26. The differences between the spectra from the air and nitrogen tests are primarily broad-band in nature with the exception of the spectra for the Mach numbers of 0.2 and 0.7 in figures 26(a) and (f) respectively. At a Mach number of 0.2, the spectrum for nitrogen shows a peak at about 3.2 kHz.

This peak is thought to be due to an acoustic standing wave associated with the heat exchanger in the settling chamber. At a Mach number of 0.7, both the air and the nitrogen spectra show a peak at about 850 Hz. Reduced bandwidth (0–2 kHz) spectra for this Mach number are shown in figure 27. The improved frequency resolution in this bandwidth shows that the peak in air is at 840 Hz, and in nitrogen at 855 Hz. These frequencies appear proportional to velocity in that both have about the same reduced frequency suggesting the possibility that they are aerodynamic in origin.

Although the Mach numbers and Reynolds numbers were the same for the air and nitrogen data, the velocities were not the same. This mismatch in velocity was a consequence of the way the test conditions were reproduced. As was mentioned earlier, the Mach numbers and the stagnation temperatures were matched, and the stagnation pressures were adjusted to match the Reynolds numbers. Because of the difference in gas constants, nominally 1716 $ft^2/sec^2{}^\circ R$ for air and 1775 $ft^2/sec^2{}^\circ R$ for nitrogen, the velocities are approximately mismatched by the square root of the ratio of the two gas constants. If the stagnation speed of sound had been matched instead of the temperatures, the velocities would then have been matched. The importance of velocity matching lies in the fact that the frequencies of aerodynamic disturbances such as vortex shedding or edge-tones are proportional to velocity so in order to reproduce these aerodynamic disturbances faithfully, the velocity should be matched as well as Mach number and Reynolds number. The large difference in amplitude between the two peaks in figure 27 raises the possibility that the aerodynamic disturbance may be coupling with another disturbance that is sensitive to resonance conditions, and may be sharply tuned.

Power spectra for the settling chamber, plenum, high speed diffuser, and liquid nitrogen injection station are shown in figure 28 at ambient temperature for air and nitrogen at a Mach number of 0.7. Stations in the settling chamber upstream of the test section, and in the high speed diffuser and at the liquid nitrogen injectors downstream of the test section do not show peaks in the 850 Hz frequency range, indicating that the

source of this disturbance is apparently localized to the vicinity of the test section and the plenum. The disturbance is present in the test section at the same Mach number with the slots covered as shown by the spectrum in figure 29, indicating that it is not directly connected with the slots or the extraction region where the flow that has entered the plenum through the slots is reintroduced back into the main stream. However, there may be an indirect connection with the extraction region since various mechanical gaps exist there even with the slots covered, and many possible sources, including edge-tone sources, remain and cannot be eliminated from consideration.

The phase shift between adjacent pressure transducers spaced 2.25 in. apart streamwise on the RHS test section sidewall at station 13 is shown in figure 30 as a function of frequency in the range from 0 to 2 kHz at a Mach number of 0.7 for both air and nitrogen. The phase angle shown is of the downstream transducer signal with respect to the upstream transducer signal so a positive phase shift indicates that the downstream signal is leading the upstream signal and that therefore, the disturbance is propagating in the upstream direction. Further comment on the source of the 850 Hz disturbance will be reserved until the Mach number effects at constant Reynolds number and drivepower are discussed in section 4.6.1.

4.4 Effect of Drivepower Variation at Constant Mach Number and Reynolds Number

Mach number, Reynolds number, and drivepower are three of the most influential factors affecting the disturbance level in wind tunnels. The test point variation shown in figure 20 illustrates the way in which either Reynolds number or drivepower can be varied holding the other two parameters constant. Although not shown in figure 20, the same can be done for Mach number. The significance of this test technique is that it allows a separation of the effects of the three variables, something not possible before the advent of the cryogenic wind tunnel.

As indicated in figure 20, at a Mach number of 0.8, the drivepower was varied from about 24 MW to 53 MW holding Reynolds number constant at 40 million per ft. The results of this test are shown in figure 31 for the RHS test section sidewall at station 13. The variation of fluctuating pressure coefficient is mostly flat with a slight tendency to rise with increased power. The results indicate that, at least at these test conditions, the disturbance level as measured by the fluctuating static pressure coefficient on the test section sidewall is relatively insensitive to variations in drivepower. The variable power data in figure 31 were taken with the drive fan system at a constant synchronous speed of 360 rpm. The effect of blade tip speed will be examined in section 4.6.3.3.

4.5 Variation of Fluctuating Pressure Coefficient with Reynolds Number

4.5.1 Effect of Constant Stagnation Pressure, Stagnation Temperature, or Drivepower

The matrix of test points shown in figure 20 includes Reynolds number variations along three paths, constant pressure, constant temperature, and constant drivepower. The results of these three variations are shown in figure 32 for the RHS test section sidewall at station 13 for a Mach number of 0.8. Above a Reynolds number of 40 million per ft., the disturbance levels are all about the same with a coefficient value of about 0.0095. At lower Reynolds numbers, the high levels or low levels of disturbance are associated with the presence or absence of discrete frequency peaks in the respective power spectra. The group of points at a Reynolds number of 40 million per ft. are essentially repeat points, all with the same values of stagnation pressure (43.2 psi), stagnation temperature (−230°F), drivepower (30 MW), and Mach number (0.8). As was mentioned in the discussion of hot wall-cold wall effects, the disturbance levels may be affected by the different wall temperatures which occur because of the different prior run temperature history of the way the data points were approached. As before, the differences in disturbance level are seen to be slight.

The variation of disturbance level with Reynolds number at constant drivepower shown in figure 32 is of particular significance because, as has already been indicated,

this type of data has not been previously available. A principal result of this test series is that the variation of disturbance level with Reynolds number at constant drivepower for a constant Mach number of 0.8 is relatively flat at Reynolds numbers from 20 to 50 million per ft. It may be noted that since the peak disturbance levels generally occur around a Mach number of 0.8, it is these peak disturbance levels which appear relatively insensitive to Reynolds number variation.

4.5.2 Effect of Reynolds Number in Air

The variation of the fluctuating pressure coefficient with Reynolds number on the RHS test section sidewall at station 13 is shown in figure 33 for a Mach number of 0.5 in air at ambient temperature. The Reynolds number range from about 3 million per ft. to 20 million per ft. was obtained by variation of stagnation pressure from 15 psi to 105 psi. As a consequence, the drivepower varied from 7.7 MW to 41.4 MW. The disturbance level on the sidewall decreased monotonically with increasing Reynolds number in this range of test variables.

The disturbance level measured on the 10.6° cone with fixed transition at the same test conditions as above has already been shown in figure 24(b). Except at the lowest Reynolds number, the trend of disturbance level is upward with increasing Reynolds number. This of course, is opposite to what was observed above on the test section sidewall but it must be borne in mind that the boundary layers in these two instances are very different. The boundary layer on the cone is undoubtedly very thin compared to that on the sidewall. On the cone, the distance from the origin of the boundary layer to the location of the orifice is less than one foot. For the test section sidewall, the virtual origin for the boundary layer probably lies somewhere in the upstream section of the contraction, possibly as much as 50 ft. from the transducer. The Reynolds numbers based on length for these two examples, wall and cone, therefore differ by this approximately 50 to 1 proportion, and will not be at all comparable to each other.

4.6 Variation of Fluctuating Pressure Coefficient With Mach Number

4.6.1 Mach Number Effects at Constant Reynolds Number and Drivepower

As was mentioned in the description of the tests, by appropriate variation of pressure and temperature, a variation of Mach number can be obtained holding Reynolds number and drivepower constant. The significance of this test technique is that it allows an isolation of the effects of Mach number separate from those of Reynolds number and drivepower, which as has already been noted, are three of the most influential factors in wind tunnel disturbance levels. The fluctuating pressure coefficients measured on the RHS test section sidewall at station 13 are shown in figure 34 for a Reynolds number of 40 million per ft. and a drivepower of 30 megawatts, held constant over a Mach number range from 0.6 to 1.0. As can be seen, the disturbance level variation with pure Mach number variation is similar to what was shown earlier in figure 25 and is a general characteristic for these and all other test section results in that the disturbance level peaks at high subsonic Mach numbers near 0.8 and falls off as a Mach number of 1.0 is approached. The fall-off above a Mach number of about 0.8 may be at least partially due to a choking effect that prevents downstream disturbances from propagating upstream into the test section. At the near-sonic speeds, all the results tend to converge on some lower level, in this case, a fluctuating pressure coefficient of about 0.0055.

The behavior of the fluctuating pressure coefficient at Mach numbers from 0.7 to 0.8 in figure 34 is similar to what was shown in figure 25 in the air-nitrogen comparison. The reasons are again to be found in the power spectra which are shown in figure 35. The frequency peaks in the 0.8 to 1.0 kHz range are seen in almost all the data points, and in particular at 860 Hz for $M = 0.694$, at 900 Hz for $M = 0.742$, and somewhat less prominently at 960 Hz for $M = 0.793$ in figures 35(b), (c), and (d), respectively. Again as earlier, for these Mach numbers, the phase shift between adjacent pressure transducers at station 13 as shown in figure 36 indicated an upstream propagation of disturbances at these frequencies. Since figure 35(g) for $M = 0.992$ also showed a disturbance at

960 Hz, it indicated that disturbances at these frequencies were not being choked off and so they probably did not originate downstream of the test section. The disturbances did not appear in the spectra for the settling chamber which indicated that the source once again is probably localized to the test section or plenum. The most likely area of origin is the extraction region at the downstream end of the test section.

The reduced frequencies shown in figure 35 are not constant. The lack of constancy may be associated with the test conditions required to achieve constant Reynolds number and constant drivepower simultaneously. Both the temperature and the pressure had to be varied over a fairly wide range. The pressure varied from 71 psi to 34 psi, and the temperature varied from $-174°F$ to $-250°F$, respectively. The temperature changes cause thermally induced changes in the dimensions of the test section. The pressure changes can contribute to the dimensional changes as well. Thus, if the extraction region of the test section is involved in the disturbances, then the dimensional changes can be responsible for changes in frequency especially if the disturbances are associated with edge-tone effects. As was the case with the air-nitrogen comparison, in the absence of more information, it is only possible to comment on the probable source of these disturbances.

An estimation of possible edge-tone frequencies associated with the geometry of the side-wall re-entry flaps at the downstream end of the test section near station 20 is presented in Appendix E. While not conclusive, the frequency estimation can be viewed as supportive of the possibility that the disturbance peaks in the spectra of figures 27 and 35 are caused by edge-tones.

Of the three variables which have been examined, Mach number, Reynolds number, and drive power, it is apparent that, at least within the range of variables considered here, Mach number effects are predominant on the fluctuating pressure coefficients. This result should not be interpreted as indicating that Reynolds number and drive power are unimportant in determining disturbance levels but rather that the coefficient formed by

dividing the rms fluctuating pressure by the dynamic pressure serves to collapse some of these effects, particularly in the case of drivepower. This collapsing effect of the dynamic pressure also occurs on the Mach number effects as would become apparent if the coefficient were formed by dividing by the static pressure instead of the dynamic pressure as is sometimes done.

4.6.2 Nitrogen Mode Performance Envelope Results

The fluctuating pressure coefficients measured on the RHS test section sidewall at station 13 for the test points in the nitrogen mode of operation indicated in figure 19 are shown in figure 37. The data for the maximum Reynolds number boundary and for the constant stagnation pressure of 43.2 psi were obtained at a constant stagnation temperature of $-250°F$. The data for a constant Reynolds number of 6 million per ft. were obtained at ambient temperatures and are the same as those shown in figure 25. They are included here for comparison. A single data point obtained at a Mach number of 1.2 and a Reynolds number of 14.3 million per ft. is also included.

To show frequency content, power spectra for the high Reynolds number data of figure 37 are presented in figures 38 and 39. For those Mach numbers where comparable data exist, the spectra for the maximum Reynolds number boundary and for a stagnation pressure of 43.2 psi are very similar. Figure 38 shows wide-band spectra from zero to 20 kHz, and figure 39 shows the same data over a reduced bandwidth of zero to 2 kHz. For Mach numbers of 0.2 and 0.4, a frequency peak at about 2 kHz is thought to be due to an acoustic standing wave associated with the heat exchanger in the settling chamber. At Mach numbers of 0.6 and 0.7, the frequency peak at about 800 Hz is thought to be associated with edge-tones originating at the sidewall reentry flaps.

The previously shown insensitivity of the disturbance coefficient levels to drive power and Reynolds number at a Mach number of 0.8 is reflected in the results shown in figure 37. The data for the constant stagnation pressure of 43.2 psi and for the maximum Reynolds number boundary show close agreement at a Mach number of 0.8 despite a

drive power increment from 26.7 MW to 76.6 MW and a Reynolds number increment from 46.0 million per ft. to 132.4 million per ft. The closeness of agreement over the rest of the Mach number range, as well, prompts the speculation that the demonstrated insensitivity may not be limited to a Mach number of 0.8 but may apply more widely.

One result of the apparent insensitivity of the NTF flow disturbance level to Reynolds number may be the possible absence of what is referred to by Elsenaar, Binion, and Stanewsky (1988) as a pseudo—Reynolds number effect (see also the discussion by Bobbitt (1981) on unit Reynolds number effects). This effect is attributed to the variation of the wind tunnel disturbance level with tunnel Reynolds number. Since, as has already been noted, the wind tunnel disturbance level can have such effects as altering the location of transition of the boundary layer, it can therefore cause false results if, when the wind tunnel Reynolds number is varied during an investigation, the disturbance level varies as well. Elsenaar et al. indicate that not only can this pseudo—Reynolds number effect occur most readily if the location of the boundary layer transition is not fixed during an investigation but it can also occur when the boundary layer transition is fixed. The apparent insensitivity of the flow disturbance level to Reynolds number in the NTF cannot be taken as complete assurance that pseudo—Reynolds number effects will not occur in this wind tunnel, but it is clearly a favorable indicator in that direction.

4.6.3 Air Mode Performance Envelope Results

The fluctuating pressure coefficients have been measured as a function of Mach number in the air mode at the Reynolds number ranges indicated on the performance envelope of figure 17. The results for the minimum and maximum Reynolds number boundaries are presented in figure 40 for the RHS test section sidewall at station 13. There is a tendency for there to be more separation of the data with Reynolds number in the air mode than was observed in figure 37 for the nitrogen mode, and the overall level near the peak at a Mach number of 0.8 is lower. Further, in contrast to the nitrogen mode results, the maximum Reynolds number boundary results for the air mode are everywhere

lower than those for the minimum boundary. In most other respects, the Mach number effects are quite similar to what has been observed earlier.

4.6.3.1 Effect of Test Section Slot Covers. Ventilated wall test sections tend to be much noisier than comparable solid wall test sections. In perforated wall test sections, the primary additional noise source tends to be edge-tones associated with the perforation holes. Slotted wall test sections tend to be quieter than perforated wall test sections, with the primary additional noise sources being the free shear layers in the slots and the extraction region of the test section where plenum flows reenter the main stream. By covering the slots, both of these additional noise sources are eliminated. The slot covers which were used are shown in place in the test section in the photograph of figure 18.

With the slots covered and the choke off, the test section wall divergence angle was set at 0.1° on the top and bottom walls. The sidewalls remained parallel. These wall settings resulted in a slight positive static pressure gradient. Quantitatively, the gradients expressed in terms of Mach number varied from $dM/d(x/h)$ of -0.00010 to -0.00595, or in terms of equivalent buoyancy induced drag coefficient increments of figure 16, from less than a half count to somewhat more than four counts of negative buoyancy drag in the Mach number range from 0.2 to 0.9. For reference, the normal operating conditions for the NTF with slots open result in less than one count of buoyancy drag over the entire operating range.

The fluctuating pressure coefficients measured on the RHS test section sidewall at station 13 are shown in figure 41. The data were taken over a Mach number range from 0.2 to 0.9 along the minimum Reynolds number boundary in air. Data taken along the same boundary with the slots open are also shown for comparison. The reduction in disturbance level with slots covered occurs only at the high subsonic Mach numbers above about 0.6. It is possible that this behavior may be connected with incomplete wave reflection at the slotted wall-plenum interface which allows test section disturbances to pass through into the plenum and possibly become dissipated at Mach numbers below

0.618. As was noted earlier in the discussion of the air-nitrogen comparison, the power spectrum with the slots covered (fig. 29) shows a disturbance peak in the 850 Hz frequency range. The presence of these disturbances with the slots covered eliminates any direct connection between these disturbance peaks and the slot flow or the reentry process in the extraction region. This result is supportive of the probability that edge-tone effects associated with the sidewall reentry flap slots are responsible for the large peaks occurring in the spectra of figures 27 and 35.

Broadband (0 to 20 kHz) power spectra for the data of figure 41 with the slots covered are compared to the spectra with the slots open in figure 42. For Mach numbers below 0.6, the power spectral densities for the slots open data are slightly higher than for the slots covered data at low frequency but are lower at high frequency. For Mach numbers above 0.6, the power spectral densities at low frequency for the slots open are significantly higher than for the slots covered but are still lower at the high frequencies. The most significant difference in power apparently occurs at Mach numbers from 0.7 to 0.9 at the low frequencies from zero to about 1 kHz where the power spectral densities for slots open are much higher than for slots covered.

4.6.3.2 Effect of Downstream Choke. A major contributor of broad-band noise at low frequencies is the noise propagating upstream from the diffuser and model support section into the test section. To investigate the effect of a downstream choke, the variable geometry features of the NTF test section were used to create a minimum flow area at the downstream end of the test section. The minimum flow area was located at the hinge line for the top and bottom wall re-entry flaps, creating a two-wall choke. The area was sized so as to choke the flow at this location when the test section Mach number was about 0.8. Although the test section geometry is capable of being fully variable while the tunnel is running, the test section wall angle, the model support wall angle and the reentry flap angles were all pre-set before tunnel start-up and were not varied during the choking runs. The choke geometry was set both for slots-open and slots-covered conditions. Because

of differences in test section wall boundary layer growth with the slots open and covered, the pre-set wall geometry was not identical for the two conditions. The test section wall divergence angle was set to accommodate the calculated boundary layer growth for the closed wall configuration so as to minimize the longitudinal static pressure gradient, and the reentry flap angles were set to blend with the test section wall. The wall geometry settings for the different runs are summarized in table 1. A photograph of the wall geometry at the downstream end of the test section is shown in figure 43. The settings pictured are for the slots-open condition. The photograph was taken when the wall geometry settings were rehearsed prior to the actual dynamic investigation. The sting configuration shown in the photograph was for a model test which was in preparation at the time and was not present during the dynamic investigation.

The effect of the downstream choke is shown by the flagged symbols in figure 41. In operation with the choke in place, the tunnel speed was increased until further increases in drive power did not result in any further increase in tunnel speed as shown in figure 44. The relatively small decrease in disturbance level with the choke deployed, on the order of 0.001 in coefficient, may be an indication that disturbances originating downstream of the test section do not contribute greatly to the disturbance level of the test section. The power spectra for the configuration with slots-open, both choked and unchoked are shown in figure 45 for a Mach number of 0.8. The reduction in disturbance levels due to the choke are seen to occur mainly at the low frequencies from 0 to 5 kHz. From the data shown in figures 41 and 45, it appears that the use of a two-wall downstream choke to reduce flow disturbance levels in the NTF test section resulted in only marginal improvements. It is possible, however, that a different choke configuration might have been more effective.

4.6.3.3 Effect of Fan RPM or Inlet Guide Vane Variation for Velocity Change. As described in Appendix A, the NTF tunnel has two relatively independent means of changing tunnel speed. In normal tunnel operations, when only the power of the

induction motors is required and the synchronous motor is not energized, the tunnel speed can be changed by either fan rpm or inlet guide vane (IGV) variation depending on circumstances. The preferred mode of operation is to select a fixed fan rpm which can be maintained while tunnel speed is varied over the desired range using IGV variation. This is especially true when the tunnel is operated automatically under computer control. Tunnel speed changes can be made much more rapidly by using IGV variation than by using fan rpm variation. When the additional power of the synchronous motor is required and the fan rpm is fixed at synchronous speed, then IGV variation must be used for tunnel speed changes.

A brief test was made to determine if the test section disturbance level would be affected by operation in one or the other of the tunnel speed changing modes. At a constant Reynolds number of 6 million per ft. in the air mode, the tunnel speed was changed from a Mach number of 0.2 to 1.0 using fan rpm variation from 160 to 595 rpm with the IGV fixed at zero degrees (neutral position). At the same test conditions, the tunnel speed was also varied from a Mach number of 0.6 to 1.0 using IGV variation from 25° (fan unloaded) to −20° (fan loaded) at a fan speed of 550 rpm. The results are shown in figure 46 for the RHS test section sidewall at station 13. The close agreement between the two sets of results would indicate that as far as fluctuating static pressure level is concerned it is immaterial which way the tunnel speed is changed, or what combinations of IGV settings and fan rpm settings are used to set a particular Mach number.

The results of this IGV versus rpm investigation also provides some information on the noise characteristics of the NTF fan system. As noted earlier, fan sound power is usually considered proportional to the fan power times the cube of the blade tip speed. Although the inflow velocities at the fan were not measured, they should be essentially a function of Mach number for the test conditions of figure 46, and should be fairly similar for both the variable rpm and the variable IGV data points. Since the blade tip speed is obtained by a vector resolution of the rotational speed and the inflow velocity, its

variation over the Mach number range is different for the variable rpm and the variable IGV data points. For data points of figure 46 below a Mach number of about 0.9, the blade tip speed would be higher for the variable IGV data compared to the variable rpm data, and the opposite is true above this Mach number. However, there is no tendency in the data for the disturbance levels to be similarly disposed. Based on the results in figures 31 and 46, it appears that the disturbance level in the NTF test section is insensitive to variations in either the blade tip speed or the shaft power of the NTF fan drive system.

4.6.3.4 Comparison with Other Wind Tunnels. The fluctuating pressure coefficients measured on the NTF RHS test section sidewall at sta. 13 for the minimum Reynolds number boundary in air (atmospheric stagnation pressure, ambient temperature), repeated from figure 40, are shown in figure 47. Data from Jones (1991) for the NASA Langley 8-Foot Transonic Pressure Tunnel (8-Foot TPT) at similar test conditions are shown for comparison. The 8-Foot TPT data are from a pressure transducer located on the LHS test section sidewall at a station corresponding to the location of test models. The LHS sidewall of 8-Foot TPT is downstream of the inside corner of turn 4, similar to the RHS for the NTF.

No test model was present in the 8-Foot TPT at the time of Jones' measurements, but a nose cone supporting 5 probes was mounted on the centerline model support system for the tunnel. This model support system regularly utilizes a pair of guy wires downstream of the model location to provide lateral restraint for the sting support system. A frequency spike caused by vortex shedding from these guy wires was identified by Jones in the spectra of the 8-Foot TPT fluctuating pressure data. Since the guy wires are normally present for conventional model testing in the 8-Foot TPT, their influence is a normal part of the flow disturbance measurements in that wind tunnel. Jones does not indicate to what extent the guy wire interference may have affected the overall level of the measurements.

The data for the 8-Foot TPT sidewall show the same characteristics as were observed for the NTF data, peaking at high subsonic Mach numbers near 0.8, and falling off steeply as sonic speeds are approached. Both tunnels show similar levels of disturbance, on the order of 0.6%, at low supersonic speeds. At the peak near a Mach number of 0.8, the level is about 1.5% for 8-Foot TPT and 0.8% for NTF.

For reference, the fluctuating pressure coefficient data measured in the NLR-HST by Ross and Rohne (1973) are also shown in figure 47. The NLR-HST data were measured on the AEDC 10° cone which is described by Dougherty (1980). The HST data appear to represent a maximum envelope of disturbance level for the test conditions in that tunnel. These data may not be directly comparable with the 8-Foot TPT or NTF data because of the differences in the methods of measurement. All three tunnels appear to have relatively quiet flows however. The peak level for the NLR-HST is about 1%. On the basis of the data in figure 47, it appears that the NTF has low levels of test section fluctuating static pressure as measured on the test section sidewall especially in the high subsonic Mach number range from 0.7 to 0.9.

As mentioned earlier, wall pressure fluctuations measured beneath a turbulent boundary layer are influenced by disturbance levels generated within the turbulent boundary layer itself. There is an interaction of the turbulence with the mean shear and an interaction of the turbulence with itself. These disturbance levels represent a floor or minimum level that can be measured on a wall. Lowson (1968) has derived an empirical expression for estimating this minimum level for attached equilibrium turbulent boundary layers,

$$\frac{\tilde{p}}{q} = 0.006/(1 + 0.14M^2)$$

which is also shown in figure 47. Most of the wind tunnel data fall above this line.

4.7 Effect of Test Section Geometry Variables

The test section geometry variables consist of variable top and bottom test section wall divergence angle, variable reentry flap angle and variable top and bottom model support section wall angle. The role of the test section wall divergence in controlling longitudinal static pressure gradients has already been mentioned. The reentry flaps can play a similar role for gradients near the downstream end of the test section. The model support section wall angle variation was used in the downstream choke test to form a flow area minimum at the location of the reentry flap hinge line. All three variables affect the tunnel power consumption. The results of the steady state calibration [Williams and Adcock (1993)] were used to select settings of these geometry variables for normal operation of the tunnel, and these settings were used for the dynamic measurements as well.

The effect that the test section geometry variables have on the disturbance level in the test section was investigated briefly by varying each setting through a small range, keeping the other two fixed. The results are shown in figure 48 for the RHS test section sidewall at station 13 for a Mach number of 0.8 and a Reynolds number of 6 million per ft. With the exception of the test section wall divergence angle of 0.3°, all the effects are slight. Wide bandwidth (0–20 kHz) power spectra for the rms data of figure 48 are shown in figure 49. For the data point at 0.3° wall divergence, the power spectrum in figure 49(a) does not show any frequency spikes, only a small broadband increase in disturbance level in the frequency range from about 100 Hz to about 2 kHz. Based on the results in figure 48, the lowest levels of disturbance are obtained at test section wall angles from parallel to slightly converged, reentry flap angles away from the flow, and model support wall angles toward the flow.

4.8 Effect of Liquid Nitrogen Injection

A process capable of spraying as much as 1000 pounds per second of volatile liquid in a confined space has the potential of being a noisemaker. The comparison tests between

air and nitrogen provided an opportunity to compare the disturbance levels at the liquid nitrogen station both with and without injection but at otherwise substantially the same test conditions. This comparison is shown in figure 50 at a test section Reynolds number of 6 million per ft. The pressure coefficient data are plotted as a function of the test section Mach number. Because the liquid nitrogen injection station is downstream of the test section, there is no tendency for the choking effect at the test section to reduce the disturbance levels as test section sonic speeds are approached, so the disturbance levels continue to rise as the Mach number is increased. Power spectra for the rms data of figure 50 are shown in figure 51.

At Mach numbers above 0.6, the disturbance levels are higher in nitrogen than in air. A comparison of the power spectra for these points figure 51(e–l) showed that the increase was primarily broad band, with no particular frequency selectivity apparent. The frequency peaks which were so prominent in the spectra of the test section pressure transducers at these test conditions figures 26, 27 were not evident in the spectra at the liquid nitrogen injection station.

In order to gain some further insight into the effect of liquid nitrogen injection, the output of the dynamic instrumentation was continuously recorded as the injection process was abruptly turned off. The initial test conditions for the cut-off test were a Mach number of 0.8 and a Reynolds number of 12.6 million per ft. The stagnation pressure was 20 psi and the stagnation temperature was $-160°F$. A playback of the continuously recorded data is shown in figure 52 for the settling chamber, RHS test section sidewall station 13, high speed diffuser and liquid nitrogen injection station. The initiation and completion times for the cut-off of injection are shown on the upper grid line. The total cut-off time from initiation to completion took about 12 seconds. The time for a disturbance to propagate by convection completely around the tunnel circuit at this test condition has been estimated to be slightly less than 7 seconds. With the possible exception of the settling chamber trace, the effects of the nitrogen cut-off

were so imperceptible, it was not possible to detect in the data signals just where the cut-off occurred. As will be discussed in the following section 4.9, the settling chamber disturbance level may be influenced by the gaseous nitrogen exhaust which is immediately controlled by the automatic tunnel control process to maintain stagnation pressure when the nitrogen injection is stopped.

During the cut-off procedure, the tunnel control system maintained the Mach number and the stagnation pressure. The stagnation temperature rose rapidly and the test was terminated after a temperature increase of 25°F. Since Mach number was being held constant, the velocity rose with the temperature. Because of the rapid change in temperature and velocity following the cut-off, the test conditions were no longer completely stationary, and the statistical analysis methods used herein were no longer strictly appropriate. However, since the disturbance amplitude did not show drastic changes as seen from the time history traces of figure 52, a short relatively stationary time sample of about 10 seconds before and after cut-off was analyzed for spectral content and rms level. The spectra are shown in figure 53 for the same four tunnel stations whose time traces are shown in figure 52. The rms levels listed on the spectra indicate that the settling chamber disturbance level decreased slightly when the liquid nitrogen injection was stopped, and either remained the same or increased slightly for the other three stations.

The apparent lack of influence of the liquid nitrogen injection process on the level of flow disturbances detected in the test section may be associated with the presence of suspended droplets in the liquid nitrogen spray. Such a droplet suspension could be inhibiting the upstream propagation of broadband fan noise similar to the attenuation of sound propagation in atmospheric fog, thus partially offsetting any direct noise created by the injection process.

4.9 Fluctuating Pressure Coefficient in Settling Chamber

The fluctuating pressure coefficients measured in the settling chamber at the test conditions along the maximum Reynolds number boundary are shown in figure 54. In this figure and in subsequent ones showing the settling chamber disturbance levels, the fluctuating pressure coefficient is formed using the dynamic pressure in the settling chamber, and is plotted as a function of the Mach number or Reynolds number in the test section. Although the coefficient levels are higher in the settling chamber, there is a marked resemblance between this figure and figure 37 which showed the disturbance level in the test section for the same test condition. For the settling chamber, there is a peak response of the fluctuating pressure coefficient of about 0.275 at a Mach number of 0.8, and a sharp drop-off to about 0.125 as sonic speeds in the test section are approached. The similar behavior shown in the two figures suggests that the disturbance levels in the settling chamber are strongly affected by the levels in the test section, indicating that these disturbances may originate in the test section region or further downstream, and propagate upstream from the test section into the settling chamber. This supposition is further borne out by the effect of the downstream choke, shown for the minimum Reynolds number boundary in air in figures 55(a) and (b) with the test section slots open and covered, respectively. When the downstream second minimum is actively choking, the fluctuating levels drop to the same level as when sonic speeds are approached, mirroring the behavior of the test section (fig. 41). There is a significant difference, however, in the levels for the maximum Reynolds number boundary (fig. 54) and the minimum Reynolds number boundary (fig. 55(a)), raising the question whether other influences, possibly fan noise and other disturbances caused by the wide-angle diffuser, the heat exchanger, and the screens, are present in the settling chamber as well, and biasing the results from minimum to maximum Reynolds number.

What follows is essentially an endeavor, by a process of elimination, to arrive at a possible identification of sources of disturbance which could be responsible for the large

differences between the rms data of figures 54 and 55. The settling chamber spectra for the maximum and minimum Reynolds number boundary at a Mach number of 0.8 are shown in figure 56. A comparison of the spectra shows that at frequencies above about 2 kHz, the higher levels of disturbance for the maximum Reynolds number boundary are primarily broadband. However at these frequencies, the contribution to the over-all power is slight. The major differences between the maximum and minimum Reynolds number boundary spectra are in three broad peaks with most of their power concentrated below about 1.2 kHz. The lowest of the three broad peaks contains a small peak at the blade passage frequency of 150 Hz, and another small peak at 110 Hz which is probably associated with vortex shedding from the tubes of the heat exchanger. The small peak at 35 Hz is probably associated with vortex shedding from some of the support structure for the heat exchanger. The support structure in question consists of vertical plates on either side of the individual tube bundles in the heat exchanger. The minor peak at 2165 Hz is probably associated with vortex shedding from the screen wires. The tentative frequency identifications above and to follow are based on assumed Strouhal numbers for the vortex shedding characteristics of the respective components.

At the maximum Reynolds number boundary test condition, the fan was operated at its synchronous speed of 360 rpm. The 25 blades of the fan produce disturbances at the fundamental blade passing frequency of 150 Hz and harmonics at integral multiples of that frequency. Except for the fundamental tone at 150 Hz, none of the blade passing tone harmonics are apparent in the spectrum for the maximum Reynolds number boundary. At the minimum Reynolds number boundary test condition, the fan was operated at its maximum speed of 600 rpm. The fundamental blade passing frequency tone of 250 Hz is barely evident among other minor peaks in that frequency range. The first, second, and third harmonics of the blade passing frequency at 500 Hz, 750 Hz, and 1000 Hz are evident but higher harmonics are not.

For the rest of the low Reynolds number boundary spectrum, the only peaks which can be tentatively identified are again the vortex shedding frequencies; at 50 Hz probably from the support structure of the heat exchanger; at 210 Hz probably from the heat exchanger tubes; and at 3420 Hz probably from the screen wires. These tentatively identified sources for the minimum and maximum Reynolds number boundaries represent only a small fraction of the total power in the respective spectra. If the source identifications are correct, then these sources cannot by themselves be responsible for the differences in the disturbance levels, and some other as yet undetermined factor must be responsible. It may be noted that disturbances from the wide-angle diffuser have not been eliminated from consideration but these disturbances are not likely to be the cause of the discrete peaks which have been observed. Another possibility to be considered, is the venting region in the cross-leg between turns 3 and 4. For the minimum Reynolds number boundary in air, the vent valves are normally closed. However, for the maximum Reynolds number boundary in nitrogen, the valves are open, venting a mass flow at a rate equal to the liquid nitrogen injection rate.

The comparison tests with air and nitrogen provide an opportunity to compare the settling chamber disturbance levels both with and without venting taking place but at otherwise similar test conditions. The fluctuating pressure coefficients in the settling chamber for these two tests are shown in figure 57 for a test section Reynolds number of 6 million per ft. Power spectra at selected Mach numbers for the test points of figure 57 are shown in figure 58. Since the test conditions for the air and nitrogen tests are very nearly identical, the differences between the tests should be directly attributable to the nitrogen injection process and the accompanying venting. The data of figure 50 showed that the injection process did not have much effect at the liquid nitrogen injection station. It can be safely assumed that the injection process will have even less effect at the settling chamber, so the differences which are observed can be attributed primarily to the venting.

The fluctuating pressure coefficient data of figure 57 show a consistent increment in the disturbance level across the Mach number range for the nitrogen test. At Mach numbers of 0.6 and above, the power spectra in figure 58 show both narrow-band and broad-band increases. At a Mach number of 0.2 in the nitrogen mode (fig. 58(a)), the peak at 3.2 kHz is thought to be due to an acoustic standing wave associated with the heat exchanger in the settling chamber. This tentative identification is based on the observation that the frequency did not vary with velocity changes but did vary approximately with the square root of the absolute temperature, and that the dimensions of the lateral spacing of the heat exchanger tubes was about right for a standing wave of this frequency. At Mach numbers of 0.2 and 0.4, the air test data show major frequency peaks at 14.8 kHz and 15.3 kHz, respectively, which are not present in the nitrogen test data. No information is currently available on the noise characteristics of the vent region on which to base any further comment. This area of the tunnel circuit and the venting process require further study.

Data taken at two different test conditions in the nitrogen mode, one at a constant Reynolds number of 40 million per ft. and at a constant drivepower of 30 MW, the other at a constant stagnation pressure of 43.2 psi and a constant stagnation temperature of $-250°F$ are compared in figure 59. The fluctuating pressure coefficients in the settling chamber are relatively insensitive to the differences in the test conditions in this intermediate Reynolds number range. Data taken over a broad range of Reynolds number at a Mach number of 0.8 are shown in figure 60 for test conditions of constant drivepower of 30 MW, constant stagnation temperature of $-230°F$ or constant stagnation pressure of 43.2 psi. These data are also relatively insensitive to the difference in test conditions, and show an increasing level of disturbance with increasing Reynolds number. The effect of the variation of fan drivepower is shown in figure 61 for a Mach number of 0.8 and a Reynolds number of 40 million per ft. The disturbance levels are relatively insensitive to changes in drivepower with only a slight tendency to decrease

with increasing drivepower. Figures 59, 60, and 61 show that the settling chamber responses are similar to those observed in the test section in that disturbance levels are a strong function of Mach number, and are relatively insensitive to drivepower. The effects of Reynolds number, though still slight, appear more distinct in the settling chamber.

4.10 Fluctuating Pressure Coefficient in High Speed Diffuser

The pressure transducer in the high speed diffuser was installed on the LHS at mid-height, about half way downstream (station 68). The fluctuating pressure coefficient was formed by using the dynamic pressure in the test section, and the coefficients were plotted as a function of test section Mach number. Data for the comparison tests in air and nitrogen at ambient temperatures are shown in figure 62 for a Reynolds number of 6 million per ft. Just as was seen for the liquid nitrogen injection station data, the disturbance levels continue to rise as sonic speeds in the test section are approached and exceeded because the measuring station is downstream of the test section, and there is no tendency for the choking effect at the test section to reduce the disturbance levels as test section sonic speeds are approached. In fact, there is a tendency for the disturbance levels to rise more steeply above a Mach number of 0.8. The reason for this may be the formation of unsteady shocks at the end of the test section and the start of the diffuser with their attendant increase in noise levels.

4.11 Fluctuating Pressure Coefficient in Plenum

The pressure transducer in the plenum was installed on the RHS at station 0, near the plenum wall and at the same height as the test section top wall. The measured fluctuating pressure coefficients, formed using the test section dynamic pressure, are shown as a function of the test section Mach number in figure 63. The test conditions represented in figure 63 are the comparison tests between air and nitrogen at a constant Reynolds number of 6 million per ft., and the minimum and maximum Reynolds number boundaries. The disturbance levels in the plenum for these test conditions are very low, increasing from about 0.001 to 0.002 with increasing Mach number from 0.2 to 1.05.

There is very little difference between the air and nitrogen results at the Reynolds number of 6 million per ft. or between the minimum and maximum Reynolds number boundaries.

Power spectra for the minimum Reynolds number boundary data for Mach numbers from 0.2 to 0.642 are shown in figure 64 for a frequency bandwidth from 0 to 1 kHz. At a Mach number of 0.2 (fig. 64(a)), line frequency interference peaks at multiples of 60 Hz are quite evident. The somewhat elevated disturbance level shown for the rms fluctuating pressure coefficient at this Mach number in figure 63(b) may be at least partially due to the interference present in the measurement. It should be noted that this is an exceptional condition where an already quiet signal from the plenum is measured at the lowest operating condition of the tunnel. At most other conditions, the data signal is large enough so that the small line frequency interference is not an appreciable part of the measurement. At a Mach number of 0.3 (fig. 64(b)), the line frequency interference is still evident but not nearly so intrusive as at the lower Mach number. At the higher Mach numbers, the line frequency interference, while still identifiable in some places, is not a significant part of the measurement.

All of the spectra in figure 64 show that there are many disturbance peaks affecting the plenum. Few if any of the peaks can be positively identified as to source, except of course the line frequency interference. Another possible exception is the fan blade passage frequency (BPF) which is known fairly accurately. This frequency (BPF) is noted on each of the spectra. A careful examination of the spectra shows peaks at or very near to this frequency. For instance, at Mach numbers from 0.6 to 0.642 (figs. 64(e), (f), and (g)) the BPF is 227 Hz. There is a modest peak in the spectra at 221 Hz. The frequency resolution in the spectra is about 1 Hz so this modest peak is not close enough in frequency to be identified as the BPF. However, the peak at 221 Hz is distorted on the high frequency side as though a second peak might be there as well. A higher resolution spectrum as shown in figure 65 for a Mach number of 0.6 (corresponding to the spectrum

of figure 64(e)) shows a separate peak of about 225 Hz which probably corresponds to the fan blade passage frequency peak.

Mabey (1976) has indicated that the slots themselves can be sources of regular disturbances with characteristic slot frequencies having Strouhal numbers in the range of 0.03 to 0.04 based on slot width. If a slot Strouhal number of 0.035 is assumed, then the characteristic slot frequencies, f_s, for the NTF slots are as indicated on the spectra of figure 64. It was not possible to make positive identification of this frequency with frequency peaks in the spectra and evidence for their existence in the spectra is not strong.

Multiple acoustic resonances can exist in the plenum but these disturbances have not been considered in the present analysis. However, wind tunnel models which experience unsteady loads and are therefore sources of excitation can be affected by one particular kind of resonance that involves the ventilated test section walls and the plenum. For this kind of resonance, the model is the source of the excitation, either through forced oscillation or aeroelastic vibration response such as flutter or buffet. In this test section-plenum resonance, transverse waves from the test section are partially transmitted through the test section-plenum boundary, travel outward in the plenum, and are reflected from the outer plenum walls back to the ventilated wall interface. If the returning wave is in phase with the outgoing wave, resonance will occur.

This kind of resonance problem has been studied by Mabey (1978), Barger (1981), and Mokry (1983) who developed analytical solutions, and more recently by Lee and Baik (1991) who extended a finite-element numerical solution to include the slotted wall boundary conditions. For resonance frequency estimates in the NTF, the closed form results of Barger were used because the analysis in this reference employed accurate boundary conditions for the slotted walls. The calculated fundamental frequencies for the test section-plenum resonance f_p are indicated on the spectra up to a Mach number of

0.6. Above a Mach number of 0.618, the solution changes character, the reflection from the slotted boundary is complete, and the influence of the plenum is greatly diminished.

As can be seen in the spectra of figure 64, the presence of the test section-plenum resonance peaks cannot be confirmed. In the absence of discrete excitation as might be provided by an oscillating or vibrating test model, this particular form of resonance is not considered to be a problem in the NTF. Apparently, flow unsteadiness by itself is not sufficient to excite this resonance to detectable levels.

Based on the spectra of figure 64, it can be concluded that excitation associated with fan blade passage frequencies, characteristic slot frequencies and slotted wall-plenum resonances do not contribute significantly to the level of disturbance measured in the plenum.

4.12 Convection Velocities

In a shear layer, disturbance patterns are transported with the stream at some fraction of the free stream velocity depending on the scale of the disturbance and on its location within the shear layer. The magnitude of the transport velocity generally depends on the frequency of the disturbance and on the separation distance over which it is measured.

In the NTF, the overall streamwise convection velocity $u_c(x)$ was measured in the test section. Three pressure transducers were spaced 2.25 in. apart streamwise on the RHS test section sidewall at station 13. Cross correlations of unfiltered signals from an adjacent pair of these transducers were used to obtain the transit time between the two transducers for disturbances convecting downstream. A sample cross correlation plot is shown in figure 66 for a Mach number of 1.0 and a Reynolds number of 6 million per ft. This measurement was made in the nitrogen mode at ambient temperatures. For this test point, an overall streamwise convection velocity ratio $u_c(x)/V$ of 0.746 was computed. Data for this and other Mach numbers from 0.2 to 1.05 are shown in figure 67 in comparison with similar data measured in air. The agreement between the two sets of data is sufficient to indicate that there are no significant differences in convection

velocities in the two different test gases. The level is relatively constant across the Mach number range at a level of about 0.76. There is a slight tendency for the level to rise with increasing Mach number.

A similar comparison is shown in figure 68 for slots open compared to slots covered. These data were measured in the air mode along the minimum Reynolds number boundary. Again, the closeness of the comparison indicates no significant effect of slots open compared to slots covered. The overall level at these Reynolds numbers is slightly lower (0.74) than for a Reynolds number of 6 million per ft., and the tendency for the level to rise with increasing Mach number is slightly more pronounced. Since Reynolds number increases with increasing Mach number along the minimum Reynolds number boundary, the apparent increase of convection velocity with Mach number may really be a Reynolds number effect.

The effects of hot wall versus cold wall on the convection velocity are shown in figure 69 for a Mach number of 0.8. There is a slight tendency for the convection velocities to be higher for the hot wall condition than for the cold wall condition, and overall the level is about 0.77. The Reynolds numbers are not constant for these data, ranging from about 7.5 million per ft. for the cold wall data to about 10 million per ft. for the hot wall data. The tendency in the convection velocity data has been for the level to increase slightly as the Reynolds number increased, which might partially account for the apparent effect of the hot wall in figure 69.

The above mentioned effect of Reynolds number is a little more apparent in the data of figure 70 where the convection velocity ratios for the maximum Reynolds number boundary are shown as a function of Mach number. The data for the minimum Reynolds number boundary (air mode-slots open) are repeated from figure 68 for comparison. The convection velocity ratios for intermediate Reynolds numbers at a stagnation pressure of 43.2 psi are also shown. There is a positive increment of about 0.05 in convection

velocity ratio from the minimum to the maximum Reynolds number boundary, with most of the increment occurring from the low to the intermediate Reynolds numbers.

5. CONCLUSIONS

Dynamic measurements of the fluctuating static pressure levels have been made at 11 locations in the circuit of the NTF, over the complete operating range resulting in flow disturbance measurements at the highest Reynolds numbers available in a transonic ground test facility. Tests were made independently at variable Mach number, variable Reynolds number, and variable drive power, each time keeping the other two variables constant, thus allowing for the first time a distinct separation of the effect of these important variables. Tests were also made with independent tunnel speed variation using either variable fan rpm or variable inlet guide vane. An analysis of these dynamic flow disturbance measurements has led to the following conclusions:

1. The results of tests to isolate the effects of Mach number, Reynolds number, and fan drivepower on flow disturbance levels indicate that of the three, Mach number effects predominate. The flow disturbance levels appear relatively insensitive to Reynolds number and drivepower.

2. One of the primary sources of noise in the NTF appears to be flow surface gaps associated with the sidewall re-entry flaps at the downstream end of the test section. The gaps appear capable of producing edge-tones at some flow conditions.

3. A downstream second minimum flow area formed on the top and bottom walls to choke the flow at subsonic test section Mach numbers produced only marginal improvements in the flow disturbance levels in the test section at a choke Mach number of 0.8.

4. The effects on flow disturbance level of intentional differences in temperature between the wall boundaries and the test gas were small, with a tendency for the cold wall data to have a slightly higher disturbance level than the hot wall data. Smaller incidental temperature differences during the tests showed even less effect on the data and were considered negligible.

5. Although indicating general agreement, a comparison between results in air and nitrogen showed differences which were thought to have been caused at least in part by a miss-match in velocity between the two tests.

6. The liquid nitrogen injection process does not contribute significantly to the level of flow disturbance in the test section.

7. Flow disturbance levels in the settling chamber appear to be adversely affected by the gas venting process which occurs during cryogenic operations using nitrogen.

8. Tests with the slots covered showed reductions in the test section sidewall static pressure fluctuation levels only at Mach numbers above 0.6.

9. Test section sidewall static pressure fluctuation levels are relatively independent of the test section geometry settings of wall divergence, re-entry flap angle, and model support wall angle.

10. Tunnel speed changes can be obtained with either fan rpm changes or inlet guide vane changes with no significant difference in test section flow disturbance levels.

11. Fan blade passage frequencies are not a significant contribution to the flow disturbance levels in the tunnel at most operating conditions. These frequencies are only apparent in the spectra at low tunnel operating conditions (corresponding to low Mach number, low stagnation pressure, and low drive power) when the background level of disturbance is sufficiently low. The disturbances associated with the characteristic slot frequencies and slotted wall-plenum resonances are also not significant.

12. Overall streamwise convection velocity ratios $u_c(x)/V$ measured using unfiltered pressure transducer signals on the test section sidewall are relatively unaffected by change in gas type from air to nitrogen, by test section slots open or covered, or by wall-to-gas temperature differences. The convection velocity ratios increase slightly with increasing Reynolds number.

13. A comparison with other transonic wind tunnels shows that the NTF has low levels of test section fluctuating static pressure especially in the high subsonic Mach number range from 0.7 to 0.9.

The following section includes some extended comments on the measured data beyond those specifically enumerated in the Conclusions.

Based on the comments of Mabey (1991), the weak sensitivity of the measured flow disturbances to Reynolds number variation in the NTF may indicate that the flow disturbances being measured could be largely due to aerodynamic noise sources which are controlled by turbulent eddy viscosity effects. Such effects are dependent on typical velocity and eddy sizes and are independent of Reynolds number. Mabey's theory specifically involves the extraction region at the downstream end of the test section where flows which have entered the plenum through the slots re-enter the mainstream. The present results do not specifically confirm the theory of Mabey, but the comparison at high subsonic Mach numbers between slots open and slots covered (fig. 41) is consistent with the Mabey theory.

The lower flow disturbance levels in the test section at Mach numbers below about 0.6 with the slots open compared to slots covered may be connected with the partial transmission of waves at the slotted wall-plenum interface which allows test section disturbances to pass through into the plenum at Mach numbers below 0.618. Waves which enter the plenum may be subject to dissipation effects through multiple reflections from the thermal insulation surface on the interior of the pressure shell or may become trapped by plenum structural elements. At Mach numbers higher than 0.618, the reflection of waves from the slotted boundary is complete, and the attenuating influence of the plenum could be greatly diminished.

Although considered separately in the Conclusions, the effect of power variation and the comparison of fan rpm versus inlet guide vane for changing tunnel speed taken together, appear to indicate that the flow disturbance levels in the NTF test section are

insensitive to either the blade tip speed or the fan shaft power of the NTF fan drive system. At this time it is not known if this apparent insensitivity is a consequence of the extensive noise attenuation treatment of the fan nacelle nose cone and tail cone.

The apparent lack of influence of the liquid nitrogen injection process on the level of flow disturbance detected in the test section may be associated with the presence of suspended droplets in the liquid nitrogen spray. Such a droplet suspension could be inhibiting the upstream propagation of broadband fan noise similar to the attenuation of sound propagation in atmospheric fog, thus partially offsetting any direct noise created by the injection process.

6.0 APPENDICES

6.1 Appendix A. - Detailed Description of the National Transonic Facility

The NTF is a single-return pressurized transonic cryogenic wind tunnel with a slotted square test section, operating at Mach numbers up to 1.2, pressures up to 130 psi and temperatures down to −320°F. Specific components of the wind tunnel are described in this appendix.

6.1.1 Thermal Insulation

Thermal insulation for the tunnel (shown shaded in fig. 6) is internal rather than external to the pressure shell. Being internal, the insulation shields the pressure shell from large temperature changes as the tunnel temperature is varied during the cryogenic mode of operation. Because the pressure shell with its large thermal inertia is not directly involved in changes in gas temperature, liquid nitrogen consumption is reduced and thermal cycling of the pressure shell is avoided.

The insulation itself is a closed-cell, high density, rigid foam of modified polyurethane material. It is attached to the inside of the pressure shell as shown in figure A1, in thicknesses varying from about 6 in. to 7.5 in. It has excellent fire-retardant properties, an important feature for all materials used in a wind tunnel such as the NTF, which can be pressurized to 130 psi in air. As can be seen in figure 6, in the high speed portion of the tunnel, from the start of the wide-angle diffuser downstream to the end of the high-speed diffuser, the insulation is completely isolated from the flow by an internal aerodynamic liner. In the remainder of the tunnel circuit, except for the fan shroud region, the insulation is separated from the flow stream by a relatively thin liner as shown in figure A1. For economy of fabrication, the liner plates are flat aluminum panels, leading to a polygonal (24 sided) cross-section in those parts of the tunnel where these plates are installed, essentially from turn 1 to turn 4, as shown in the photograph of figure A2.

6.1.2 Principal Components

The principal components of the NTF circuit are shown in figure A3. As has already been mentioned, in the cryogenic mode of operation, nitrogen is used as the test gas, with cooling accomplished by the injection of liquid nitrogen directly into the flow stream. The liquid nitrogen injection nozzles are located upstream of the fan nacelle. It has been shown by Adcock (1977) that liquid nitrogen injection upstream of the fan results in lower power requirements and lower liquid nitrogen flow rates compared to downstream injection. This location may also be favorable with respect to the complete evaporation of the injected liquid, with respect to attenuation of upstream moving fan noise by liquid nitrogen spray droplets, and with respect to the level of injection noise which reaches the test section.

The aerodynamic design of the NTF has been strongly influenced by the need for economy of operation. The cryogenic concept permits the achievement of high Reynolds numbers at relatively low energy consumption levels compared to other high Reynolds number ground test facility concepts. However, even for the cryogenic tunnel, the overall consumption of energy is high and must be carefully managed. The main item of energy consumption for the NTF in the cryogenic mode of operation is the energy required to produce the liquid nitrogen used for cooling. In order to minimize the cost of nitrogen required to pressurize the tunnel and also to reduce the cost of the pressure shell, the internal volume of the NTF circuit was designed to be as small as practical. Within these limitations, the settling chamber was made with as great a length as the economics of the pressure shell and the internal fill volume would permit.

The corners of the NTF circuit are mitered to form 90° turns. The turning vanes in these corners have what is known as arithmetic progression spacing, introduced initially by Dimmock (1950) for gas turbine research and used in other wind tunnels such as the LaRC 0.3-Meter Transonic Cryogenic Tunnel, and the RAE 5 Metre Pressurized Low Speed Wind Tunnel.

6.1.2.1 Wide-Angle Diffuser. The wide-angle diffuser shown in figure A4 is located immediately upstream of the settling chamber. The use of a wide-angle diffuser in this location allowed the return duct of the tunnel circuit to be kept to small diameter, but still permitted a large settling chamber and a high contraction ratio with its attendant benefits on tunnel performance and flow quality. The wall curvature in the wide-angle diffuser was designed in the manner described by Küchemann and Weber (1953) to have a nearly constant static pressure along the walls in the streamwise direction. This desired pressure gradient, with its reduced tendency for boundary layer separation, is obtained by proper curvature of the walls. The centrifugal force acting on the flow as it follows the curved wall contour is balanced by the stream pressure gradient as the flow is slowed due to the increased area of the wide-angle diffuser. At the downstream end, the flow direction must be returned toward the axial direction. In the NTF, the turning is accomplished by the finned-tube heat exchanger which also supplies the downstream pressure loss required to prevent flow separation from the diffuser walls. In the heat exchanger, the tubes carrying the cooling water are elliptical in cross-section and are oriented vertically. The plate-like fins attached to the tubes are oriented horizontally. The aerodynamic and gravity loads on the heat exchanger are supported by a truss with radial and annular elements located near the downstream end of the wide-angle diffuser. The annular elements have been shaped so as to conform to the flow field curvature in the streamwise direction. The wide-angle diffuser has an exit-to-inlet area ratio of 2.08, a length-to-inlet diameter ratio of 0.465, and an exit wall angle of about 61°.

6.1.2.2 Turbulence Damping Screens. The exit of the wide-angle diffuser is followed by a settling chamber about 19 ft. long. There are four turbulence damping screens in the settling chamber, spaced 2 ft. apart with the last screen about 5 ft. from the start of the contraction. The four screens are each the same; square-mesh wire cloth woven of 0.032 in. diameter wires at a spacing of 6 wires per in., with a resulting porosity of about

0.65. Because of the large diameter of the settling chamber (35.7 ft.) and of the high pressure at which the NTF can operate (130 psi), the limiting factor in the selection of the screens was the stress in the screen wires under load. The 18 ft. wide rolls of screen cloth are joined together at their edges by butt-welding the individual wires, thereby producing aerodynamically clean seams. The screens are installed pre-slacked to allow them to deflect about 2 ft. downstream under maximum load as a means of reducing the screen wire stress.

6.1.2.3 Contraction Section. The area ratio of the contraction is 14.95 to 1. It was designed to produce uniform flow at the throat under choked conditions, or in other words, to have an essentially straight sonic line. The prescribed area distribution for the contraction was calculated by a streamline curvature method developed by Barger (1973) for axially symmetrical flow using the exact equations for an inviscid compressible flow.

The NTF contraction, shown in figure A5, consists of three subsections. The first part is axially symmetrical with the prescribed area distribution matched exactly. The second part is a transition section where the cross-sectional shape changes from round to flat-sided with circular arc corner fillets. Here the prescribed area distribution is matched only approximately. The third part is a continuation of the essentially square cross-section with corner fillets. In this third part, the corner fillet shape changes from circular arc to flat about 9 ft. upstream of the test section.

The length of the contraction is about 48 ft. An upstream section of the contraction, about 39 ft. long, is a movable structure which can be detached from the rest of the contraction and moved upstream within the pressure shell to permit deployment of 1 of 2 isolation valves which seal the test section and plenum from the rest of the circuit. The isolation valves permit access to the test section without depressurizing the entire tunnel circuit.

6.1.2.4 Test Section. A planview of the NTF test section is shown in figure A6. The design of the NTF test section closely resembles that of the Langley 8-Foot Transonic

Pressure Tunnel, especially in the flow re-entry region at the downstream end of the test section. The cross-section is nominally square, 8.2 ft. wide, with flat fillets at 45° angles in the corners resulting in a test section cross-sectional area of 66.77 sq. ft. There are 6 longitudinal slots in the horizontal (top and bottom) walls and provision for two slots in the vertical (side) walls.

The NTF slot shape for the top and bottom walls is shown in figure A7. In the portion of the test section normally occupied by test models, the slots are constant width, 6% open. The upstream portion of the slots is contoured to obtain a uniform Mach number distribution at a Mach number of 1.2. The contour shape was designed using a modified method of characteristics developed by Ramaswamy and Cornette (1982). The side wall slots are currently blanked-off providing a solid side wall. Since the current configuration of the test section is only slotted on the top and bottom walls at this time, the overall open area ratio is 3% open.

The length of the slotted region is approximately three test section widths. The side walls are parallel to each other, but the top and bottom walls have flexures at the upstream end which permit variation in wall angle from about 0.5° converged to 1.0° diverged. As shown in the sketches of figures A8 and A9, the sidewalls have provision for three large windows for flow field observations. Smaller ports are located in both the top and bottom and side walls for lighting and viewing.

Remotely adjustable re-entry flaps are located at the downstream end of each slot, occupying the rear 20% of the length of each slot. The angle of these flaps can be varied to control test section flow gradients and to minimize power consumption. The range of flap angle adjustment is from 4° toward the flow to 15° away from the flow on the top and bottom walls and from 0° to 15° away from the flow on the side walls.

6.1.2.5 Model Support Section. The model support section, located immediately downstream of the test section, is rectangular in cross-section with corner fillets which are tapered in the streamwise direction. The side walls adjacent to the model support

strut are indented to relieve strut blockage. The top and bottom walls in this section are attached to flexures at their downstream end. The angle of inclination of these walls can be varied from 0° (walls parallel to tunnel centerline) to about 4.5° inward (leading edge toward flow). The offset vertical height between the top and bottom test section walls and the model support section walls is variable from near zero offset to about 8 in. independently on the top and bottom. This offset vertical height can be varied as a function of tunnel flow conditions to accommodate varying reentry flow requirements and thus to minimize tunnel power consumption. Generally, test models are sting supported from a circular arc strut as shown in figure A9.

6.1.2.6 High-Speed Diffuser. The high-speed diffuser, shown in figure A10, is located immediately downstream of the model support section. It consists of two sections, a three-stage transition section and a conical section. The three stages of the transition section approximate the area distribution of a cone with a half-angle of about 2.6°, the same angle as the actual conical section. The transition cross-sectional shape progresses from a rectangular section with flat corner fillets to a fully round section in three stages of nearly equal length. The flat corner fillets are faired out within the first stage of the transition. Except for these fillets, the shapes in the transition section consist of flat panels, joined at the corners of the cross-section by quarter-round conical sections. The diffuser, including the model support section, has an overall area ratio of 2.92 to 1. As with the contraction, the high-speed diffuser is a movable structure. It can be detached from the model support section and moved downstream within the pressure shell to permit deployment of the downstream isolation valve (see fig. A9).

6.1.2.7 Fan Drive System. The fan is located 29 ft. downstream of corner number 2. As shown in figure A11, the upstream fan nacelle fairing is bent through that corner. The single stage fan has 25 fixed-pitch blades with fan loading changed by 24 variable inlet guide vanes (IGV) upstream of the fan, or by variable rotational speed. There are 26 fixed-downstream stators. The fan blades are fabricated of fiberglass reinforced plastic.

Flat acoustic panels are located in the fan nacelle and the adjacent tunnel walls at the nose and tail cones of the nacelle. A sketch of these panels is shown in figures A12(a) and (b) for the nose and tail cone of the nacelle respectively. These panels are intended to attenuate the fan noise propagating upstream and downstream from the fan. As described by Lassiter (1981), they use a dual Helmholtz resonator concept and are designed to provide about a 13 db. reduction of fan noise at the test section. The geometry of the two-layer perforated sheet honeycomb lining forming the dual Helmholtz resonator acoustic panels is shown in figure A13.

The fan is powered by two variable-speed wound rotor induction motors and a synchronous motor with maximum power ratings of 66,000 hp (49.2 MW) and 60,000 hp (44.8 MW) respectively. As has been mentioned earlier, the induction motors were left over from the 4-Foot Supersonic Pressure Tunnel on whose original site the NTF was constructed. As shown in the upper part of figure A14, they are coupled to the fan drive shaft through a two-speed gear box with gear ratios (motor to fan speed) of 835 to 360 in low gear and 835 to 600 in high gear. The purpose of the two-speed gear box is to provide a better match of the motor torque available to the fan torque required at different operating temperatures. The synchronous motor is in-line with the fan drive shaft and rotates at fan speed at all times.

The maximum shaft power available from the drive motor combination as a function of fan rotational speed is shown in the lower part of figure A14 for both the high and low gear ratios. The synchronous motor is operated at the fan shaft speed corresponding to the maximum speed of the induction motors in the low gear ratio, and is brought up to synchronous speed by the induction motors. The rotational speed of the induction motors is controllable within 1/4% over the entire range using a modified Kraemer drive control system.

Under high power conditions, when the power of both the induction and synchronous motors is required, the fan is rotated at the synchronous motor speed of 360 rpm (6 Hz),

and tunnel speed control is accomplished by variation of the inlet guide vane angles. At lower power conditions where only the induction motor power is required, tunnel speed can be varied either by inlet guide vane angle variation or by motor rotational speed variation.

In the air mode of operation, since cooling is then accomplished by the water-cooled heat exchanger, the maximum usable power is limited by the capacity of the heat exchanger. At the design capacity of the cooling towers, this limit is about 55,000 hp (41 MW).

6.1.2.8 Exhaust System. When the NTF is operating in the cryogenic mode, liquid nitrogen is continuously introduced into the circuit to maintain temperature. In order to maintain pressure and constant mass flow, an equal amount of gaseous nitrogen must be removed from the circuit. As seen in figure A3, the exhaust ports are in the cross-leg between turns 3 and 4. A sketch of the exhaust muffler and vent stack is shown in figure A15. The maximum flow rate of liquid nitrogen into the circuit is on the order of 9,000 gallons per minute or about 1,000 pounds per second. The muffler and vent stack are sized to exhaust an equal mass flow rate of gaseous nitrogen. The exhaust system is also used as the means of venting the tunnel pressure whether in the air mode or nitrogen mode of operation.

6.2 Appendix B. Longitudinal Static Pressure and Mach Number Gradients

The longitudinal force induced on a body by a static pressure gradient is

$$\Delta F_x = \int_o^l \frac{dp}{dx} A_x d_x \tag{B1}$$

which, for a linear change in static pressure with longitudinal distance, simplifies to

$$\Delta F_x = \frac{dp}{dx} \bullet \text{vol} \tag{B2}$$

where the volume is

$$\text{vol} = \int_o^l A_x d_x \tag{B3}$$

A somewhat idealized cross-sectional area distribution of a representative transport aircraft model is shown in figure B1. A polynomial fit to the area distribution can be expressed as

$$\frac{A_x}{A_{\max}} = \sum_{n=0}^{N} A_n (\frac{x}{l})^n \tag{B4}$$

For simplicity, the polynomial in equation (B4) will be limited to second order as also shown in figure B1.

$$\frac{A_x}{A_{\max}} = 4\frac{x}{l}\left(1 - \frac{x}{l}\right) \tag{B5}$$

Substituting equation (B5) into equation (B3), the volume is obtained as

$$\text{vol} = \frac{2}{3}\, l\, A_{\max} \tag{B6}$$

Substituting this result into equation (B2) there is obtained

$$\Delta F_x = \frac{2}{3}\,\frac{dp}{dx}\, l\, A_{\max} \tag{B7}$$

If a coefficient form is introduced into equation (B7)

$$\Delta C_x = \frac{\Delta F_x}{qS} = \frac{2}{3}\frac{1}{q}\frac{dp}{dx}\frac{l}{S}\, A_{\max} \tag{B8}$$

and the various terms are non-dimensionalized as

$$\Delta C_x = \frac{2}{3}\,\frac{1}{q/pt}\,\frac{dp/p_t}{dx/h}\,\frac{l/h}{S/A_T}\,\frac{A_{\max}}{A_T} \tag{B9}$$

it is now possible to recognize the various geometrical ratios which relate the model size to the test section dimensions

$$k_1 = \frac{A_{\max}}{A_T} = \text{model blockage ratio}$$

$$k_2 = \frac{S}{A_T} = \text{wing area to test section area ratio}$$

$$k_3 = \frac{l}{h} = \text{model length to test section height ratio}$$

then

$$\Delta C_x = \frac{2}{3}\,\frac{1}{q/p_t}\,\frac{dp/p_t}{dx/h}\,\frac{k_1 k_3}{k_2} \tag{B10}$$

The recommended maximum limits for these ratios based on avoiding large test section wall interferences are given as follows:

model blockage (k_1)	0.005, Baals and Stokes (1971)
wing/test section area ratio (k_2)	0.05, Monti (1971)
model length/test section height (k_3)	0.6, Baals and Stokes (1971)

There are no firm criteria on what constitutes an acceptable pressure gradient. In reality, the pressure gradient is practically never exactly zero, and even when it is quite small, higher order effects due to non-linearity may assume some importance. One possible approach is to examine the magnitude of a gradient which would cause an increment in drag coefficient of ± 0.0001, or ± 1 drag count in the terminology of wind tunnel experimentalists.

Solving equation (B10) for the non-dimensionalized pressure gradient

$$\frac{dp/p_t}{dx/h} = \frac{3}{2}\,\Delta C_x\,\frac{q}{p_t}\frac{k_2}{k_1 k_3} \tag{B11}$$

and substituting the above values for $\Delta C_x, k_1, k_2$, and k_3, there is obtained

$$\frac{dp/p_t}{dx/h} = .0025\frac{q}{p_t} \tag{B12}$$

If perfect gas relations are assumed, q/p_t is solely a function of Mach number, and the non-dimensional static pressure gradient can be plotted as shown in figure 15, where the allowable gradients under present assumptions are those that fall beneath the line. Perfect gas relations are adequate in this instance because the results are to be applied to air mode tests with the test section slots covered, where the stagnation pressure was near atmospheric, and the stagnation temperature was near ambient. It is often the case that test section gradients are expressed in terms of Mach number instead of static pressure. Again assuming perfect gas relations, equation (B12) can be rewritten in terms of Mach number, where the ratio of specific heats has been taken as 1.4

$$\frac{dM}{dx/h} = .00125M(1 + .2M^2) \tag{B13}$$

and is shown plotted in figure 16. Another question to be considered is the accuracy of measurement of the local static pressures that make up the pressure gradient, and the effect of this accuracy on the computed magnitude of that gradient. This question is addressed next in Appendix C.

6.3 Appendix C. Accuracy of Test Section Gradients Using Least Squares

The question addressed here is how accurate the individual readings on pressure must be in order to obtain least squares slopes to a given accuracy. First, the usual equations for a least squares straight line fit will be shown. With reference to figure C1, the increment between the i^{th} data point and the least squares straight line is

$$\delta_i = P_i - (ax_i + b) \tag{C1}$$

The sum of the squares of these increments is to be minimized

$$\delta^2 = \sum_{i=1}^{j} \delta_i^2 = \sum_{i=1}^{j} [P_i - (ax_i + b)]^2 = \min . \tag{C2}$$

where the values of the slope a and the intercept b are to be chosen to obtain the minimization

$$\frac{\partial \delta^2}{\partial a} = -2\Sigma x_i[P_i - (ax_i + b)] = 0 \tag{C3}$$

$$\frac{\partial \delta^2}{\partial b} = -2\Sigma[P_i - (ax_i + b)] = 0 \tag{C4}$$

where the summation is now understood to be on i from 1 to j. Equations (C3) and (C4) are solved simultaneously for a and b.

$$\Sigma\ x_i P_i - a\Sigma x_i^2 - b\Sigma x_i = 0 \tag{C5}$$

$$\Sigma\ P_i - a\Sigma x_i - jb = 0 \tag{C6}$$

from equations (C5) and (C6) there is obtained

$$a = \frac{j\Sigma x_i P_i - \Sigma x_i \Sigma P_i}{j\Sigma x_i^2 - (\Sigma x_i)^2} \tag{C7}$$

$$b = \frac{\Sigma x_i \Sigma x_i P_i - \Sigma x_i^2 \Sigma P_i}{(\Sigma x_i)^2 - j\Sigma x_i^2} \tag{C8}$$

Equations (C7) and (C8) are the standard equations to determine the slope and intercept for a least squares straight line fit to the data points P_i. At this point it is convenient to introduce a simplification such that

$$\Sigma x_i = 0$$

which would be true, for instance, if the distribution of the points x_i were symmetrical about $x = 0$. Since in the present case the origin for the x_i coordinates is at the midpoint of the distribution and the value of the intercept is to be used as the Mach number at the midpoint, the simplification is justified. With this simplification equations (C7) and (C8) become

$$a = \frac{\Sigma x_i P_i}{\Sigma x_i^2} \tag{C9}$$

$$b = \frac{1}{j}\Sigma P_i \tag{C10}$$

In equation (C9), it may be noticed that the influence of a particular data point P_i depends on its position x_i in the distribution, and on the total number of points.

Now introduce an error ϵ_i in the data points P_i such that

$$P_i = p_i + \epsilon_i \tag{C11}$$

then

$$a + \Delta a = \frac{\Sigma x_i (p_i + \epsilon_i)}{\Sigma x_i^2} = \frac{\Sigma x_i p_i}{\Sigma x_i^2} + \frac{\Sigma x_i \epsilon_i}{\Sigma x_i^2} \tag{C12}$$

where the first term on the right may be associated with the true value of a and the second term may be associated with the error. A root-sum-square (rss) version of this latter term is

$$\Delta a(\text{rss}) = \frac{(\Sigma(x_i \epsilon_i)^2)^{1/2}}{\Sigma x_i^2} \tag{C13}$$

For the NTF steady state calibration, the error in pressure measurement was

$$\epsilon = \pm .003\ p_{\max}$$

then

$$\Delta a(\text{rss}) = \frac{.003\ p_{\max}}{(\Sigma x_i^2)^{1/2}} \tag{C14}$$

Also, for the distribution of static pressure orifices in the NTF centerline calibration tube, there were 25 orifices spaced 3 in. apart in a length of 6 ft. centered about test section sta 13, so

$$\frac{1}{h}\ (\Sigma\ x_i^2)^{1/2} = 1.099$$

and

$$\frac{dp/p_t}{dx/h}(\text{error}) = \frac{.003}{1.099}\frac{p_{\max}}{p_t} \tag{C15}$$

The ESP unit used for the steady state calibration had a maximum pressure range of ± 2.5 psi, and if a worst case (lowest) value for total pressure is taken as 15 psi, then the static pressure gradient error term becomes

$$\frac{dp/p_t}{dx/h}(\text{error}) = .000455 \tag{C16}$$

If it is desirable to express the gradient error in terms of Mach number, for present purposes it will again be satisfactory to assume perfect gas relations, and to take the ratio of specific heats as 1.4 to get

$$\frac{dM}{dx/h}(\text{error}) = .000325\ \frac{(1+.2M^2)^{9/2}}{M} \tag{C17}$$

During the dynamic investigation, when the slots were covered, the longitudinal static pressure gradient was determined by a distribution of 13 test section wall static pressure orifices in a length of 7.5 ft. centered about test section sta 13. In this case

$$\frac{1}{h}\left(\Sigma\ x_i^2\right)^{1/2} = .892$$

and since the same ESP unit for pressure measurement was used, the error term equivalent to equation (C16) becomes

$$\frac{dp/p_t}{dx/h}(\text{error}) = .00056 \tag{C16a}$$

In terms of Mach number gradient, the error term increases to

$$\frac{dM}{dx/h}(\text{error}) = .00040\ \frac{(1+.2M^2)^{9/2}}{M} \tag{C17a}$$

From this it can be seen that the accuracy of the determination of the test section longitudinal gradients for the configuration with the slots covered was slightly degraded compared to that for the steady state calibration. Equations (C16), (C16a) and (C17), (C17a) are included in figures 15 and 16 respectively for reference.

6.4 Appendix D. Preliminary Test Results with Steady State Calibration Probe Installed in Test Section

As mentioned in section 3.3 on cryogenic mode tests, prior to the start of the present investigation, while the steady state calibration was being planned, it was thought that simultaneous testing for both the steady state and the dynamic characteristics of the tunnel would be an efficient use of the tunnel test time and of liquid nitrogen resources if the requirements for both sets of measurements could be satisfied at the same time. For steady state calibration purposes, as has already been indicated, a long slender survey probe containing several hundred static pressure orifices was installed on the tunnel centerline, stretching the entire length of the test section and extending well upstream into the contraction where it was secured with support cables as shown in the photograph of figure D1. At the downstream end, the survey probe was mounted in the arc-sector centerbody, and the junction was aerodynamically faired using the same fiber-glass reinforced plastic conical fairing as was used for the present investigation.

Fluctuating static pressure data were taken at some of the test conditions covered in the steady state calibration. The test points for the power spectra shown in figure D2 are for test conditions near the maximum Reynolds number boundary in the cryogenic mode (105 psi $< p_t <$ 125 psi and $T_t = -250°$F). The data are for the RHS test section sidewall at station 13. A large peak can be seen in the spectra ranging in frequency from about 1.5 kHz at a Mach number of 0.2 to about 5.2 kHz at a Mach number of 1.0. As a help in identifying the source of this peak, it may be observed that since the peak frequency changes with Mach number and therefore also with velocity, the indication is that the source is likely aerodynamic. Further, it may be observed that the source is not choked-off at a Mach number of 1.0 indicating that the source is not downstream of the test section. With these readily obvious clues, it would be reasonable to suspect the upstream support cables. To further document this suspicion, the vortex shedding frequency of the cables was estimated assuming a Strouhal number of 0.2 and is shown

as a function of test section Mach number in figure D3 for test conditions corresponding to ambient temperature, low pressure air tests. The frequency for peaks in the spectra at these same test conditions are also shown for comparison, indicating a reasonable probability that support cable vortex shedding is the source.

In an attempt to determine the magnitude of the added disturbance, a notch or band-reject filter consisting of a combination of low-pass and high-pass filters was used to filter the suspect peak. Filtered results were obtained for all of the spectra, and are shown by the dashed lines in figure D2. The integrated rms fluctuating pressure coefficients for these spectra are shown in figure D4. The large reduction due to filtering, as much as 25% at Mach numbers of 0.5 and 0.6, indicate the importance of obtaining the dynamic data with all extraneous interferences removed. These preliminary results led to the decision to obtain dynamic data under dedicated conditions, with the test section empty. The actual empty test section results were even lower than those indicated by the filtered data.

6.5 Appendix E. Estimation of Edge-Tone Frequency in Free Shear Layer

The subject of edge-tones has been extensively studied as indicated for example by the survey paper on jet-wedge edge-tones by Karamcheti et. al (1969) and by the introductory paper on free shear layer edge-tones by Hussain and Zaman (1978). It is not the purpose here to analyze the edge-tone generation characteristics of free shear layers but rather to investigate the plausibility of such edge-tones existing in the NTF test section. Attention is concentrated on aerodynamic gaps in the test section wall surface which exist at the downstream end of the test section. These gaps are on the test section sidewall immediately upstream of the leading edges of the sidewall reentry flaps as may be seen in the photograph of figure 43.

A sketch of the gap profile is shown in figure E1. The upstream lip is considered to act as the point of separation of the wall boundary layer to form a free shear layer between the lip and the downstream wedge which is formed by the leading edge of the sidewall reentry flap. As shown in the sketch, a vortex is considered to be periodically shed from the lip, traveling downstream in the free shear layer to impact on the wedge creating an edge-tone, and an acoustic feedback mechanism is assumed to maintain a self-sustained tone. The path of the feedback signal is considered to be through the quiescent region on the plenum side of the free shear layer.

The tone phenomena involved appears similar to what is encountered in open cavities. An expression for the frequency of periodic disturbances found with open cavities was given by Rossiter (1964) as

$$f = \frac{V}{L}\frac{m-\gamma}{V/u_c + M} \tag{E1}$$

where m is the stage number for the periodic disturbance and γ is a factor involving the lag between the interaction of the vortex with the downstream edge, and the emittance of the associated acoustic feedback disturbance. Equation (E1) can be rewritten as

$$f = \frac{m-\gamma}{\frac{L}{u_c} + \frac{L}{c}} \tag{E2}$$

The denominator in equation (E2) can be recognized as the time required for the shed vortex to travel the length of the gap L downstream at a convection velocity u_c in the free shear layer, plus the time for an acoustic disturbance emitted by the interaction of the vortex with the downstream edge to travel back to the lip at an acoustic velocity c through the quiescent region.

The acoustic velocity in equation (E2) has been assumed to be equal to the free stream speed of sound. Heller, Holmes, and Covert (1971) have shown that better agreement between predicted and measured frequencies for cavities is obtained if the stagnation speed of sound is used. This modified form of the Rossiter equation is then written as

$$f = \frac{m - \gamma}{\frac{L}{u_c} + \frac{L}{c_t}} \tag{E3}$$

or in reduced frequency form as

$$\frac{fL}{V} = \frac{m - \gamma}{\frac{V}{u_c} + \frac{V}{c_t}} \tag{E4}$$

The value for the convection velocity ratio u_c/V used by Rossiter was 0.57. The lag factor γ has been shown by Rossiter to be a function of the length-to-depth ratio of the cavity, diminishing nearly linearly from a value of 0.54 at a length-to-depth ratio of 8, to a value of 0.25 at a length-to-depth ratio of 4.

Reduced frequencies calculated using equation (E4) for the test conditions of figures 27 and 35 are shown in table 2 and figure E2. For these calculations, the convection velocity ratio u_c/V was assumed as 0.6 which is appropriate for a free shear layer, the lag factor γ was taken as zero, and the velocity V was taken as the free stream velocity in the test section.

The measured frequency results listed in table 2 and shown in figure E2 bracket the calculated values, being lower at the low Reynolds numbers and higher at the high Reynolds numbers. The agreement is considered good enough to support the contention that the measured frequency spikes are caused by free shear layer edge-tones which are

generated at the gap region upstream of the sidewall re-entry flaps under certain flow conditions and are detectable in the test section.

7.0 REFERENCES

1. Adcock, Jerry B.: Real-Gas Effects Associated with One-Dimensional Transonic Flow of Cryogenic Nitrogen. NASA TN-D-8274, December 1976.
2. Adcock, Jerry B.: Effect of LN2 Injection Station Location on the Drive Fan Power and LN2 Requirements of a Cryogenic Wind Tunnel. NASA TM-X-74036, June 1977.
3. Adcock, Jerry B. and Johnson, Charles B.: A Theoretical Analysis of Simulated Transonic Boundary Layers in Cryogenic Nitrogen Wind Tunnels. NASA TP-1631, March 1980.
4. Adcock, Jerry B.: Private Communication. February 1992.
5. Baals, D. D. and Stokes, G. M.: A Facility Concept for High Reynolds Number Testing at Transonic Speeds. Paper No. 28, AGARD-CP-83-71, August 1971.
6. Barger Raymond L.: Streamline Curvature Design Procedure for Subsonic and Transonic Ducts. NASA TN-D-7368, December 1973.
7. Barger, Raymond L.: A Theory for Predicting Boundary Impedance and Resonance Frequencies of Slotted-Wall Wind Tunnels Including Plenum Effects. NASA TP-1880, July 1981.
8. Bendat, Julius S.; and Piersol, Allan G.: Engineering Applications of Correlation and Spectral Analysis. John Wiley & Sons, 1980.
9. Bobbitt, Percy J.: Report of the Panel on Fluid Dynamics, High Reynolds Number Research—1980, L. Wayne McKinney, and Donald D. Baals, eds. NASA CP 2183, 1981.
10. Boyles, George B., Jr.: Description and Operational Status of the National Transonic Facility Computer Complex. AIAA Paper No. 86-0383-CP, AIAA 14th Aerodynamic Testing Conference, West Palm Beach, FL, March 5–7, 1986.

11. Braslow, Albert L.; and Knox, Eugene C.: Simplified Method for Determination of Critical Height of Distributed Roughness Particles for Boundary Layer Transition at Mach Numbers From 0 to 5. NACA TN-4363, September 1958.

12. Braslow, Albert L.; Hicks, Raymond M.; and Harris, Roy V., Jr.: Use of Grit-Type Boundary-Layer-Transition Trips on Wind-Tunnel Models. NASA TN-D-3579, September 1966.

13. Bruce, W. E., Jr.: The U.S. National Transonic Facility, Parts I and II. Papers No. 14 and 15, AGARD-R-722, April 1985.

14. Chiu, Wen-Shyang; and Lauchle, Gerald C.: Subsonic Axial Flow Fan Noise and Inflow Velocity Disturbance. Engineering for Environmental Noise Control, Proceedings, 1989 International Conference on Noise Control Engineering, George C. Maling, Jr., ed., Vol. 1, pp. 133–138, Dec. 1989.

15. Coe, Charles F.: Surface-Pressure Fluctuations Associated with Aerodynamic Noise. In "Basic Aerodynamic Noise Research" (Conf. held at NASA Headquarters, Washington, D. C., July 14–15, 1969). Ira R. Schwartz ed., NASA SP-207, pp. 409–424.

16. Corcos, G. M.: Resolution of Pressure in Turbulence. J. Acoust. Soc. America, Vol. 35, No. 2, pp. 192–199, Feb. 1963.

17. Corcos, G. M.: The Resolution of Turbulent Pressures at the Wall of a Boundary Layer. J. Sound Vib., 6 (1), pp. 59–70, 1967.

18. Dimmock, N. A.: The Development of a Simply Constructed Cascade Corner for Circular Cross-Section Ducts. N.G.T.E.M. 78, February 1950.

19. Dolling, D. S.; and Dussauge, J. P.: Fluctuating Wall-Pressure Measurements. Chaper 8, A Survey of Measurements and Measuring Techniques in Rapidly Distorted Compressible Turbulent Boundary Layers, H. H. Fernholz, P. J. Finley, J. P. Dussauge and A. J. Smits, eds., AGARD-AG-315, May 1989.

20. Dougherty, N. S. and Fisher, D. F.: Boundary Layer Transition on a 10-Degree Cone: Wind Tunnel/Flight Data Correlation. AIAA Paper 80-0154, January 1980.

21. Dougherty, N. Sam, Jr.: Influence of Wind Tunnel Noise on the Location of Boundary-Layer Transition on a Slender Cone at Mach Numbers From 0.2 to 5.5. Vols. I and II, AEDC-TR-78-44, March 1980.

22. Dryden, Hugh L.; and Abbott, Ira H.: The Design of Low-Turbulence Wind Tunnels. NACA TN-1755, Nov. 1948.

23. Eckelmann, Helmut: A Review of Knowledge on Pressure Fluctuations. Near-Wall Turbulence, 1988 Zoran Zaric Memorial Conference, S. J. Kline and N. H. Afgan, eds., pp. 328–347, Hemisphere Publishing Corp., 1990.

24. Elsenaar, A.; Binion, T. W., Jr.; and Stanewsky, E.: Reynolds Number Effects in Transonic Flow. AGARD-AG-303, H.G. Hornung, ed., Dec. 1988.

25. Elsenaar, A.: The Windtunnel as a Tool for Laminar Flow Research. ICAS- 90-6.1.1, ICAS Proceedings, 17th Congress of the International Council of the Aeronautical Sciences, Stockholm, Sweden, Sept. 9–14, 1990.

26. Foster, Jean M. and Adcock, Jerry B.: User's Guide for the National Transonic Facility Data System. NASA TM-100511, December 1987.

27. Fuller, Dennis E.: Private Communication. 1980.

28. Fuller, Dennis E.: Guide for Users of the National Transonic Facility. NASA TM-83124, July 1981.

29. Goodyer, Michael J.; and Kilgore, Robert A.: The High Reynolds Number Cryogenic Wind Tunnel. AIAA Paper 72-995, September 1972. Also AIAA Journal, Vol. 11, No. 5, May 1973.

30. Hall, Robert M. and Adcock, Jerry B.: Simulation of Ideal Gas Flow by Nitrogen and Other Selected Gases at Cryogenic Temperatures. NASA TP-1901, September 1981.

31. Hanly, Richard D.: Effects of Transducer Flushness on Fluctuating Surface Pressure Measurements. AIAA Paper 75-534, AIAA 2nd Aero-Acoustics Conf., Hampton, VA, March 24–26, 1975.

32. Heller, H. H.; Holmes, D. G.; and Covert, E. E.: Flow-Induced Pressure Oscillations in Shallow Cavities. Jour. of Sound and Vibr., 18(4), 1971.

33. Horstman, C. C.; and Rose, W. C.: Hot-Wire Anemometry in Transonic Flow. NASA TM X-52495, Dec. 1975. (See also AIAA Jour. Vol. 15, No. 3, March 1977, pp. 395–401).

34. Howell, Robert R. and McKinney, Linwood W.: The United States 2.5 Meter Cryogenic High-Reynolds-Number Tunnel. Paper presented at the 10th Congress of the International Council of the Aeronautical Sciences (ICAS), Ottowa, Canada, October 3–9, 1976. Also NASA CP-2009, 1977, pp. 27–51.

35. Hussain, A. K. M. F.; and Zaman, K. B. M. Q.: The Free Shear Layer Tone Phenomenon and Probe Interference. J. Fluid Mechanics (1978), Vol. 87, Part 2, pp. 349–383.

36. Igoe, William B.: Characteristics and Status of the United States National Transonic Facility. Paper No. 17, AGARD-LS-111, May, 1980.

37. Jones, Gregory S.: The Measurement of Wind Tunnel Flow Quality at Transonic Speeds. Ph.D. Dissertation, VPI&SU, April 1991.

38. Karamcheti, K.; Bauer, A. B.; Shields, W. L.; Stegen, G. R.; and Woolley, J. P.: Some Features of an Edge-Tone Flow Field. In "Basic Aerodynamic Noise Research," (Conf. held at NASA Headquarters, Washington D.C., July 14–15, 1969), Ira Schwartz, ed., NASA SP-207, pp. 275–304.

39. Kern, F. A.; Knight, C. W.; and Zasimowich, R. F.: National Transonic Facility Mach Number System. ISA Transactions Vol. 25, No. 2, 1986.

40. Kilgore, Robert A.: The Cryogenic Wind Tunnel for High Reynolds Number Testing. Ph.D. Dissertation, University of Southampton, February 1974. (Available as NASA TM-X-70207).

41. Kilgore, Robert A.; Adcock, Jerry B.; and Ray, Edward J.: Flight Simulation Characteristics of the Langley High-Reynolds-Number Cryogenic Transonic Tunnel. Journal of Aircraft, Vol. 11, No. 10, October 1974, pp. 593–600.

42. Kovasznay, Leslie S. G.: The Hot-Wire Anemometer in Supersonic Flow. Jour. Aero. Sci., Vol. 17, No. 9, p. 565, 1950.

43. Kovasznay, Leslie S. G.: Turbulence in Supersonic Flow. Jour. Aero. Sci., Vol. 20, No. 10, pp. 657–682, Oct. 1953.

44. Küchemann, Dietrich and Weber, Johanna: Aerodynamics of Propulsion. McGraw Hill Book Co., Inc., 1953, pp. 274–278.

45. Lassiter, William S.: Design Predictions for Noise Control in the Cryogenic National Transonic Facility. Noise Control Engineering, September–October 1981, pp. 76–84.

46. Lee, In; and Baik, Ki-Young: Resonance Prediction for Slotted Circular Wind Tunnel Using Finite Element. AIAA Journal, Vol. 29, No. 12, pp. 2266–2269, December 1991.

47. Lowson, M. V.: Prediction of Boundary Layer Pressure Fluctuations. AFFDL-TR-67-167, April 1968.

48. Mabey, D. G.: Flow Unsteadiness and Model Vibration in Wind Tunnels at Subsonic and Transonic Speeds. ARC CP-1155, 1971.

49. Mabey, Dennis G.: Some Remarks on the Design of Transonic Tunnels with Low Levels of Flow Unsteadiness. NASA CR-2722, August 1976.

50. Mabey, D. G.: The Resonance Frequencies of Ventilated Wind Tunnels. RAE TR-78038, April 1978.

51. Mabey, D. G.: A Semi-empirical Theory of the Noise in Slotted Tunnels Caused by Diffuser Suction. RAE TR-91-023, 1991.

52. Margoulis, W.: A New Method of Testing Models in Wind Tunnels. NACA TN-52, August 1921.

53. Meyers, James F.; and Wilkinson, Stephen P.: A Comparison of Turbulence Intensity Measurements Using a Laser Velocimeter and a Hot Wire in a Low Speed Jet Flow. Intl. Symposium on Application of Laser-Doppler Anemometry to Fluid Mechanics, Lisbon, Portugal, July 5–7, 1982.

54. Meyers, James F.; and Clemmons, James I., Jr.: Frequency Domain Laser Velocimeter Signal Processor. NASA TP-2735, September 1987.

55. Michel, Roger: Boundary Layer Development and Transition. AGARD-AR-224, Boundary Layer Simulation and Control in Wind Tunnels, Section 4.3, April 1988.

56. Michel, U.; and Froebel, E.: Lower Limit for the Velocity Fluctuating Level in Wind Tunnels. Experiments in Fluids, Vol. 6, No. 1, pp. 49–54, 1988.

57. Mokry, M.: Prediction of Resonance Frequencies for Ventilated Wall Wind Tunnels. AGARD-CP-348, Wind Tunnels and Testing Techniques, September 1983.

58. Monti, R.: Wall Corrections for Airplanes with Lift in Transonic Wind Tunnel Tests. Part III, Report of the AGARD Ad Hoc Committee on Engine-Airplane Interference and Wall Corrections in Transonic Wind Tunnel Tests, AGARD-AR-36-71, August 1971.

59. Morkovin, Mark V.: Fluctuations and Hot-Wire Anemometry in Compressible Flows. AGARDograph 24, November 1956.

60. Murthy, S. V.; and Steinle, F. W.: On Boundary Layer Transition in High-Subsonic and Transonic Flow Under the Influence of Acoustic Disturbances and Free-Stream Turbulence. AIAA Paper No. 85-0082, AIAA 23rd. Aerospace Sciences Meeting, Reno, NV, January 14–17, 1985.

61. Murthy, S. V.; and Steinle, F. W.: Effects of Compressibility and Free-Stream Turbulence on Boundary Layer Transition in High-Subsonic and Transonic Flow. AIAA Paper No. 86-0764, West Palm Beach, FL, March 1986.

62. Prandtl, L.: Der Luftwiderstand von Kugeln (On the Air Resistance of Spheres), Göttingen Nachrichten, 1914, pp. 177–190.

63. Ramaswamy, M. A. and Cornette, E. S.: Supersonic Flow Development in Slotted Wind Tunnels. AIAA Journal Vol. 20, No. 6, June 1982.

64. Robinson, Russell G.: Sphere Tests in the NACA 8-foot High Speed Tunnel. Jour. Aero. Sci., Vol. 4, No. 5, March 1937, pp. 199–201.

65. Rose, William. C.; and McDaid, Edward P.: Turbulence Measurement in Transonic Flow. AIAA 9th Aerodynamic Testing Conference, Arlington, TX, June 7–9, 1976, Proceedings.

66. Ross, R.; and Rohne, P. B.: Noise Environment in the NLR Transonic Wind Tunnel HST. NLR TR-74128 U, August 1973.

67. Rossiter, J. E.: Wind Tunnel Experiments on the Flow Over Rectangular Cavities at Subsonic and Transonic Speeds. RAE TR-64037, Oct. 1964.

68. Schewe, Günter: On the Structure and Resolution of Wall-Pressure Fluctuations Associated With Turbulent Boundary-Layer Flow. J. Fluid Mech., Vol. 134, pp. 311–328, 1983.

69. Siddon, Thomas E.: On The Response of Pressure Measuring Instrumentation in Unsteady Flow. (An Investigation of Errors Induced by Probe-Flow Interaction). UTIAS Report No. 136, Jan. 1969.

70. Smelt, R.: Power Economy in High-Speed Wind Tunnels by Choice of Working Fluid and Temperature. Rep. No. Aero. 2081, Brit. R.A.E., August 1945.

71. Spangenberg, W. G.: Heat Loss Characteristics of Hot-Wire Anemometers at Various Densities in Transonic and Supersonic Flow. NACA TN-3381, 1955.

72. Spangler, J. G.; and Wells, C. S., Jr.: Effects of Freestream Disturbances on Boundary-Layer Transition. AIAA Jour., Vol. 6, No. 3, pp. 543–545, March 1968.

73. Stainback, P. Calvin; Johnson, Charles, B.; and Basnett, Constance B.: Preliminary Measurements of Velocity, Density and Total Temperature Fluctuations in Compressible Subsonic Flow. AIAA 21st Aerospace Sciences Meeting, Reno, NV, January 10–14, 1983, Paper 83-0384.

74. Timme, Adalbert: Effects of Turbulence and Noise onWind-Tunnel Measurements at Transonic Speeds. AGARD-R-602, Fluid Motion Problems in Wind Tunnel Design, April 1973.

75. Williams, John: Aeroacoustic Requirements for Model Noise Experiments in Subsonic Windtunnels. A Further Review of Current Research Related to the Design and Operation of Large Windtunnels, Appendix 4, pp. 61-91, AGARD-AR-105, Aug. 1977.

76. Williams, M. Susan and Adcock, Jerry B.: Calibration of the National Transonic Facility (prospective formal NASA publication, 1993).

77. Willmarth, W. W.; and Roos, F. W.: Resolution and Structure of the Wall Pressure Field Beneath a Turbulent Boundary Layer. J. Fluid Mech., Vol. 22, Part 1, pp. 81-94, 1965.

Vita

The author was born in the [redacted] on [redacted] attended grammar school and high school in the borough of Brooklyn, and served in the United States Navy from 1944 to 1946. He received an SB degree in Aeronautical Engineering from MIT in 1947, and a MS degree in Aerospace Engineering from GWU in 1971. From 1947 until the present, he has been employed by NASA and by its predecessor organization NACA at LaRC where he is currently a member of the staff at the NTF. He is a member of AIAA.

Table 1. NTF Test Section Wall Geometry Variables

Including Downstream Choke Settings

Test Section Configuration		Test Section Wall Angle (degree)	Model Support Section Wall Angle (degree)	Reentry Flap Angle (degree)	Mach Number Range
Slots	Choke				
covered	on	0.1	−4.23	0.87	0.2 to 0.8
covered	off	0.1	−3.79	−0.1	0.2 to 0.9
open	on	0	−4.23	1.86	0.2 to 0.8
open	off	0	−1.76	0	0.2 to 1.05

Table 2. Free Shear Layer Edge-Tone Frequency Calculation

Gas Type	M	R/ft.	V(fps)	c_t (fps)	T_t (°F)	f meas. (Hz)	$\frac{fL}{V}$ meas.	$\frac{fL}{V}$ calc.
Air	.695	6.0×10^6	764	1151	91.4	840	.36	.43
Nitrogen	.695	6.0	777	1172	92.2	855	.36	.43
Nitrogen	.598	39.9	481	834	-174.0	890	.60	.45
Nitrogen	.694	39.9	519	784	-206.2	860	.54	.43
Nitrogen	.742	39.8	538	764	-218.6	900	.54	.42
Nitrogen	.793	39.8	558	747	-228.7	960	.56	.41
Nitrogen	.839	39.8	576	734	-236.2	(1410)	(.80)	(.82)*
Nitrogen	.892	39.9	601	725	-241.4	960	.52	.40
Nitrogen	.992	40.1	644	710	-250.2	960	.48	.39

*Quantities in parentheses are possible second stage frequencies.

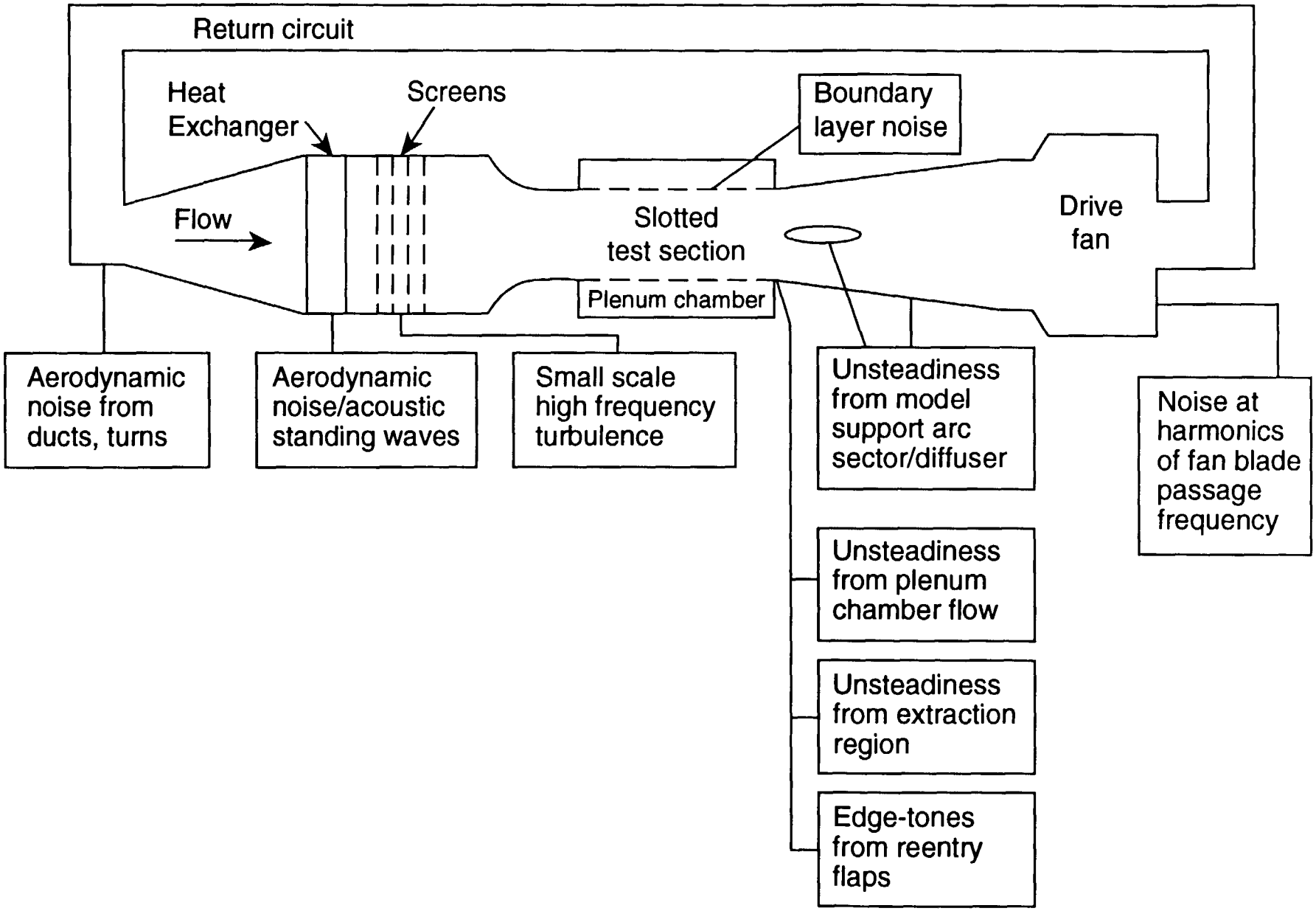

Figure 1. Sources of unsteadiness in transonic wind tunnels [adapted from Mabey (1971)].

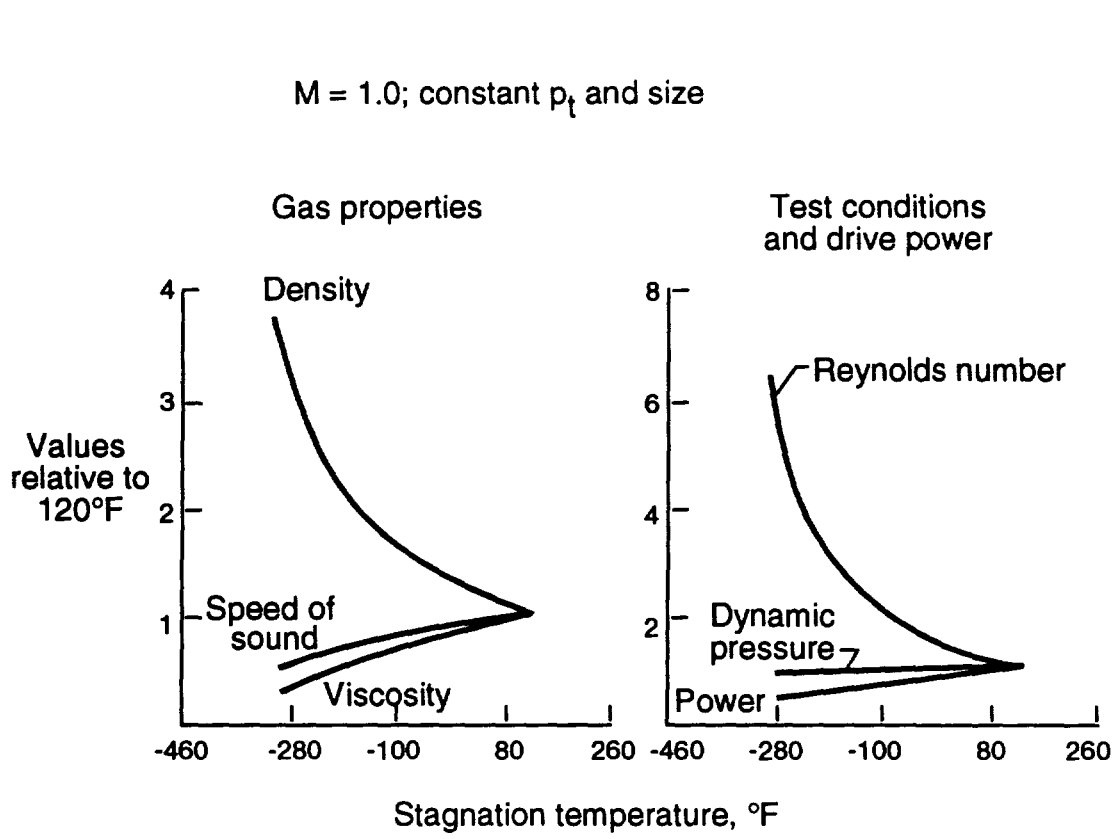

Figure 2. Variation of gas properties and wind tunnel conditions with temperature.

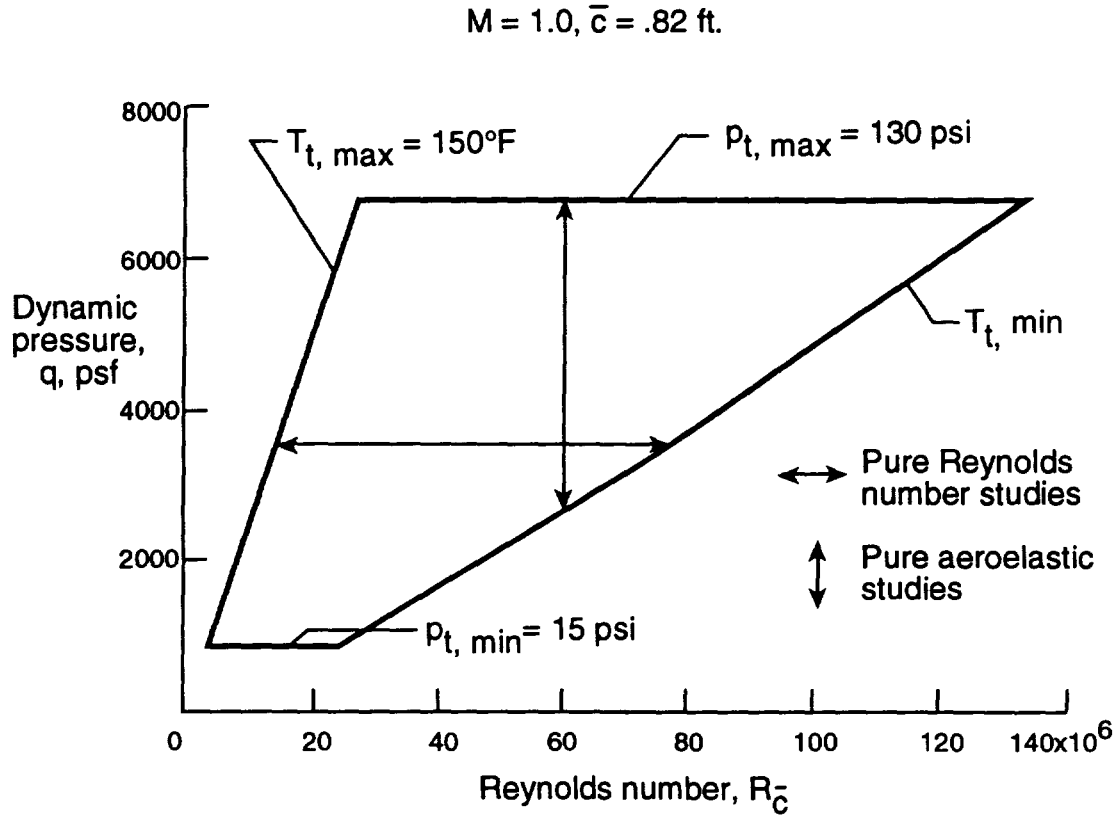

Figure 3. Constant Mach number operating envelope

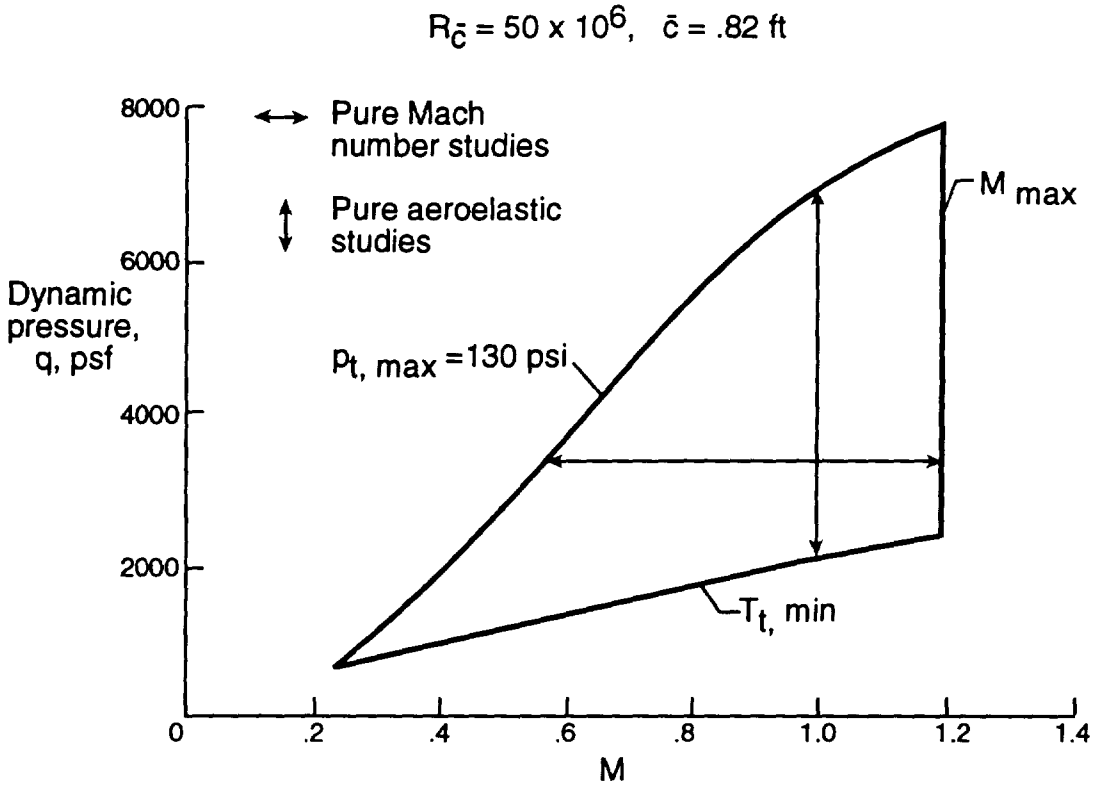

Figure 4. Constant Reynolds number operating envelope.

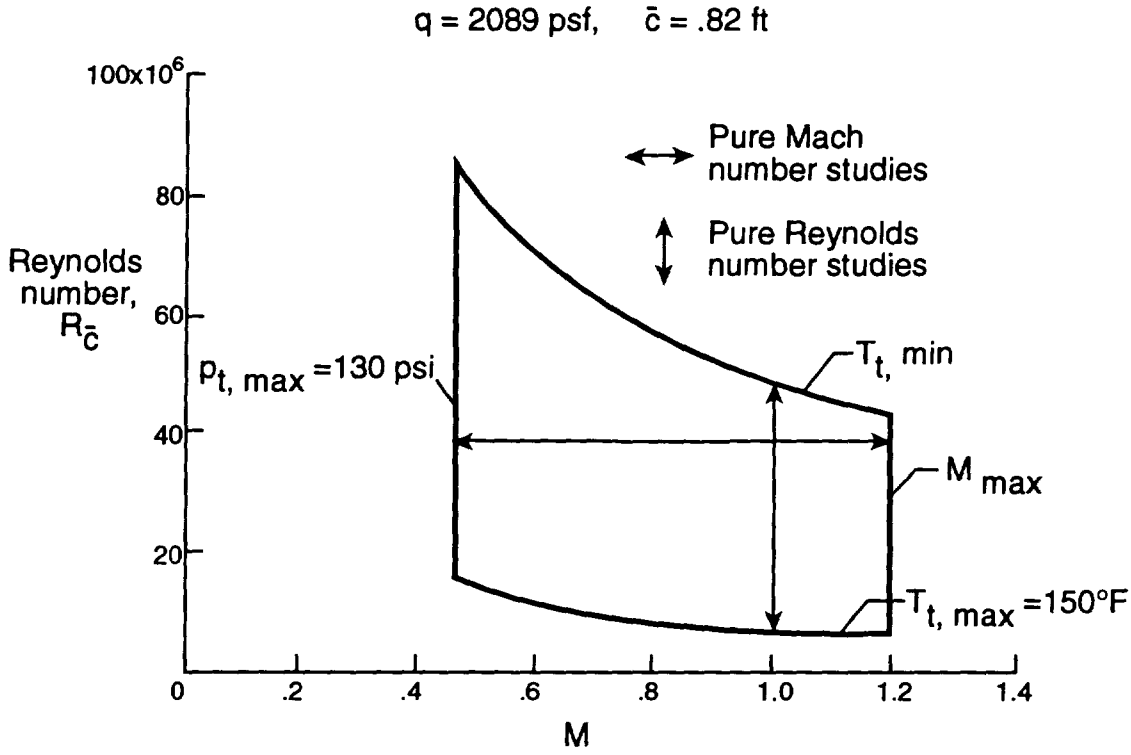

Figure 5. Constant dynamic pressure operating envelope.

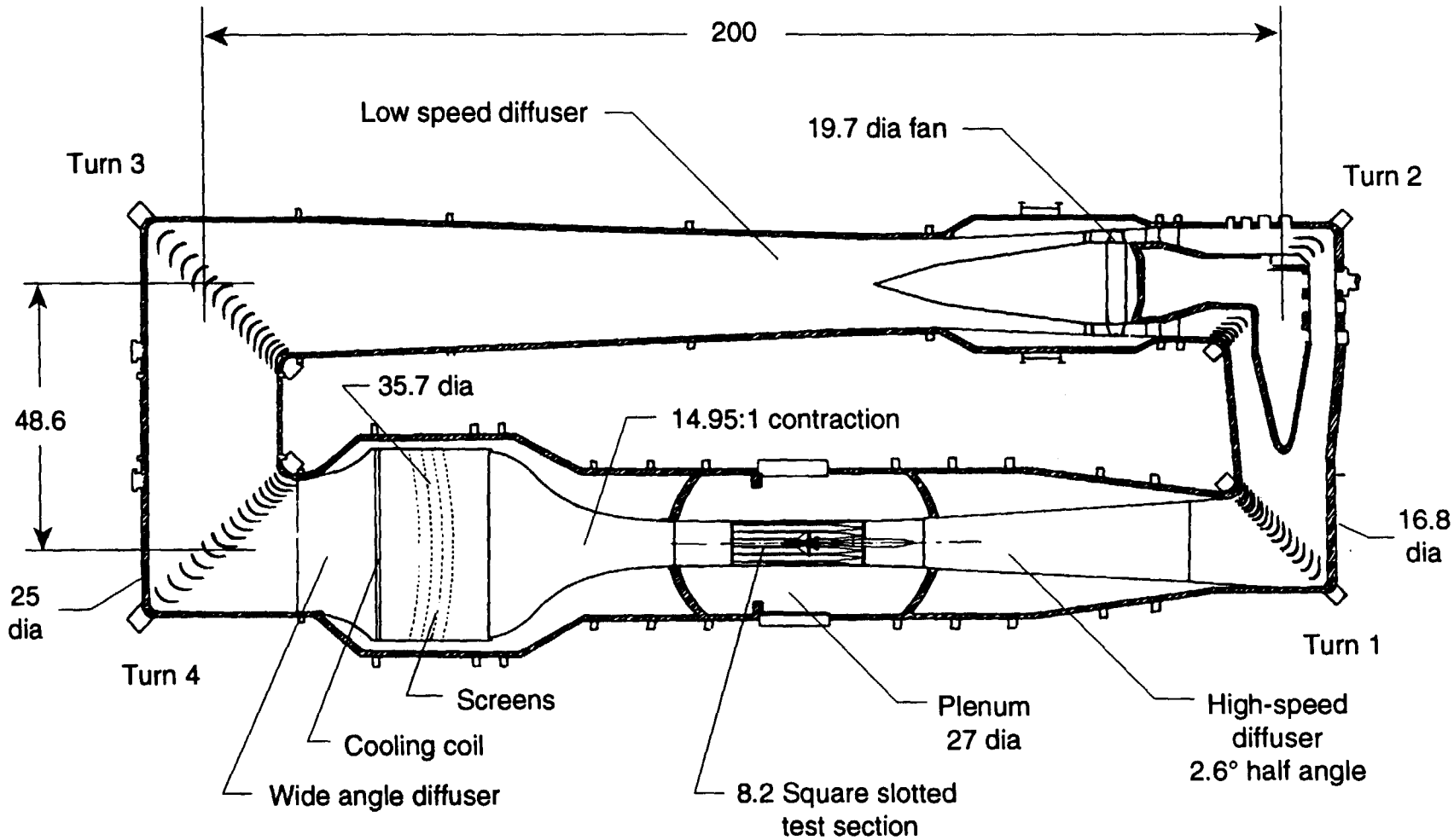

Figure 6. National Transonic Facility planview of tunnel circuit (all dimensions in ft. except where noted).

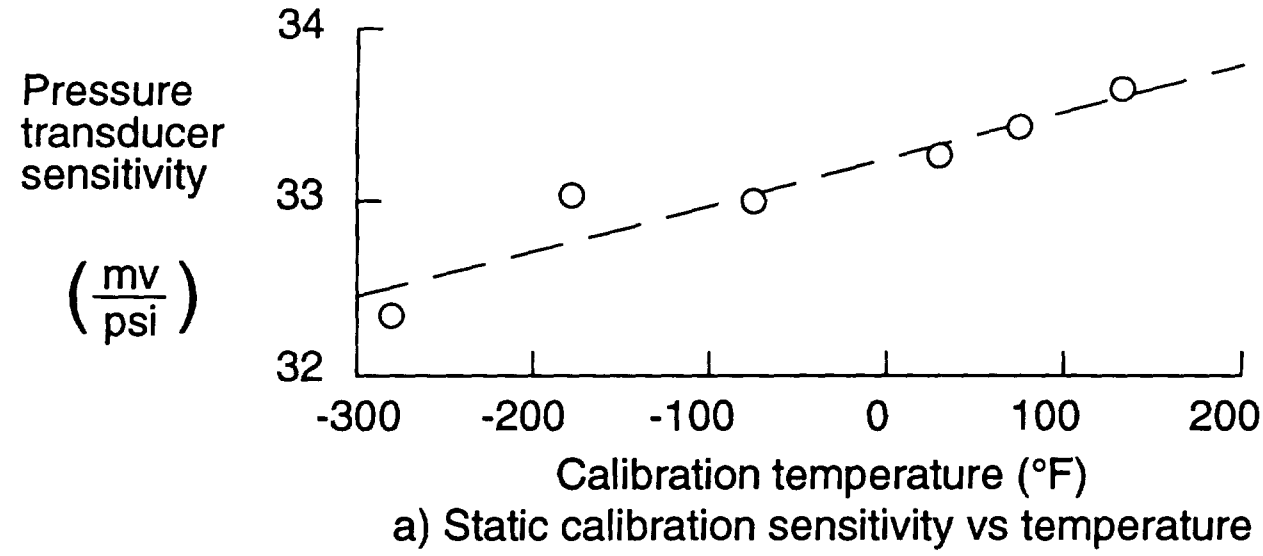

a) Static calibration sensitivity vs temperature

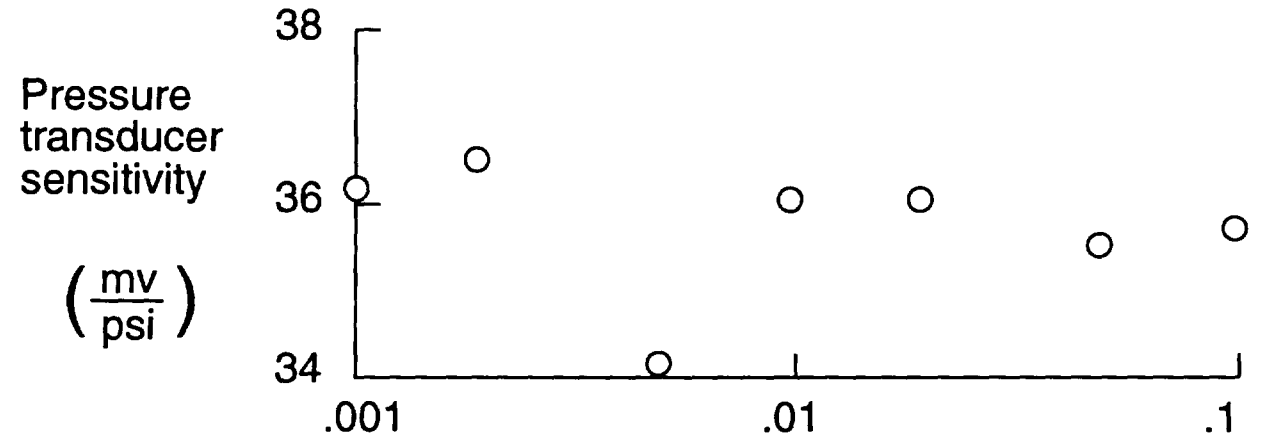

b) Dynamic range at 1 kHz frequency

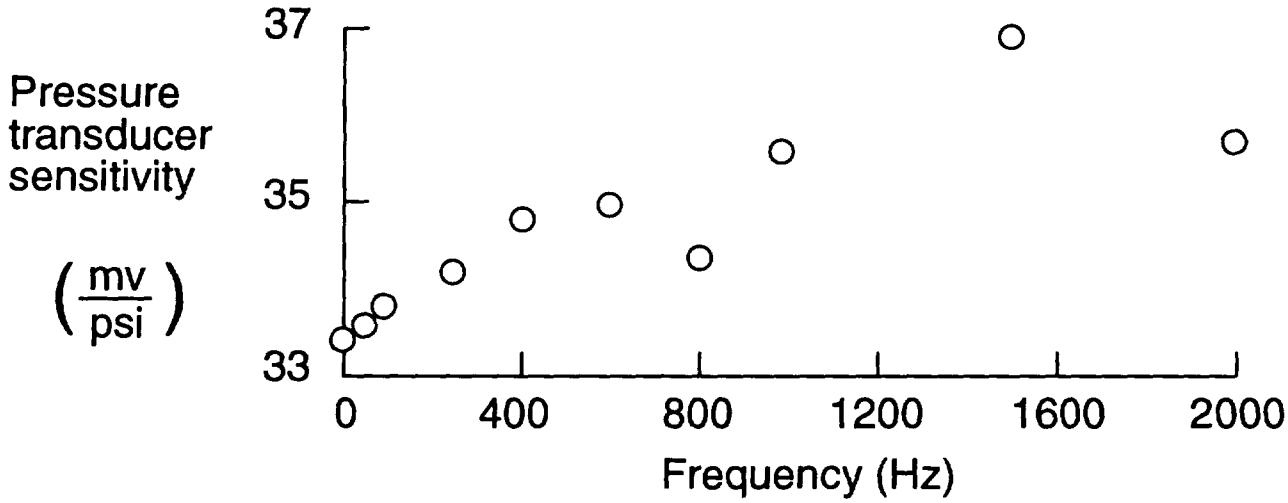

c) Frequency response at 0.05 psi amplitude

Figure 7. Pressure transducer 64 RY static and dynamic calibration sensitivities.

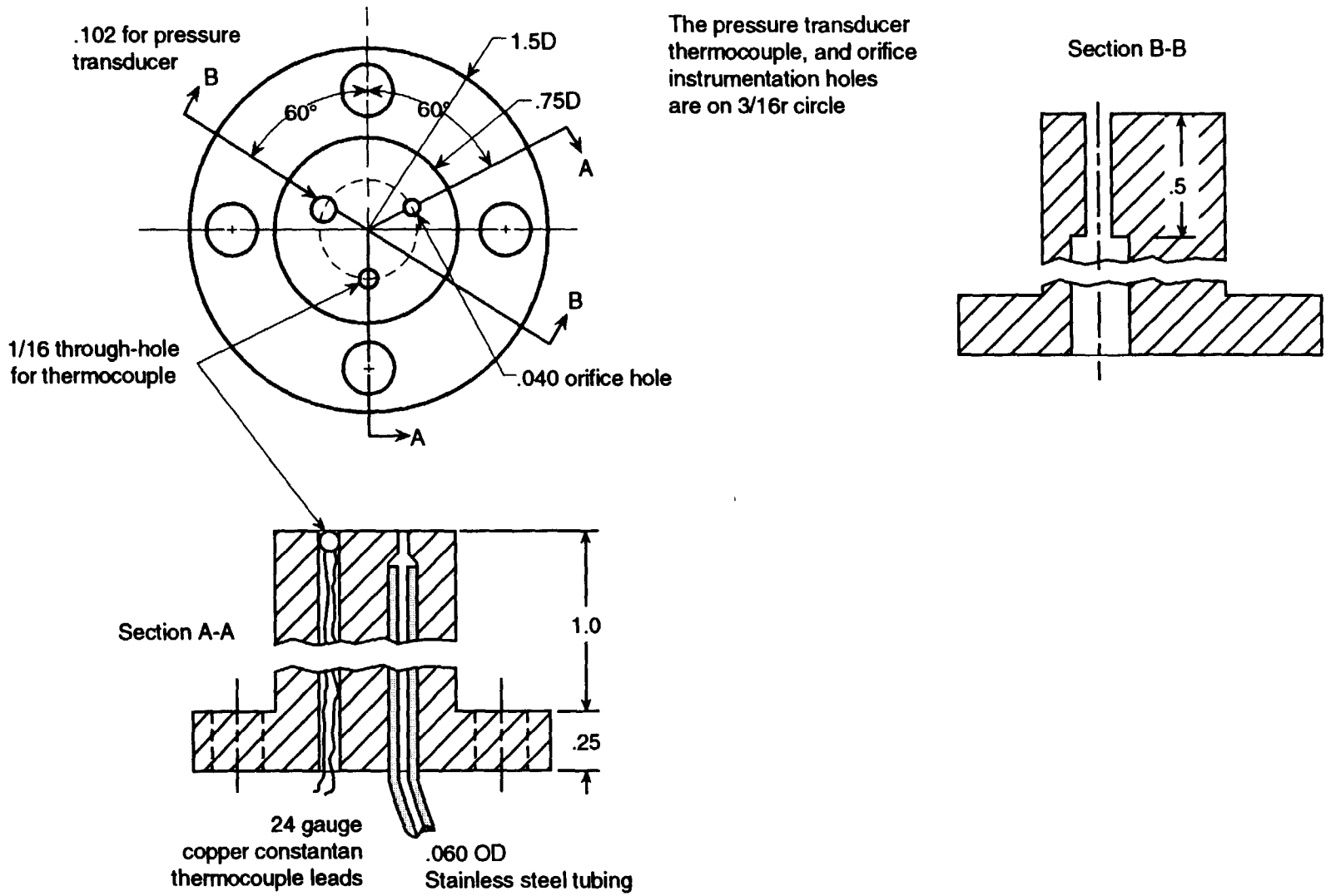

Figure 8. NTF pressure transducer instrumentation plug (all dimens. in inches except where noted.)

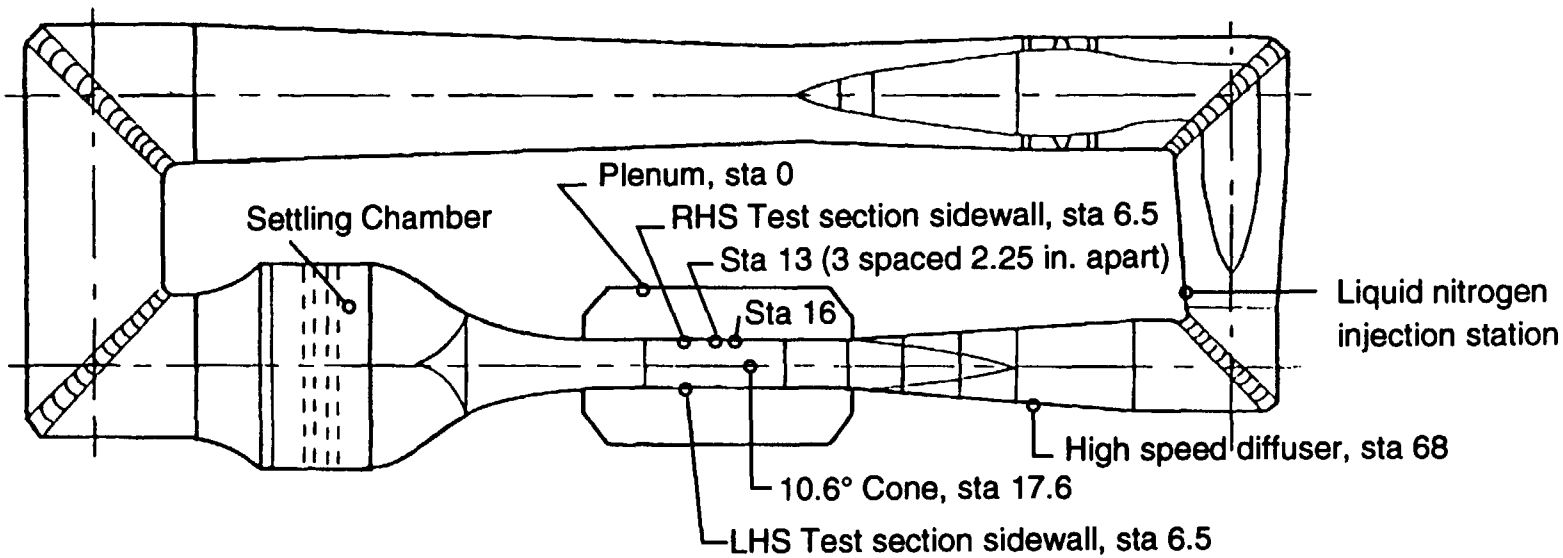

Figure 9. Locations of dynamic pressure transducers installed in the NTF circuit.

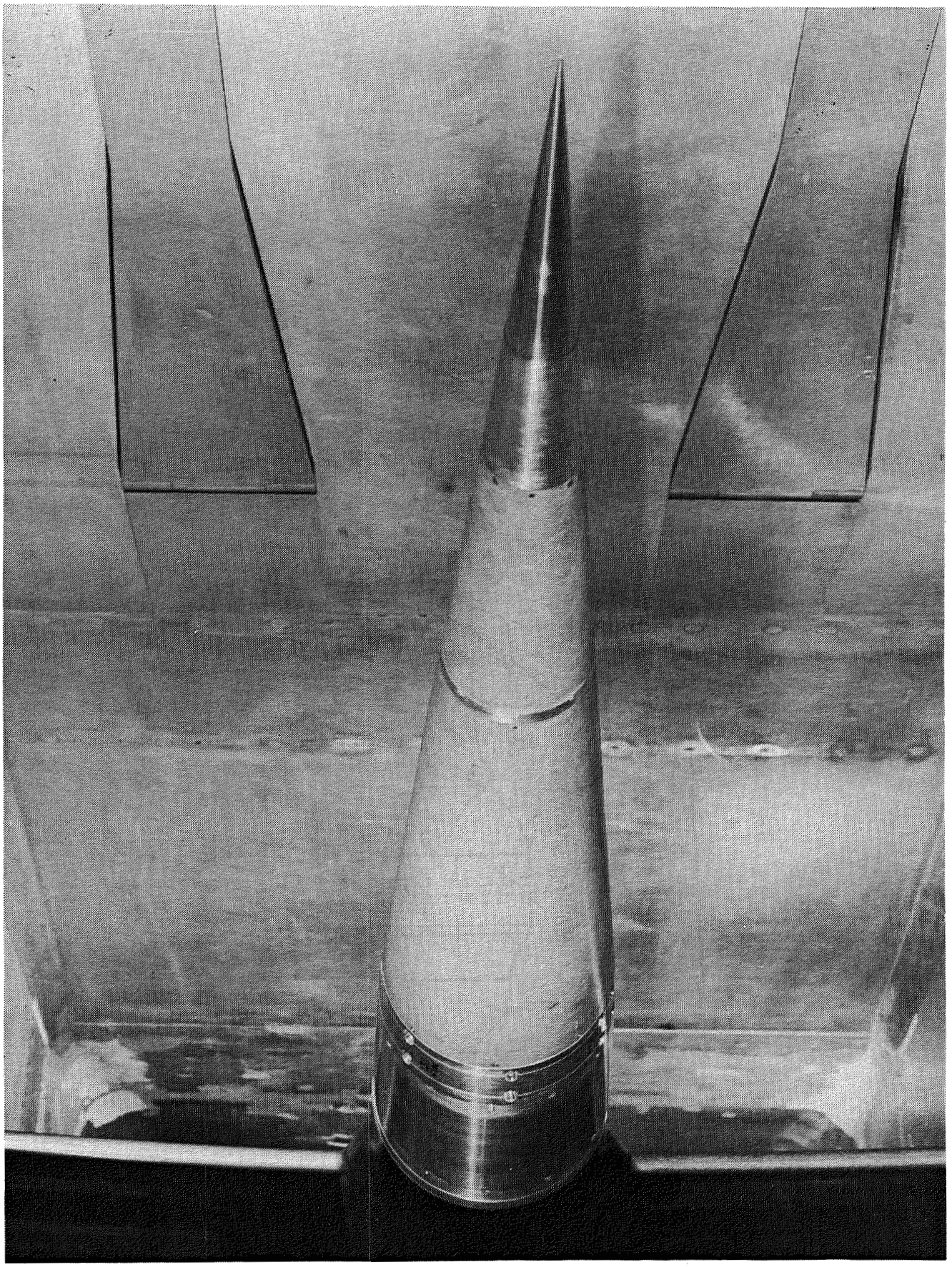

Figure 10. Photograph of 10.6° conical fairing on NTF model support strut center body.

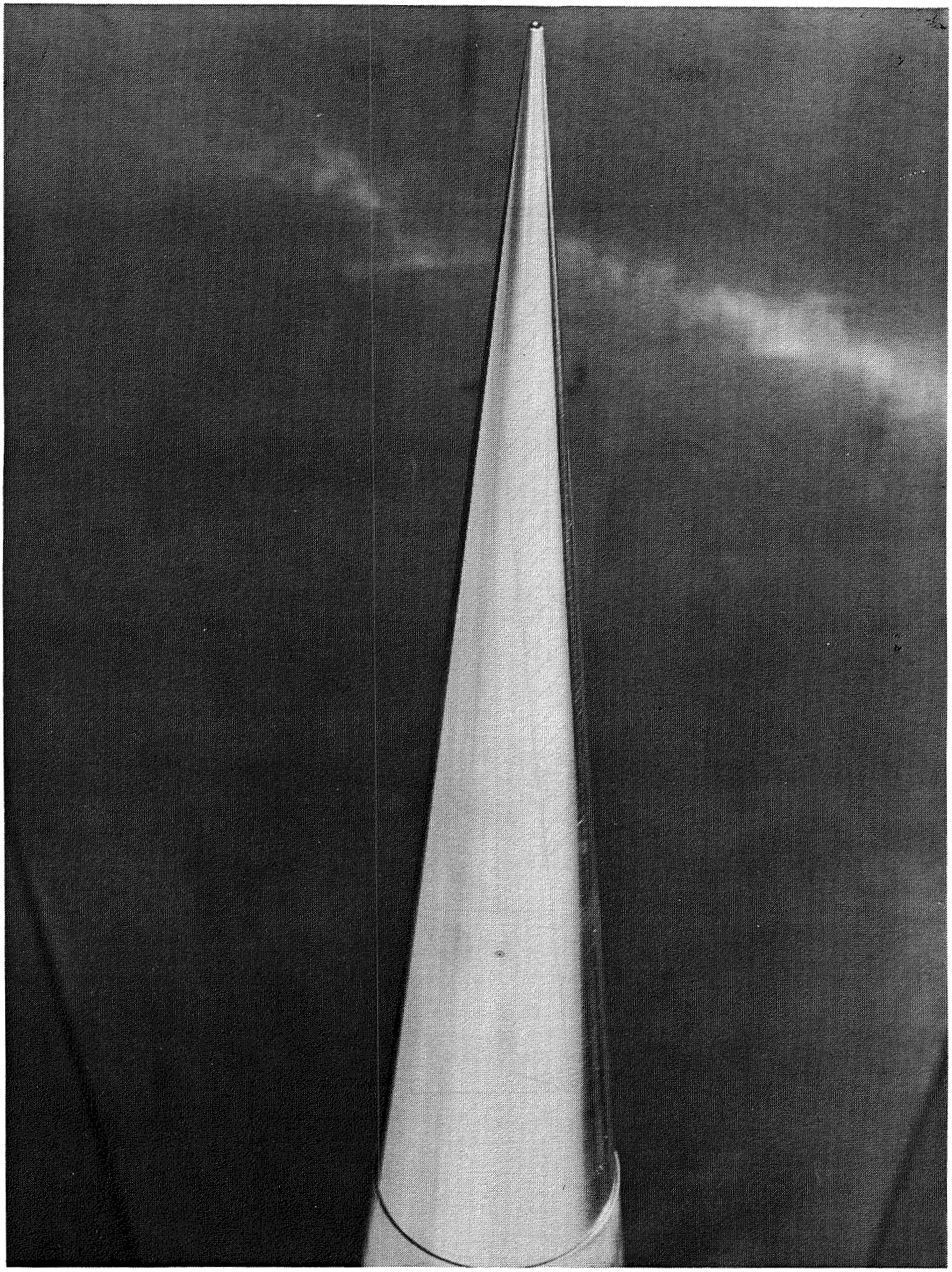

Figure 11. Photograph of 10.6° conical fairing nose tip showing dynamic pressure transducer installation.

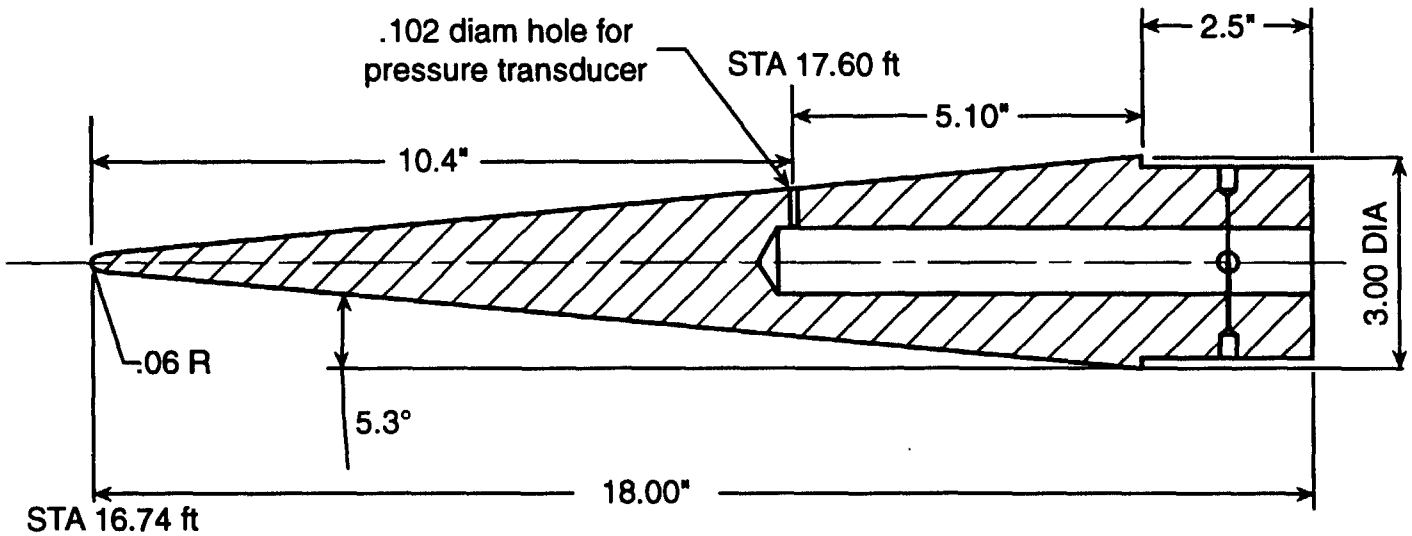

Figure 12. Sketch of 10.6° cone fairing tip (all dimensions in inches except where noted.)

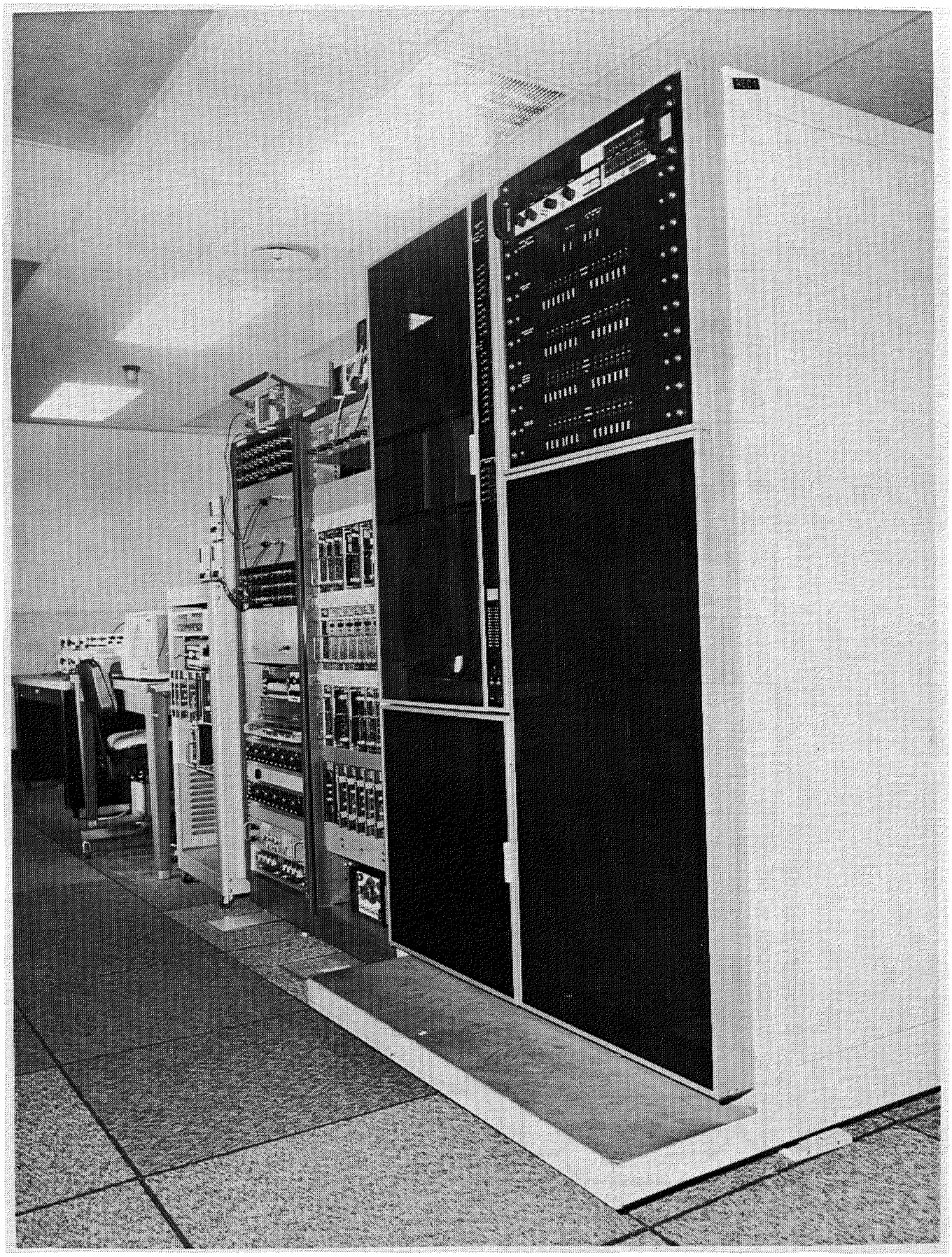

Figure 13. Photograph of dynamic data acquisition instrumentation in NTF control room.

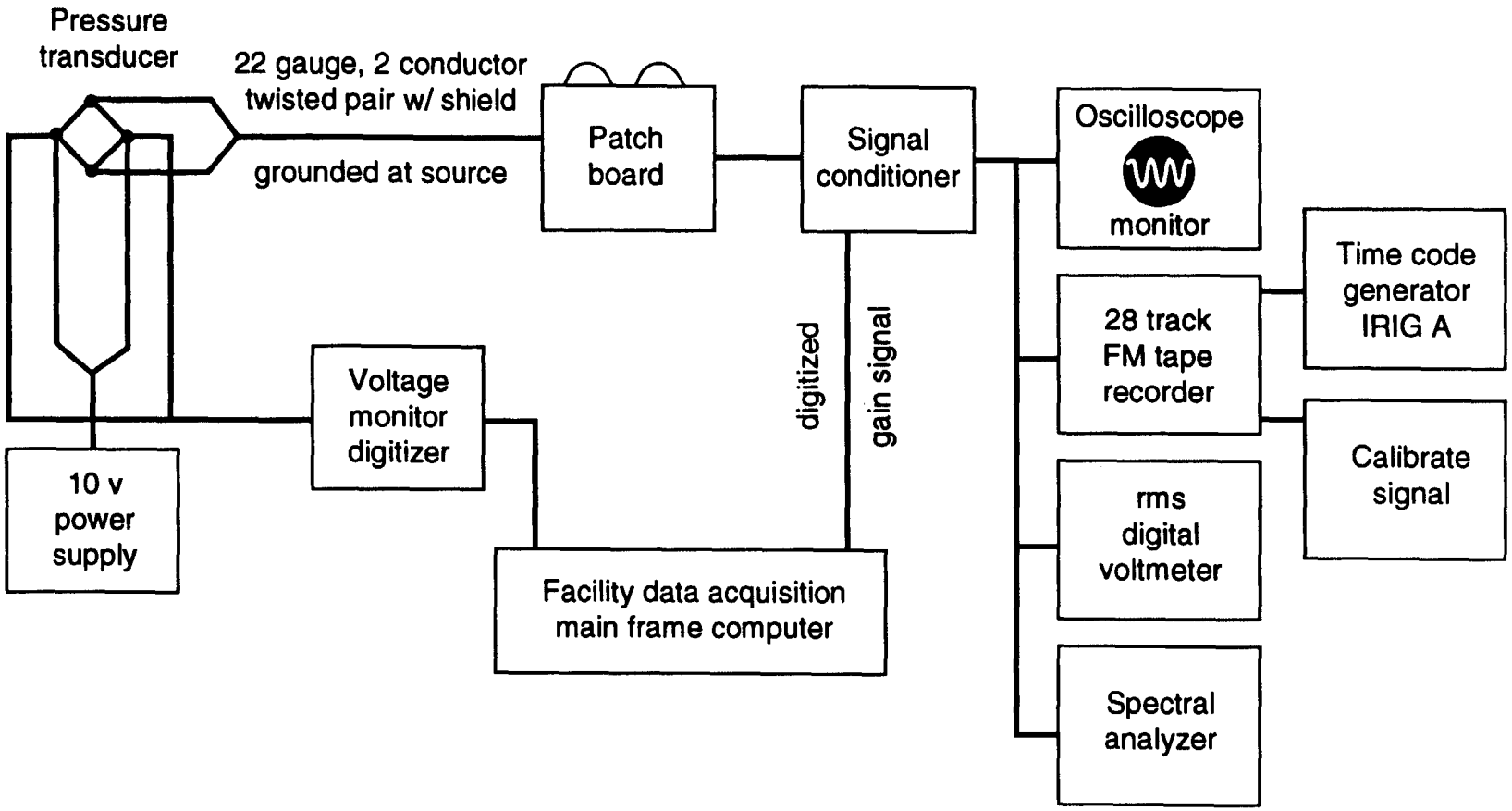

Figure 14. NTF dynamic data system wiring block diagram.

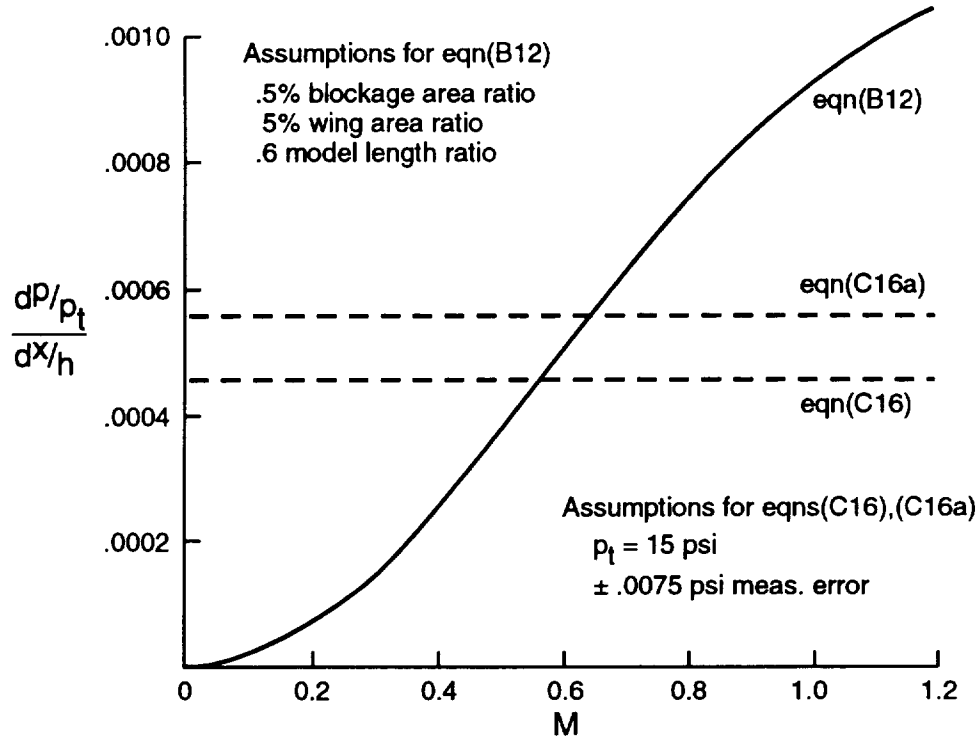

Figure 15. Longitudinal static pressure gradient for 1 count of buoyancy-induced drag coefficient.

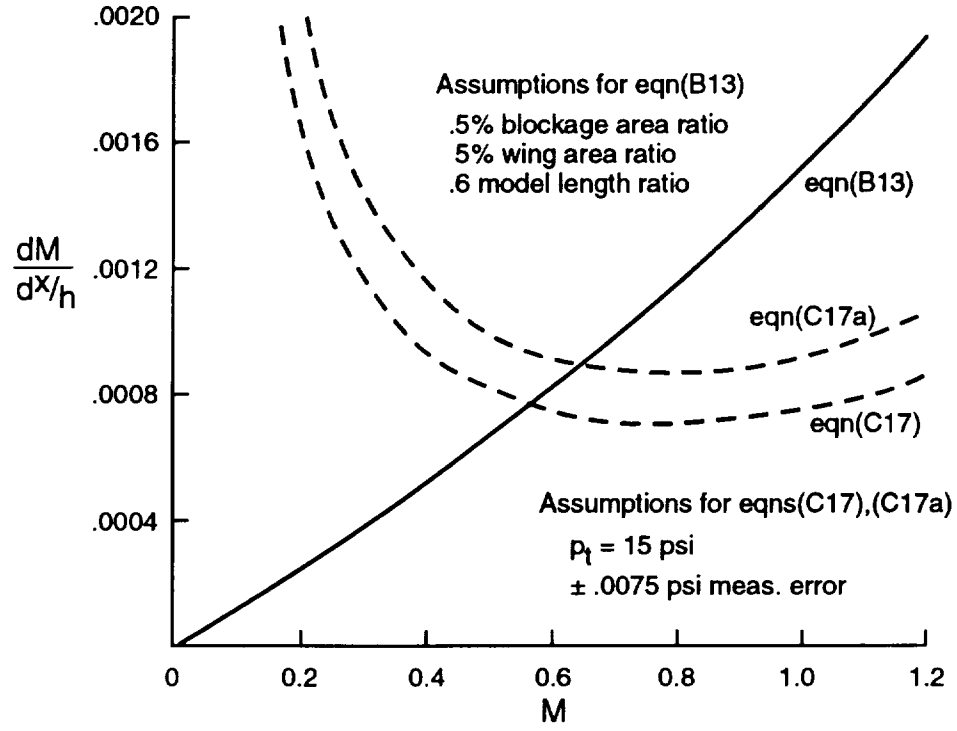

Figure 16. Longitudinal Mach number gradient for 1 count of buoyancy-induced drag coefficient.

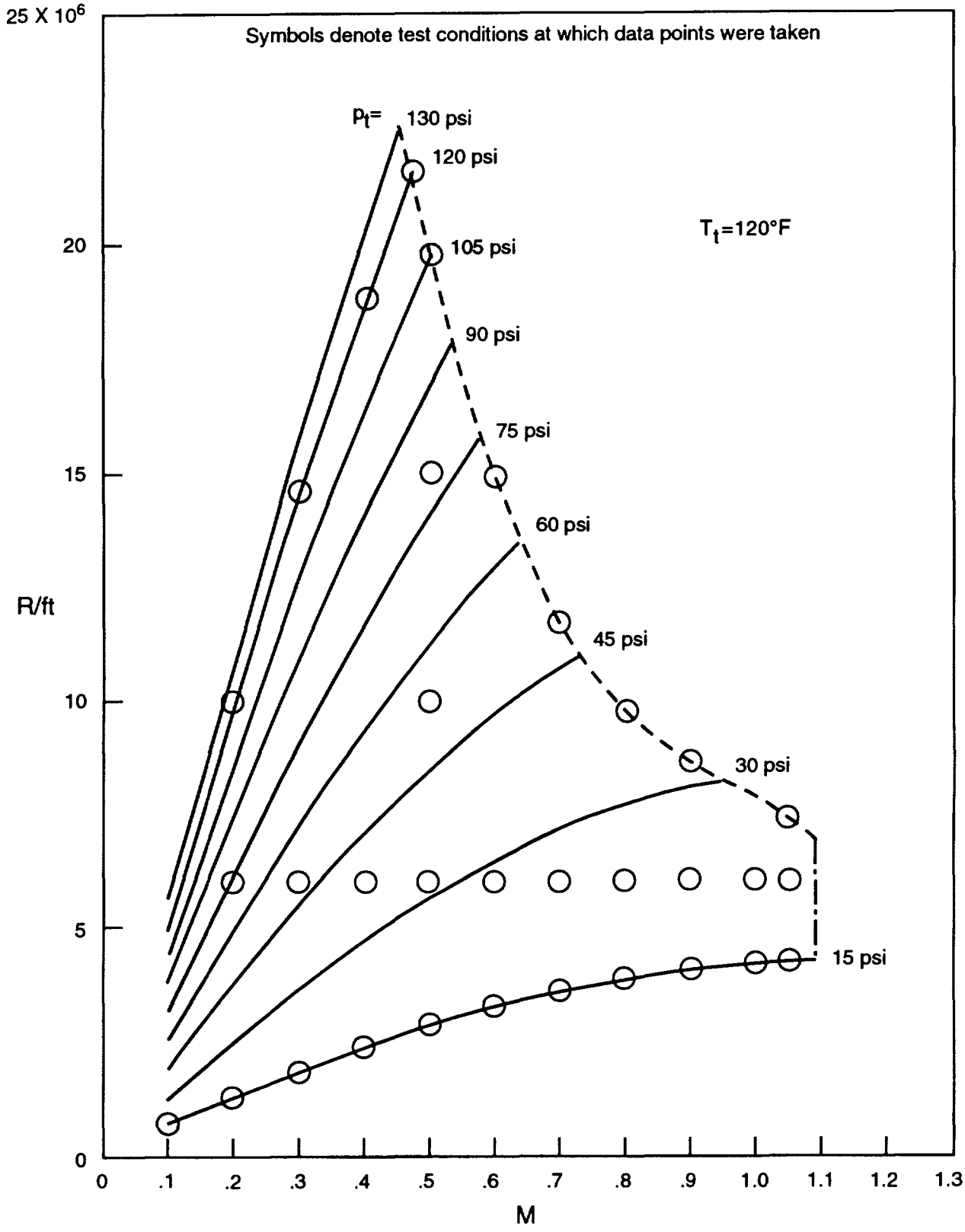

Figure 17. NTF performance envelope in air mode, Reynolds number per foot versus Mach number for various stagnation pressures at a stagnation temperature of 120°F.

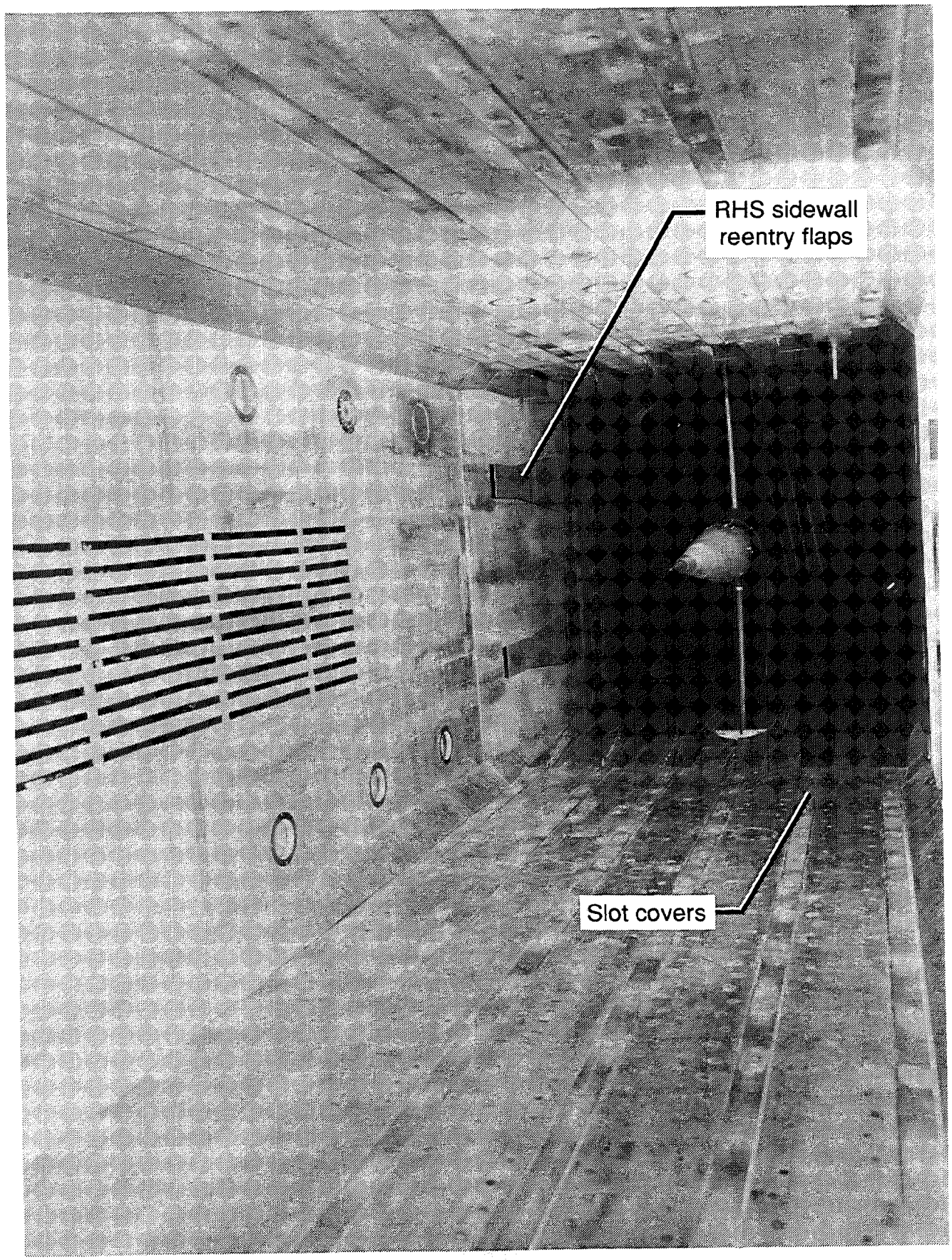

Figure 18. Photograph of NTF test section walls showing slot covers in place.

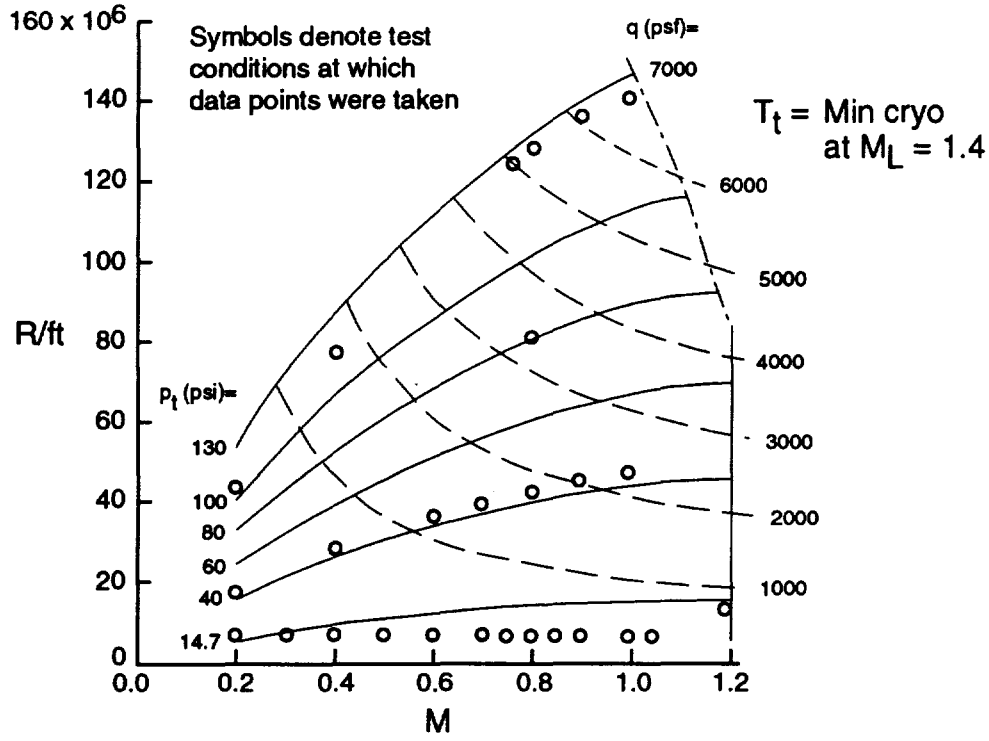

Figure 19. NTF performance envelope in the cryogenic mode, Reynolds number per foot versus Mach number for various stagnation pressures at the minimum stagnation temperature for cryogenic operation at a local Mach number of 1.4.

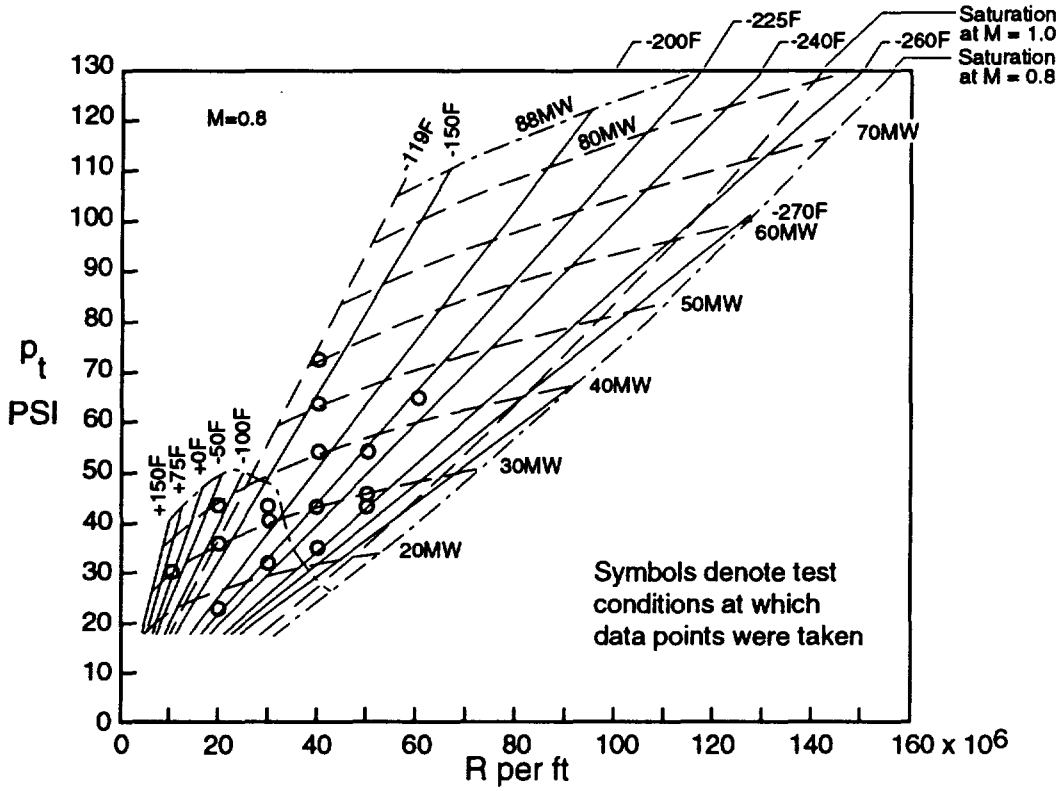

Figure 20. NTF Operating envelope for a Mach number of 0.8, stagnation pressure versus Reynolds number per foot for various stagnation temperatures.

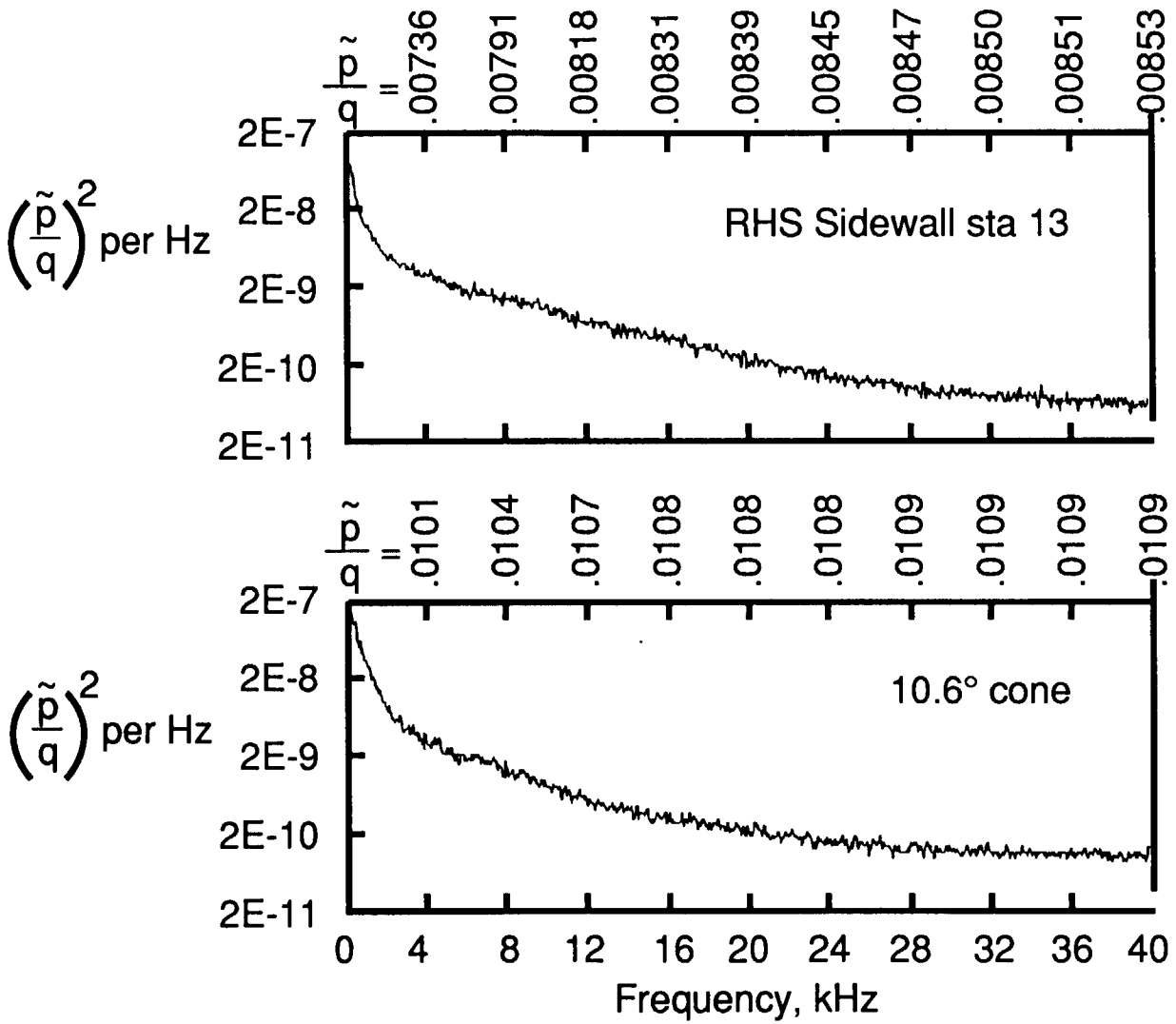

Figure 21. Power spectral density function versus frequency for fluctuating static pressure coefficient on RHS test section sidewall sta13, and on 10.6° cone, M=.801, R=3.8x10^6/ft, p_t=14.92 psi, T_t= 121.1°F, air.

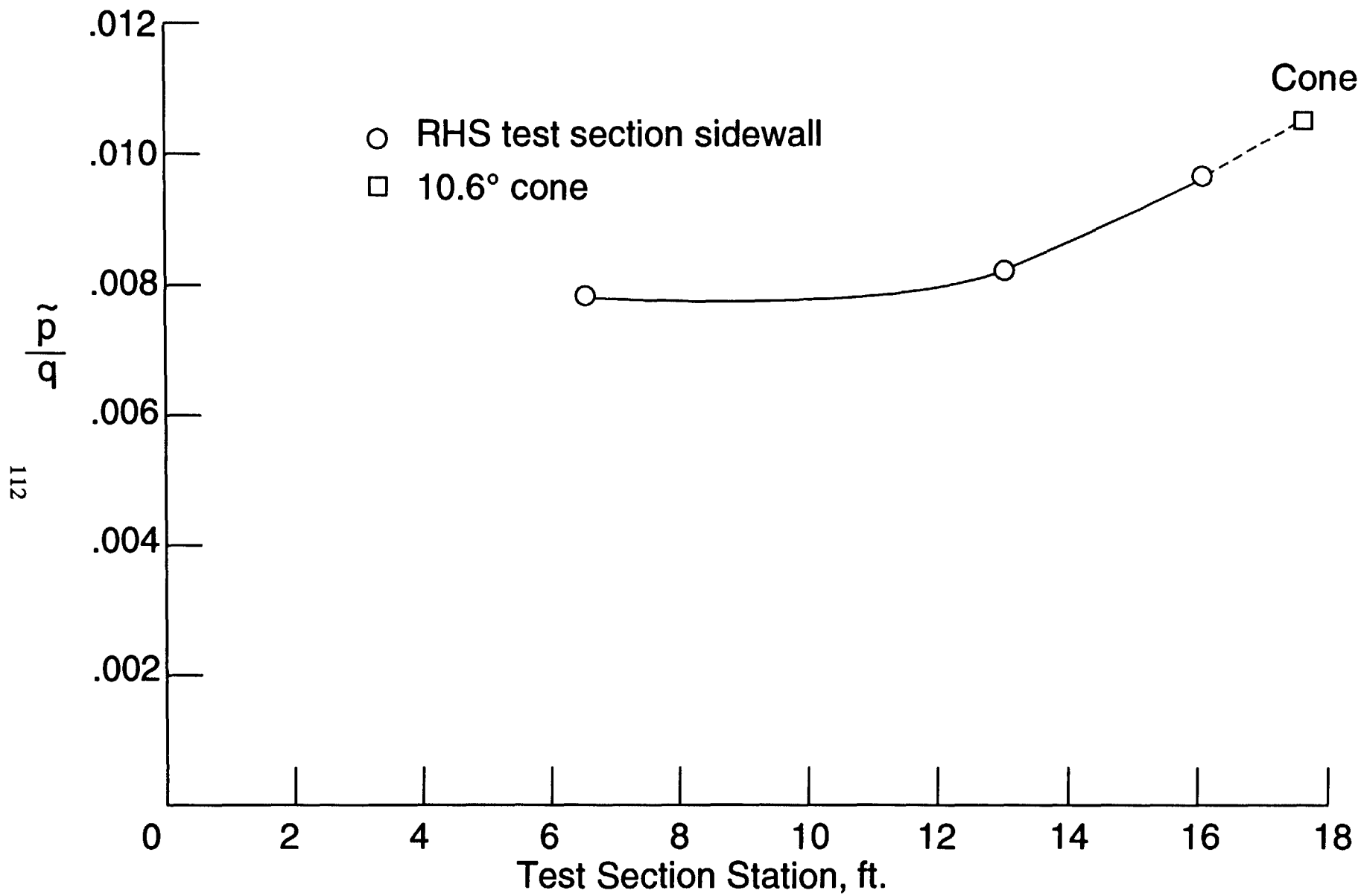

Figure 22. Variation of fluctuating pressure coefficient with streamwise location in NTF test section, M= 0.8, R=3.8x10^6/ft, (min. R boundary), air.

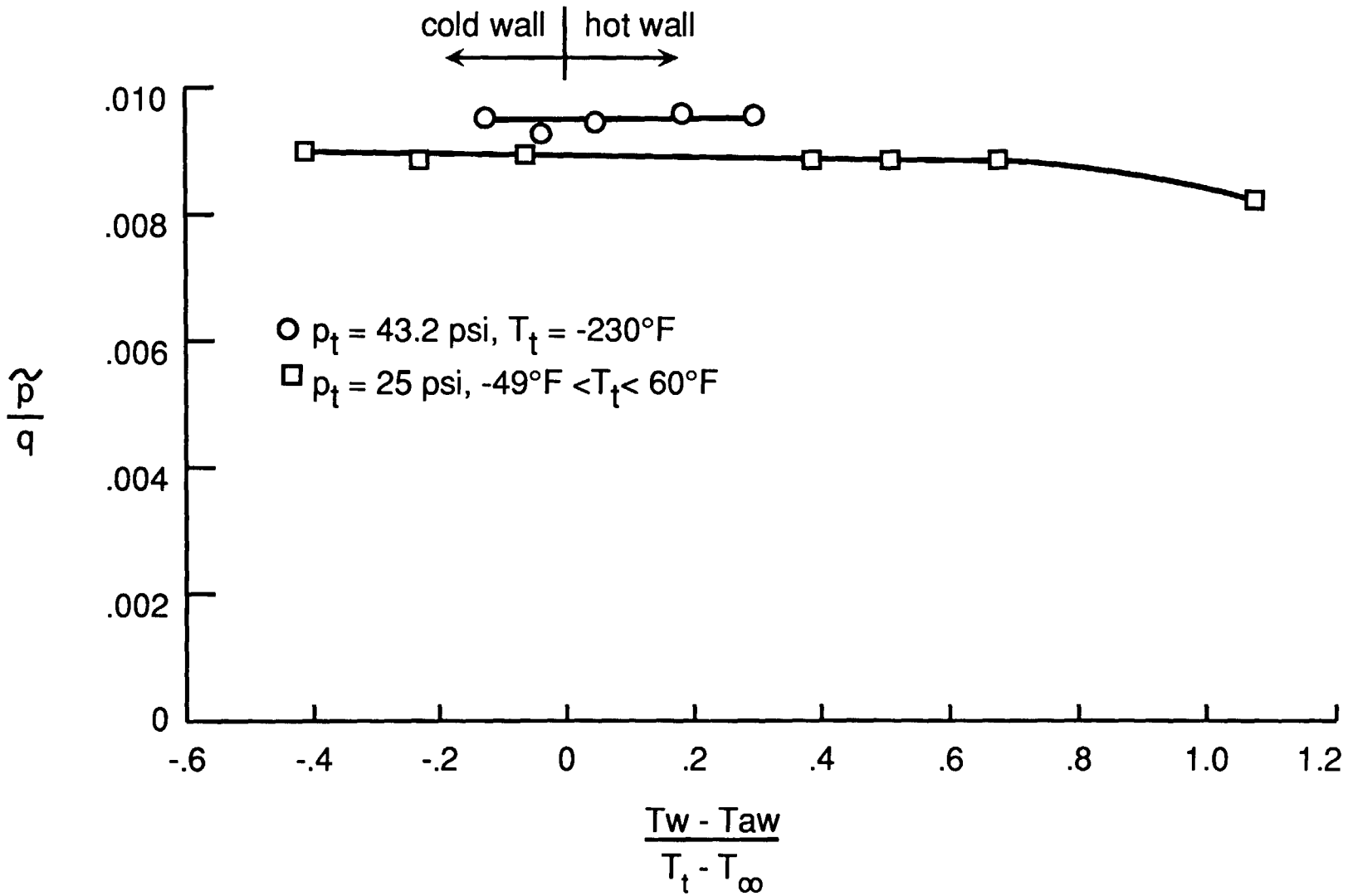

Figure 23. Effect of hot wall and cold wall on fluctuating pressure coefficients on RHS test section wall, sta 13, for M = .8, nitrogen.

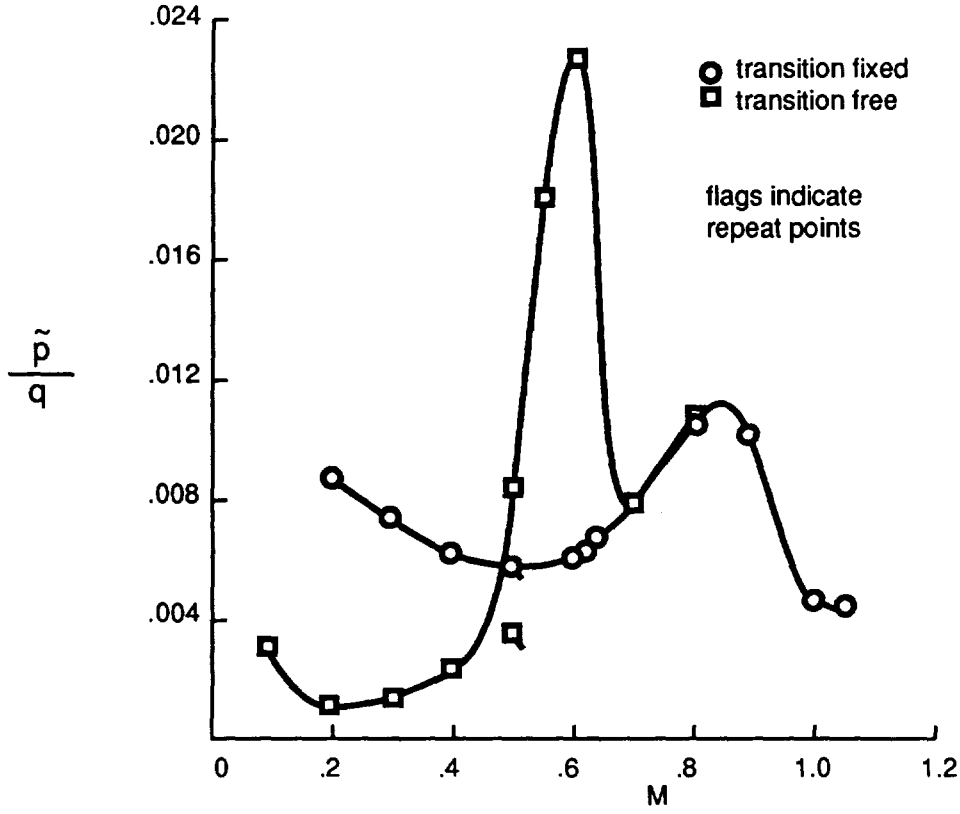

(a) p_t = 15 psi, ambient temperature, minimum Reynolds number boundary, air.

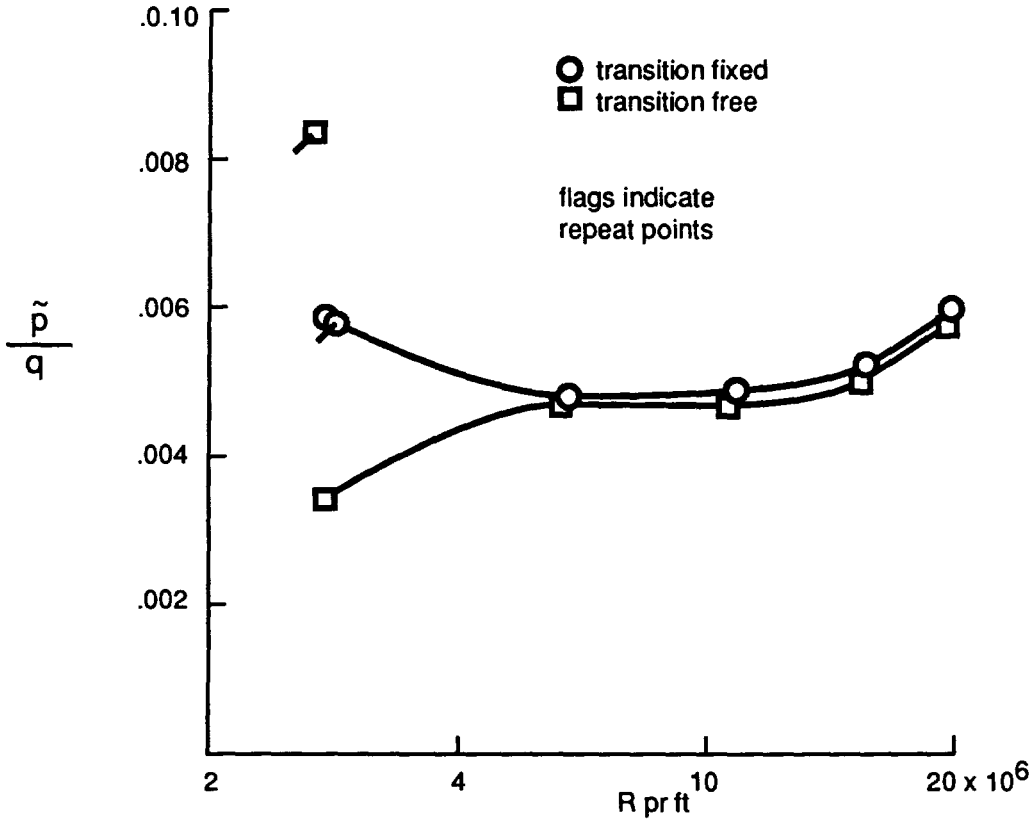

(b) M = 0.5, ambient temperature, air.

Figure 24. Effect of fixing boundary layer transition on 10.6° cone.

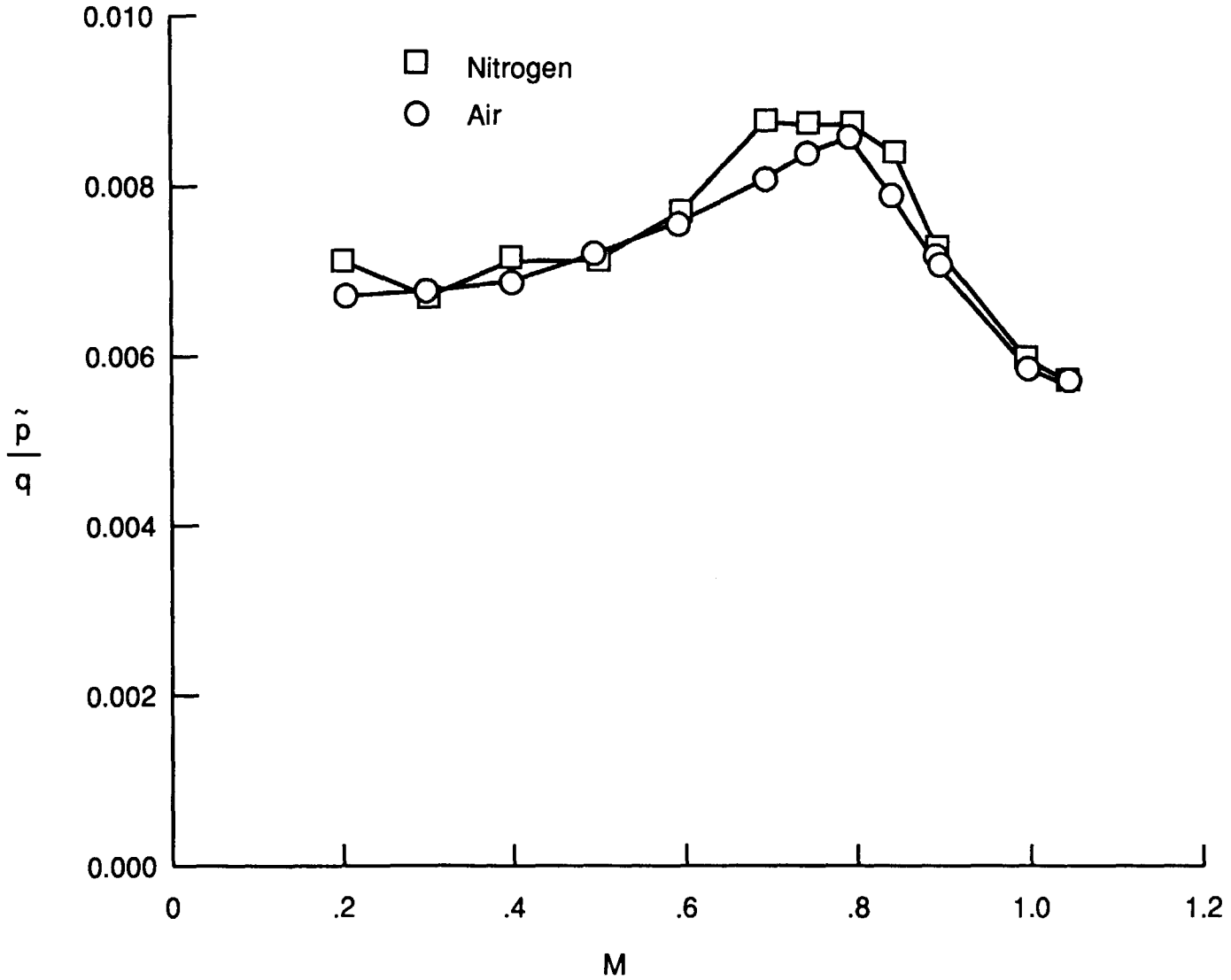

Figure 25. Fluctuating pressure coefficient measured on RHS test section sidewall at sta 13, $R = 6 \times 10^6$/ft, ambient temperature, comparison between air and gaseous nitrogen.

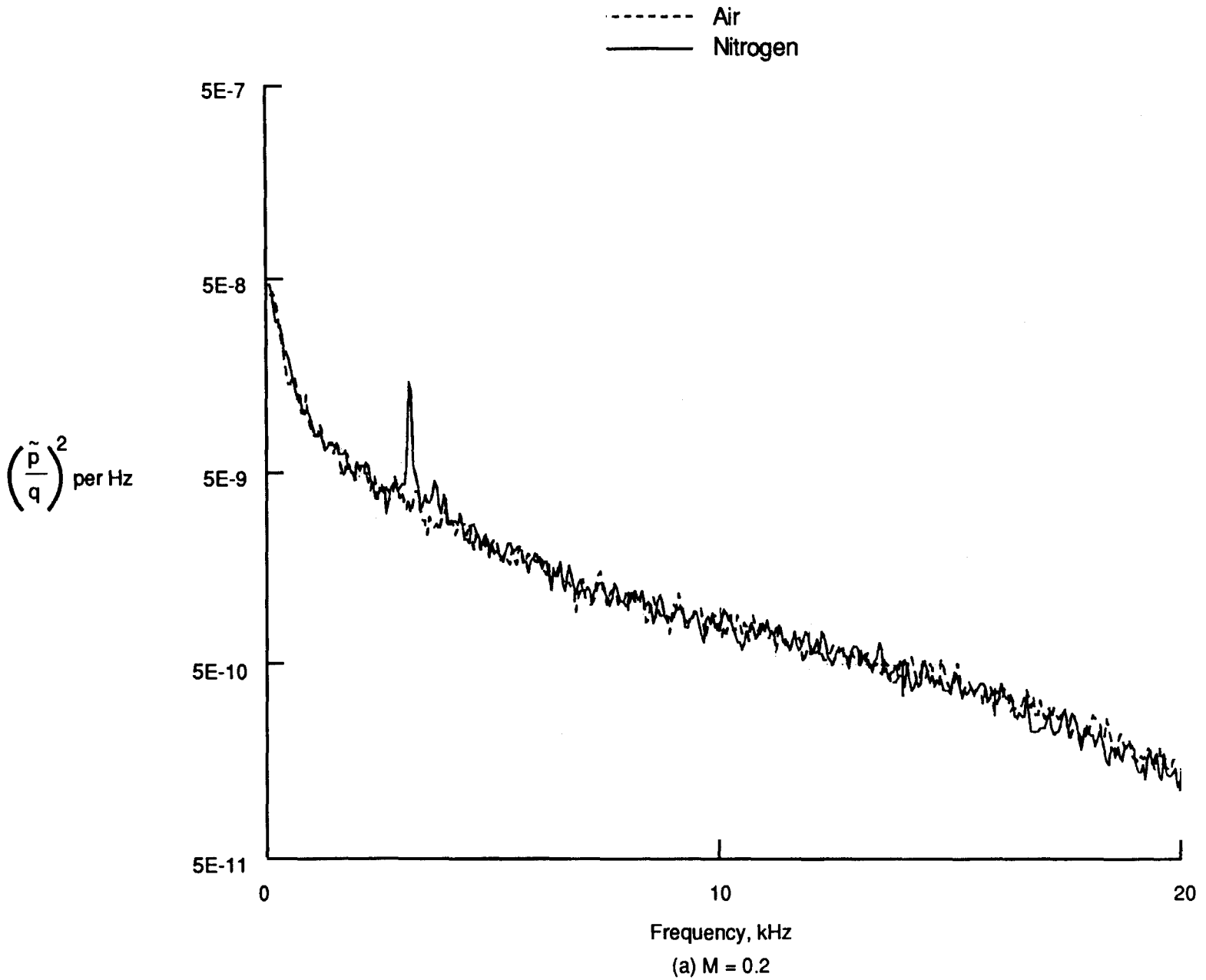

Figure 26. Power spectra of fluctuating pressure coefficient on RHS test section sidewall at sta 13, R = 6 x 10^6/ft., ambient temperature, comparison between air and gaseous nitrogen.

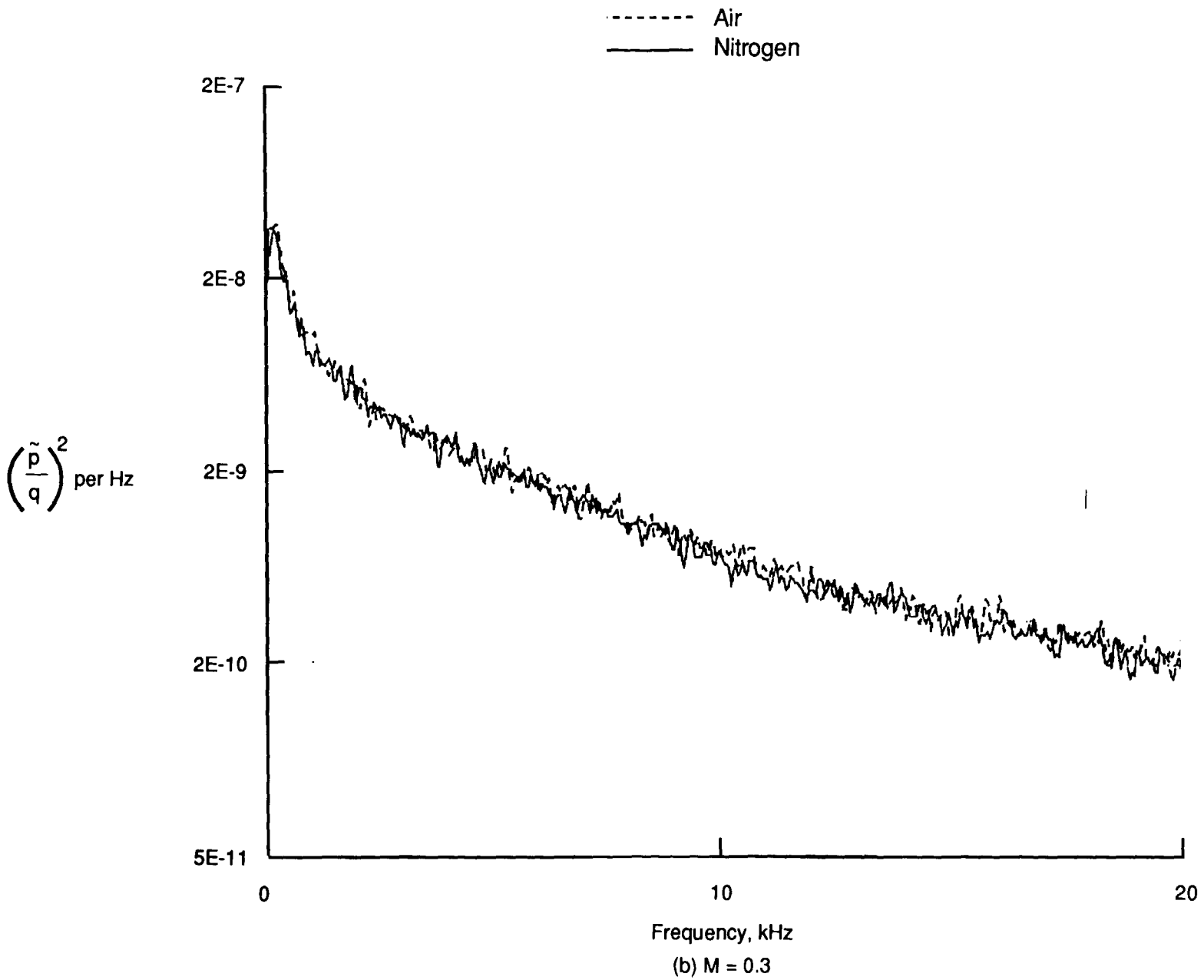

Figure 26. Continued.

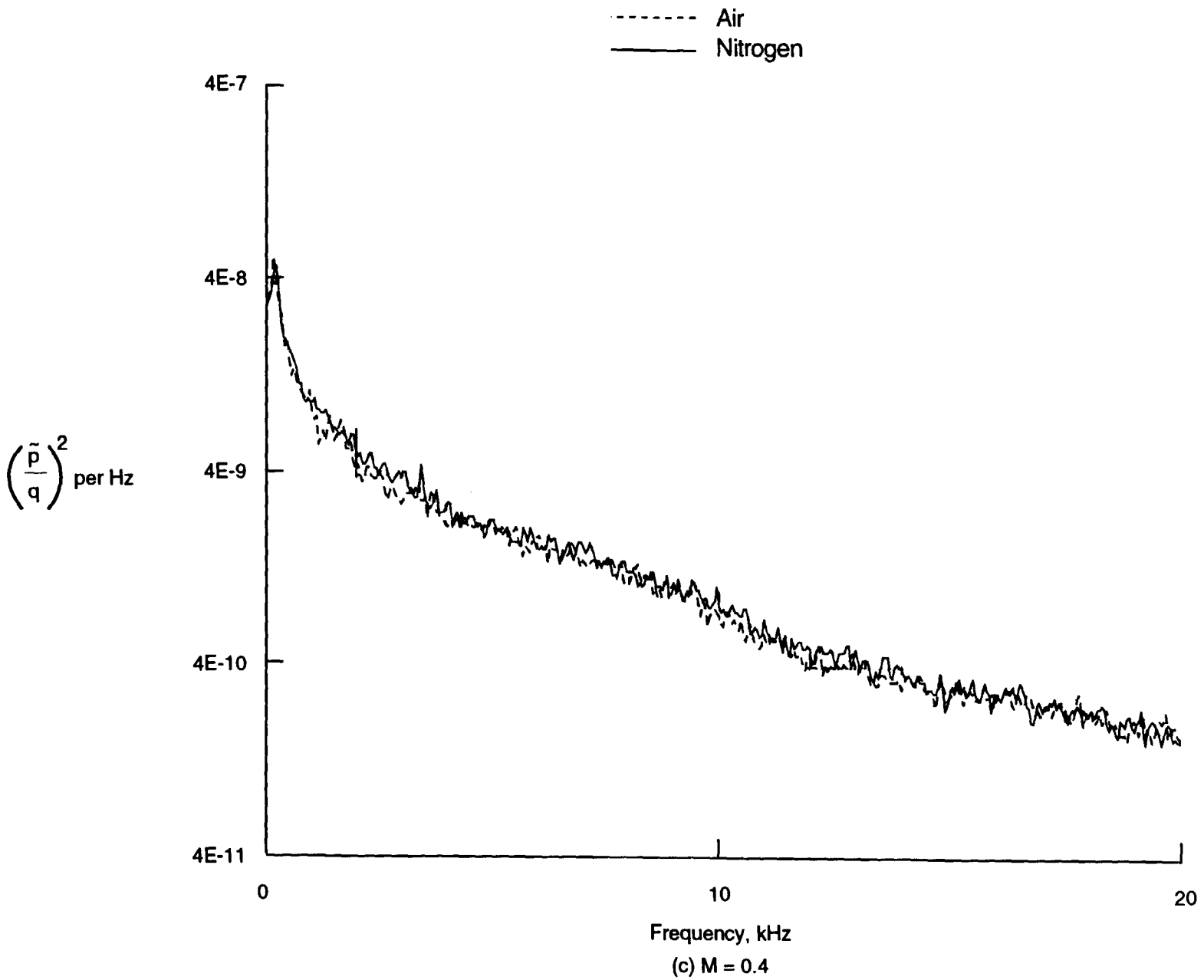

Figure 26. Continued.

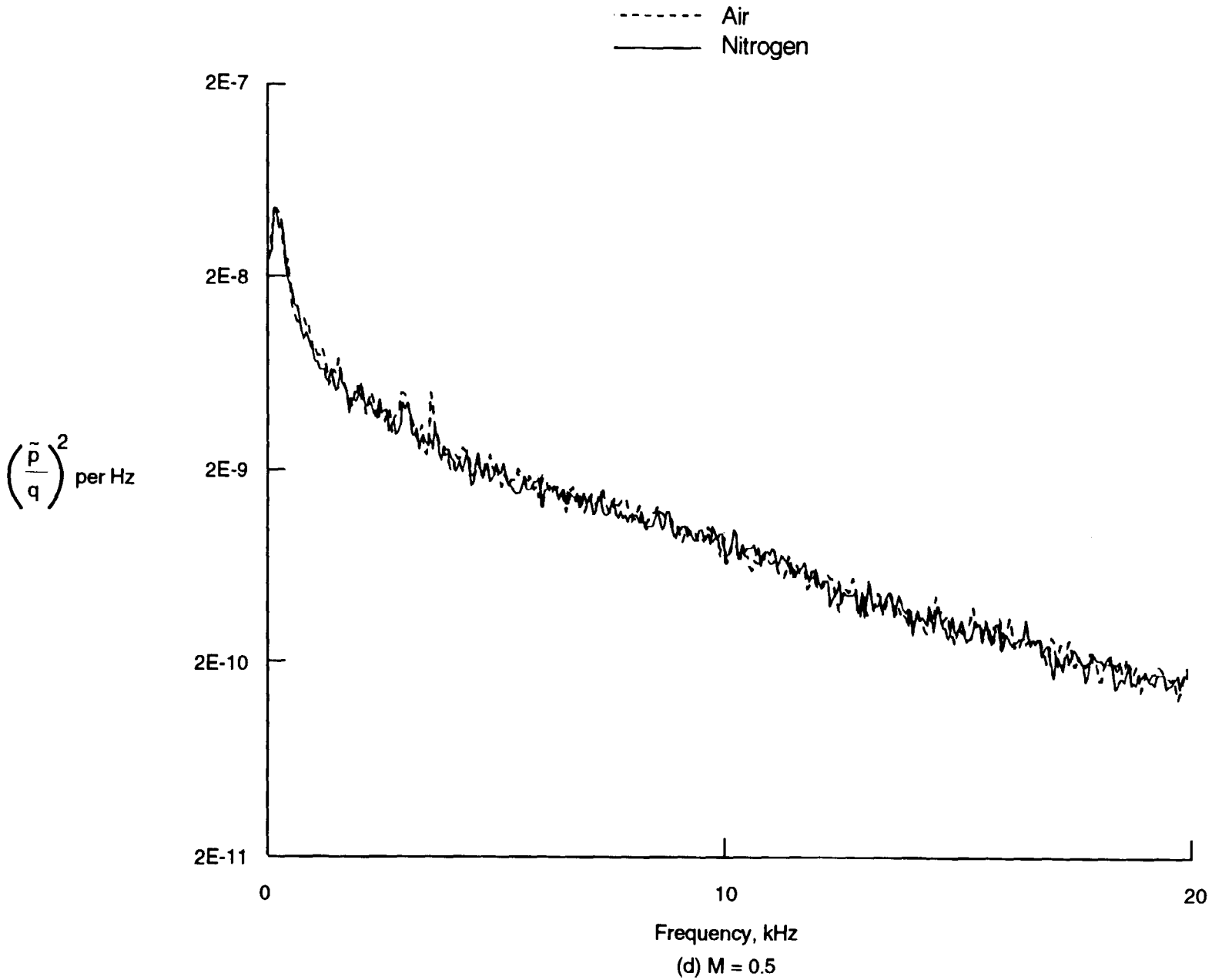

Figure 26. Continued.

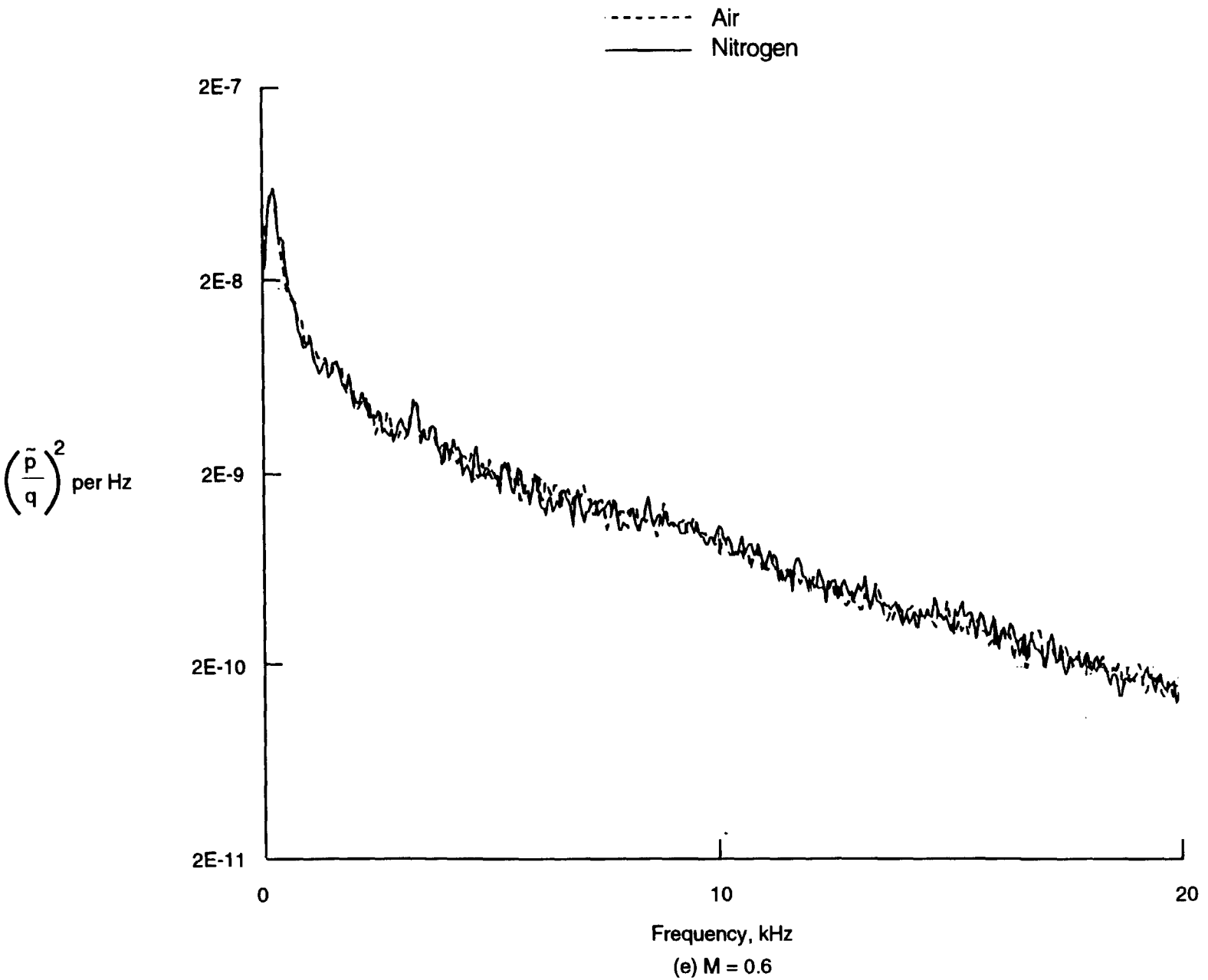

Figure 26. Continued.

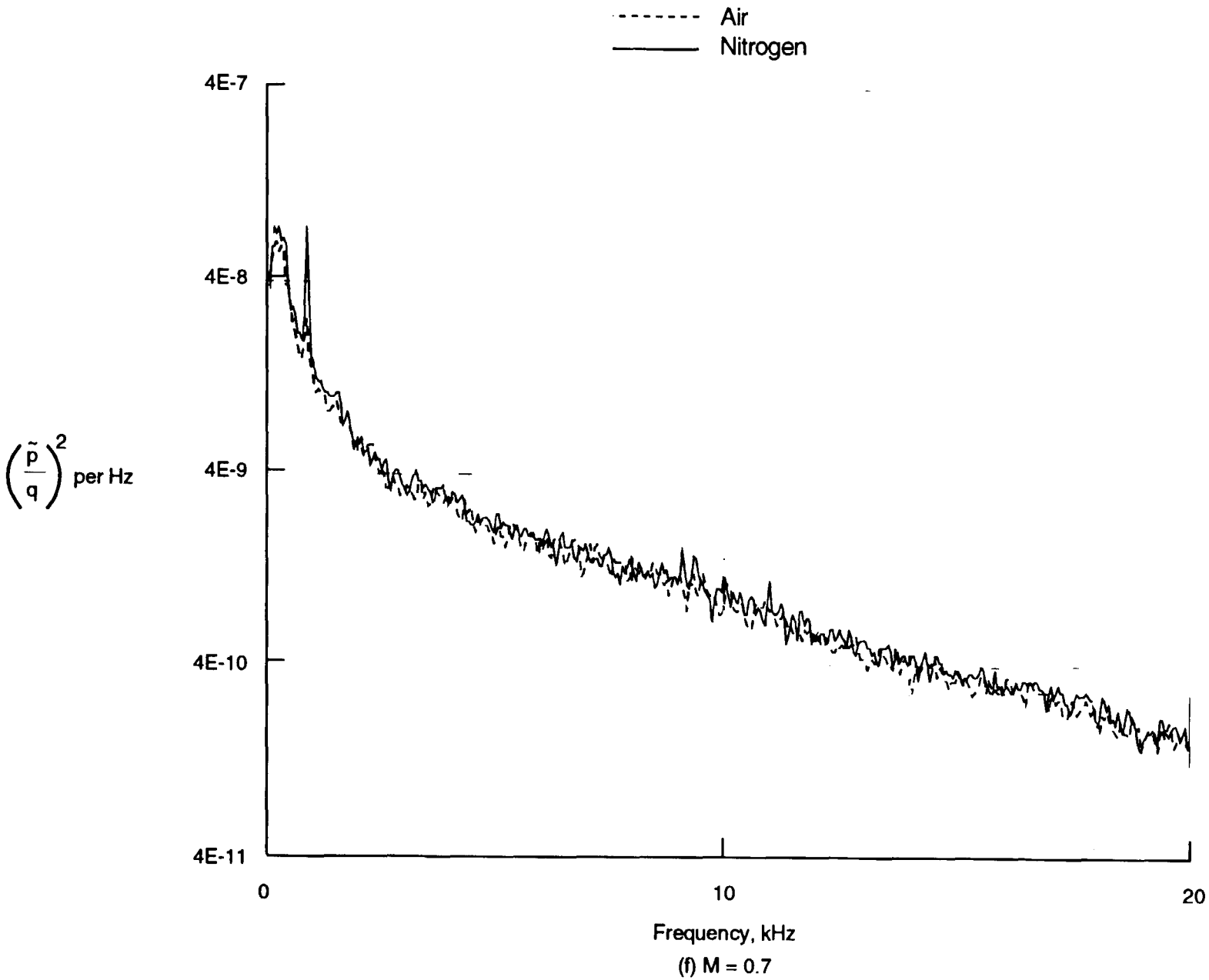

Figure 26. Continued.

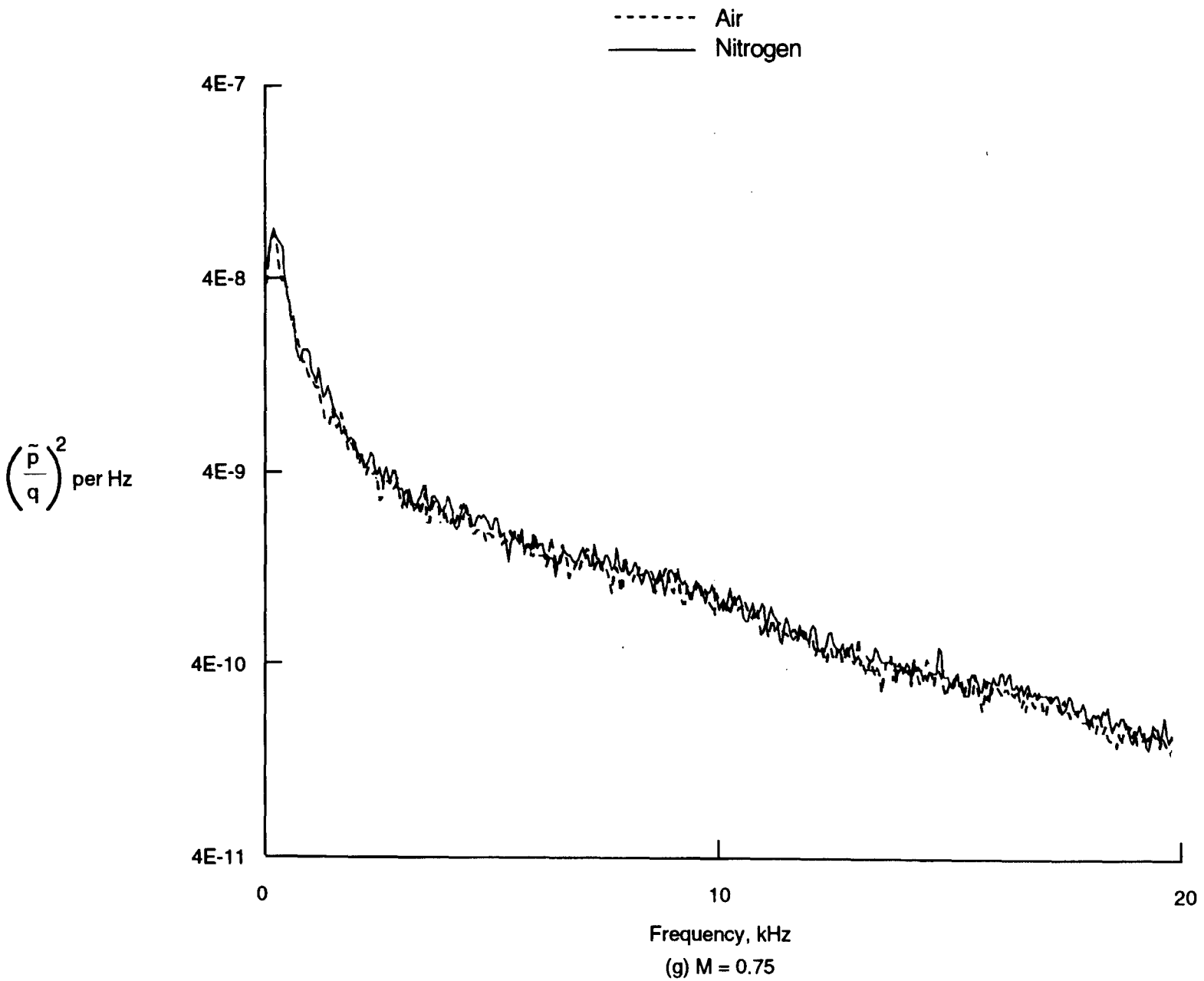

Figure 26. Continued.

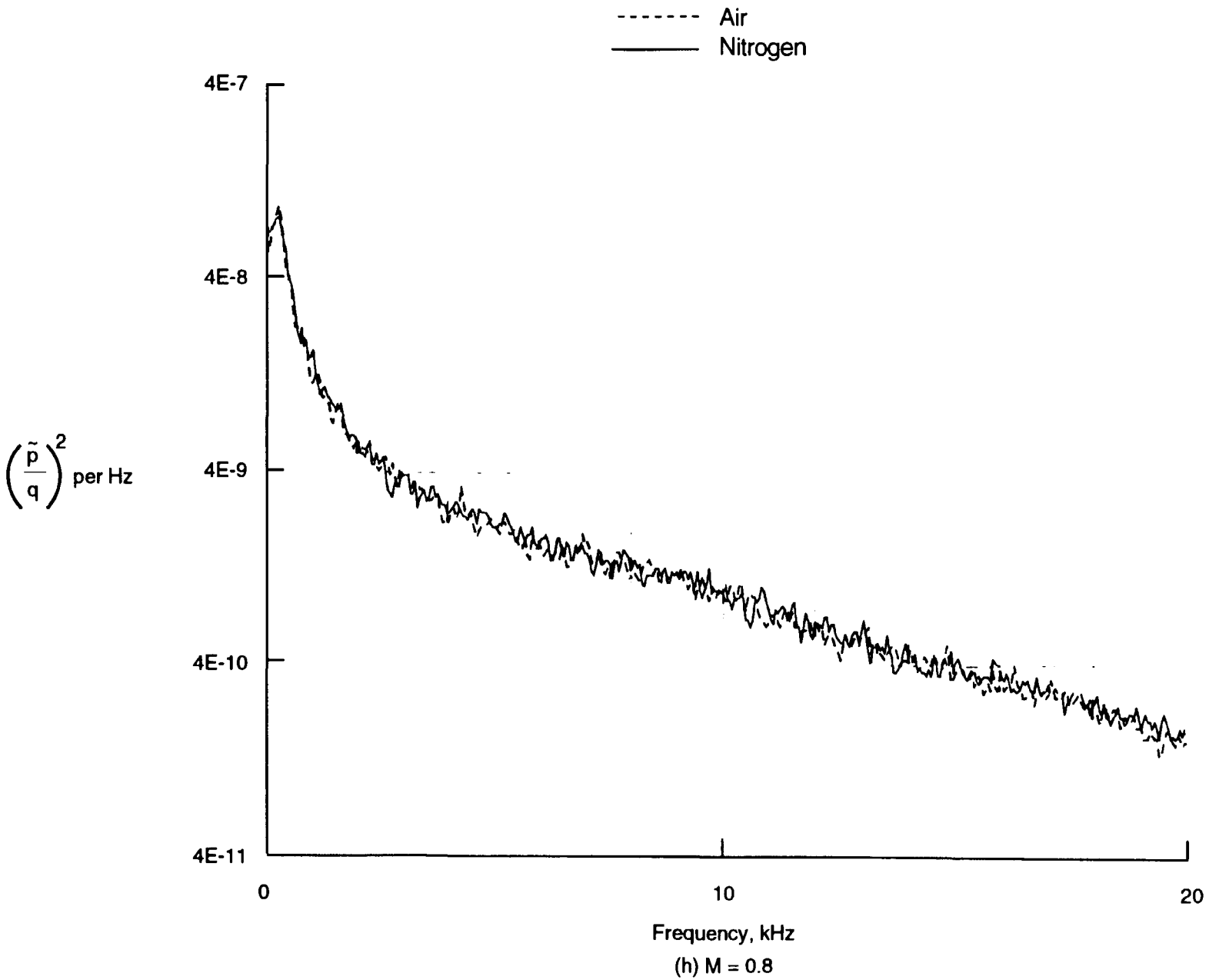

Figure 26. Continued.

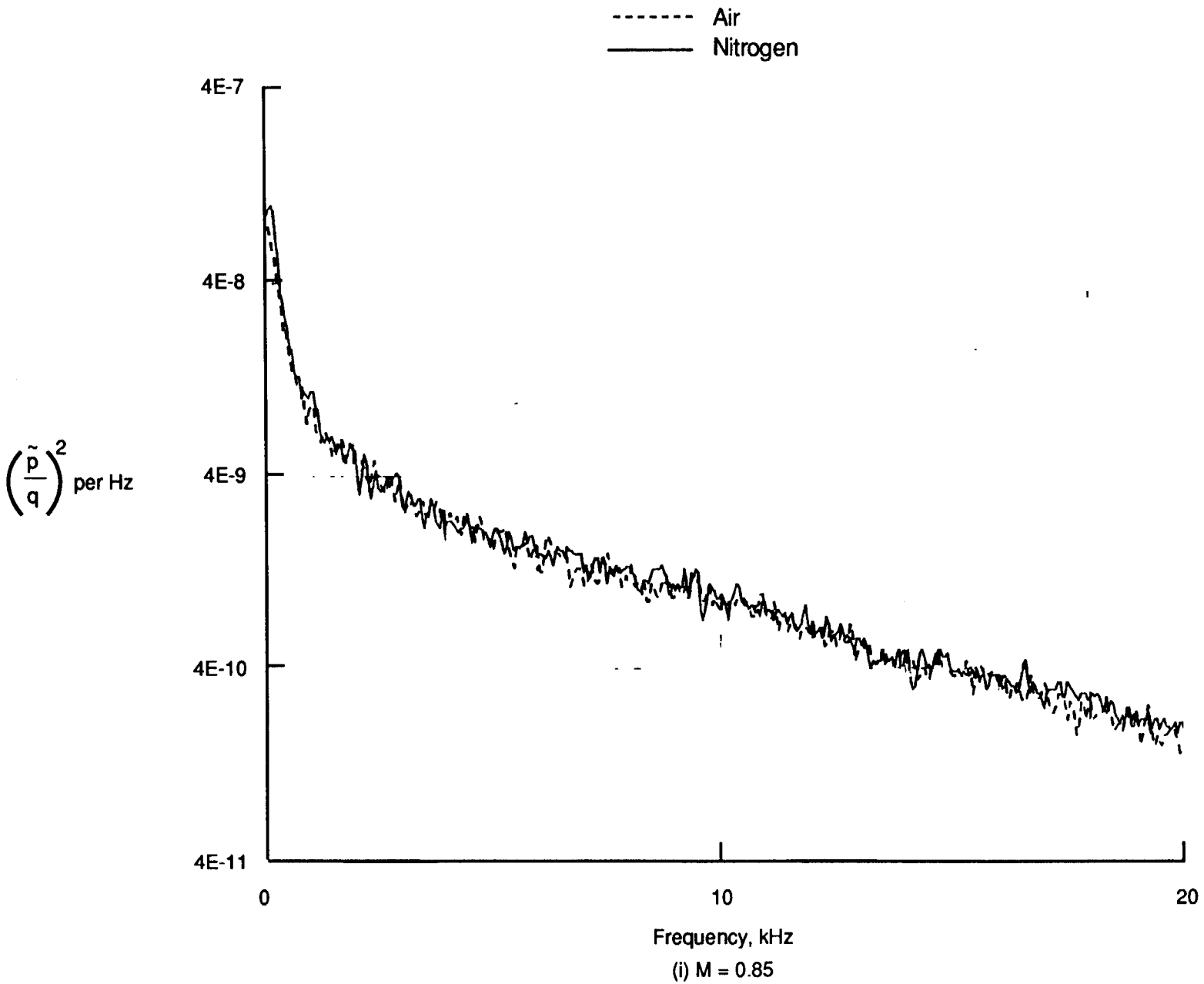

Figure 26. Continued.

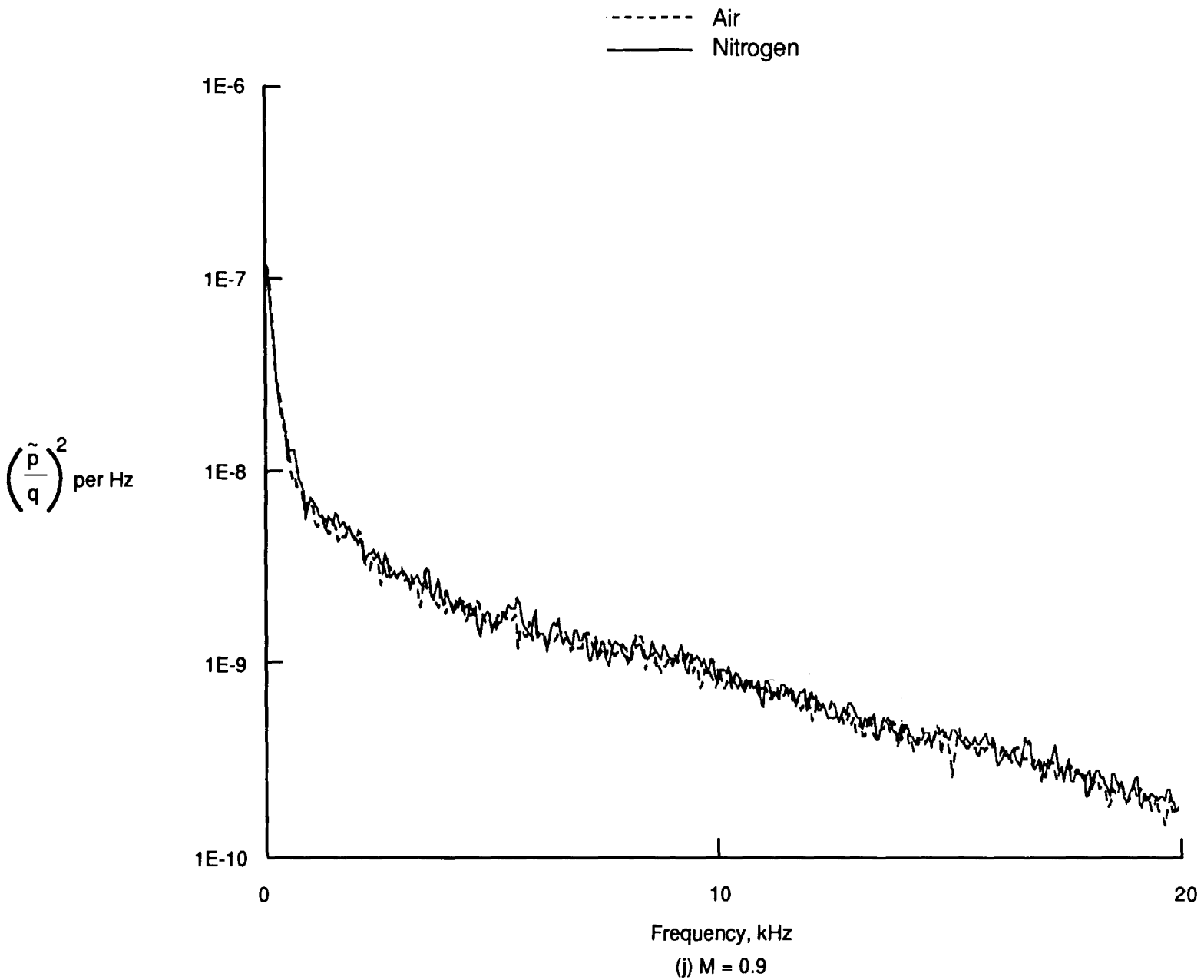

Figure 26. Continued.

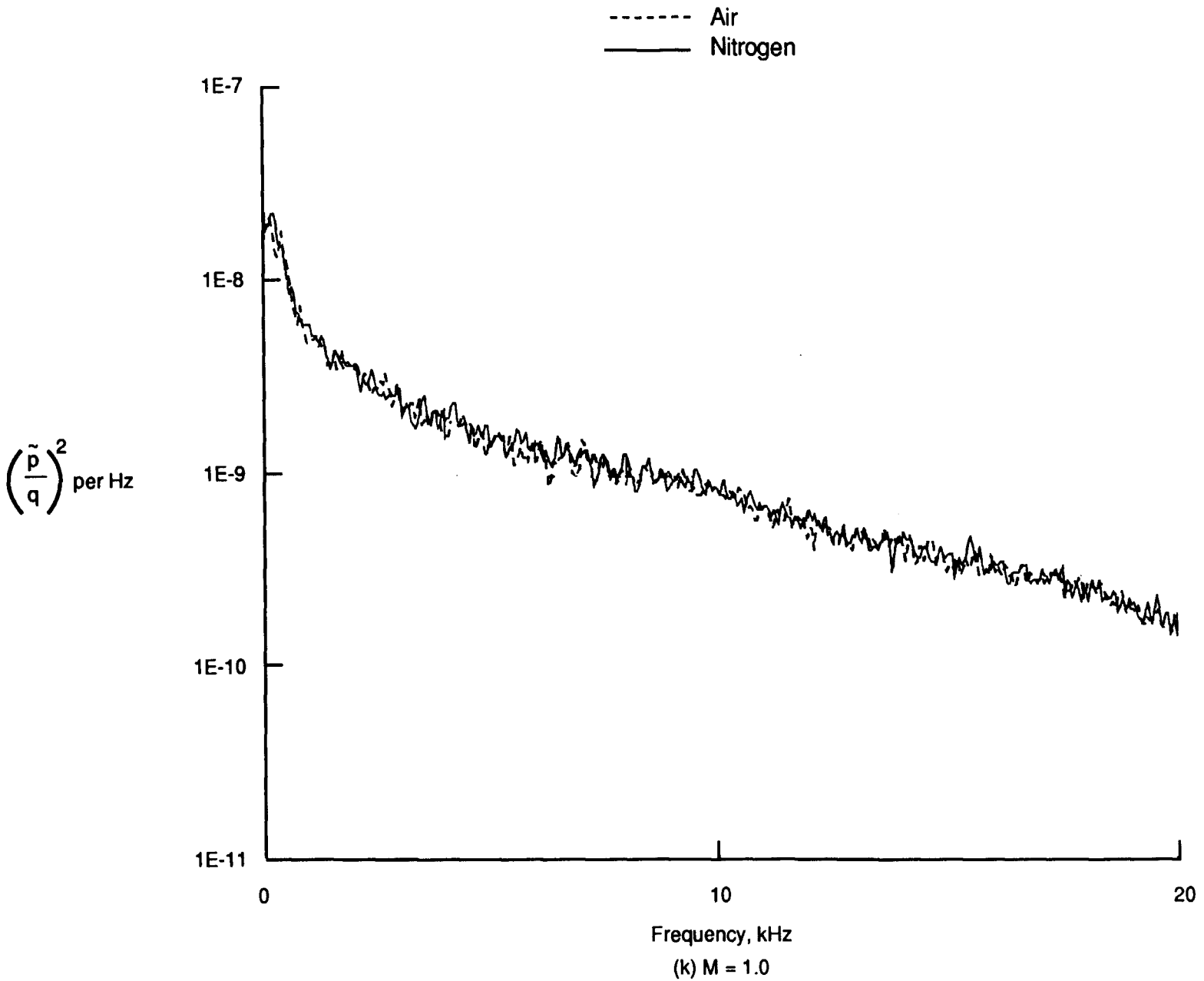

Figure 26. Continued.

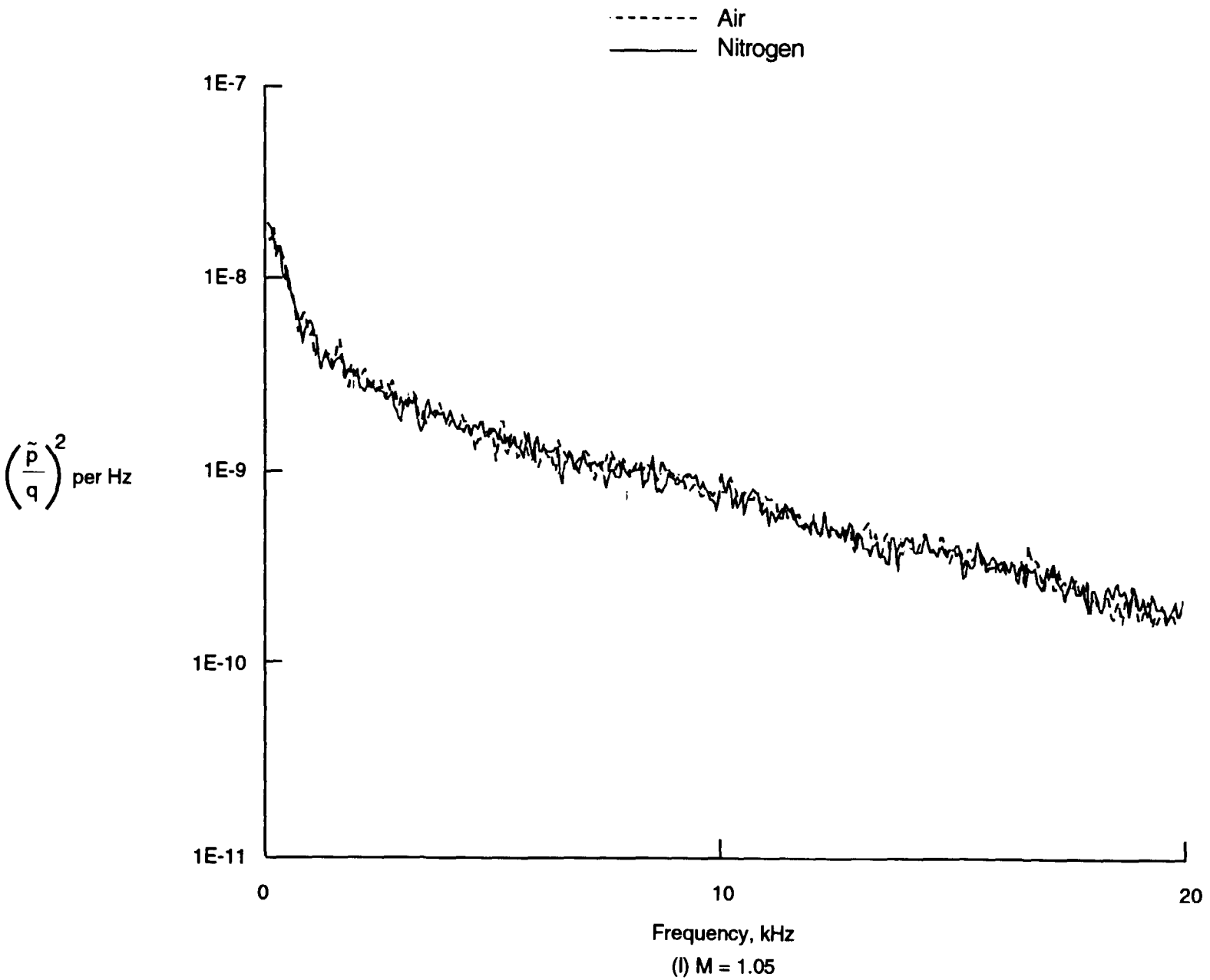

Figure 26. Concluded.

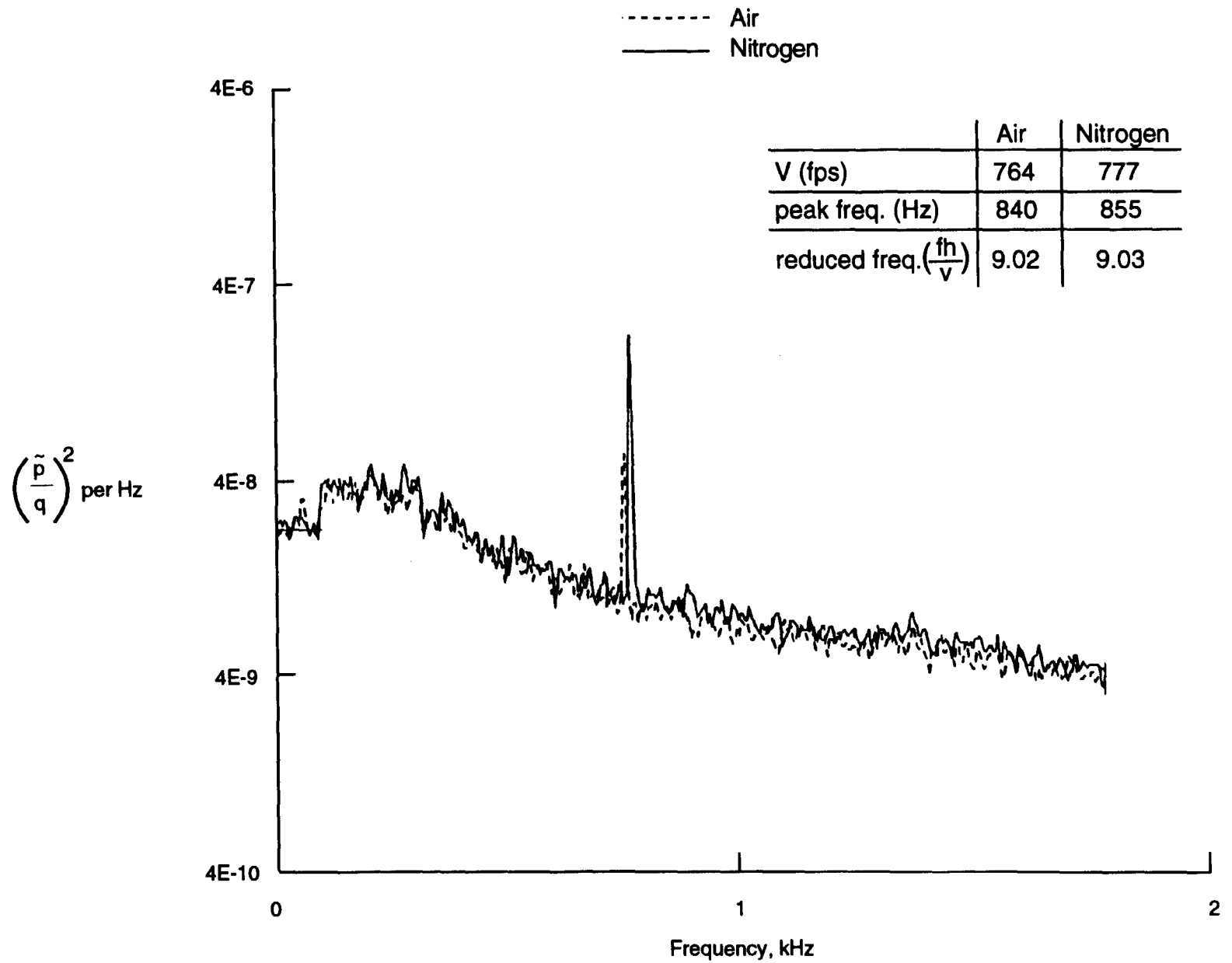

	Air	Nitrogen
V (fps)	764	777
peak freq. (Hz)	840	855
reduced freq. $\left(\frac{fh}{V}\right)$	9.02	9.03

Figure 27. Power spectra of fluctuating pressure coefficient on RHS test section side wall at sta 13, M = 0.7, R = 6 x 10^6/ft., ambient temperature, comparison between air and gaseous nitrogen.

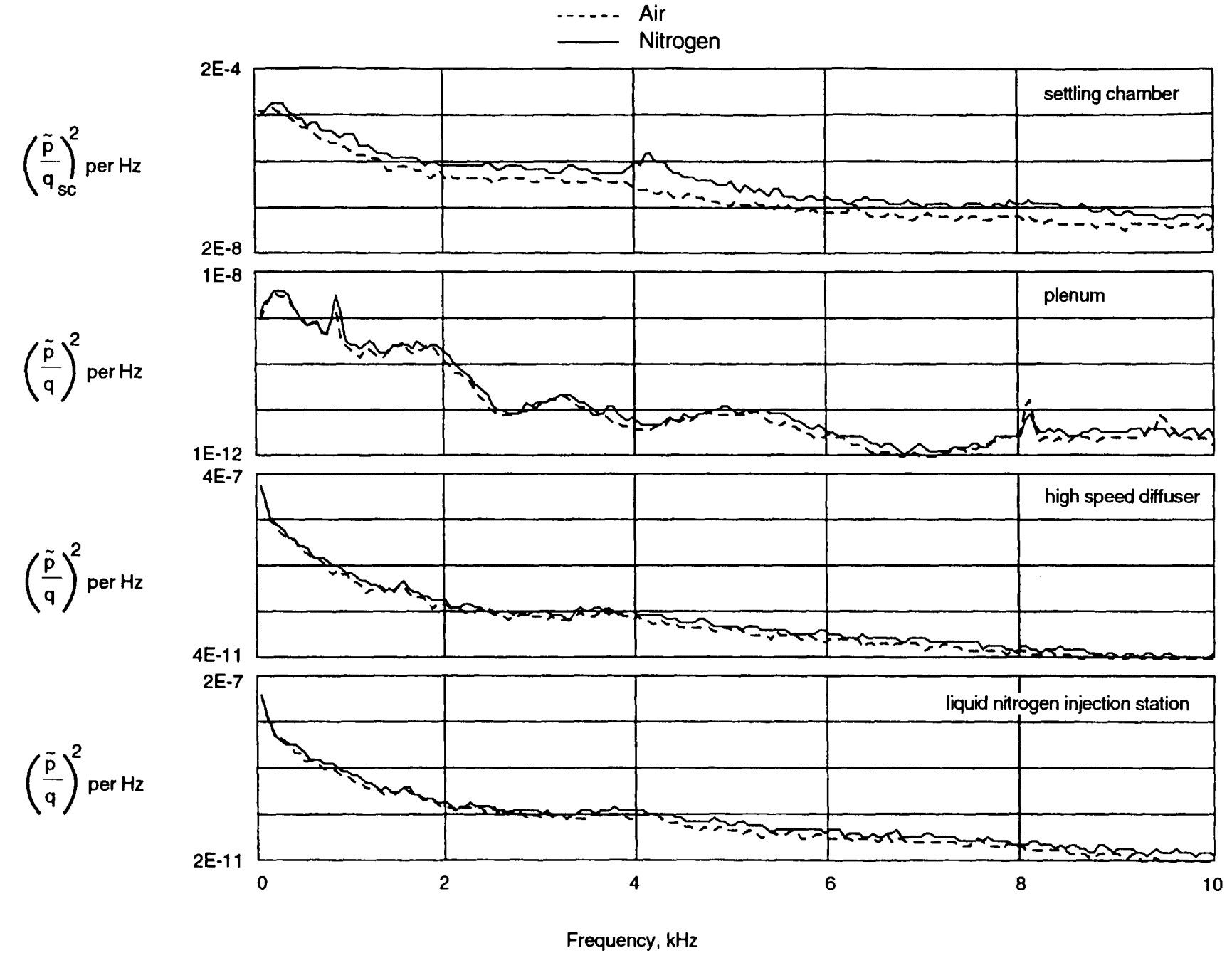

Figure 28. Power spectra of fluctuating pressure coefficient in settling chamber, plenum, high speed diffuser and liquid nitrogen injection station, M = 0.7, R = 6 x 10^6/ft., ambient temperature, comparison between air and gaseous nitrogen.

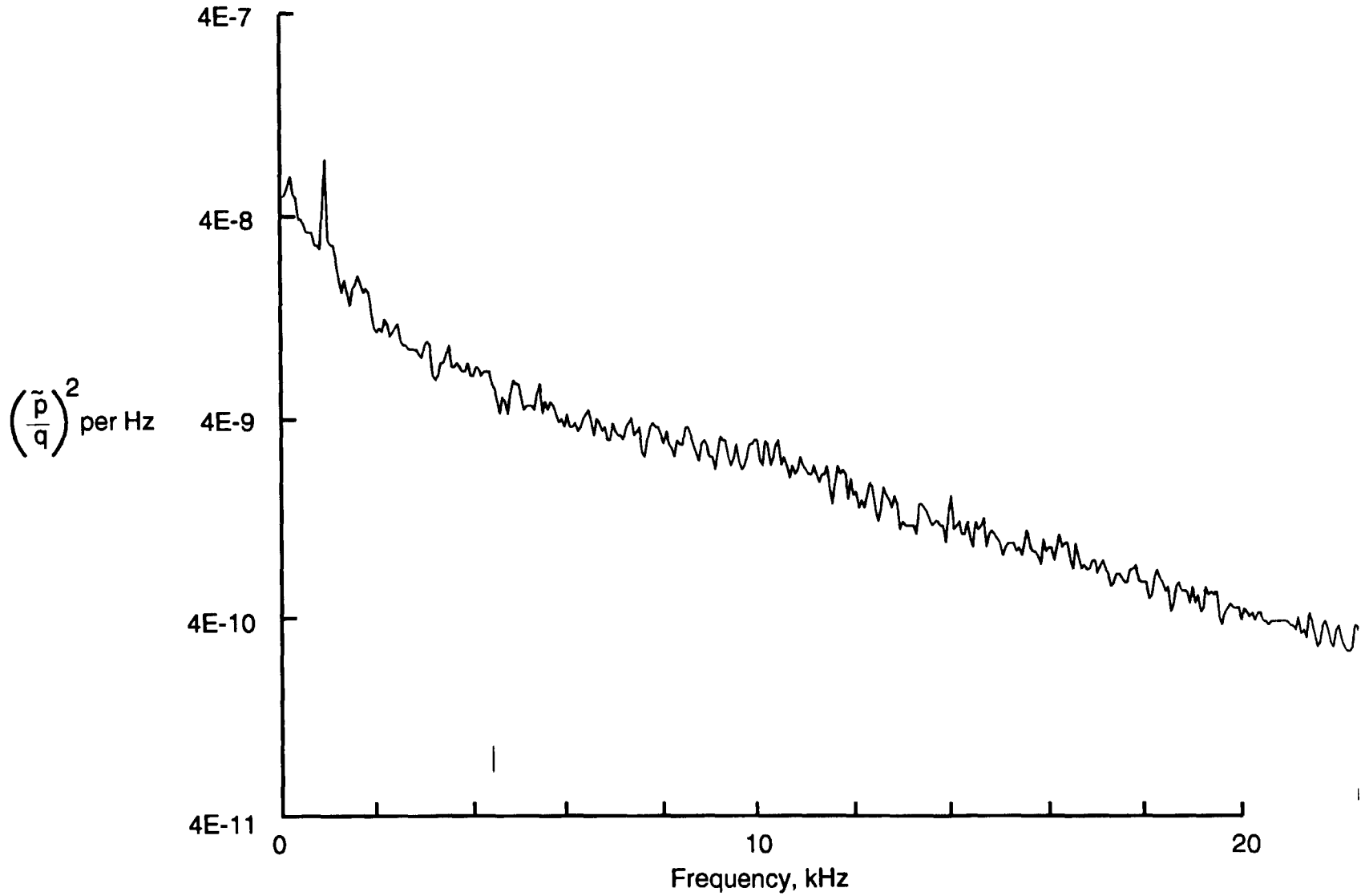

Figure 29. Power spectrum of fluctuating pressure coefficient on RHS test section sidewall, sta 13, M = 0.7, minimum Reynolds number boundary, slots covered, air.

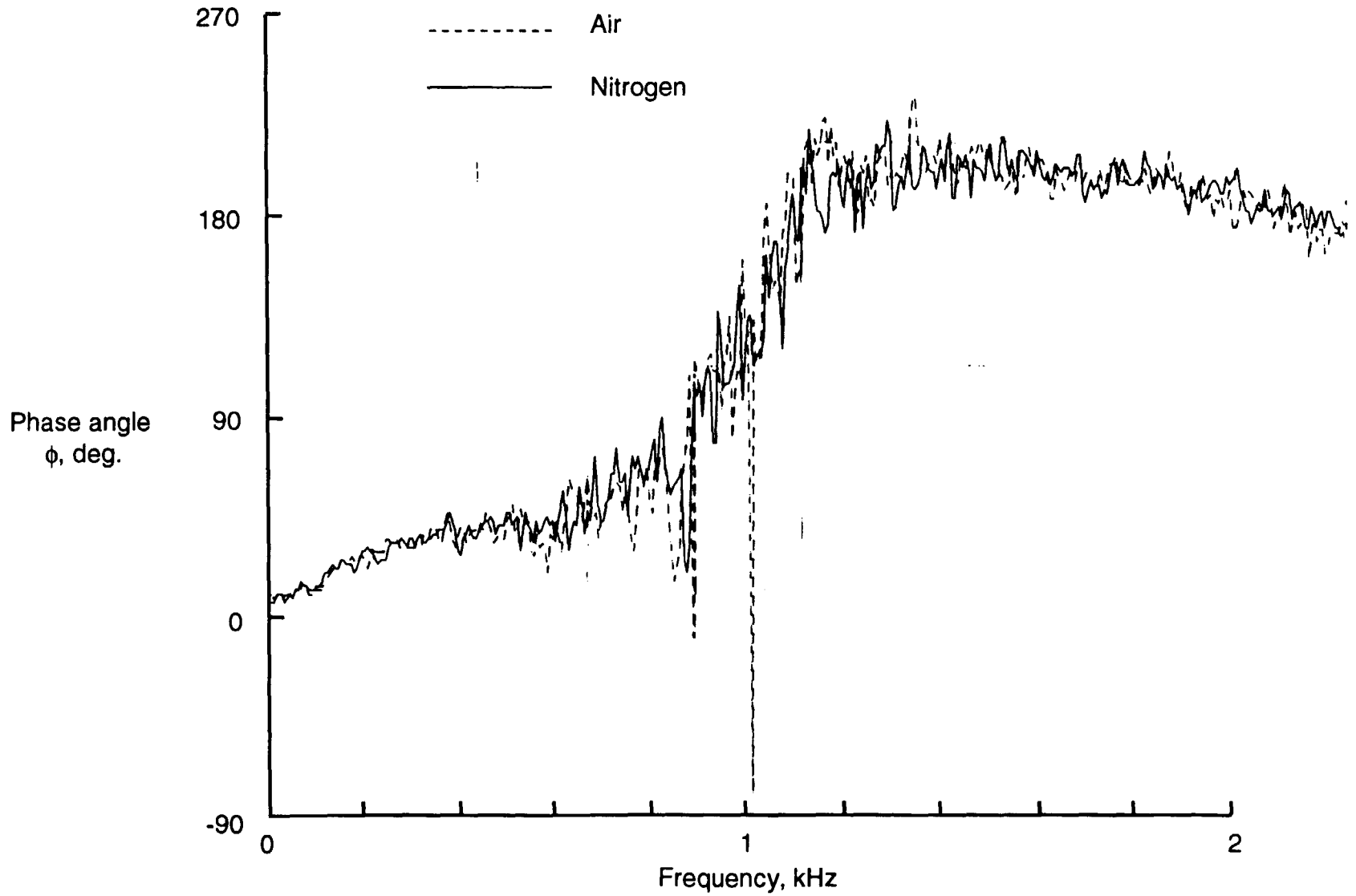

Figure 30. Phase shift of disturbance signal between adjacent pressure transducers on RHS test section sidewall at sta 13, M = 0.7, R = $6x10^6$/ft., ambient temperature, comparison between air and nitrogen.

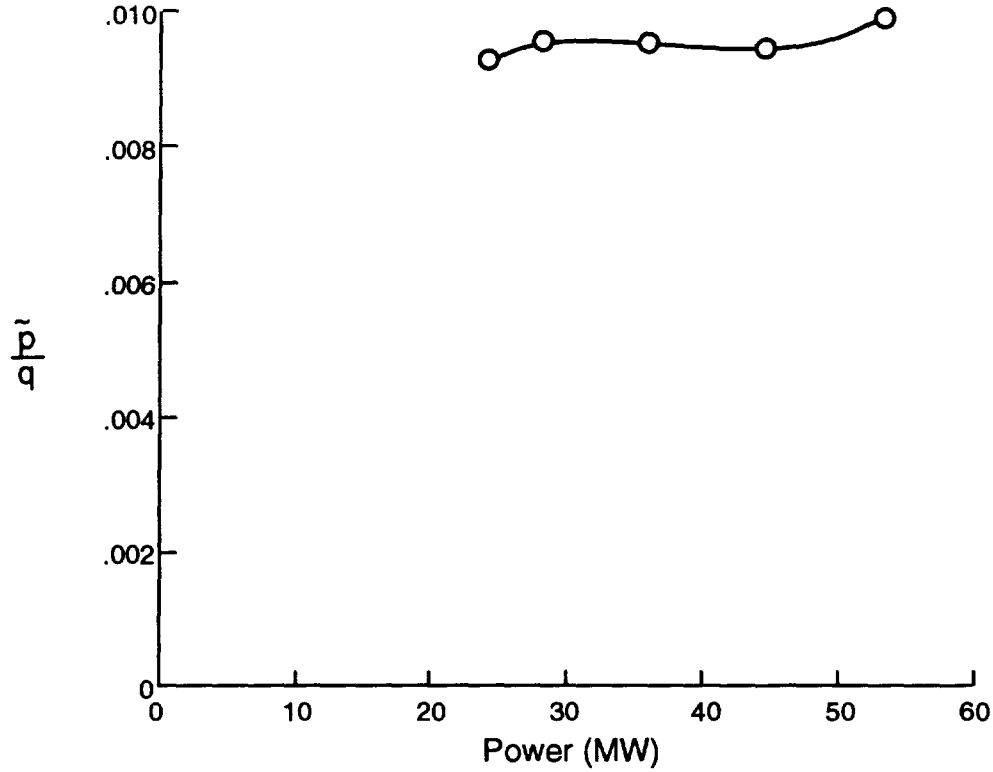

Figure 31. Fluctuating pressure coefficient on NTF RHS test section side wall at sta 13 showing effect of drive power variation at constant M = 0.8 and R = 39.7 x 10^6/ft.

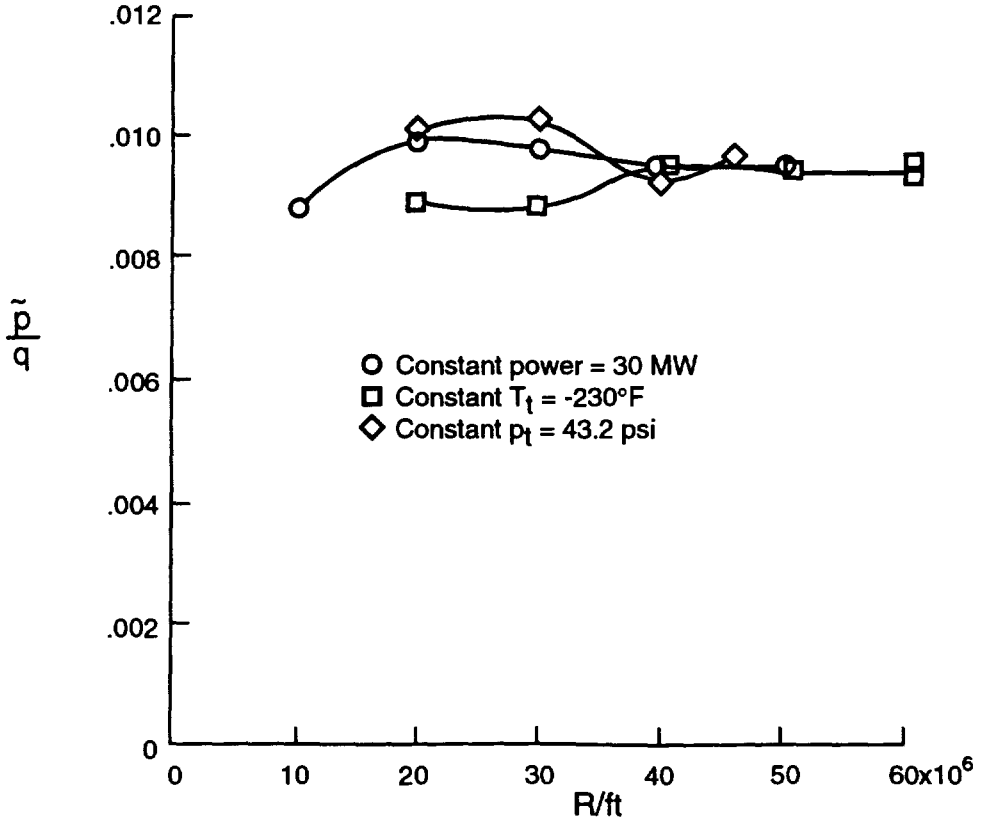

Figure 32. Fluctuating pressure coefficient on NTF RHS test section side wall at sta 13, M = 0.8, nitrogen mode.

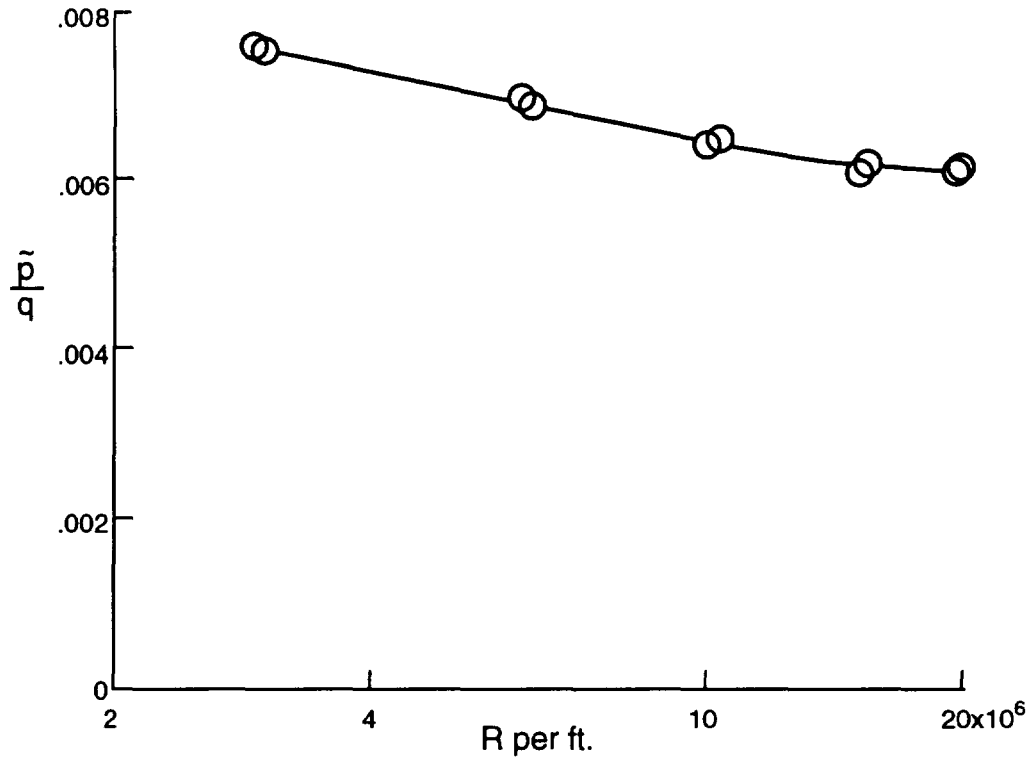

Figure 33. Variation of fluctuating pressure coefficient on NTF RHS test section side wall at sta 13 for M = 0.5 in air at ambient temperature.

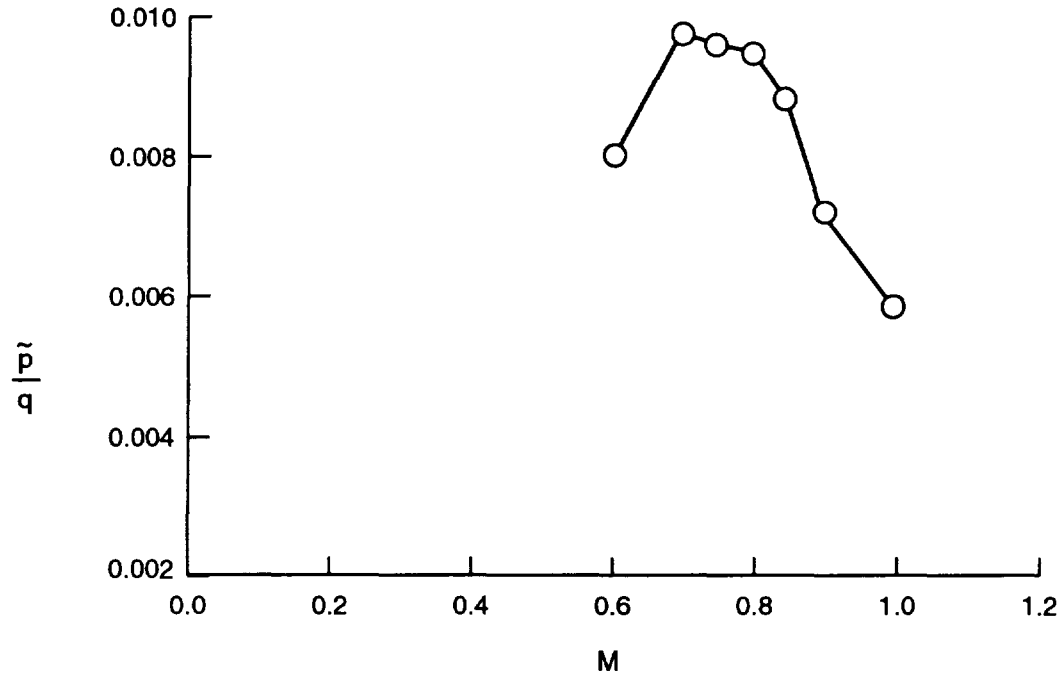

Figure 34. NTF fluctuating pressure coefficient on RHS test section sidewall, sta 13 for R = 40 x 10^6 per ft. and drivepower = 30 MW.

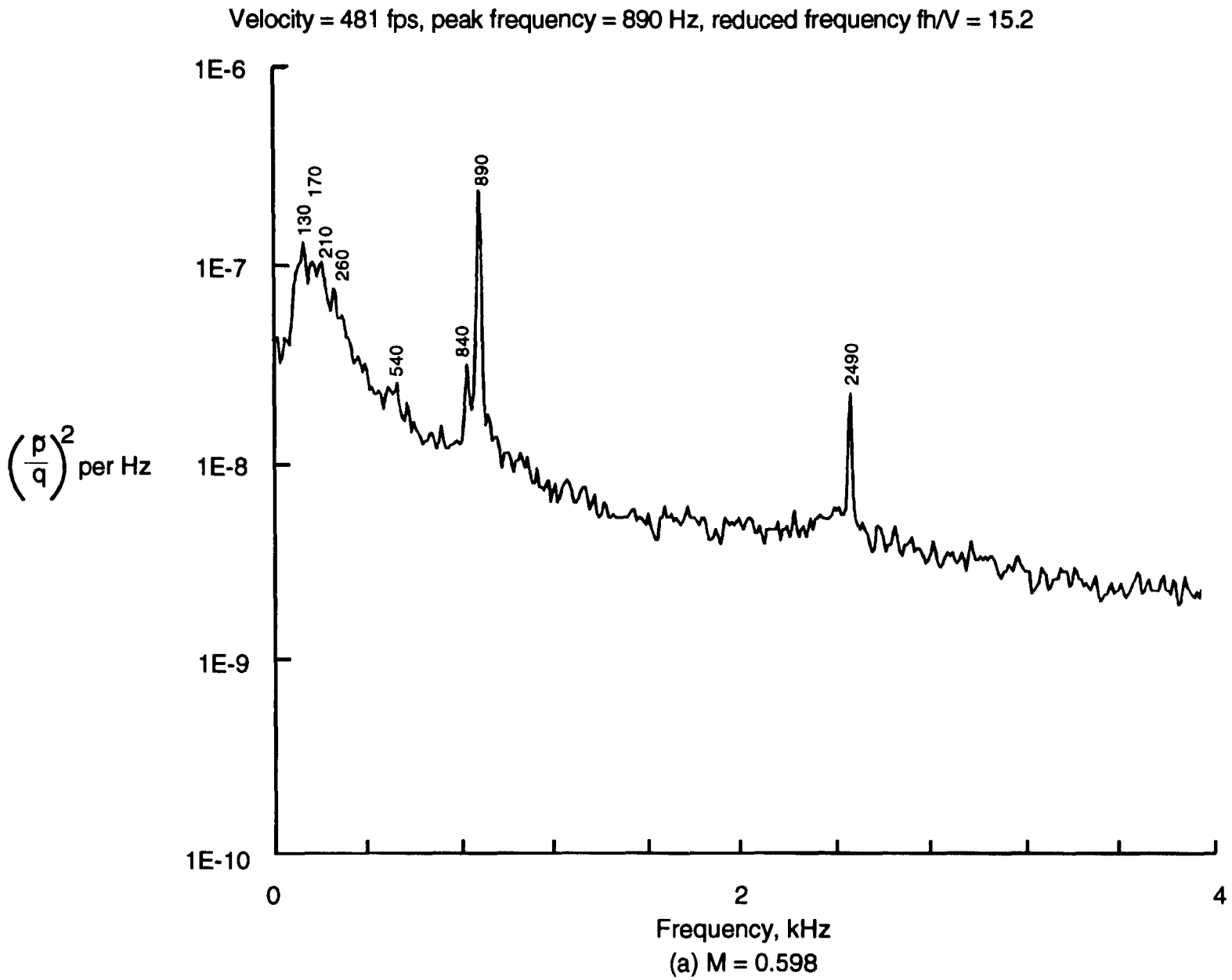

Figure 35. Power spectra of fluctuating pressure coefficient on RHS test section side wall, sta 13 for R = 40 x 10^6/ft and drive power = 30 MW

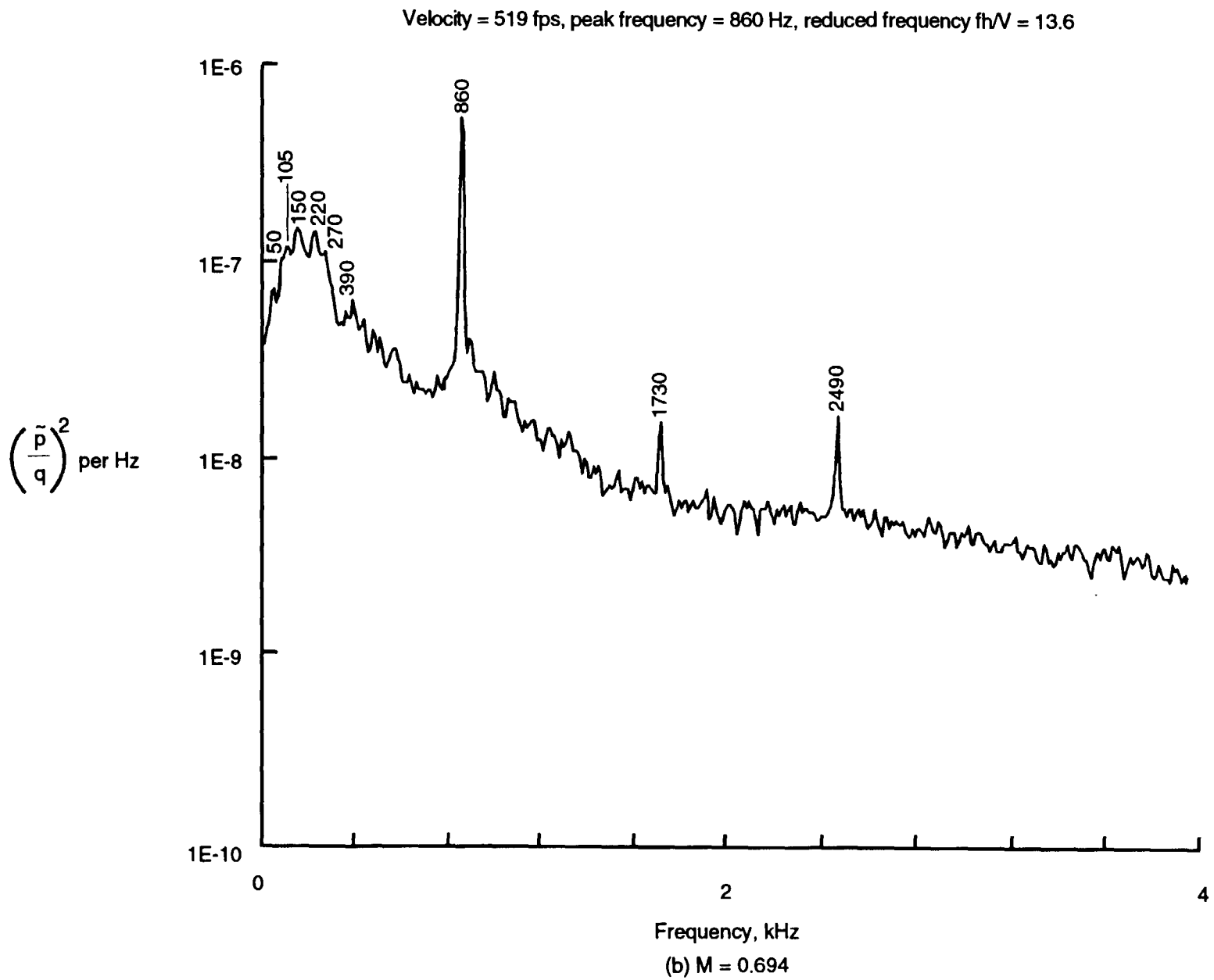

Figure 35. Continued

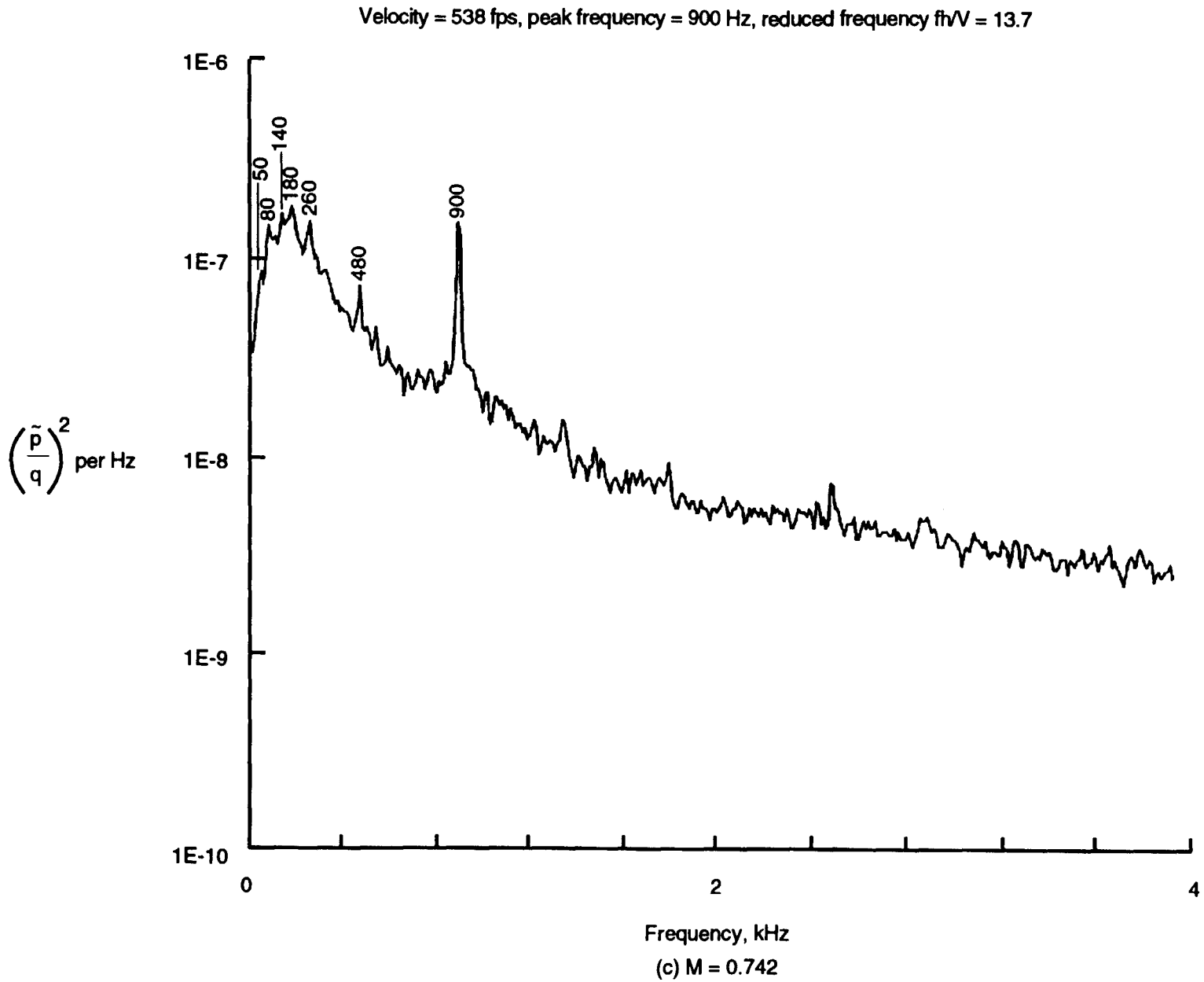

Figure 35. Continued

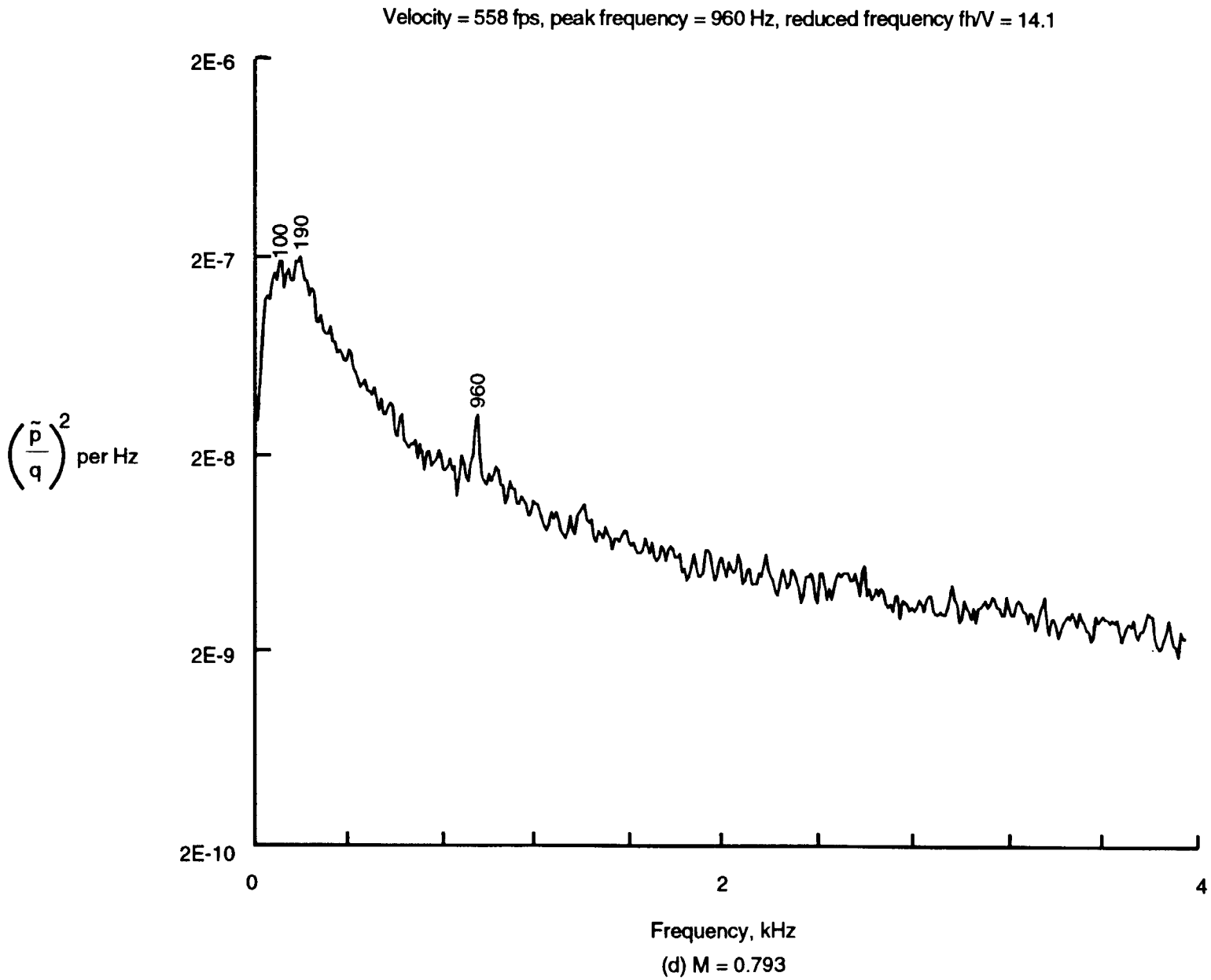

Figure 35. Continued

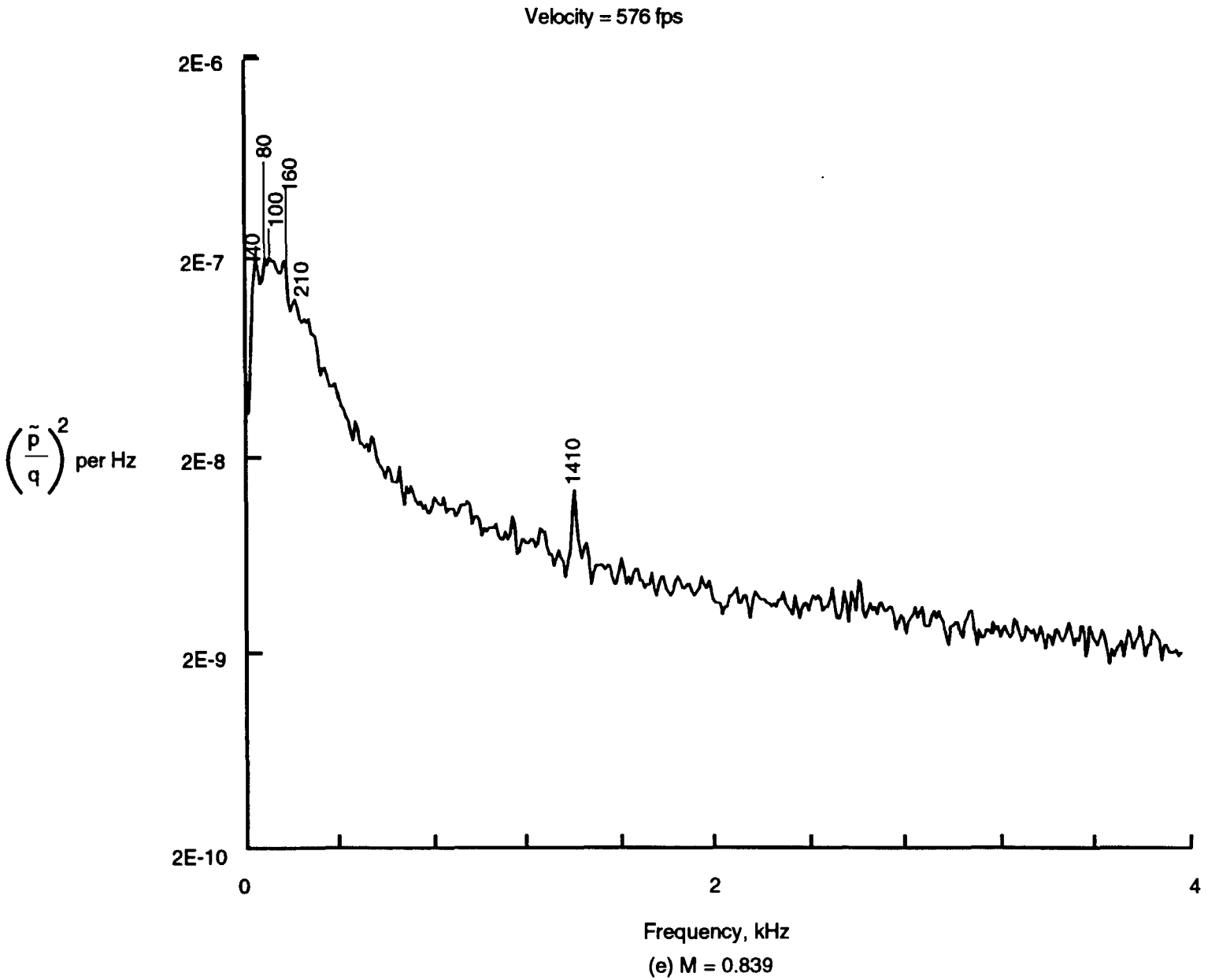

Figure 35. Continued

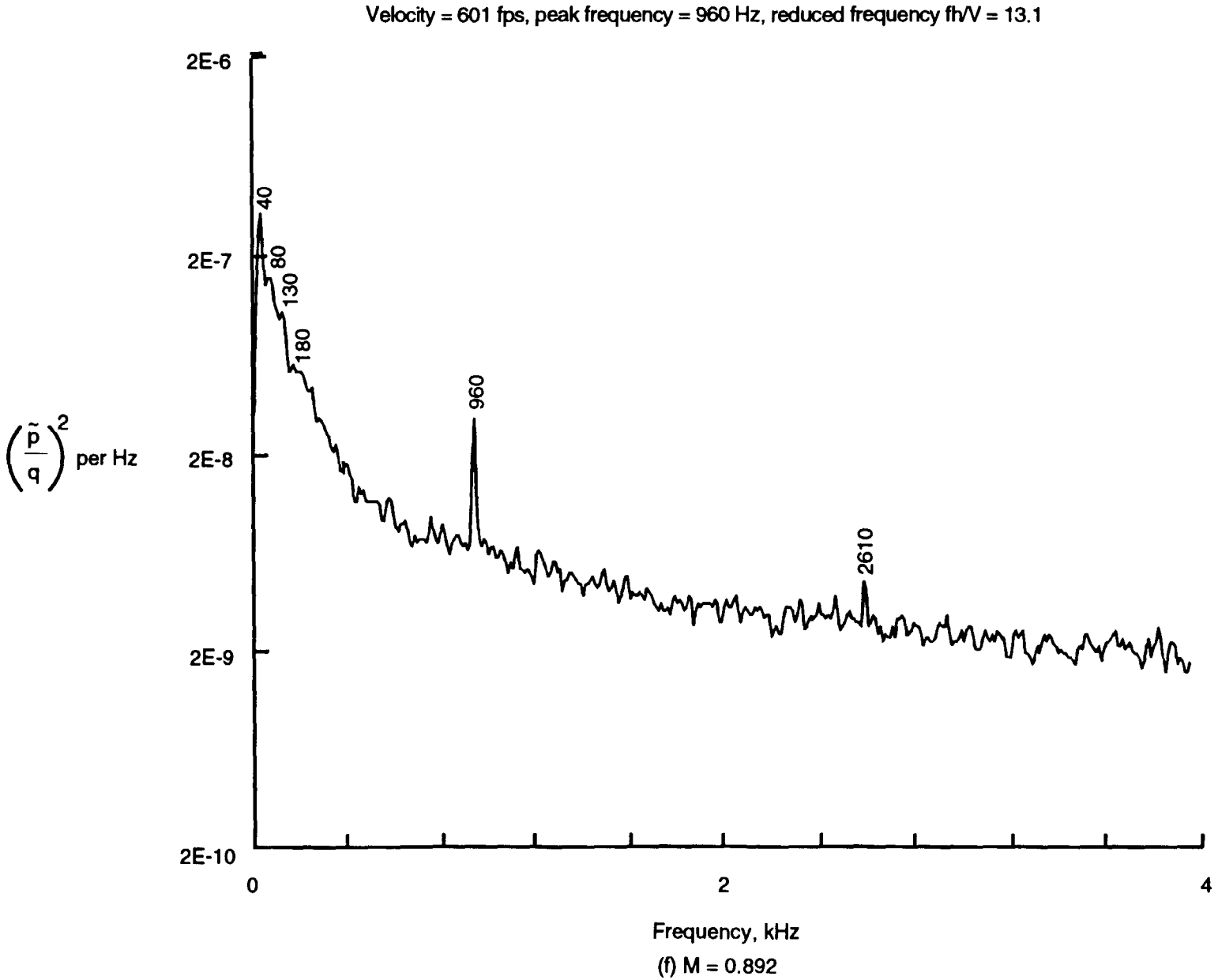

Figure 35. Continued

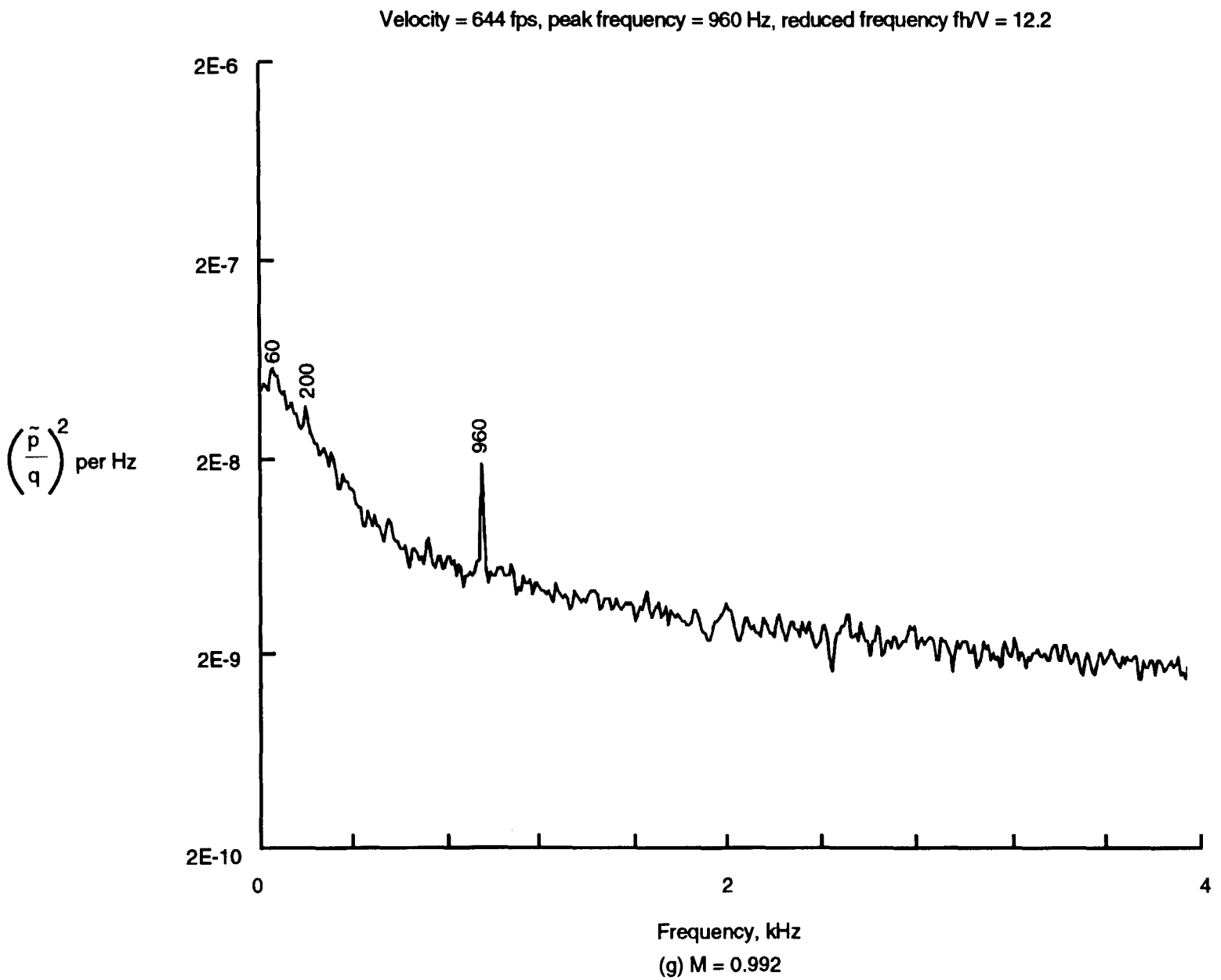

Figure 35. Concluded

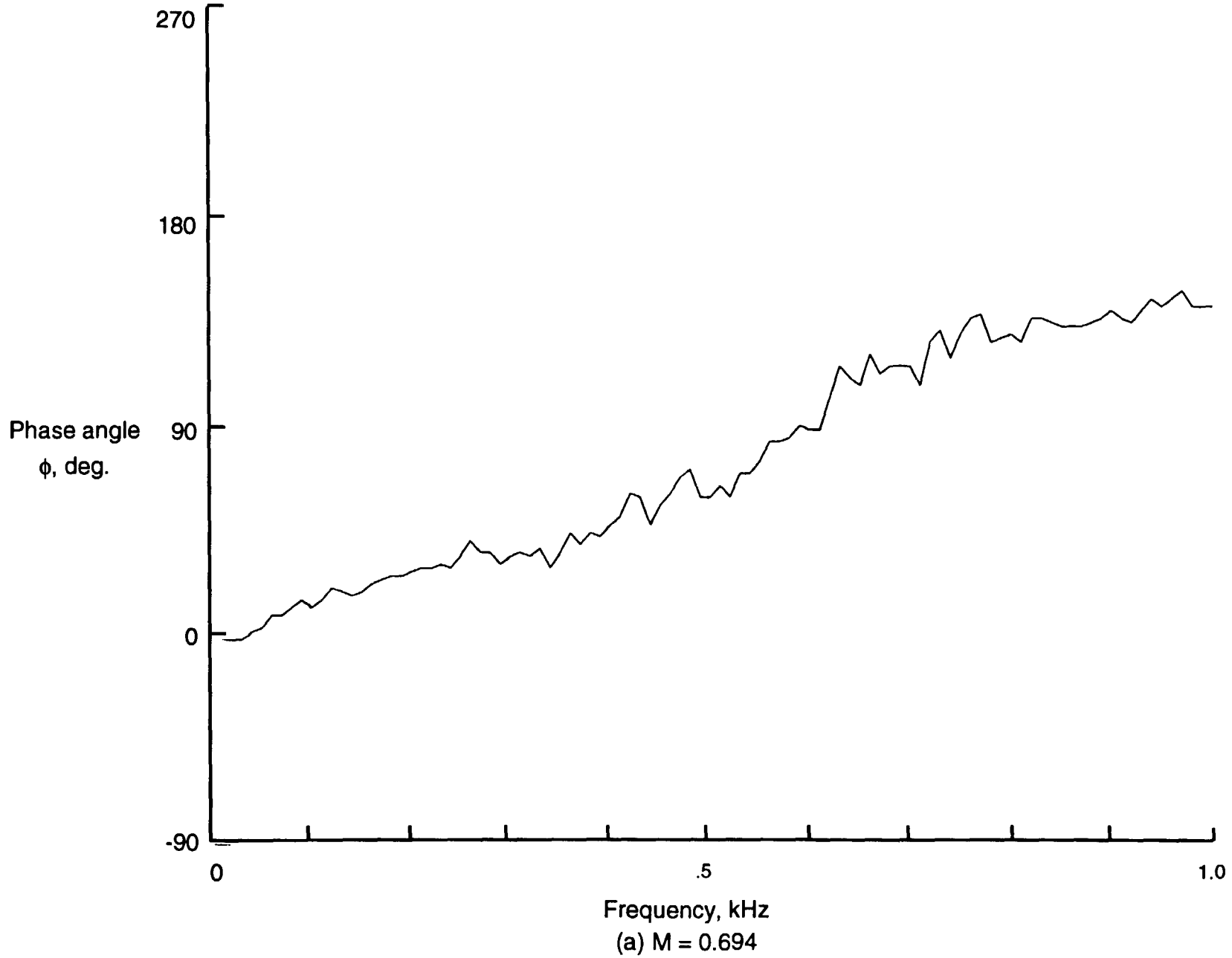

Figure 36. Phase shift of disturbance signal between adjacent pressure transducers on RHS test section sidewall, sta 13, for constant R = 40×10^6/ft and drivepower = 30 MW, nitrogen.

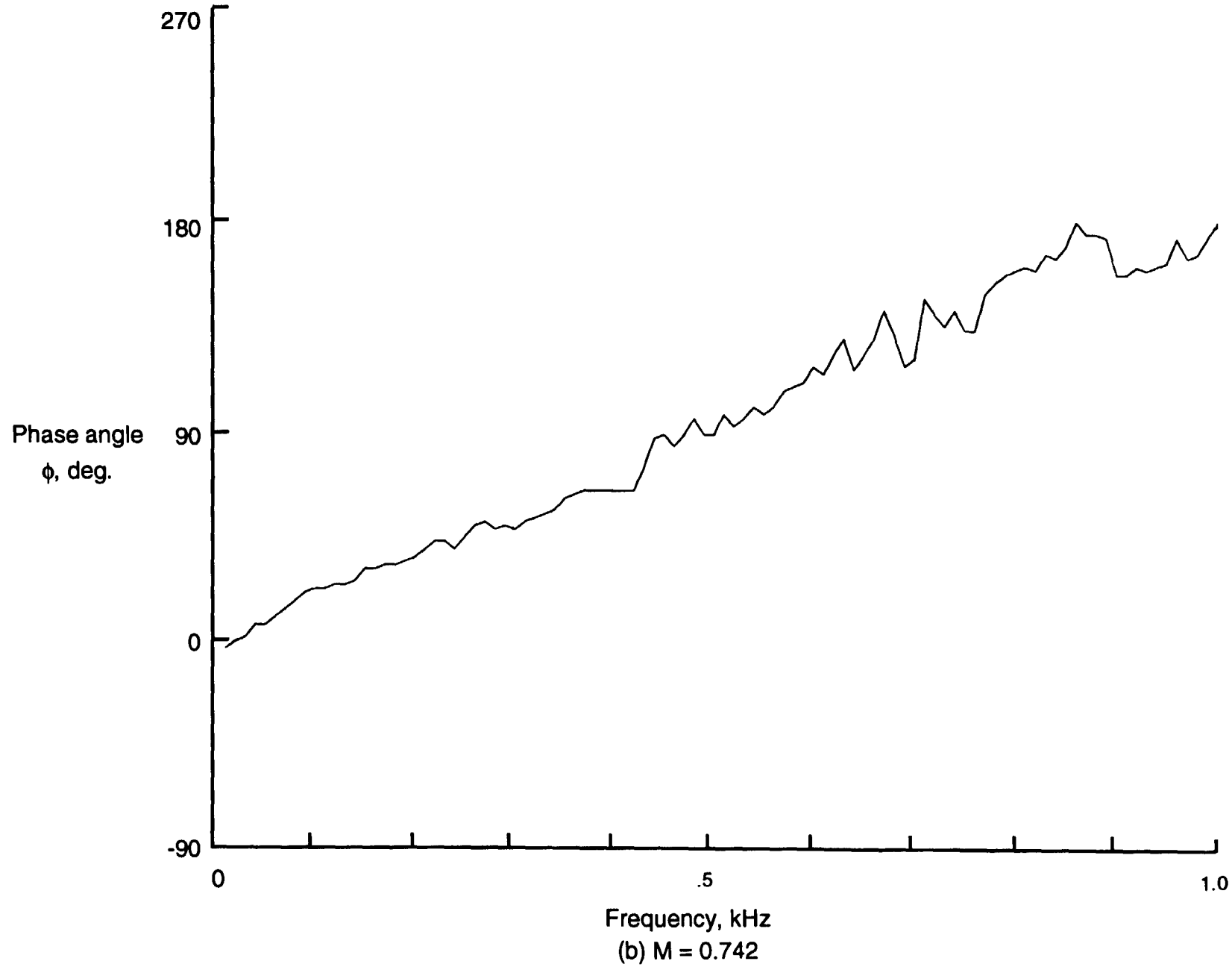

Figure 36. Continued

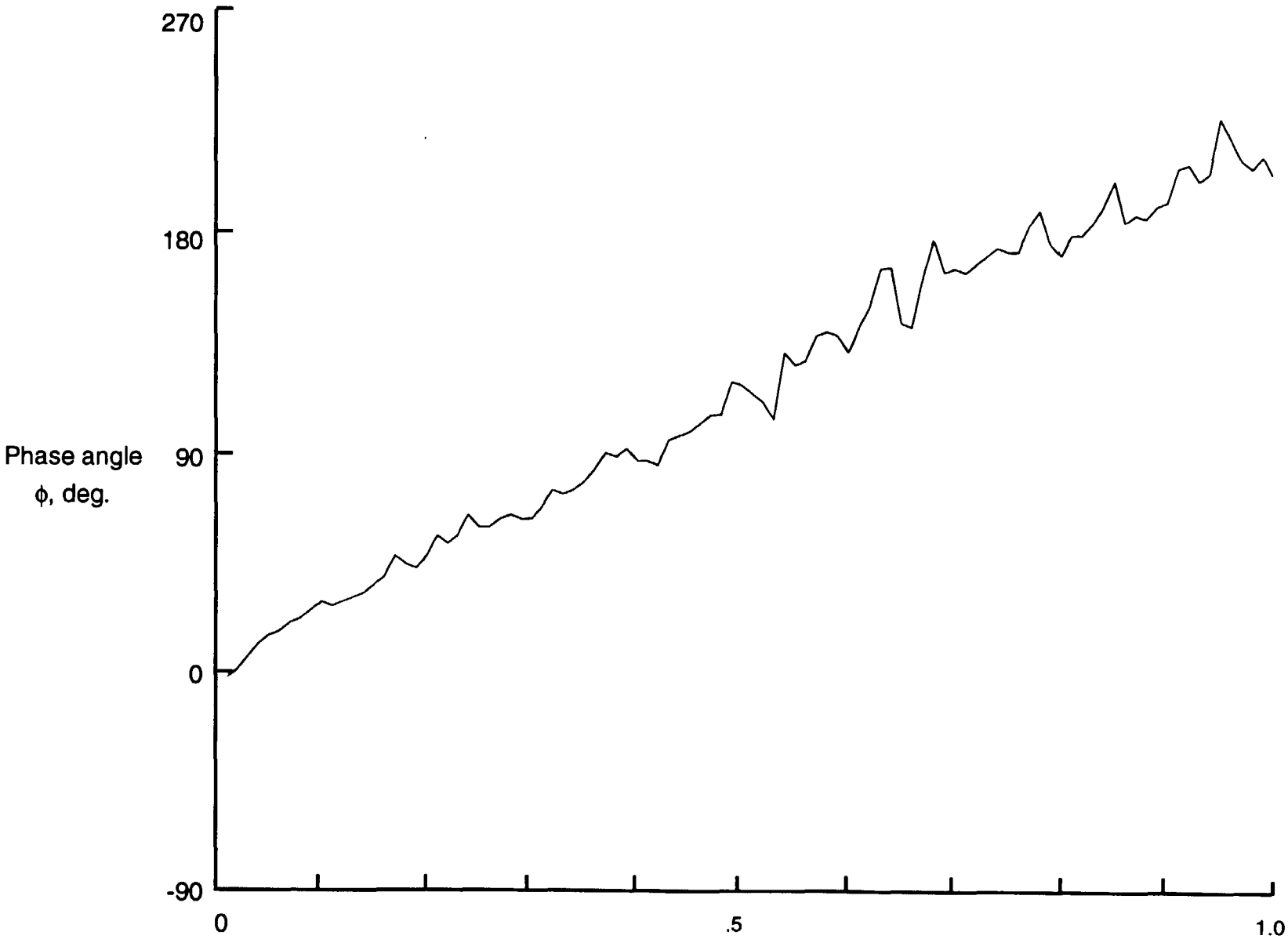

Figure 36. Concluded

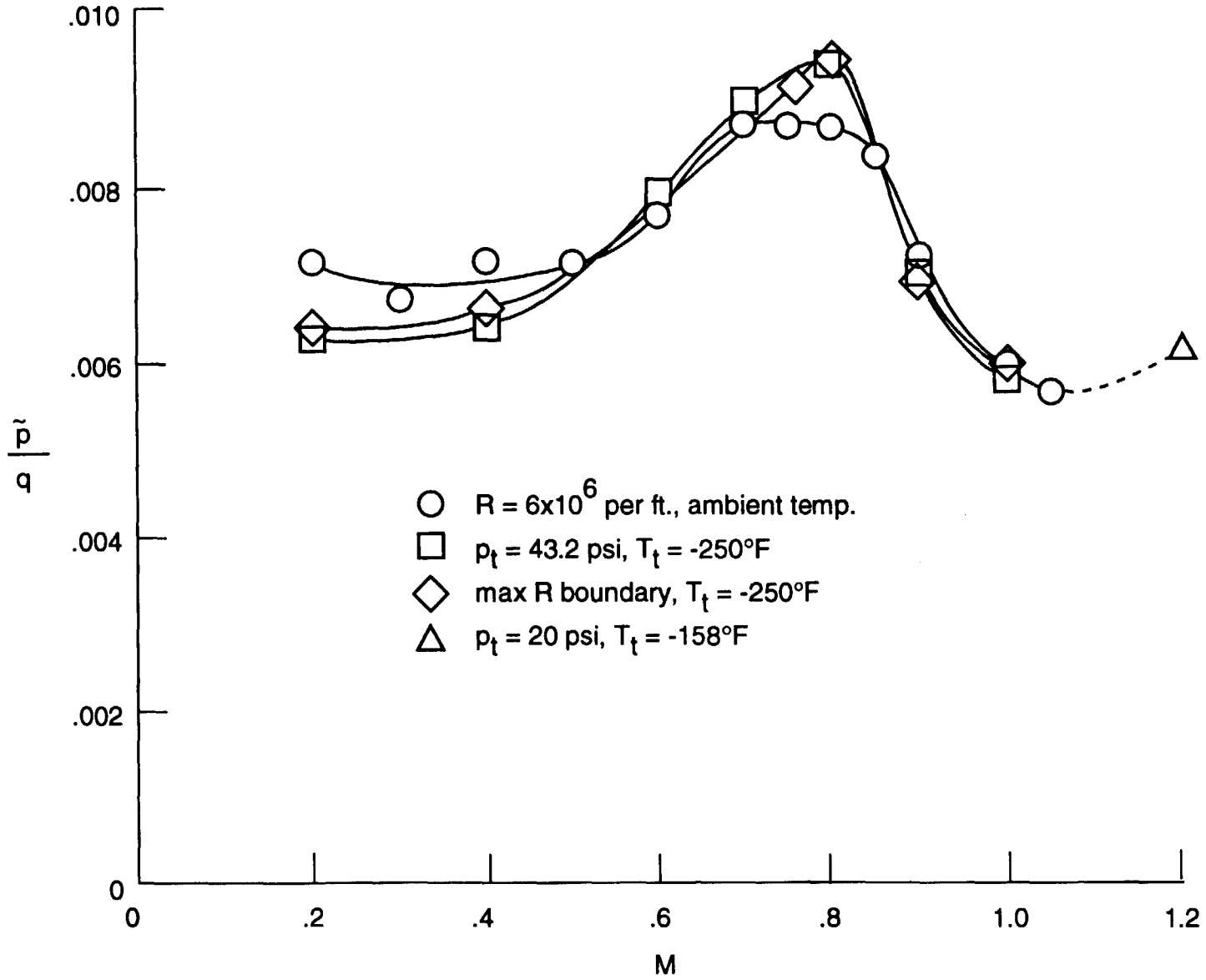

Figure 37. NTF fluctuating pressure coefficient on RHS test section side wall at sta 13, nitrogen mode.

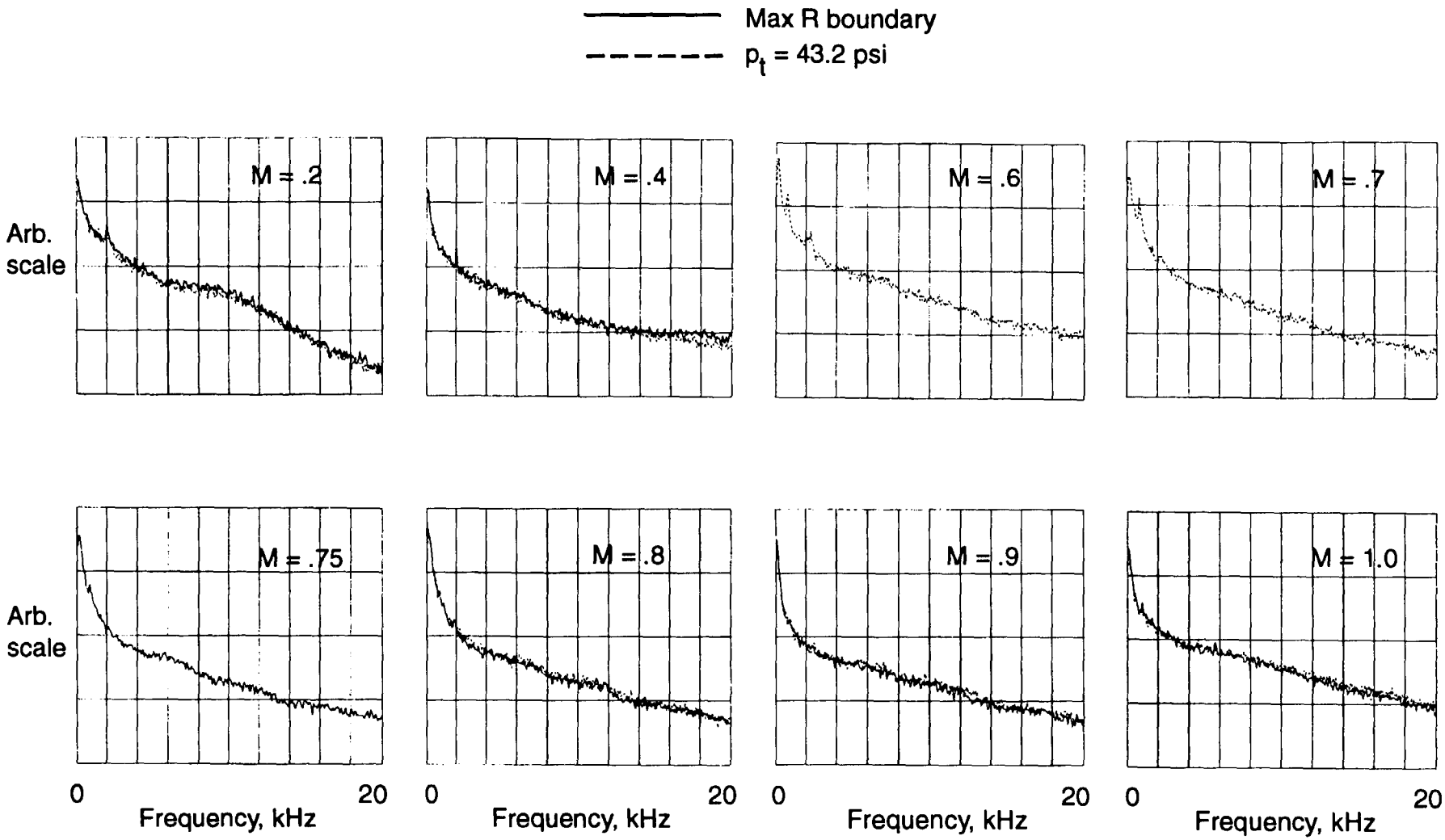

Figure 38. Power spectra of fluctuating pressure coefficient on NTF RHS test section sidewall, sta 13, T_t = -250°F, comparison at max R boundary and p_t = 43.2 psi.

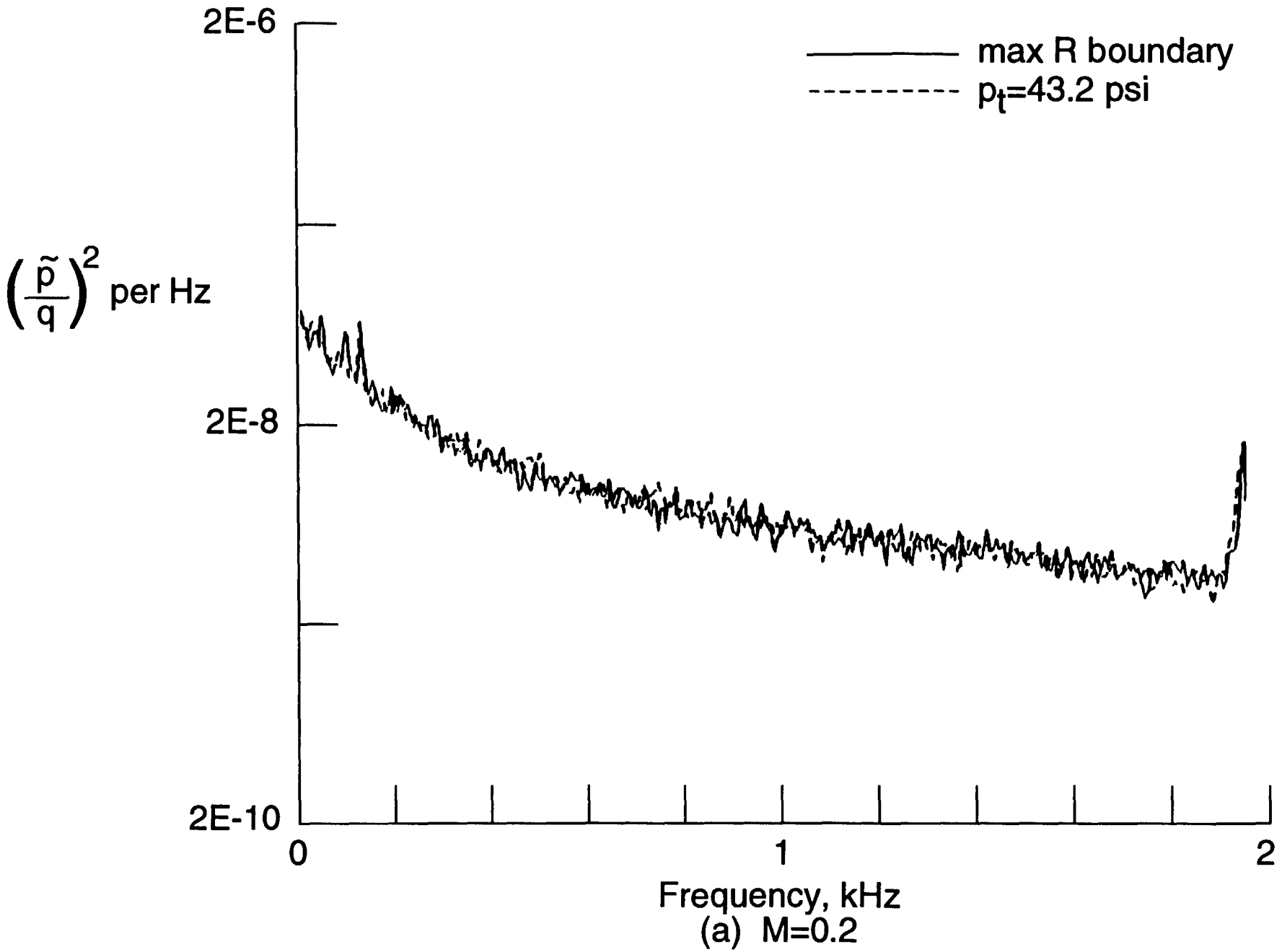

Figure 39. Power spectra of fluctuating pressure coefficient on NTF RHS test section sidewall, sta 13, T_t=-250°F, comparison at max R boundary and p_t=43.2 psi,zero to 2 kHz bandwidth.

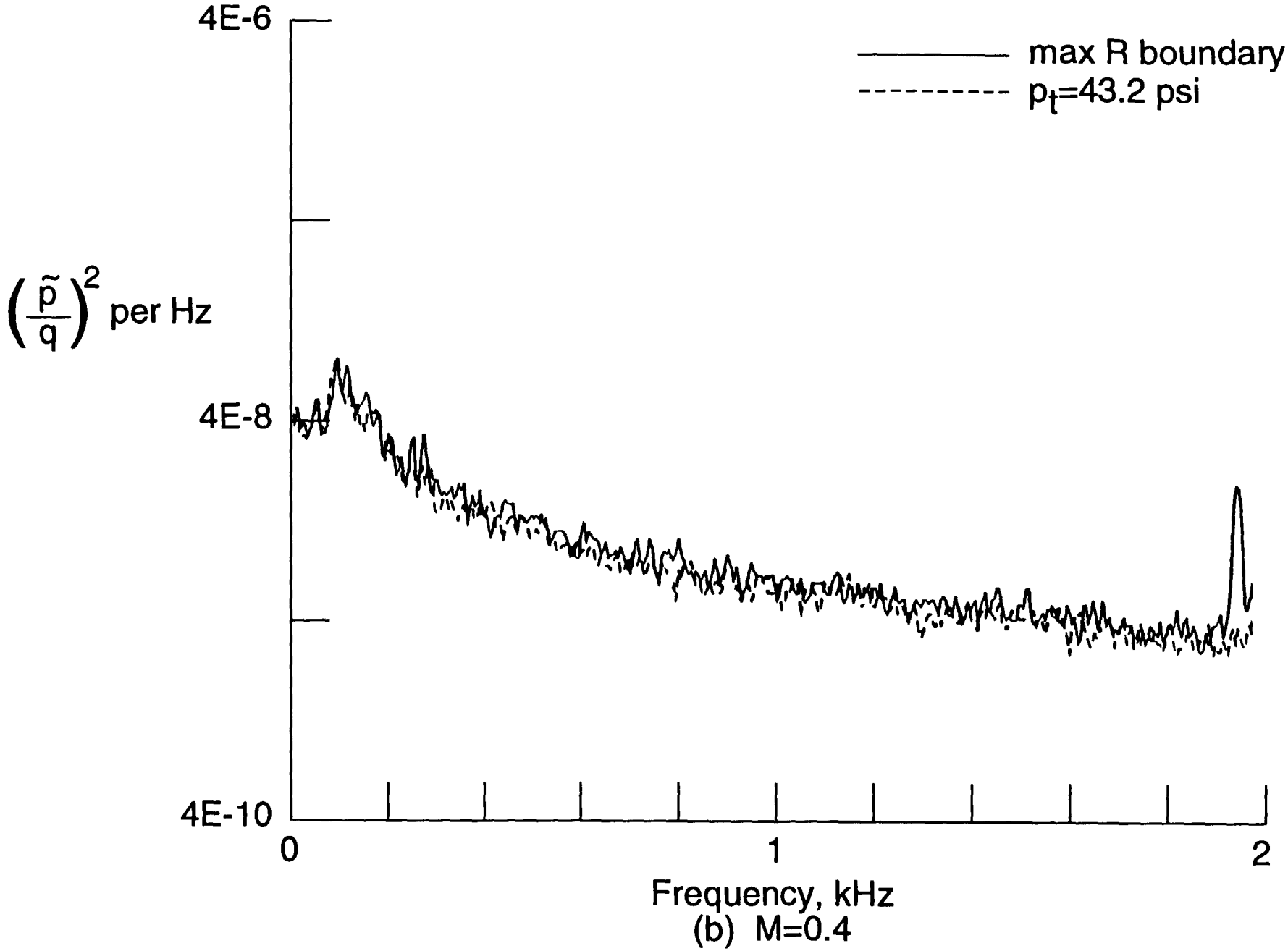

Figure 39. Continued.

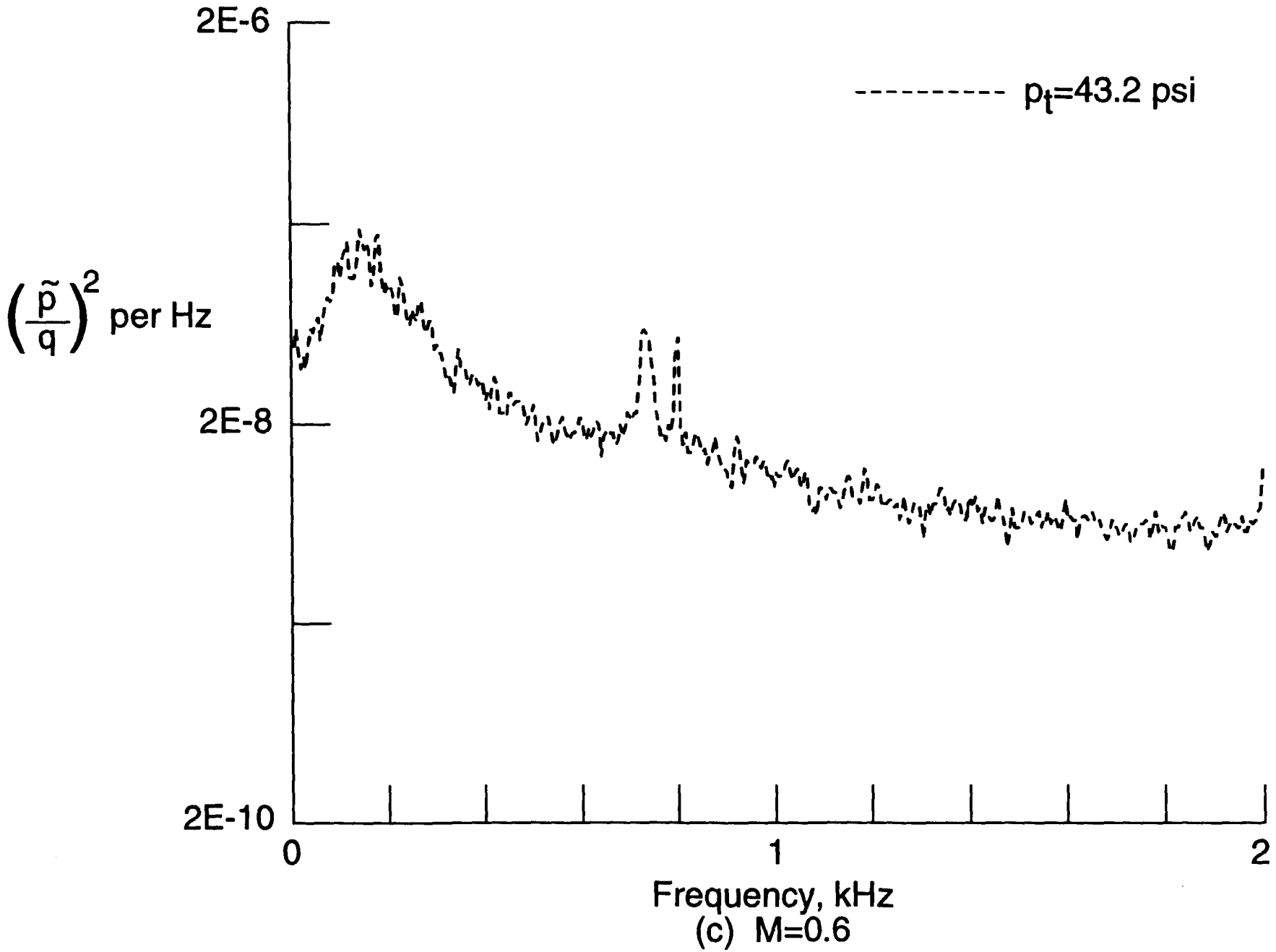

Figure 39. Continued.

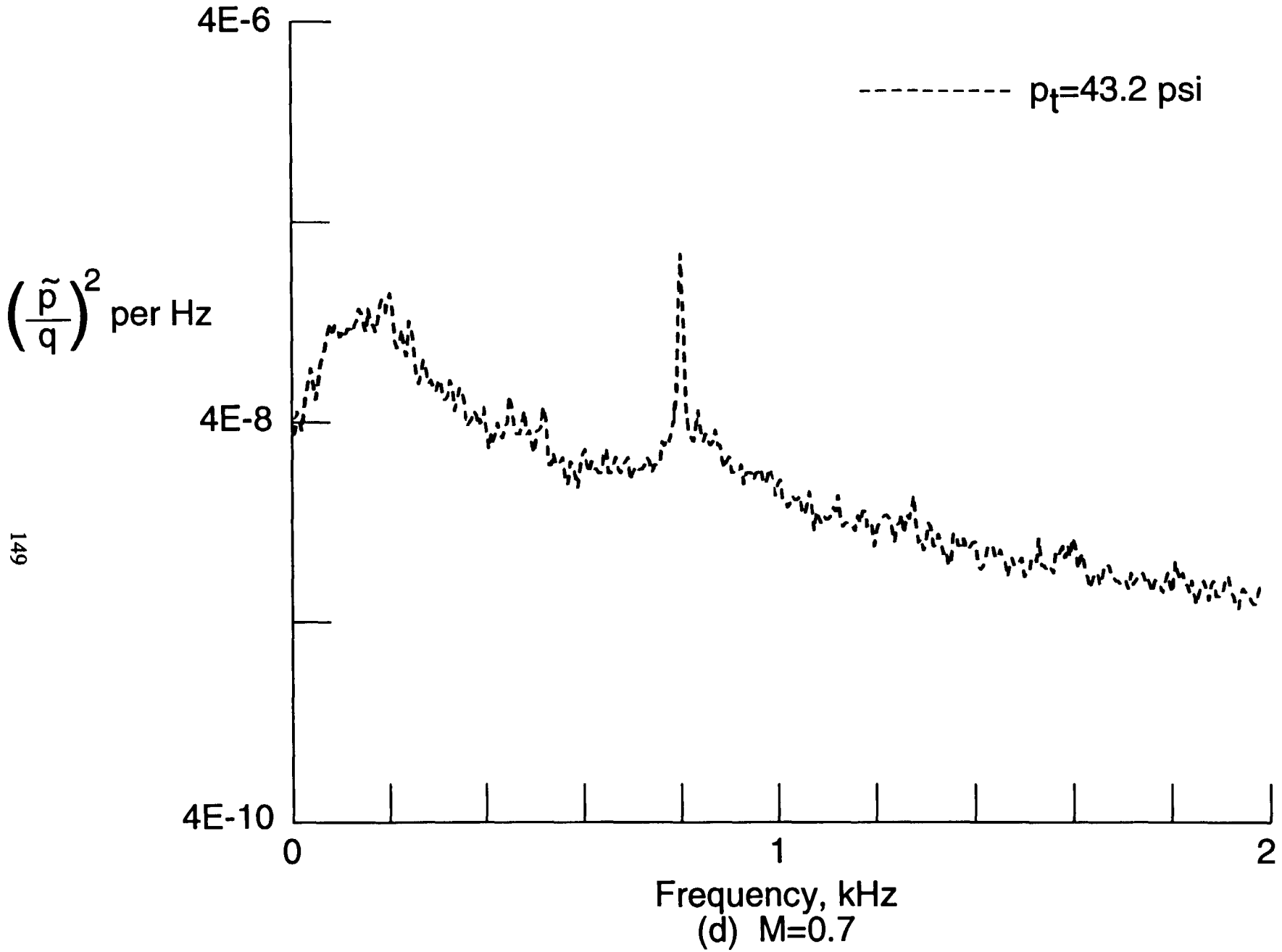

Figure 39. Continued.

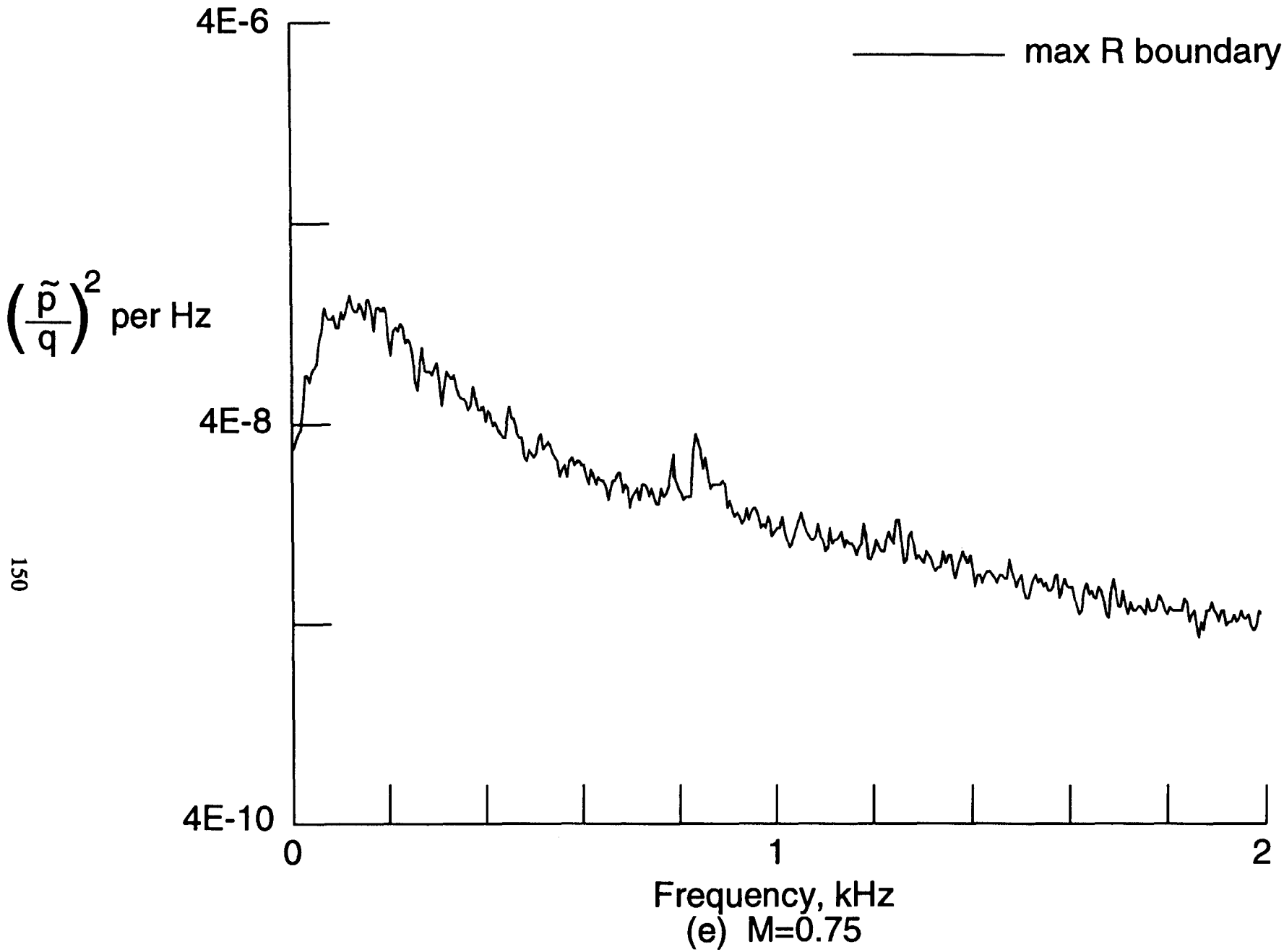

Figure 39. Continued.

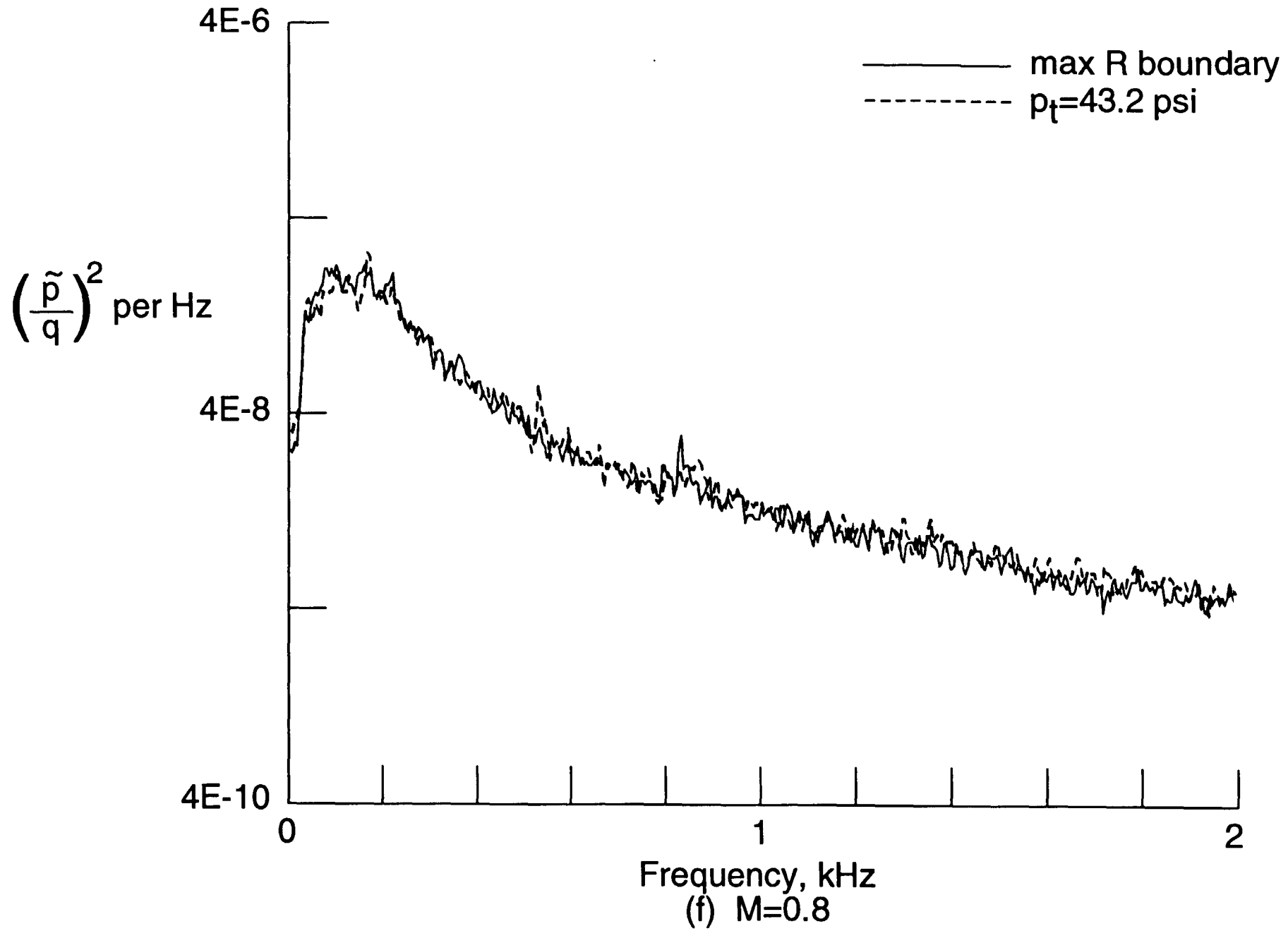

Figure 39. Continued.

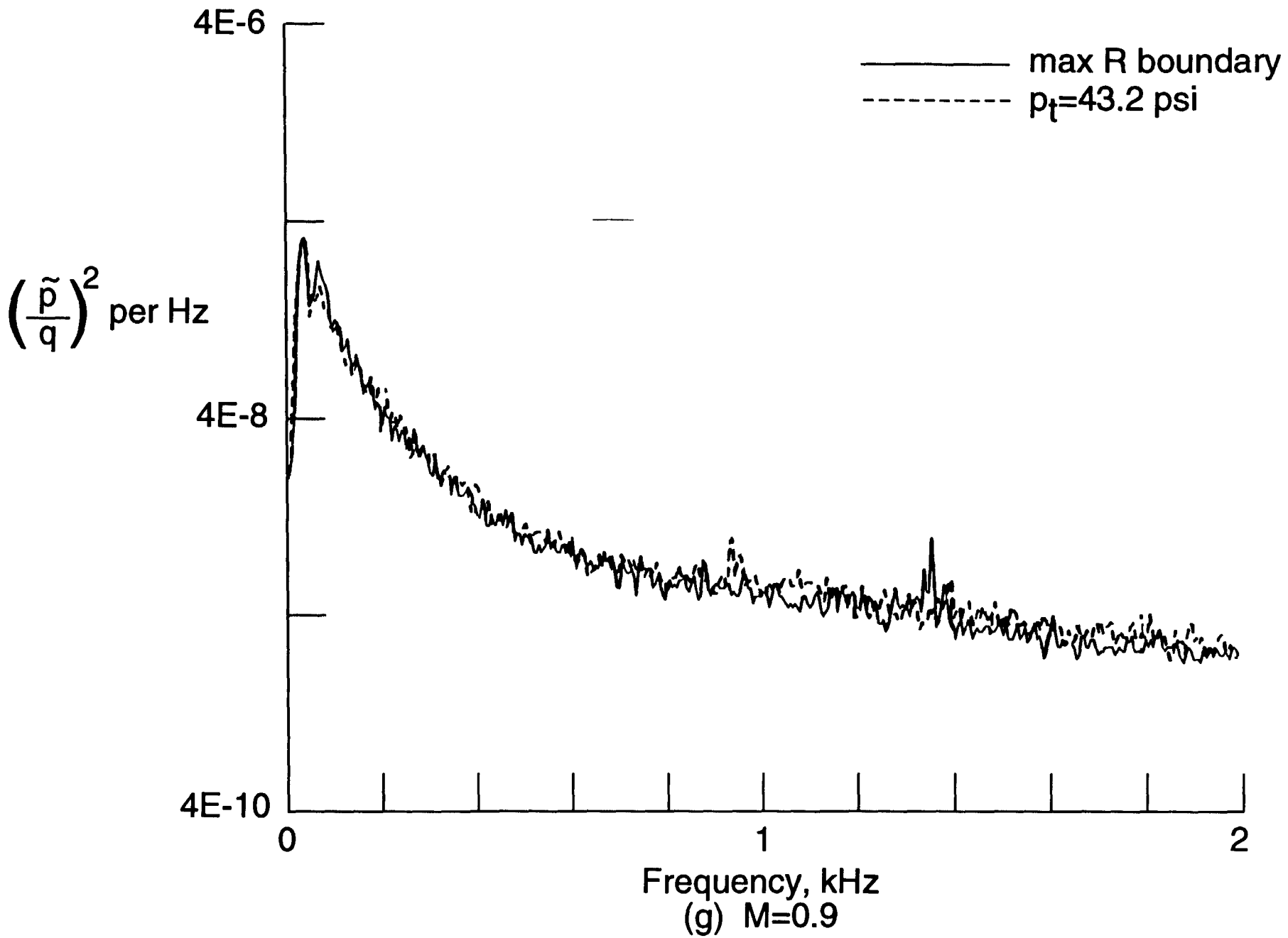

Figure 39. Continued.

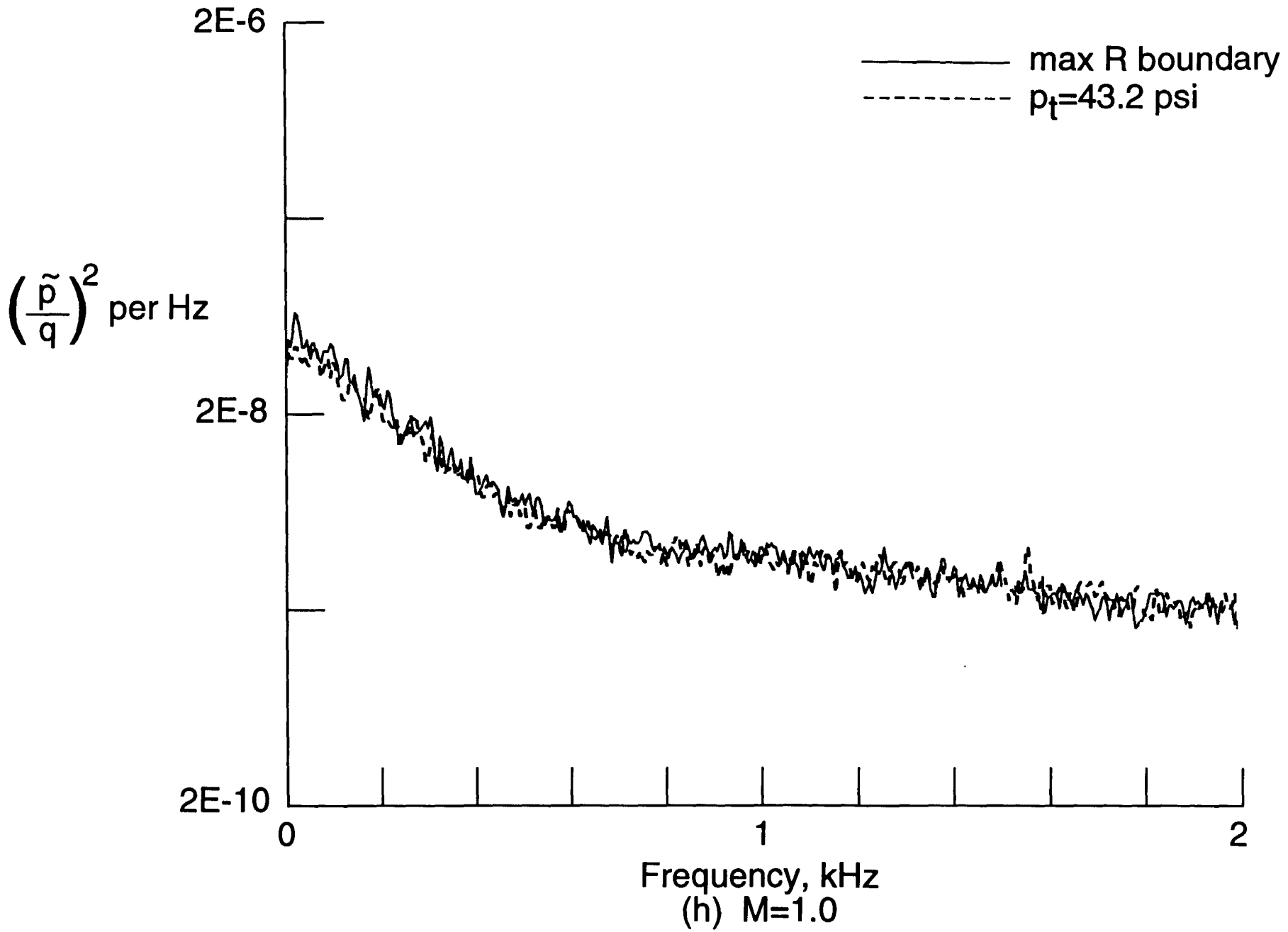

Figure 39. Concluded.

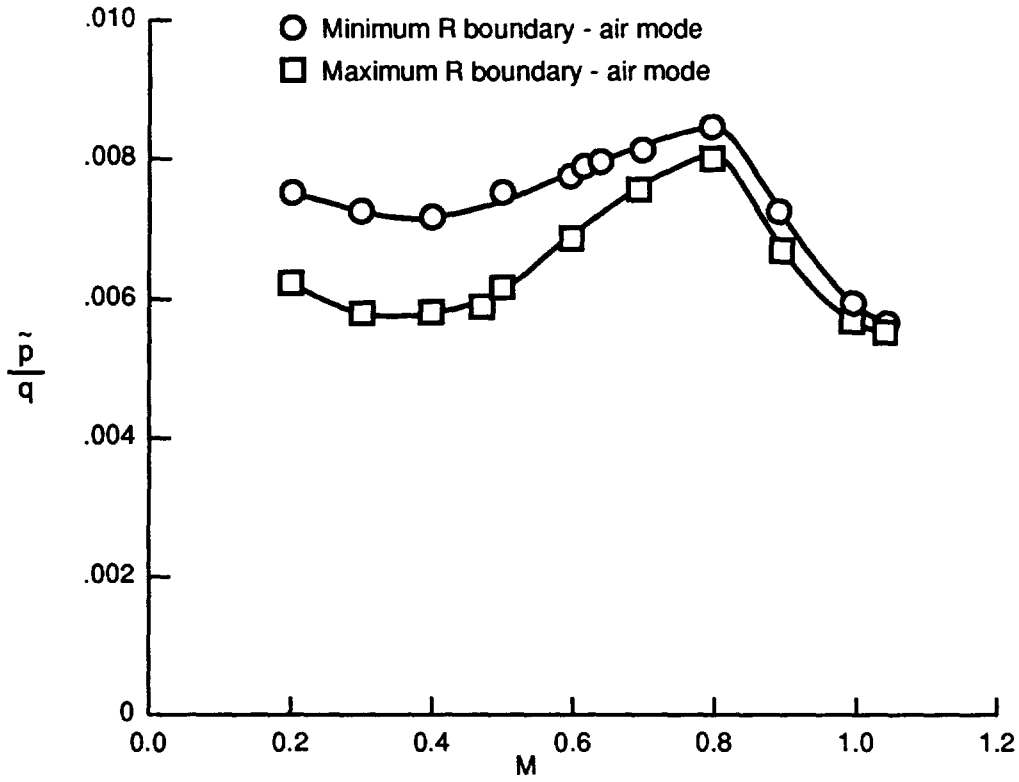

Figure 40. Fluctuating pressure coefficient on RHS test section side wall at sta 13, air mode.

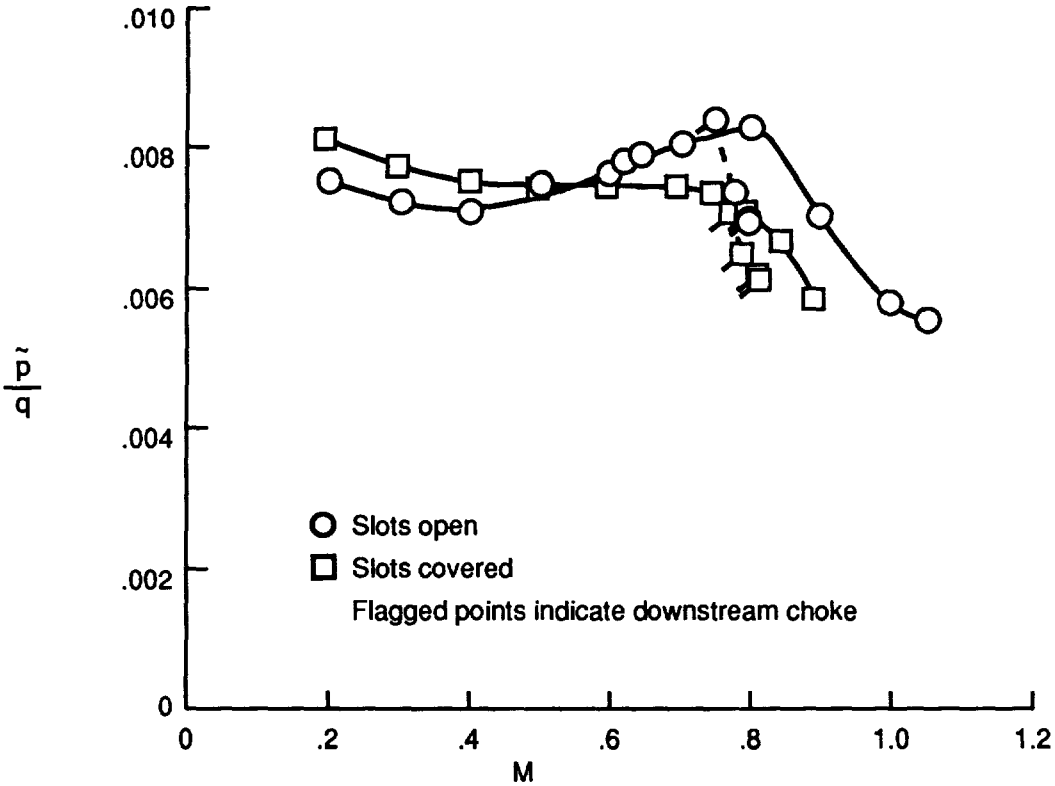

Figure 41. Fluctuating pressure coefficient on NTF RHS test section side wall at sta 13 showing effect of slot covers and downstream choke, minimum Reynolds number boundary, air mode.

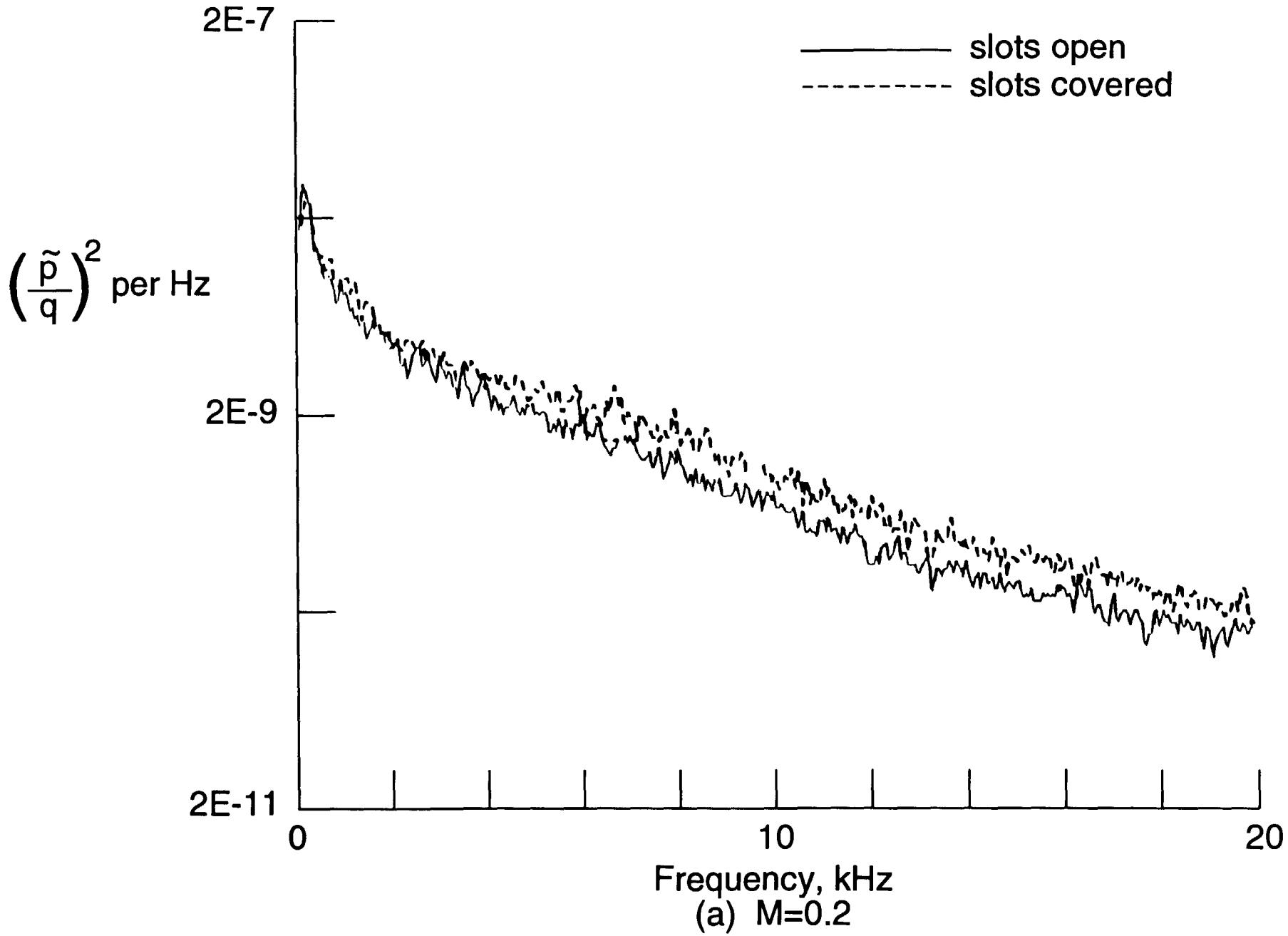

Figure 42. Power spectra of fluctuating pressure coefficient on RHS test section sidewall, sta 13, minimum Reynolds number boundary, air, comparison of slots open and covered.

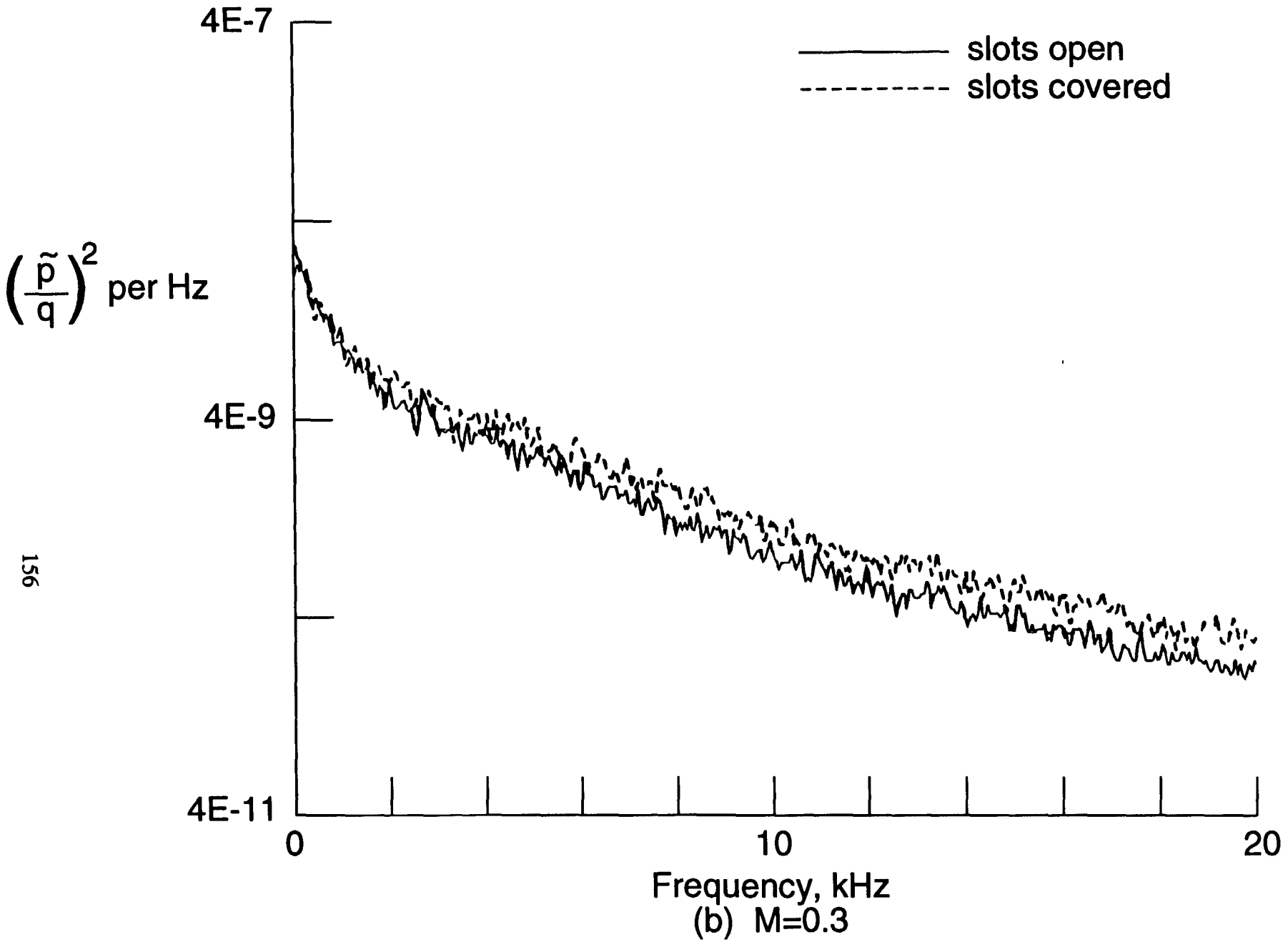

Figure 42. Continued.

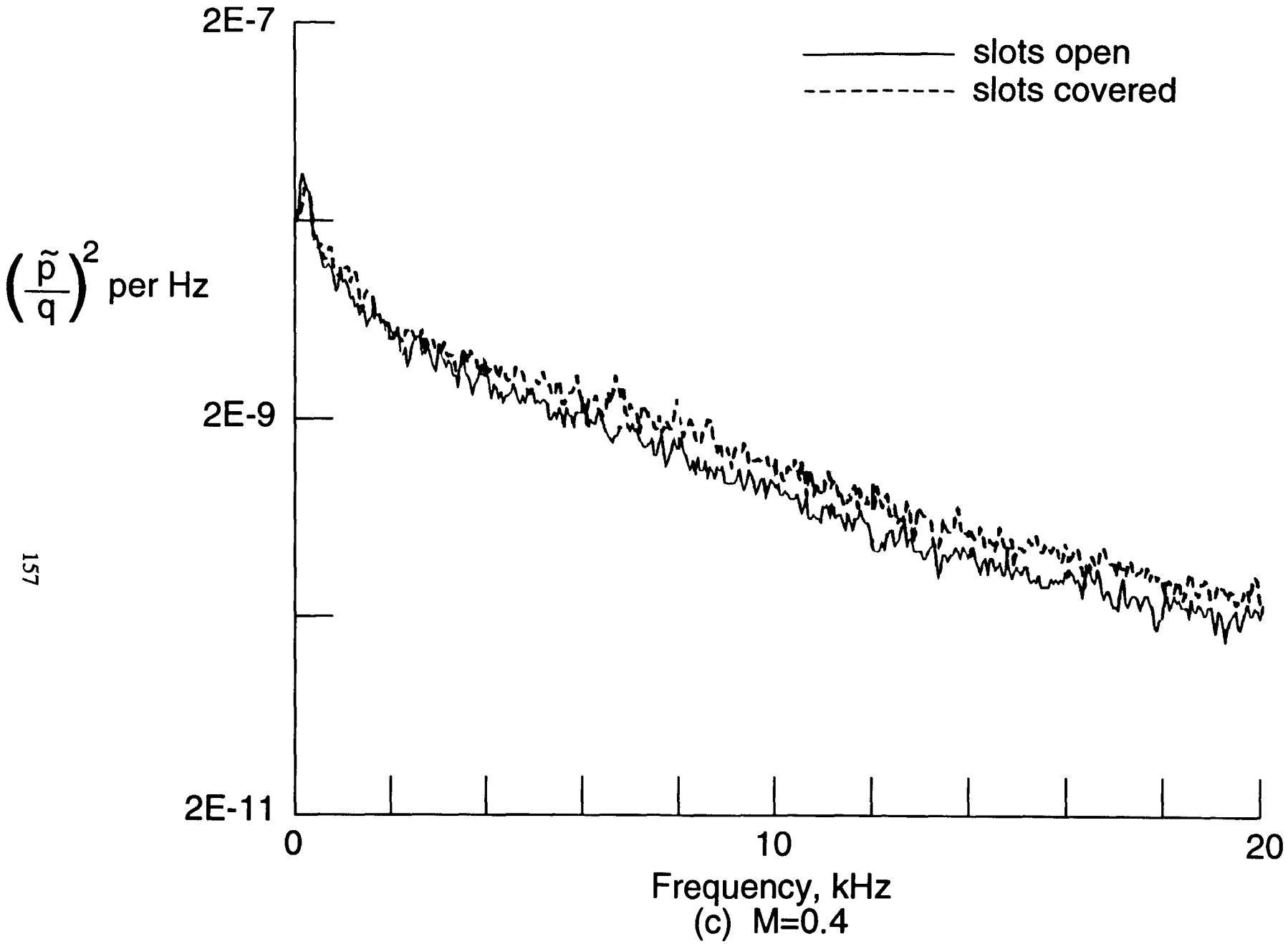

Figure 42. Continued.

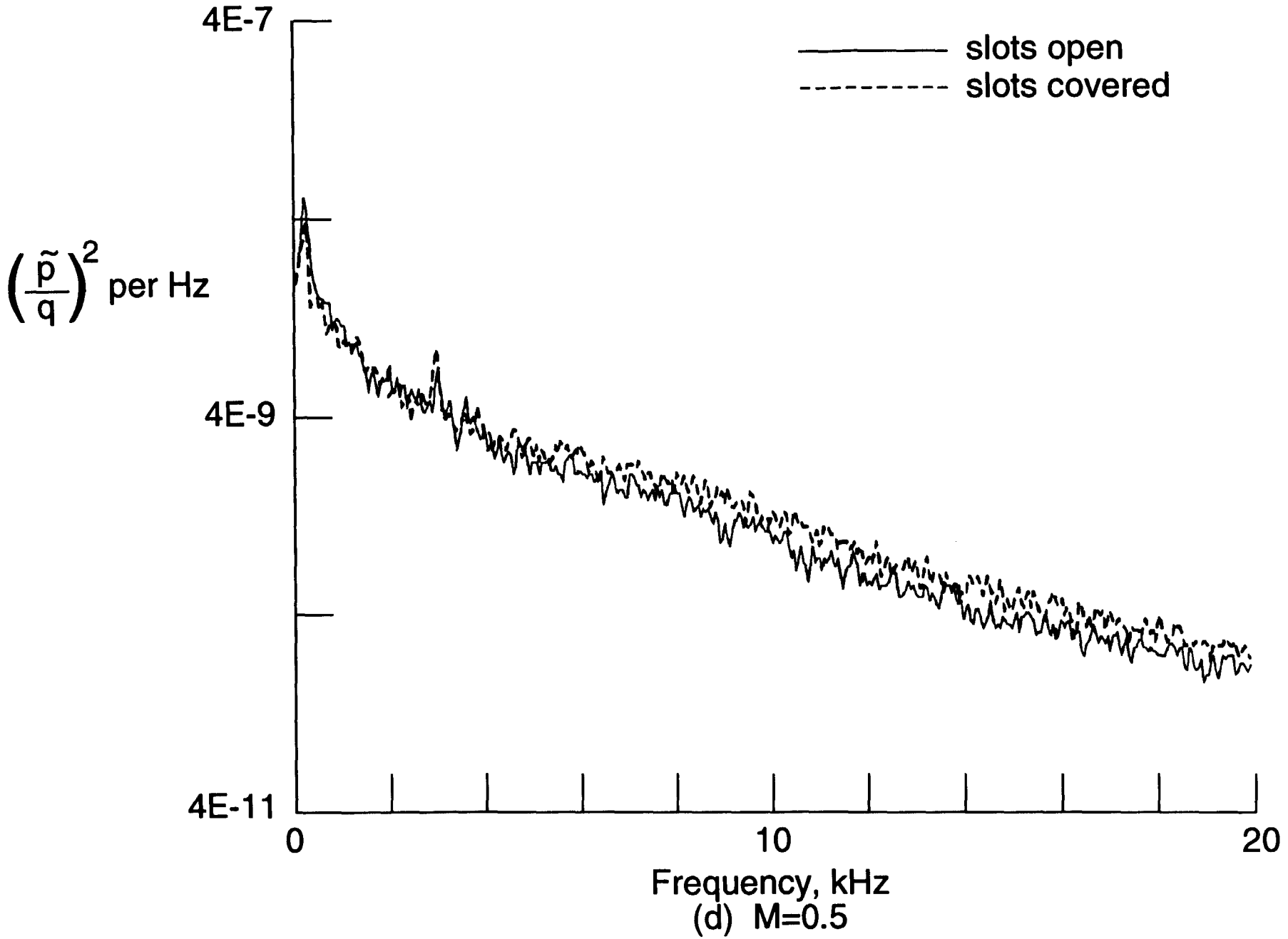

Figure 42. Continued.

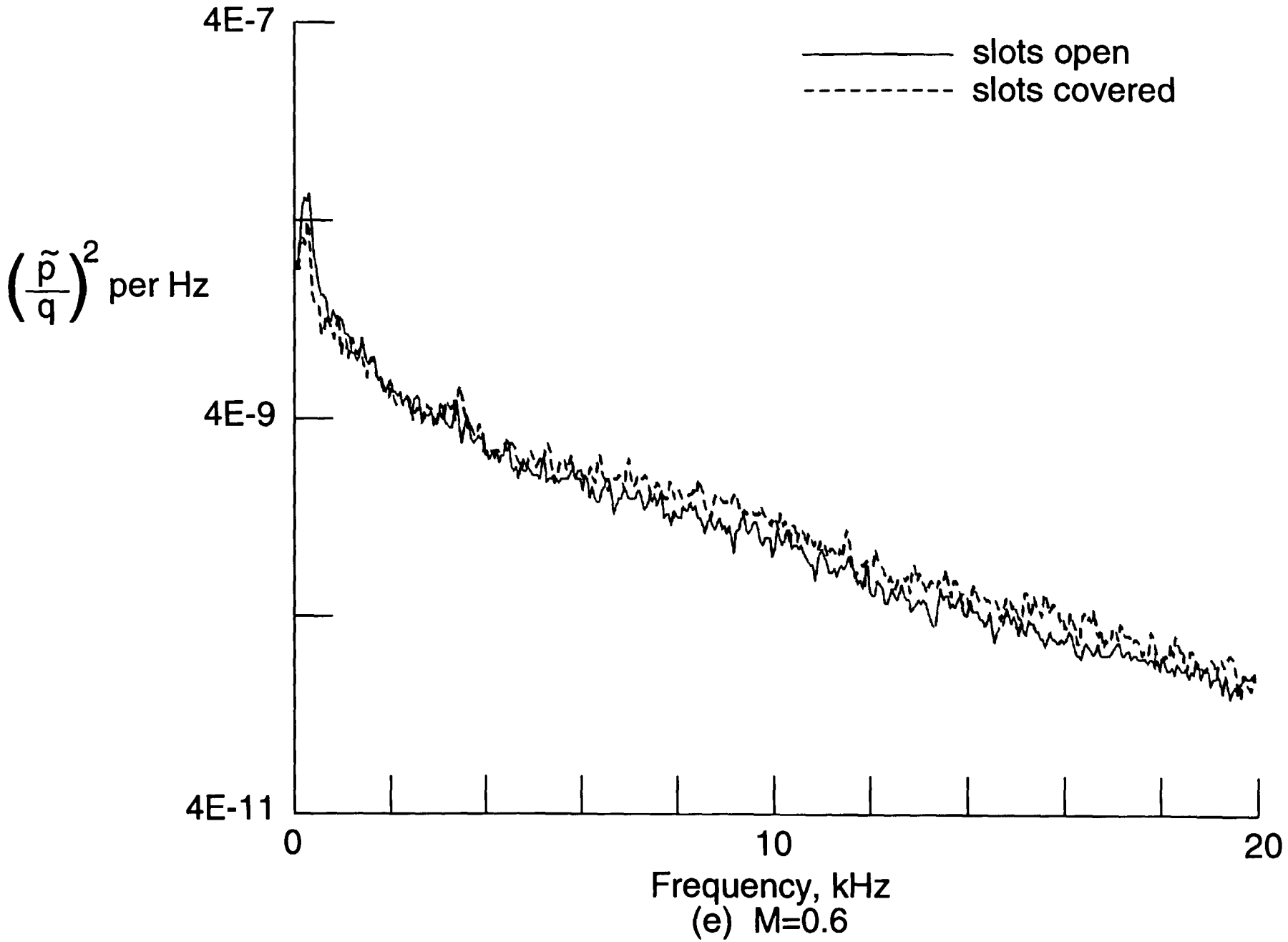

Figure 42. Continued.

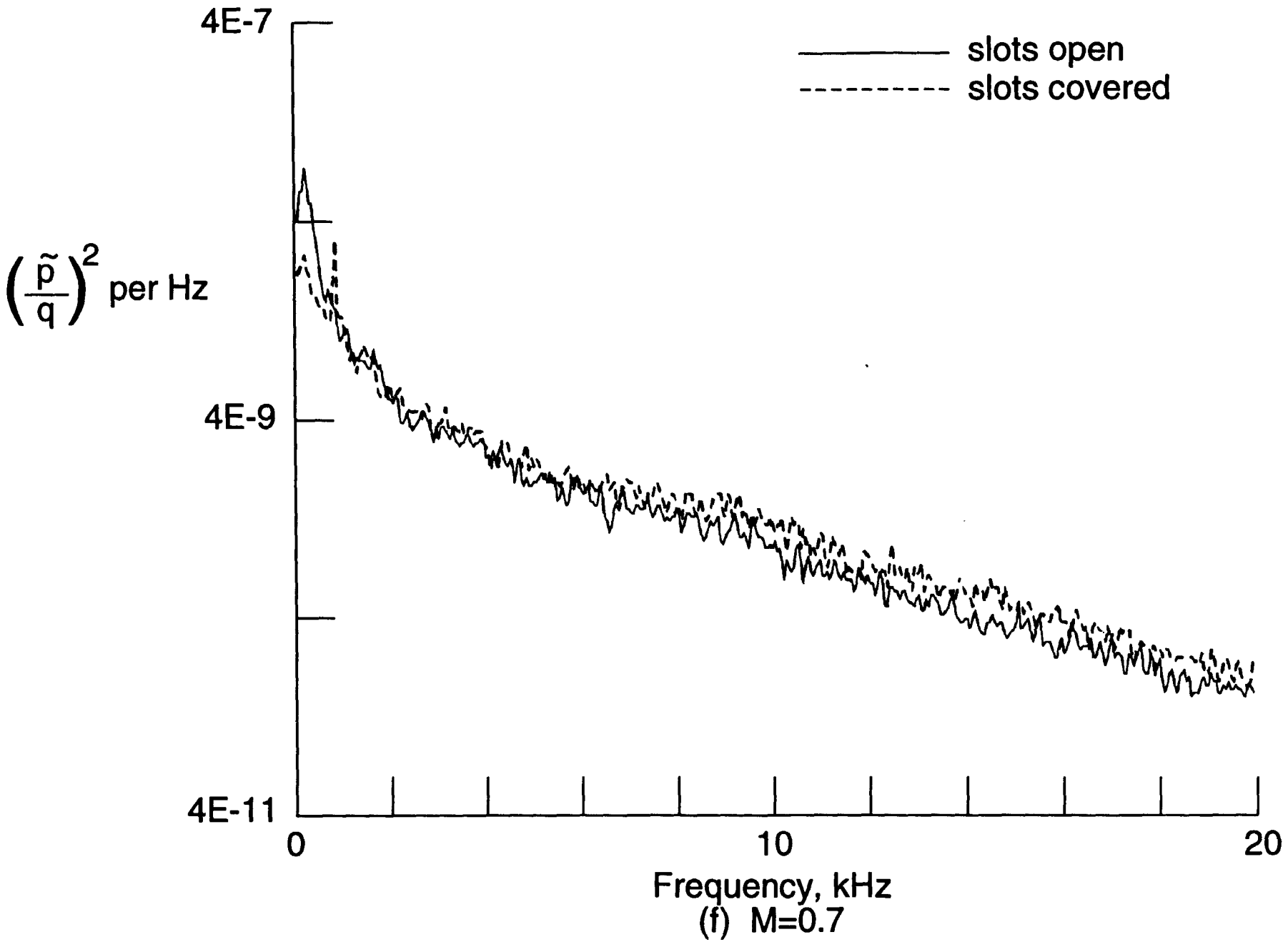

Figure 42. Continued.

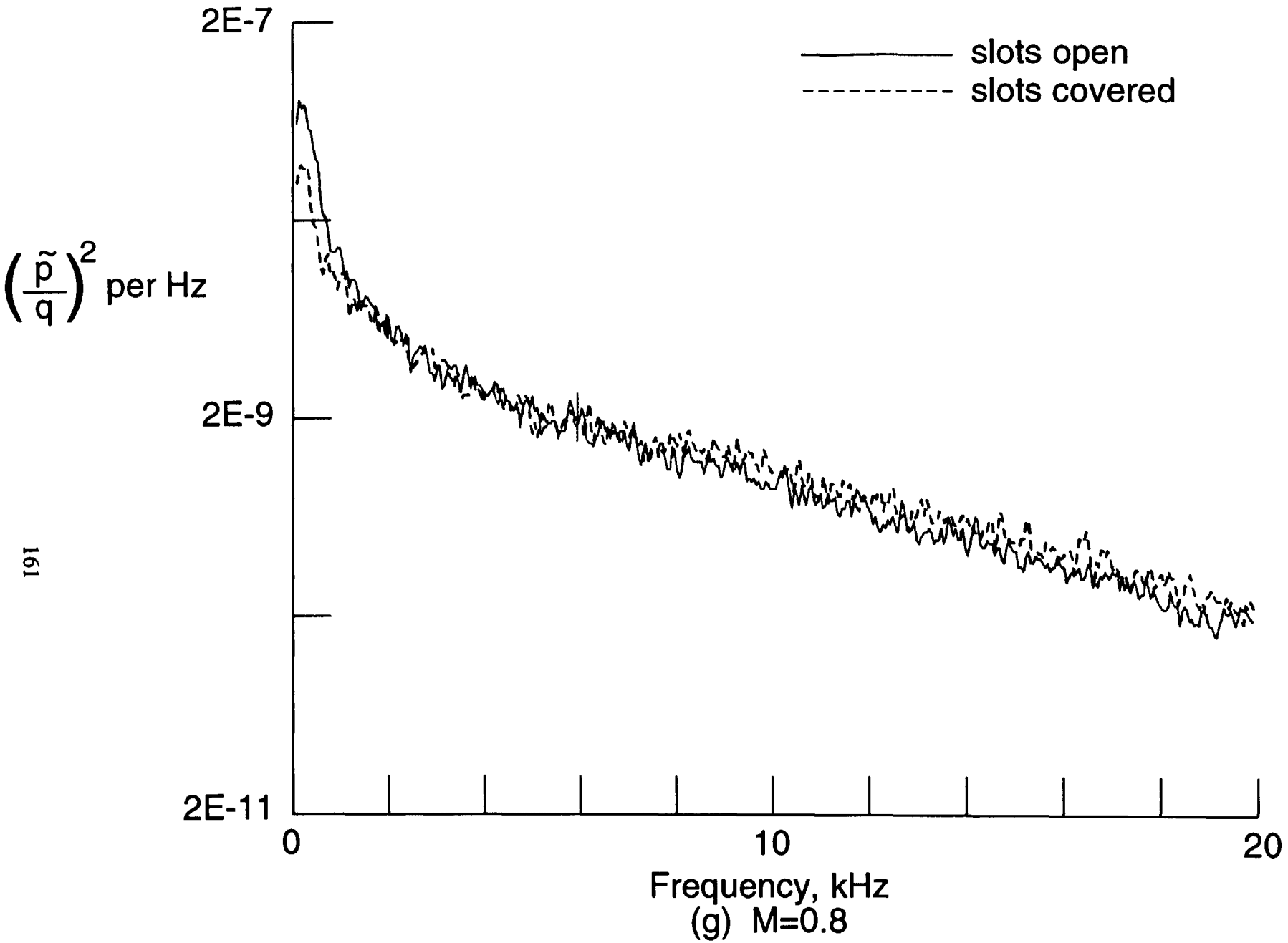

Figure 42. Continued.

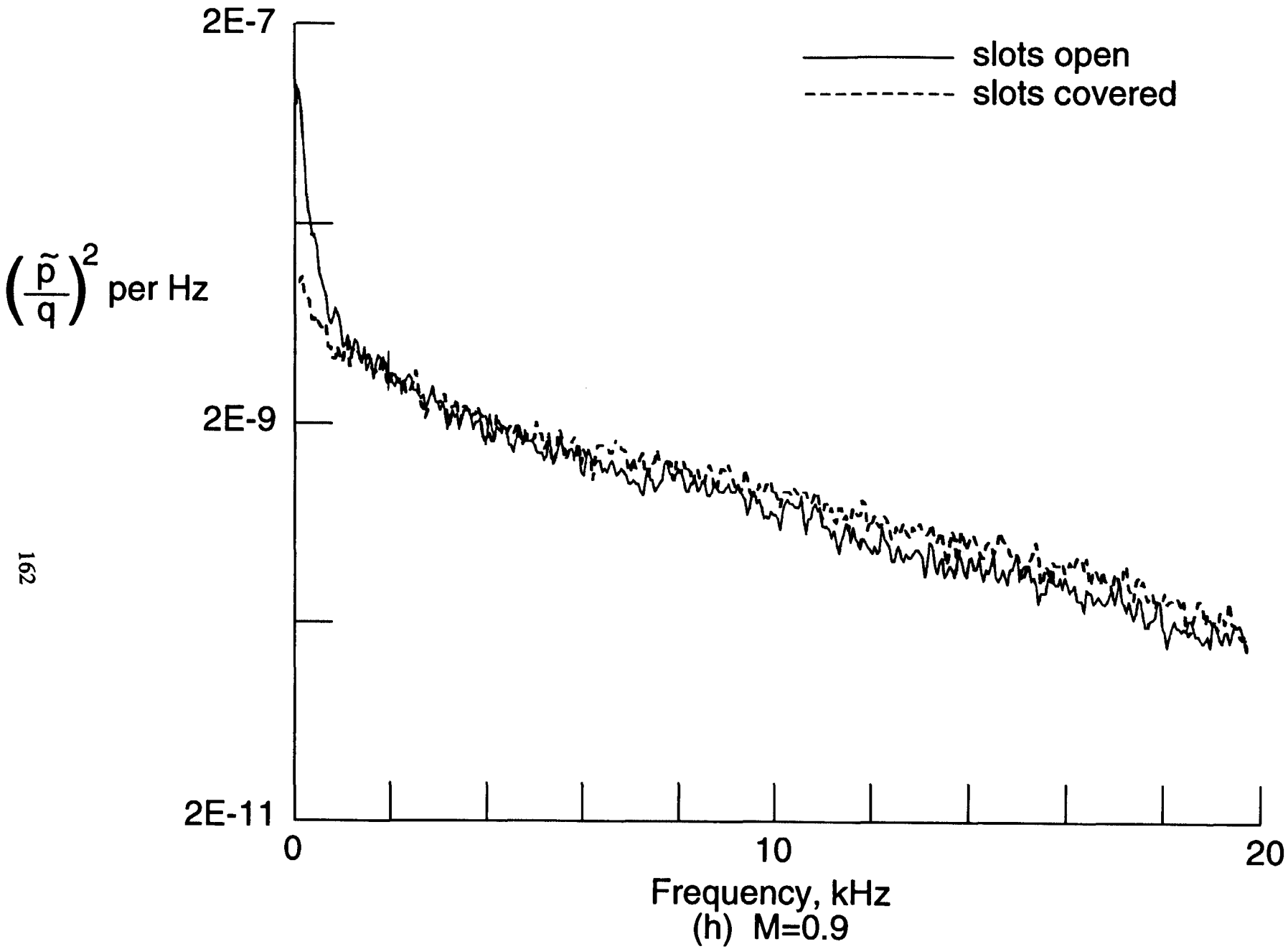

Figure 42. Concluded.

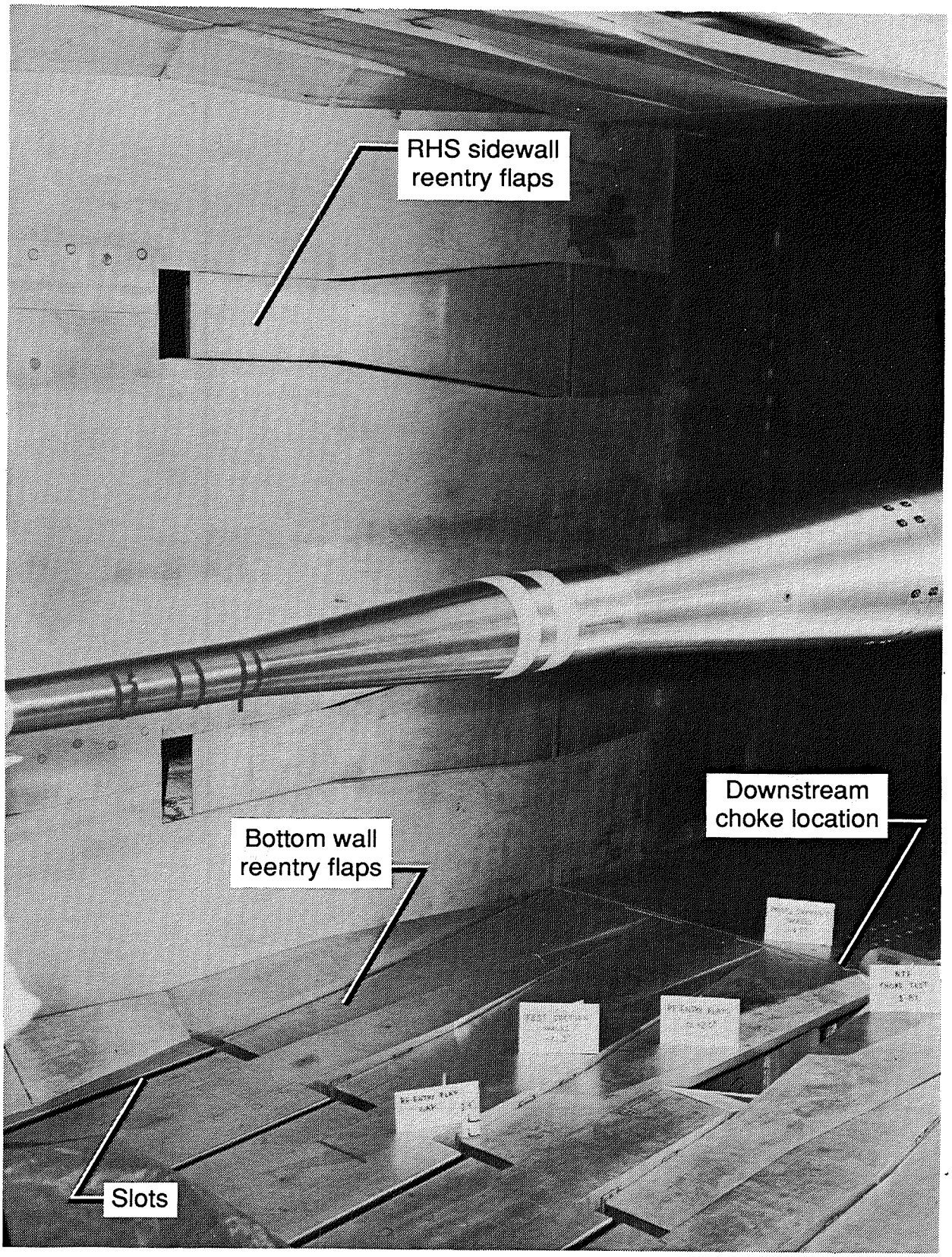

Figure 43. Photograph of NTF test section wall geometry variables for downstream choke with slots open.

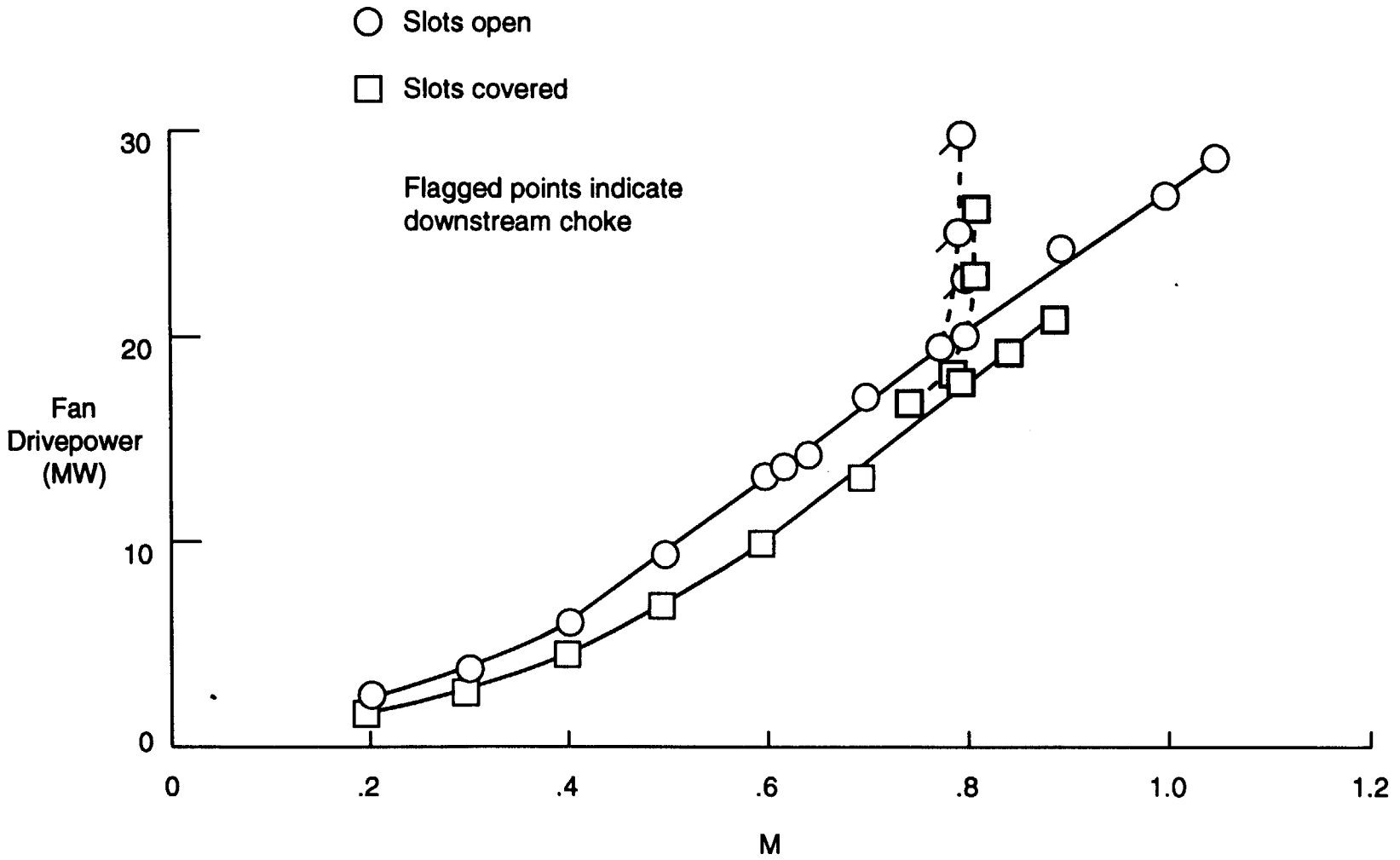

Figure 44. NTF fan drivepower for minimum Reynolds number boundary in air mode showing effect of slot covers and downstream choke.

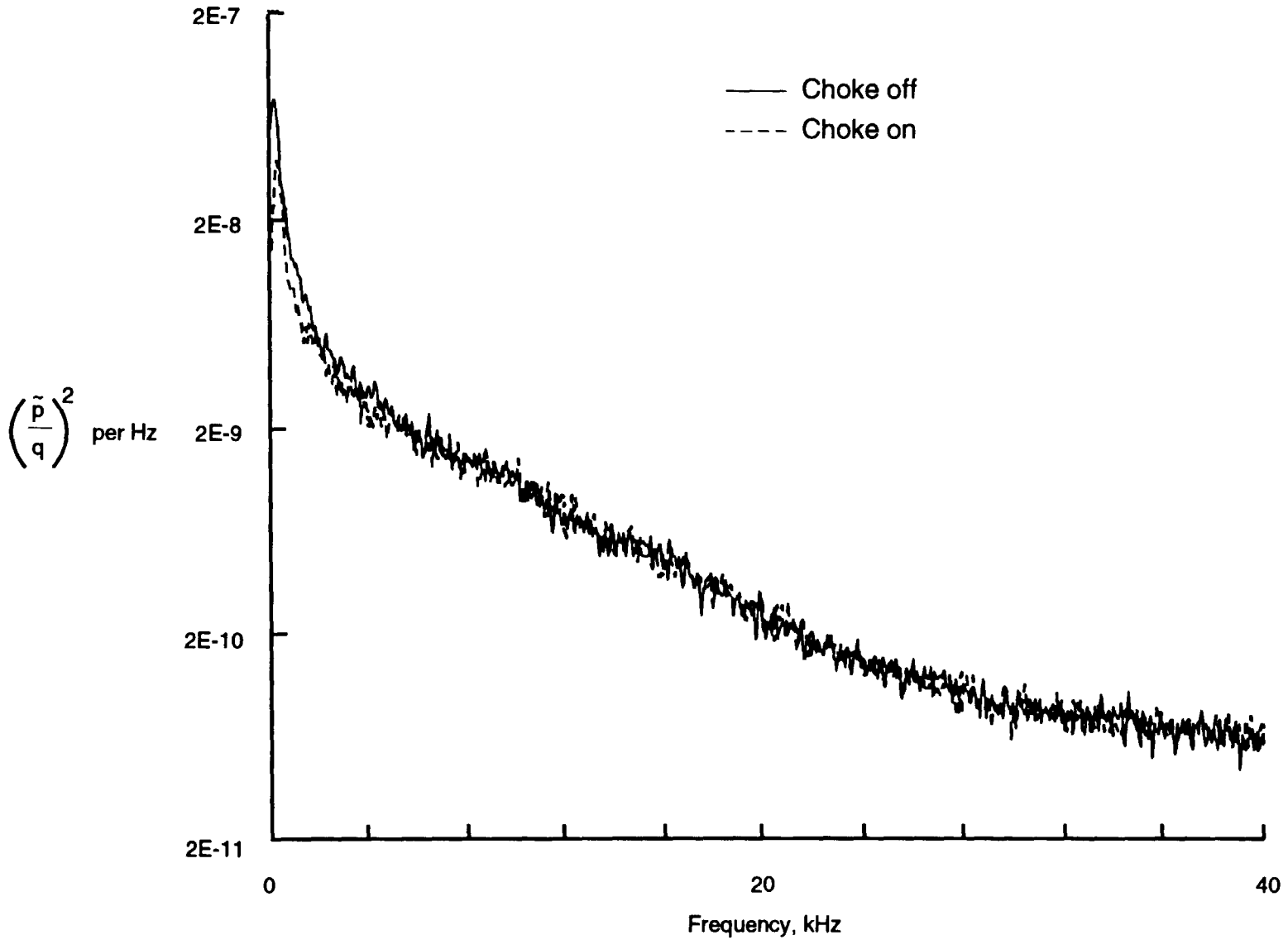

Figure 45. Power spectra of fluctuating pressure coefficient on NTF RHS test section side wall at sta 13, slots open, M = 0.8, R = 4 x 10^6/ft, air mode.

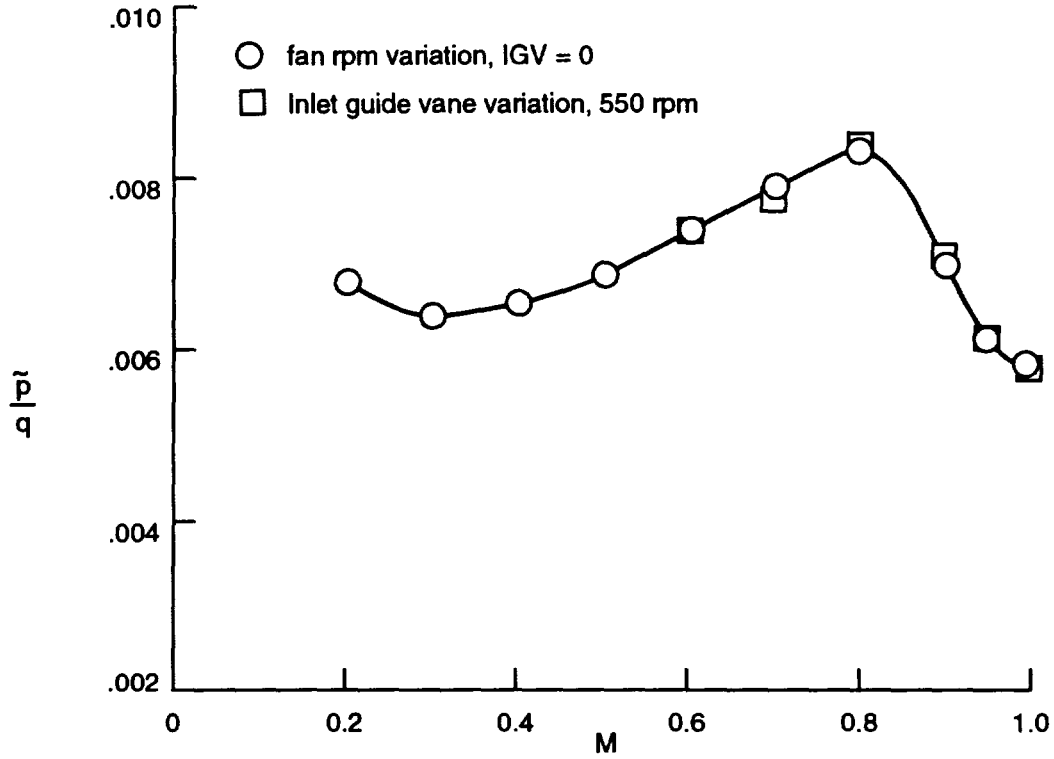

Figure 46. Fluctuating pressure coefficient on NTF RHS test section sidewall at sta 13, R= $6x10^6$ per ft., ambient temperature, air mode, showing effect of fan rpm and inlet quide vane variation for velocity change.

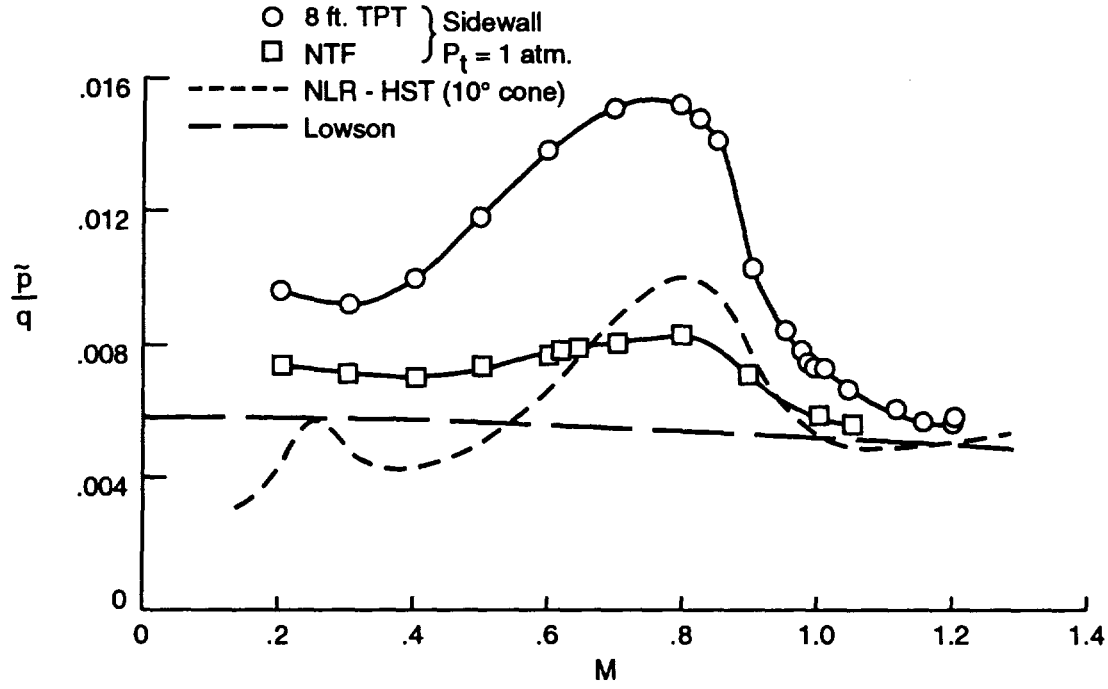

Figure 47. Comparison of NTF and 8 ft. TPT fluctuating pressure coefficient on test section sidewall at atmospheric stagnation pressure and ambient temperature in air.

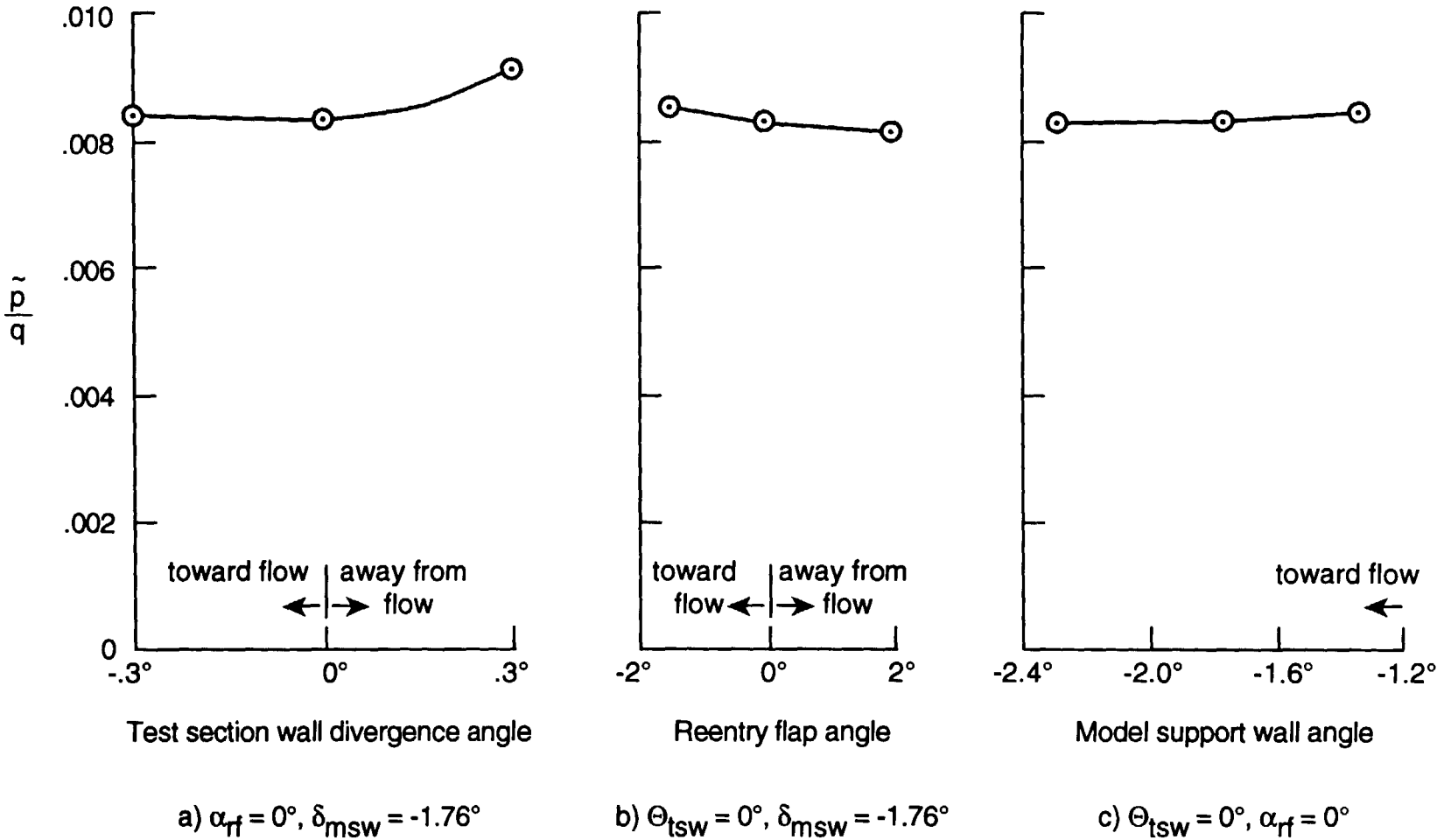

Figure 48. Effect of test section geometry variables on fluctuating pressure coefficient on RHS test section side wall at sta 13, M = 0.8, R = 6 x 10^6 per ft., ambient temperature, air mode.

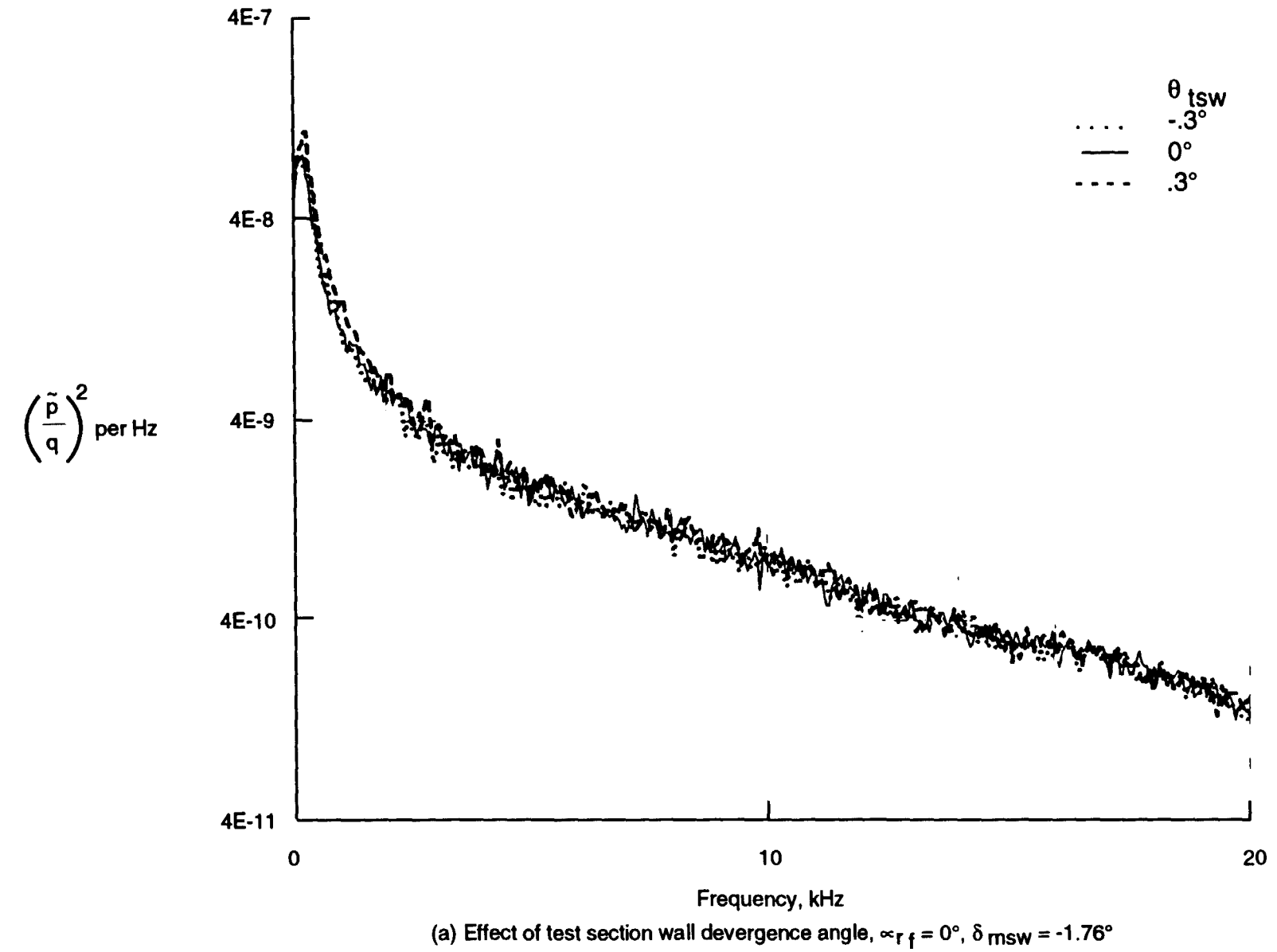

(a) Effect of test section wall devergence angle, $\alpha_{r\,f} = 0°$, $\delta_{msw} = -1.76°$

Figure 49. Effect of test section geometry variables on power spectra of fluctuating pressure coefficient on RHS test section side wall at sta. 13, M = 0.8, R = 6 x 10^6 per ft., ambient temperature, air mode.

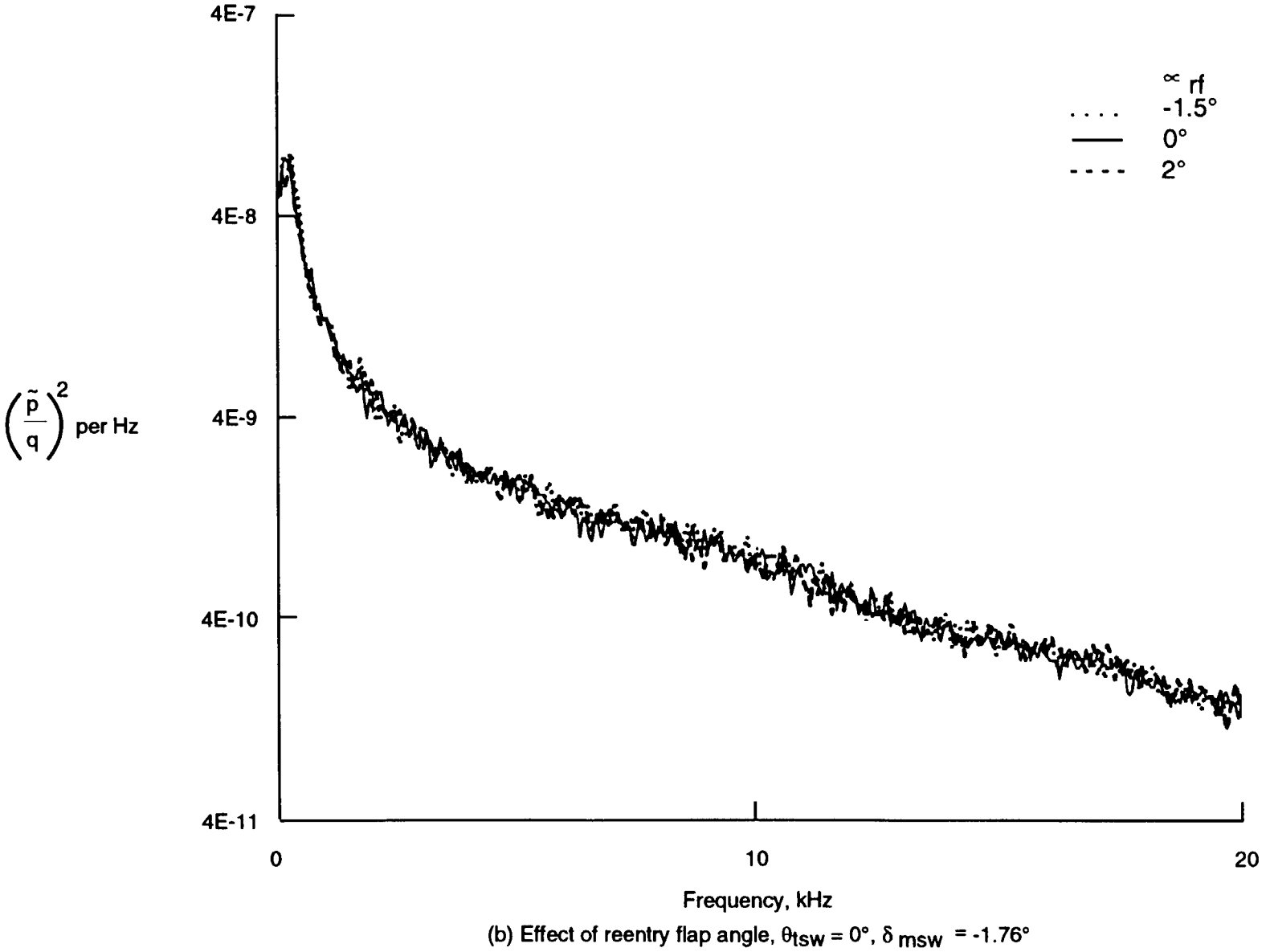

(b) Effect of reentry flap angle, $\theta_{tsw} = 0°$, $\delta_{msw} = -1.76°$

Figure 49. Continued.

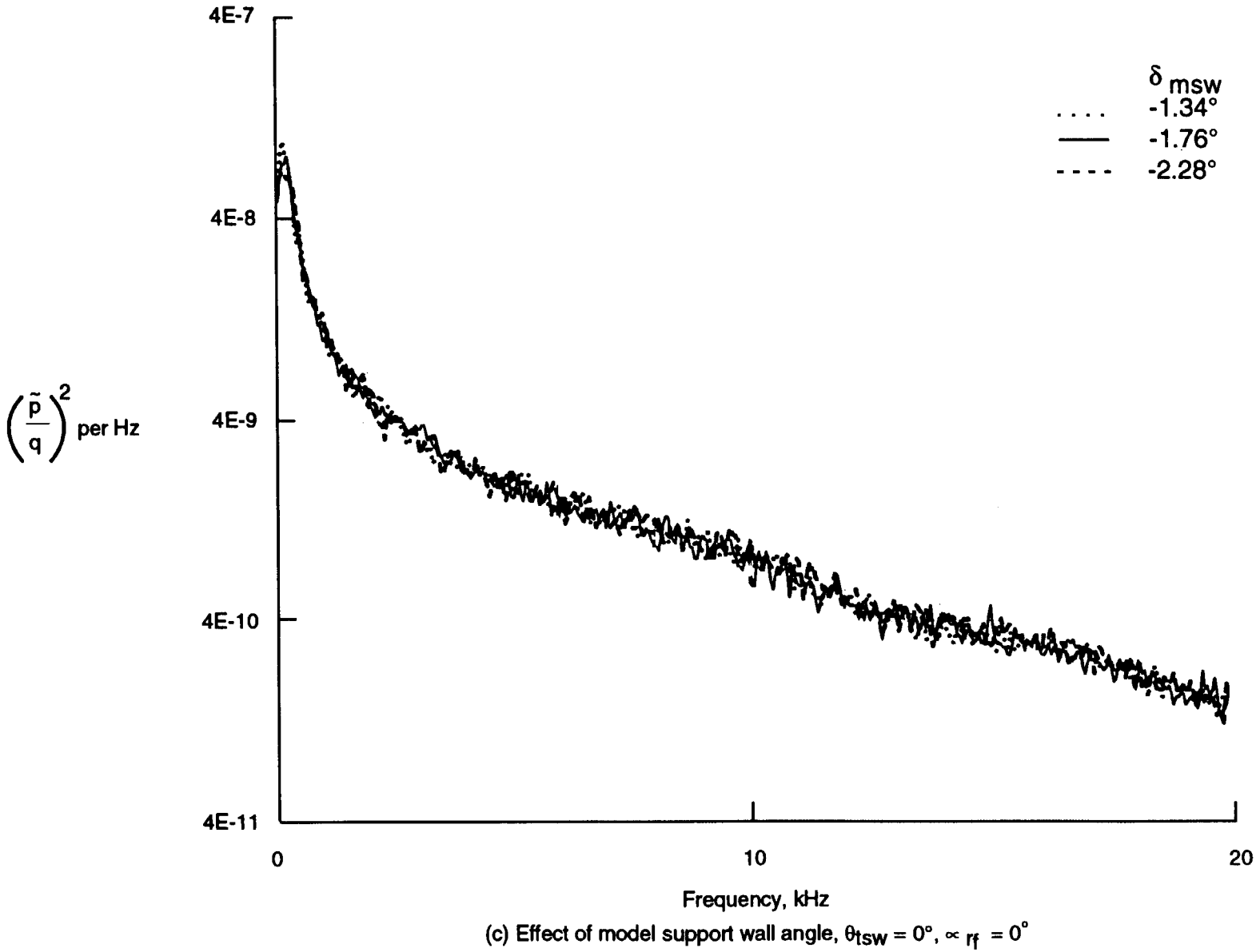

Figure 47. Concluded.

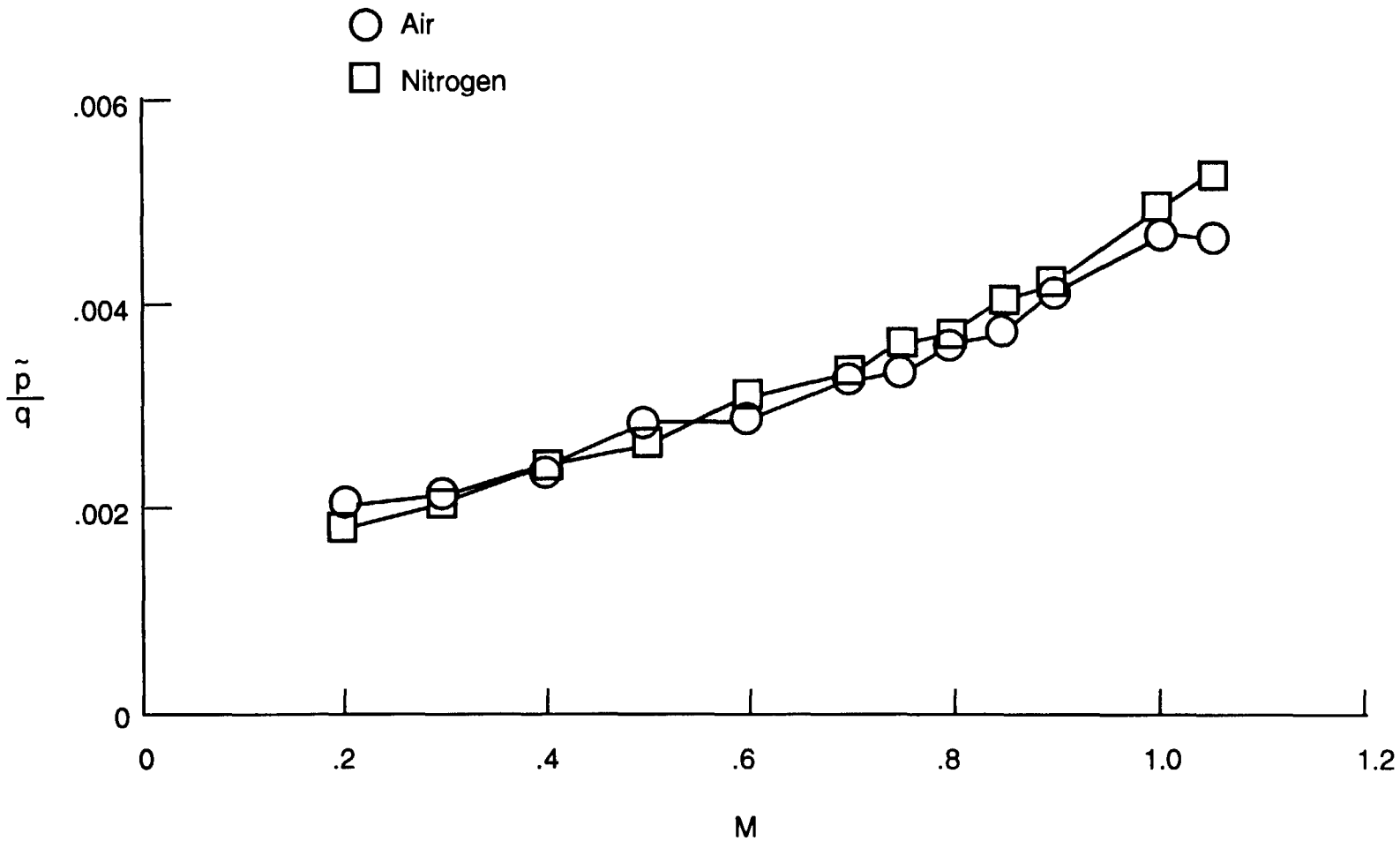

Figure 50. Fluctuating pressure coefficient at liquid nitrogen injection station for a test section Reynolds number of 6 million per ft., ambient temperature, comparison between air and nitrogen.

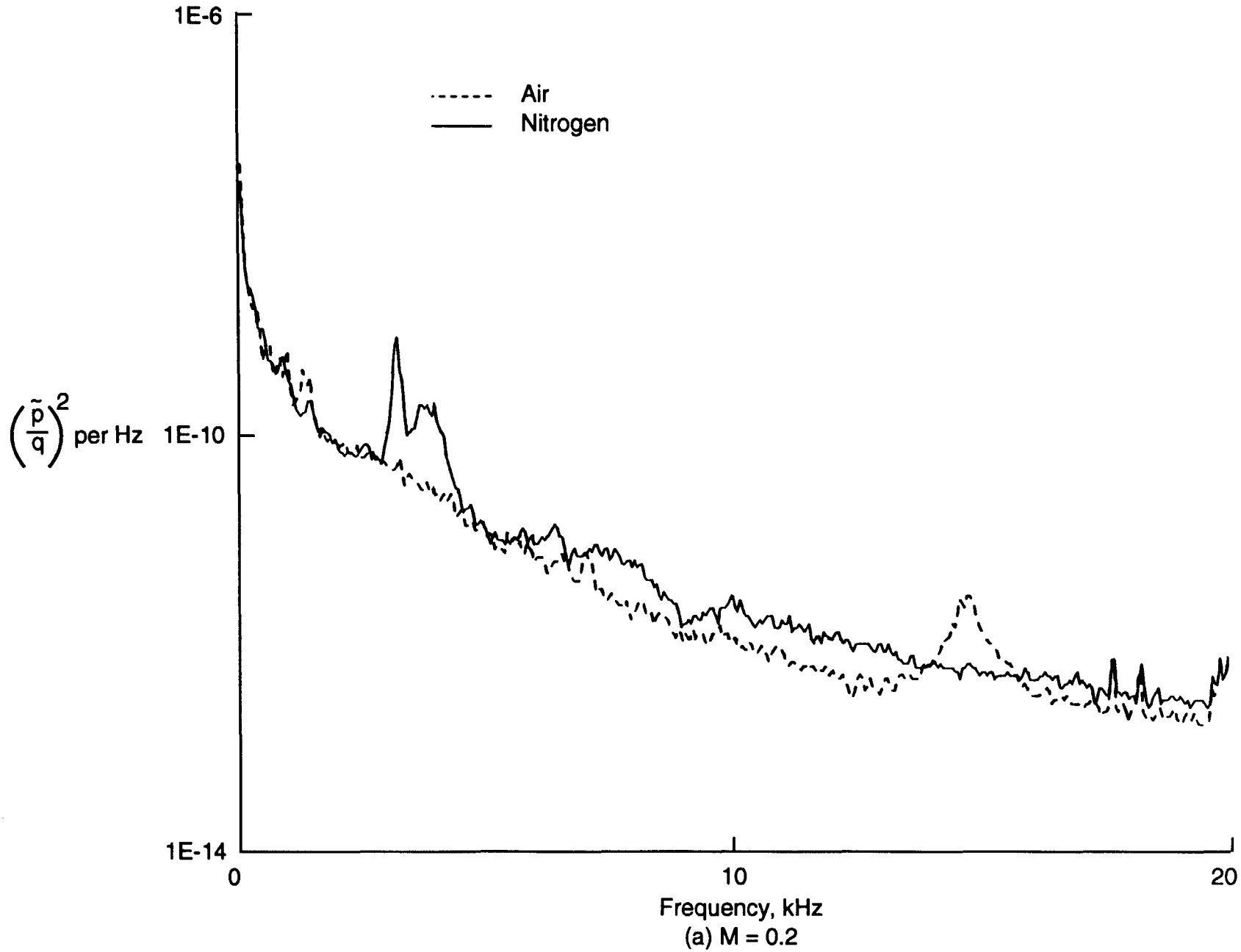

Figure 51. Power spectra of fluctuating pressure coefficient at liquid nitrogen injection sta., R= 6×10^6/ft., ambient temperature, comparison between air and nitrogen.

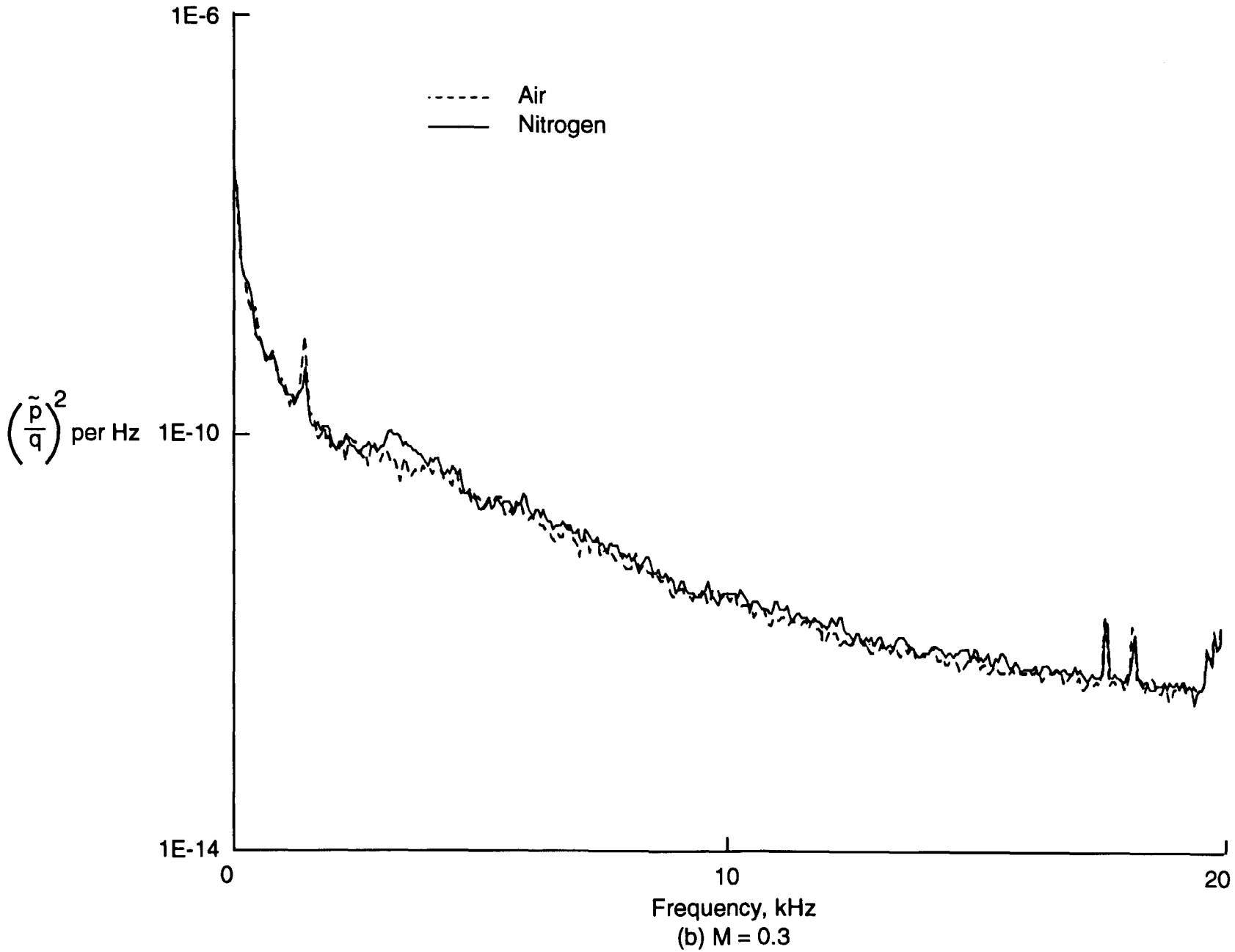

Figure 51. Continued

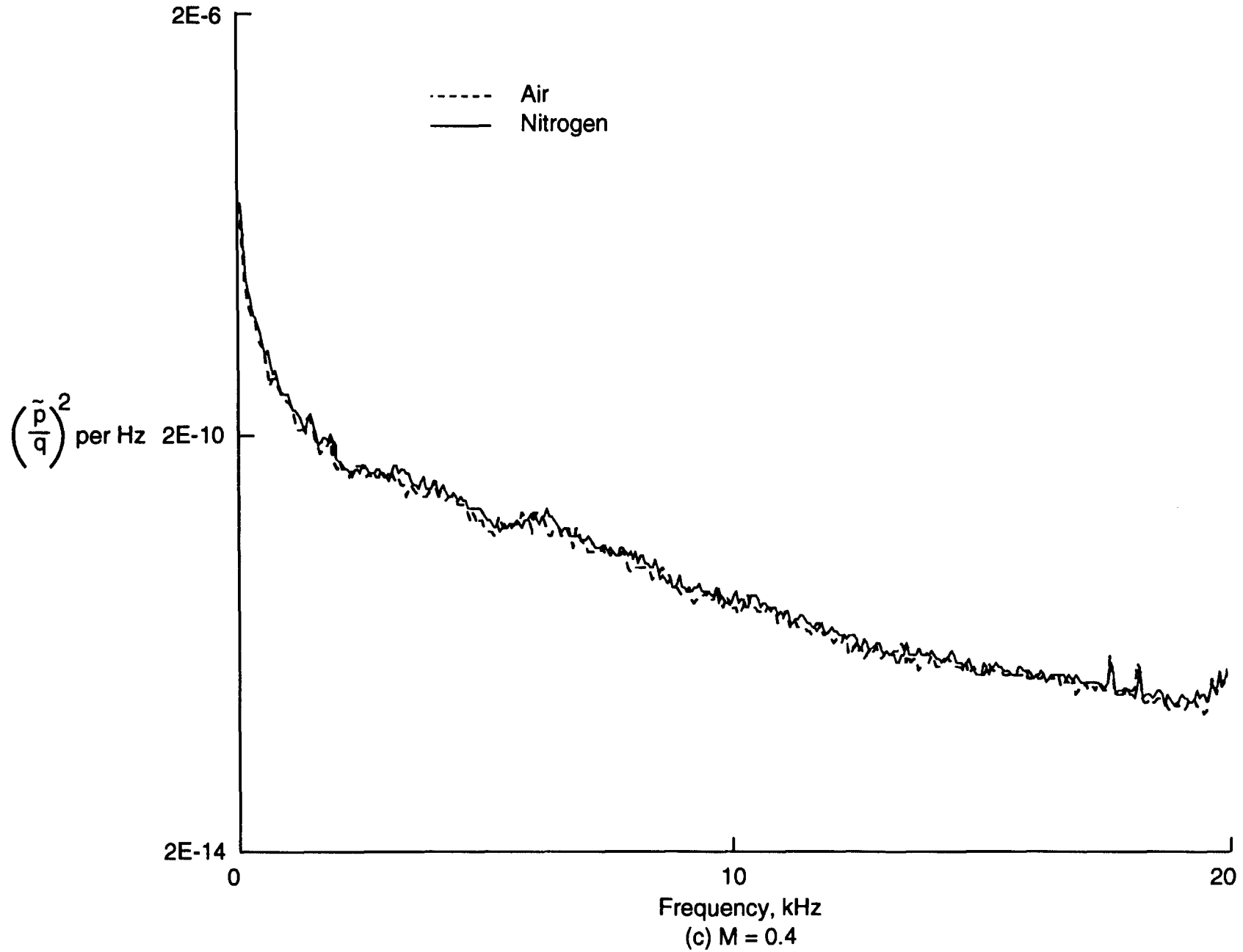

Figure 51. Continued

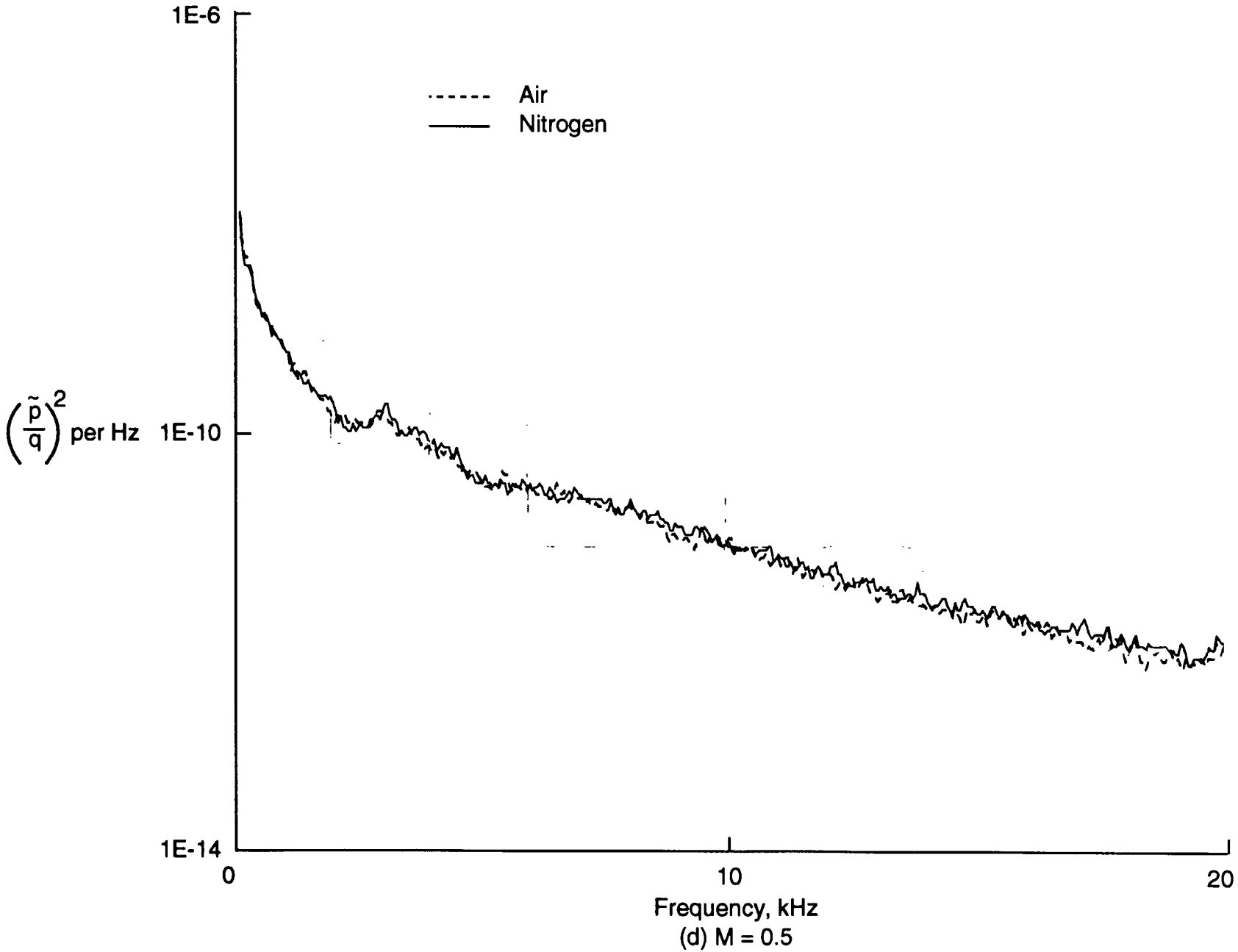

Figure 51. Continued

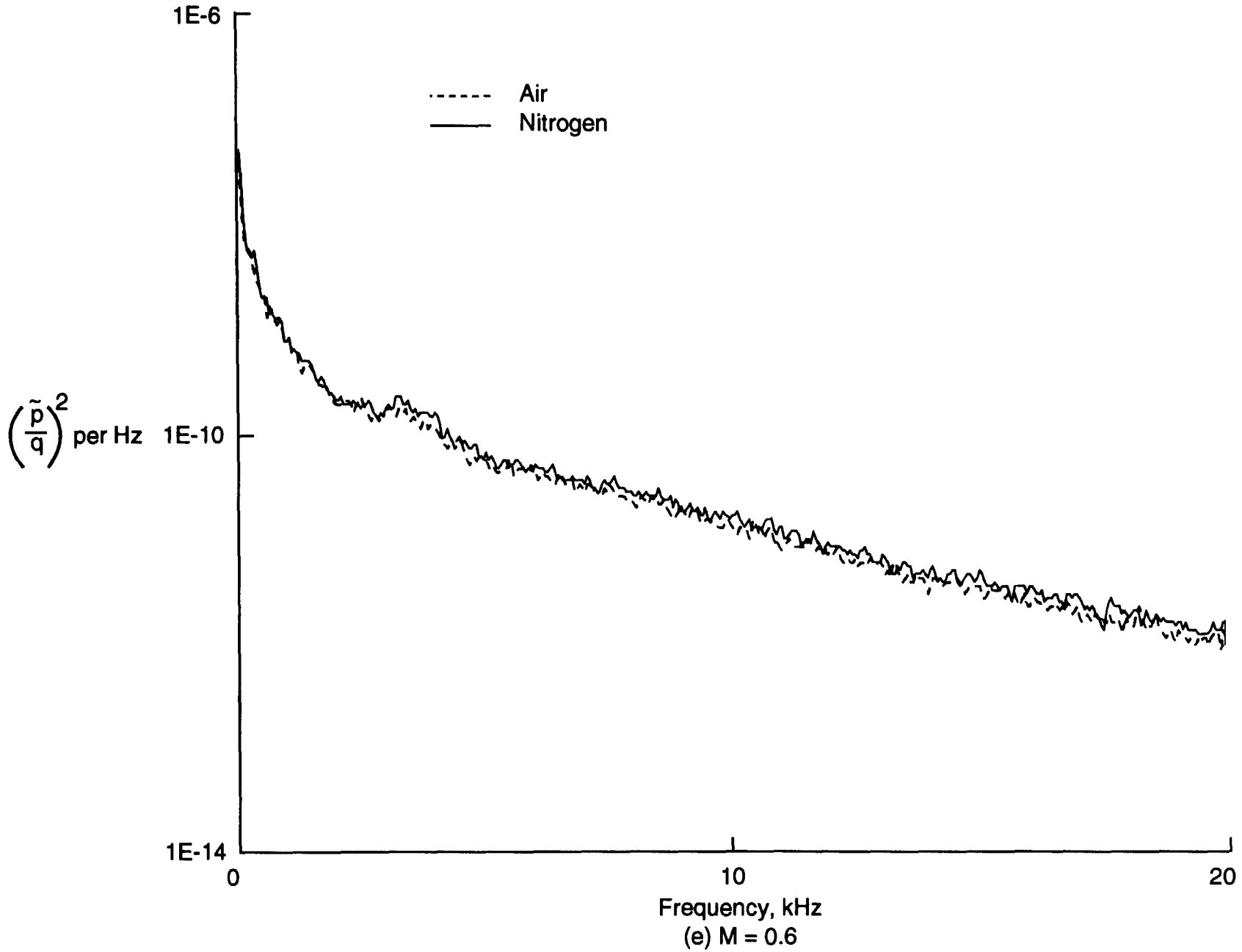

Figure 51. Continued

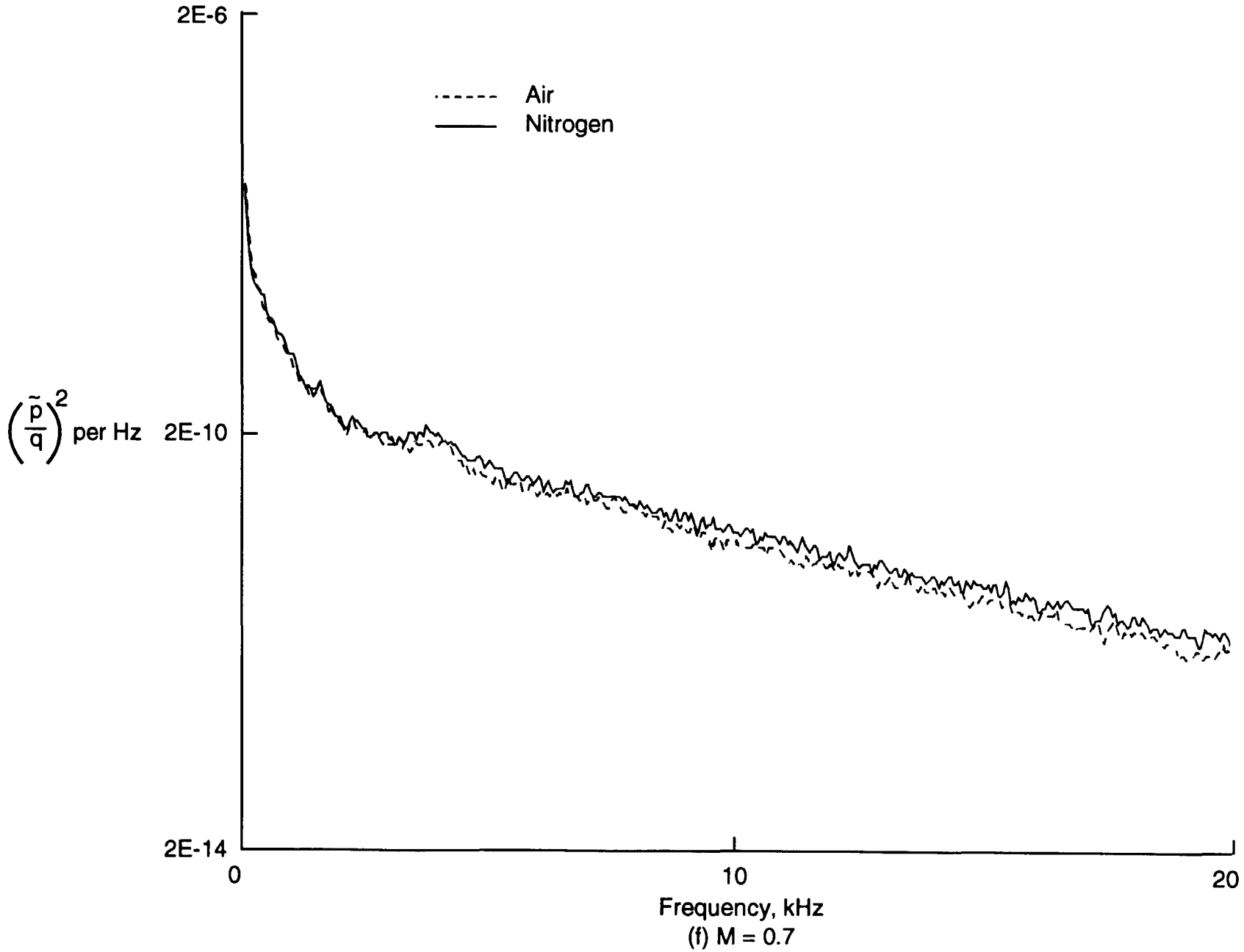

Figure 51. Continued

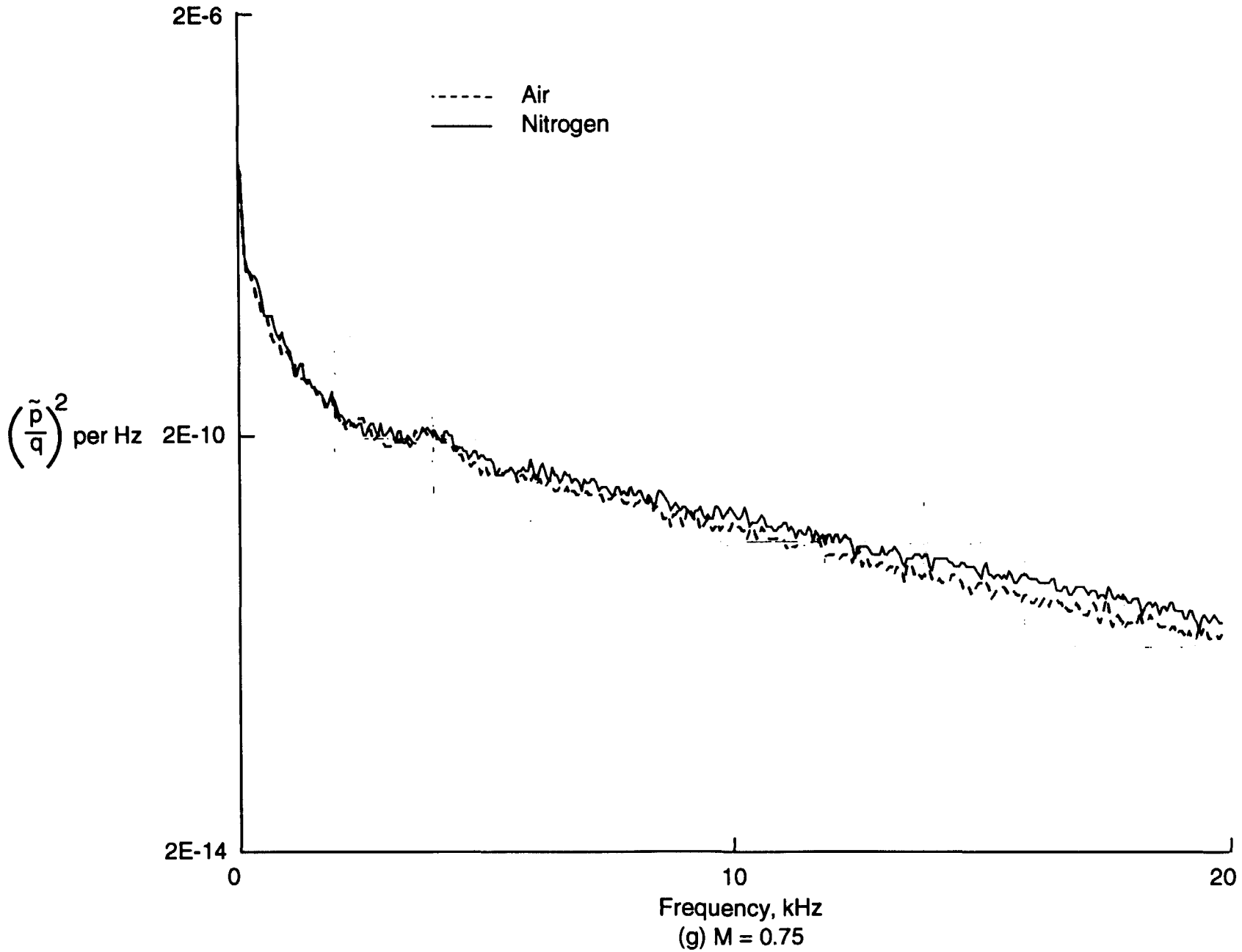

Figure 51. Continued

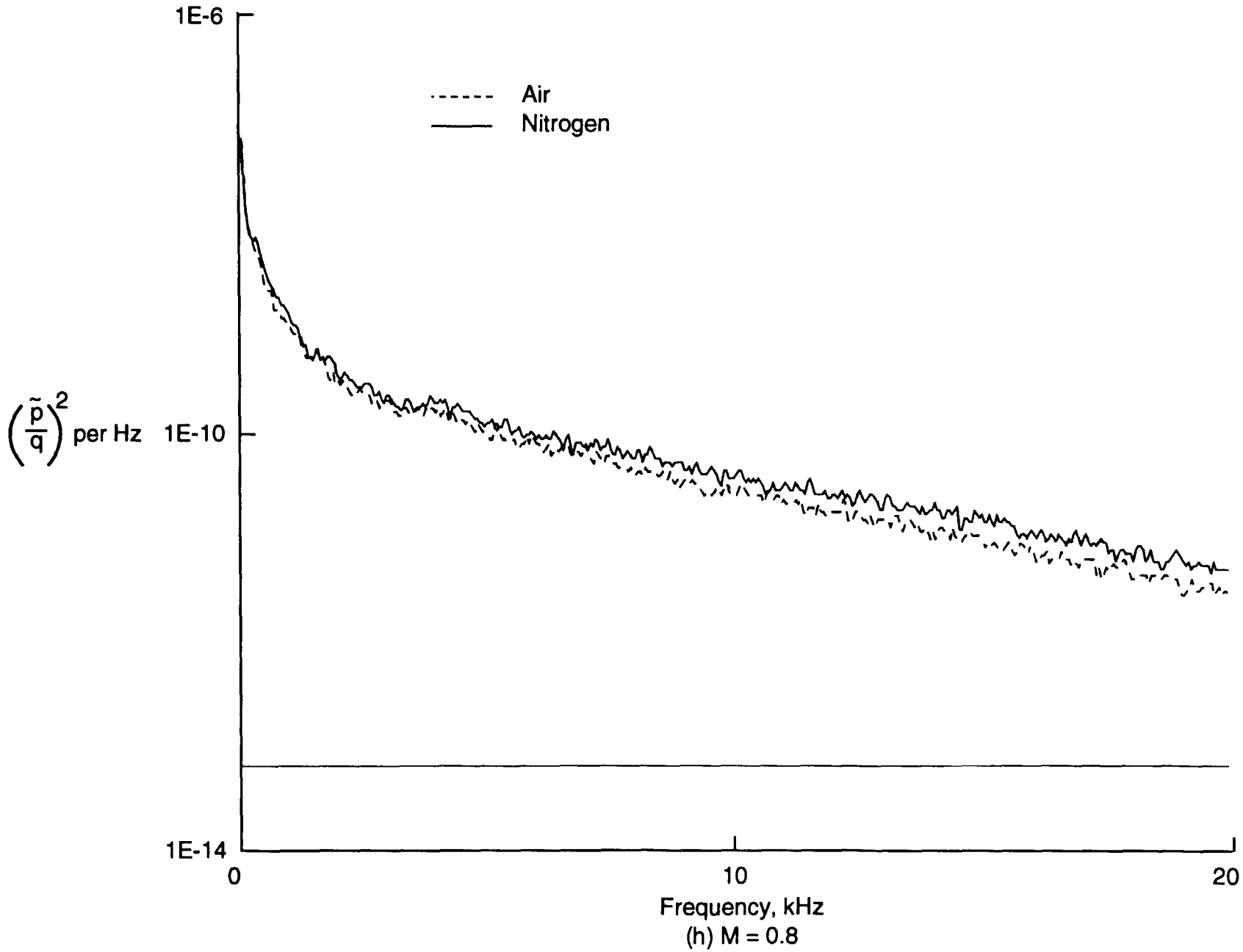

Figure 51. Continued

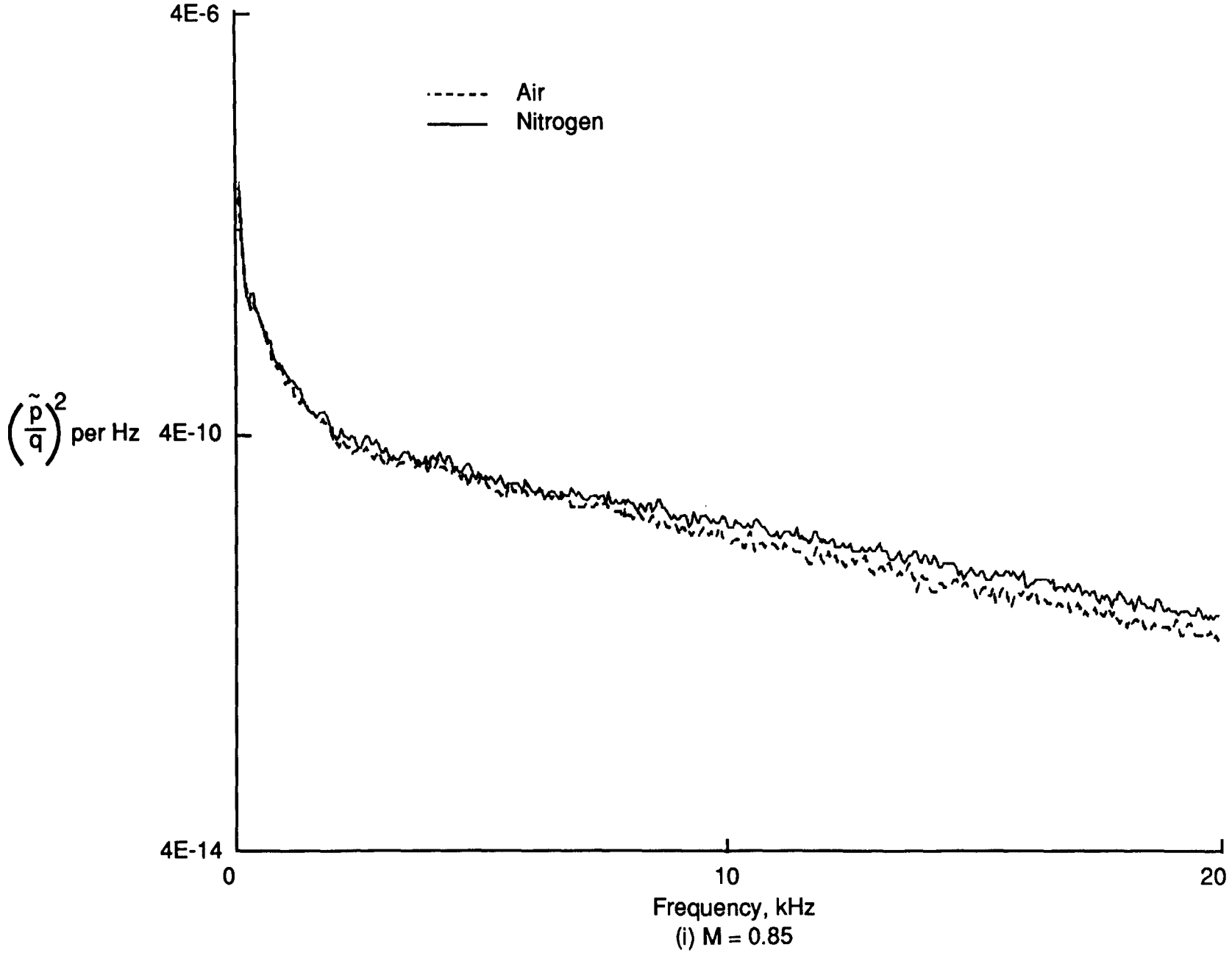

Figure 51. Continued

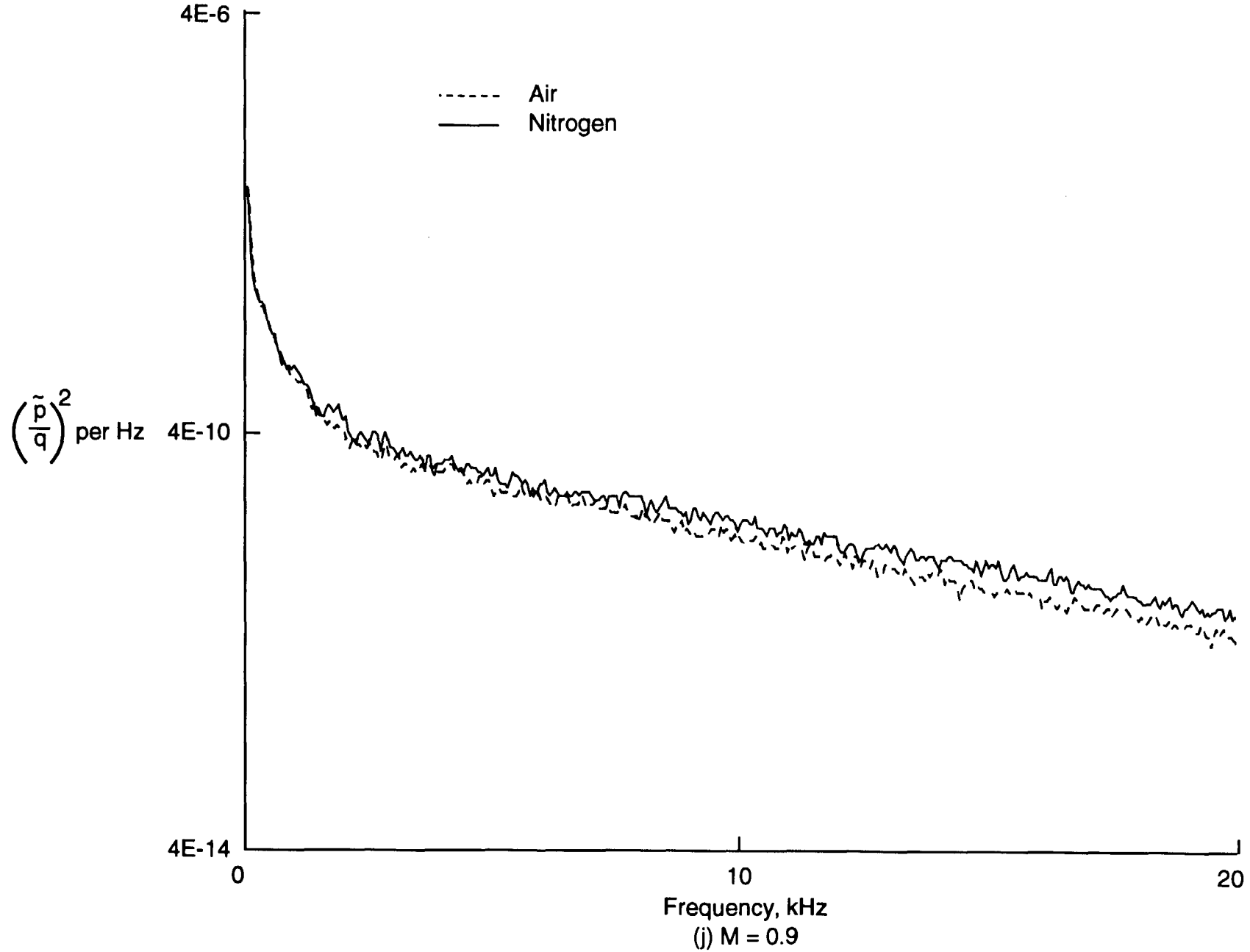

(j) M = 0.9

Figure 51. Continued

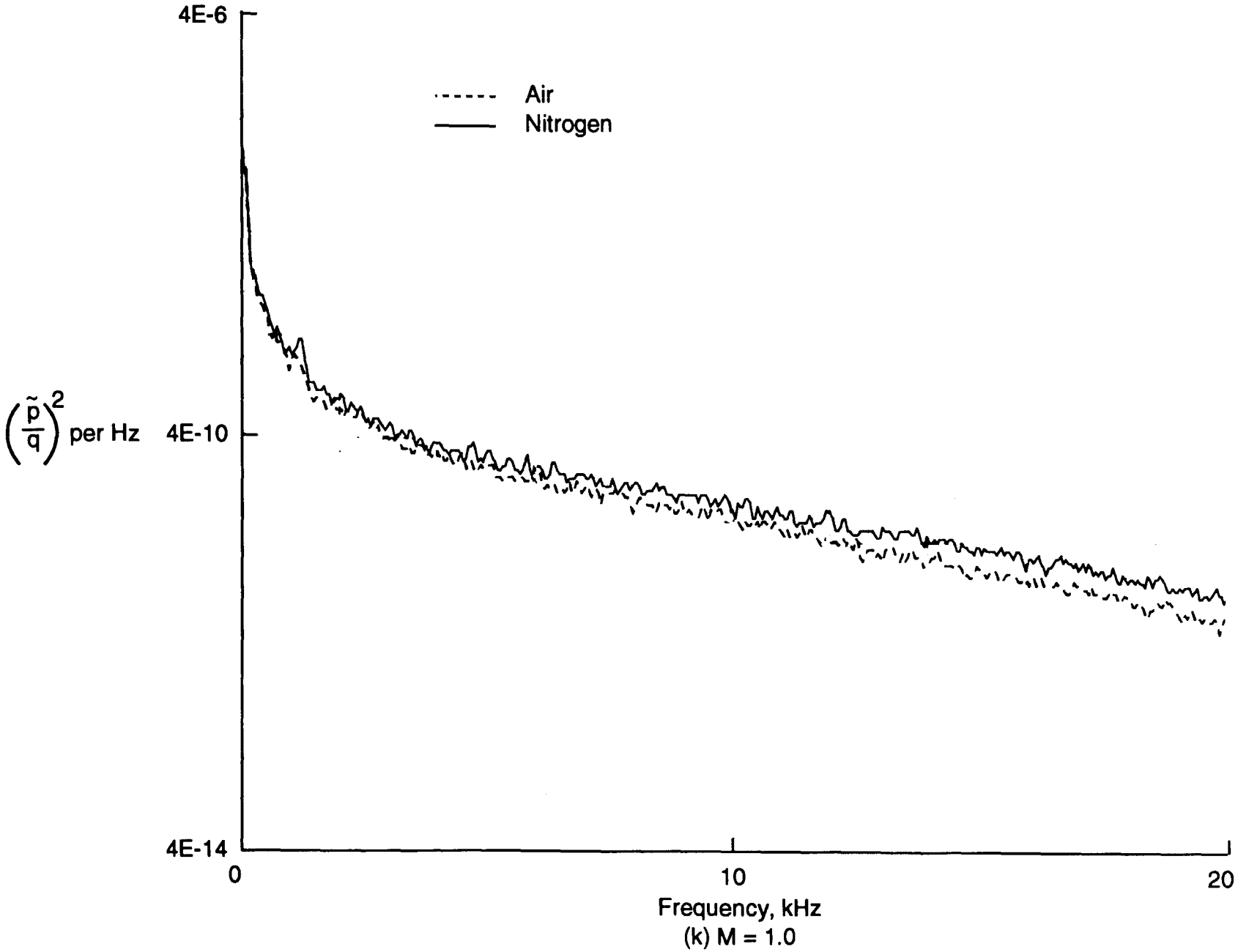

Figure 51. Continued

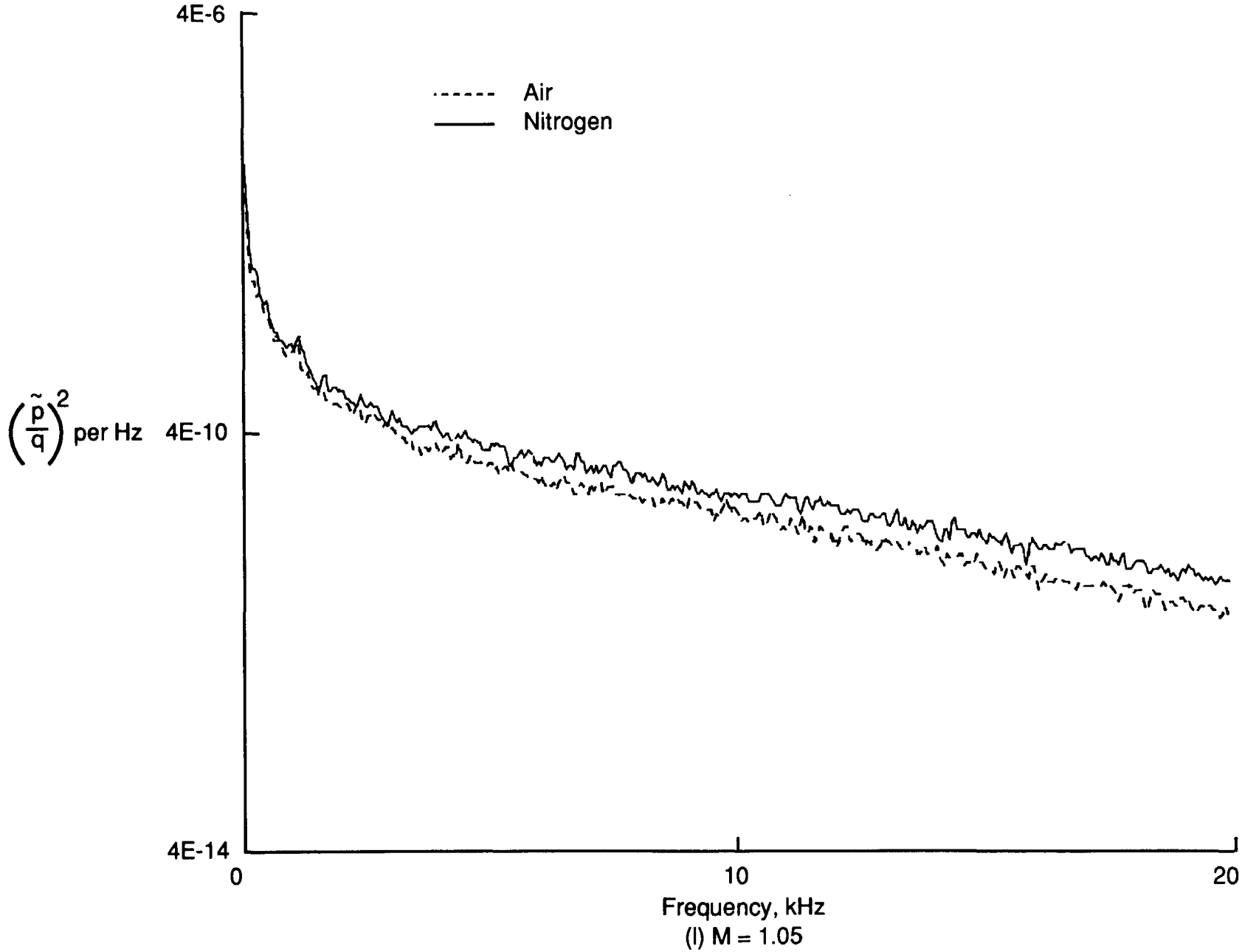

Figure 51. Concluded.

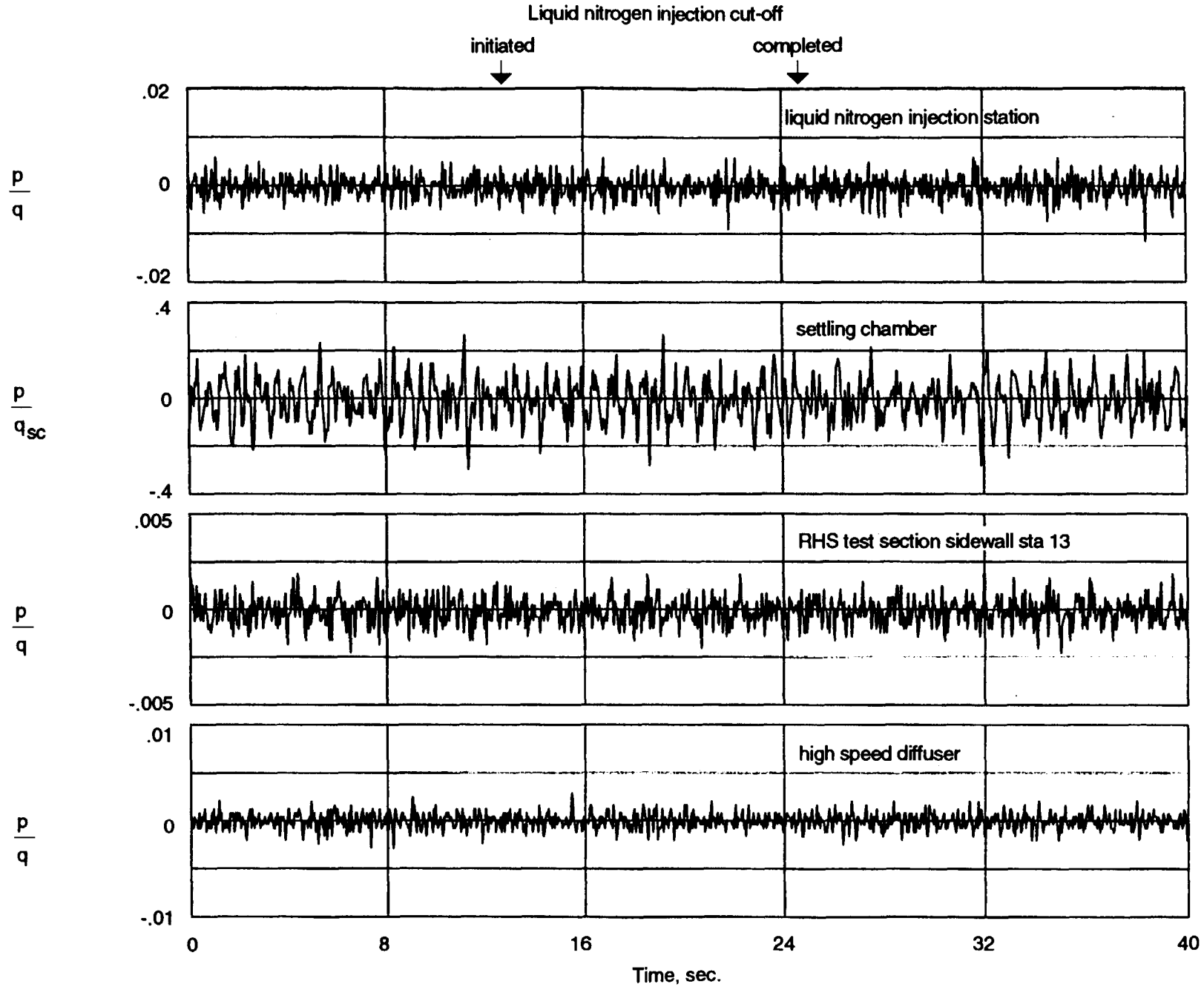

Figure 52. Time history traces of the fluctuating static pressure coefficient at four tunnel stations during cut-off of liquid nitrogen injection, M = 0.8, P_t = 20 psi, T_t = -160°F at initiation.

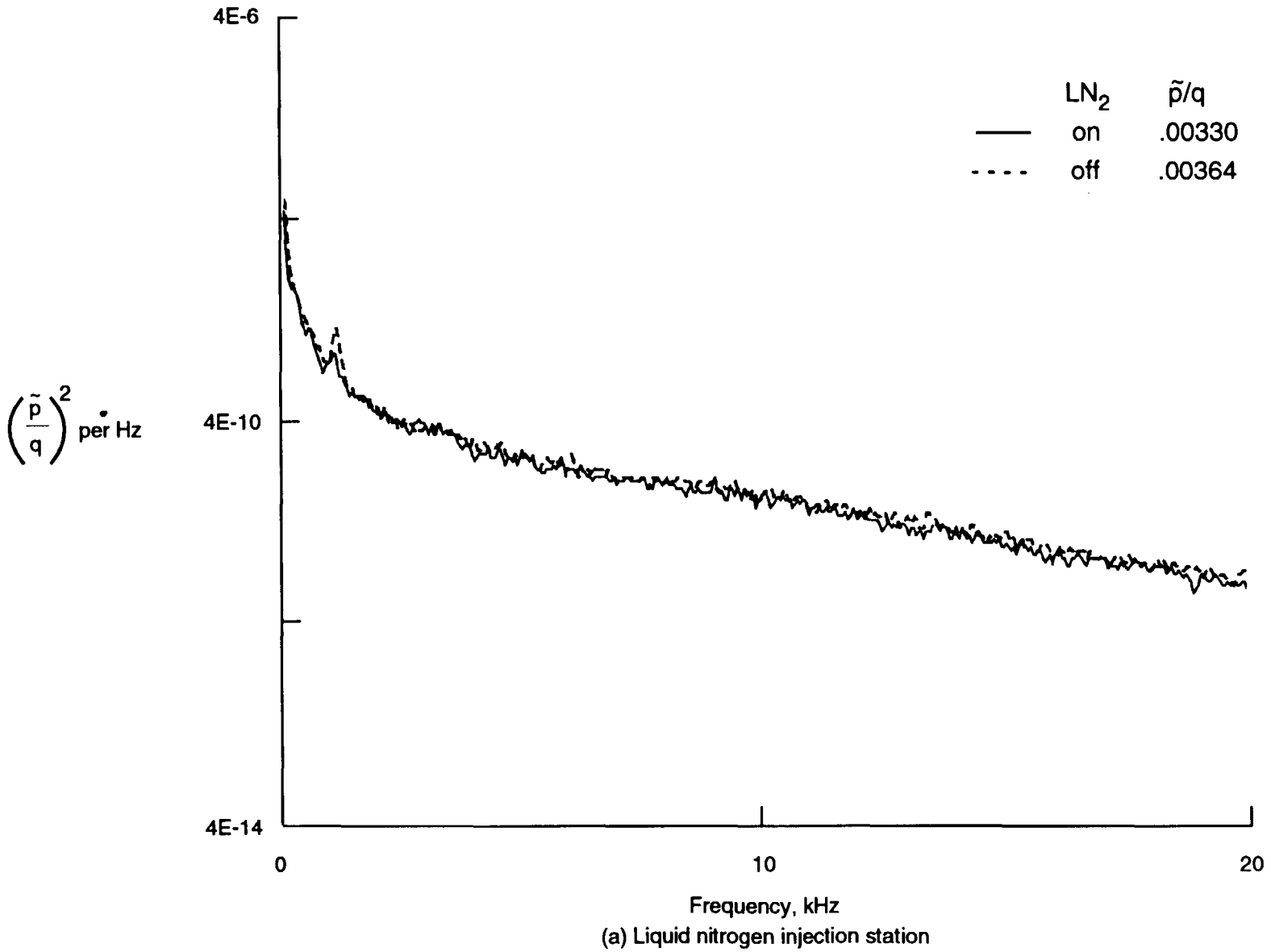

Figure 53. Power spectra of fluctuating pressure coefficient before and after cut-off of liquid nitrogen injection, M = 0.8, P_t = 20 psi, T_t = -160° before cut-off.

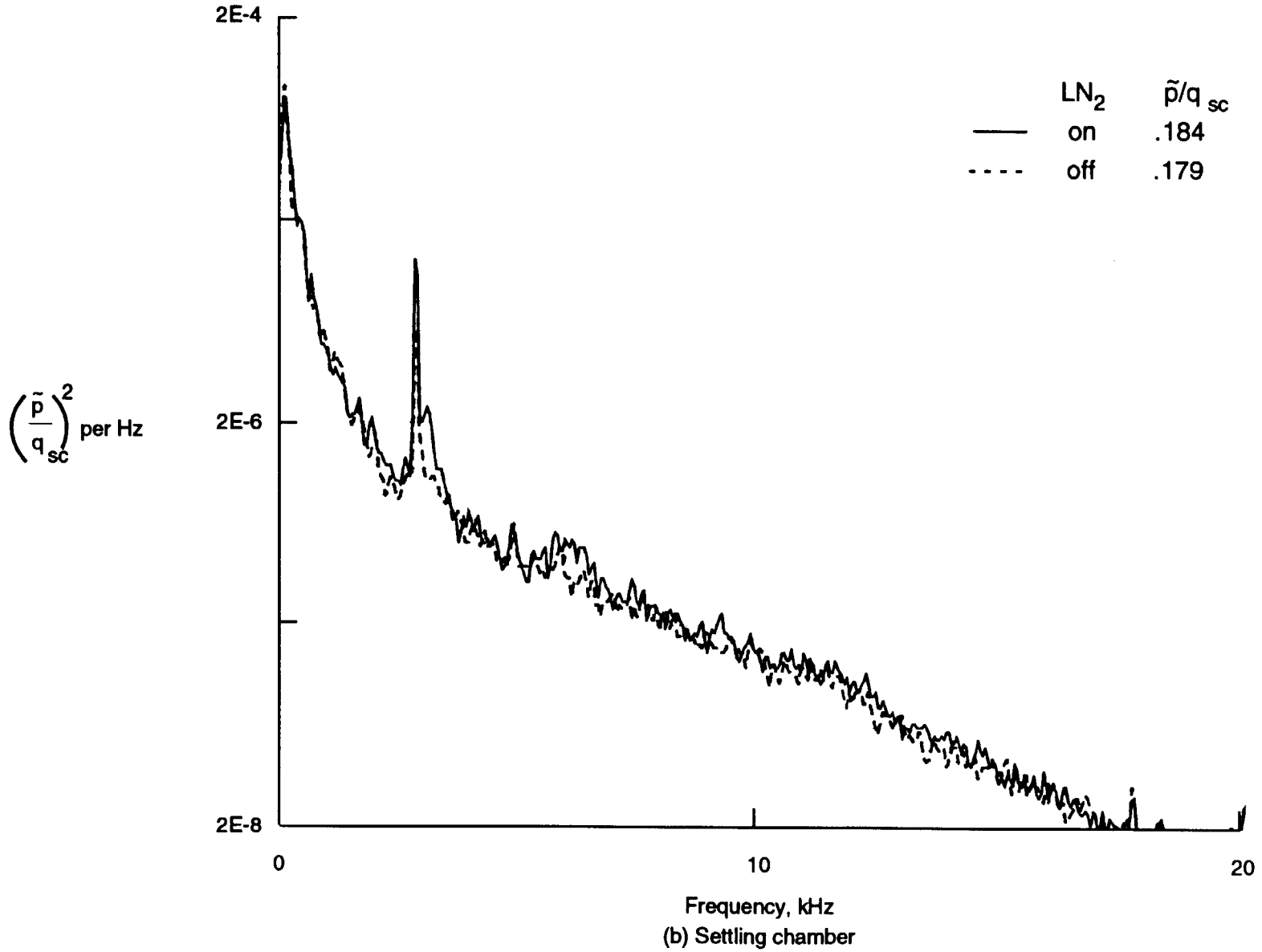

Figure 53. Continued.

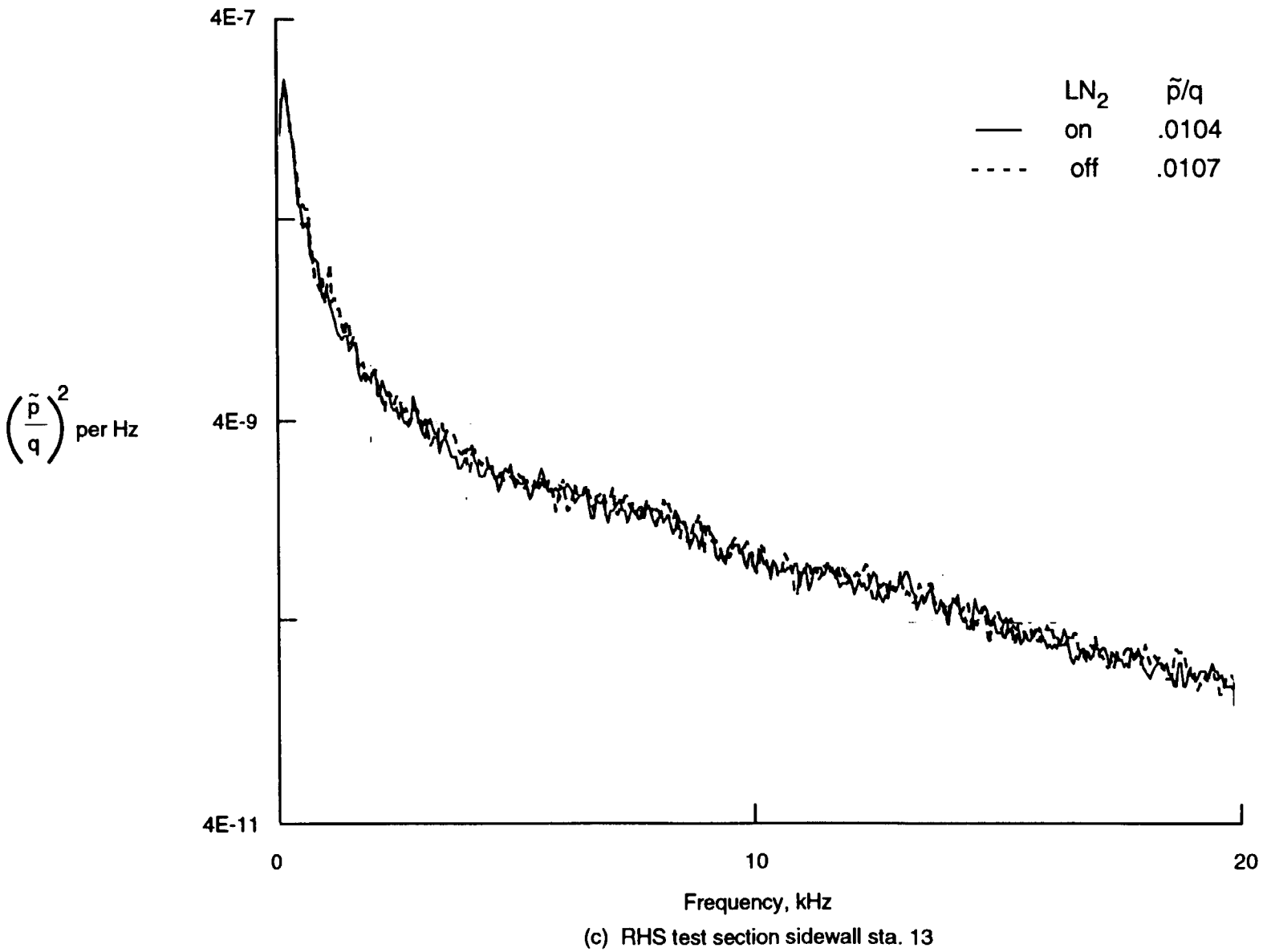

(c) RHS test section sidewall sta. 13

Figure 53. Continued.

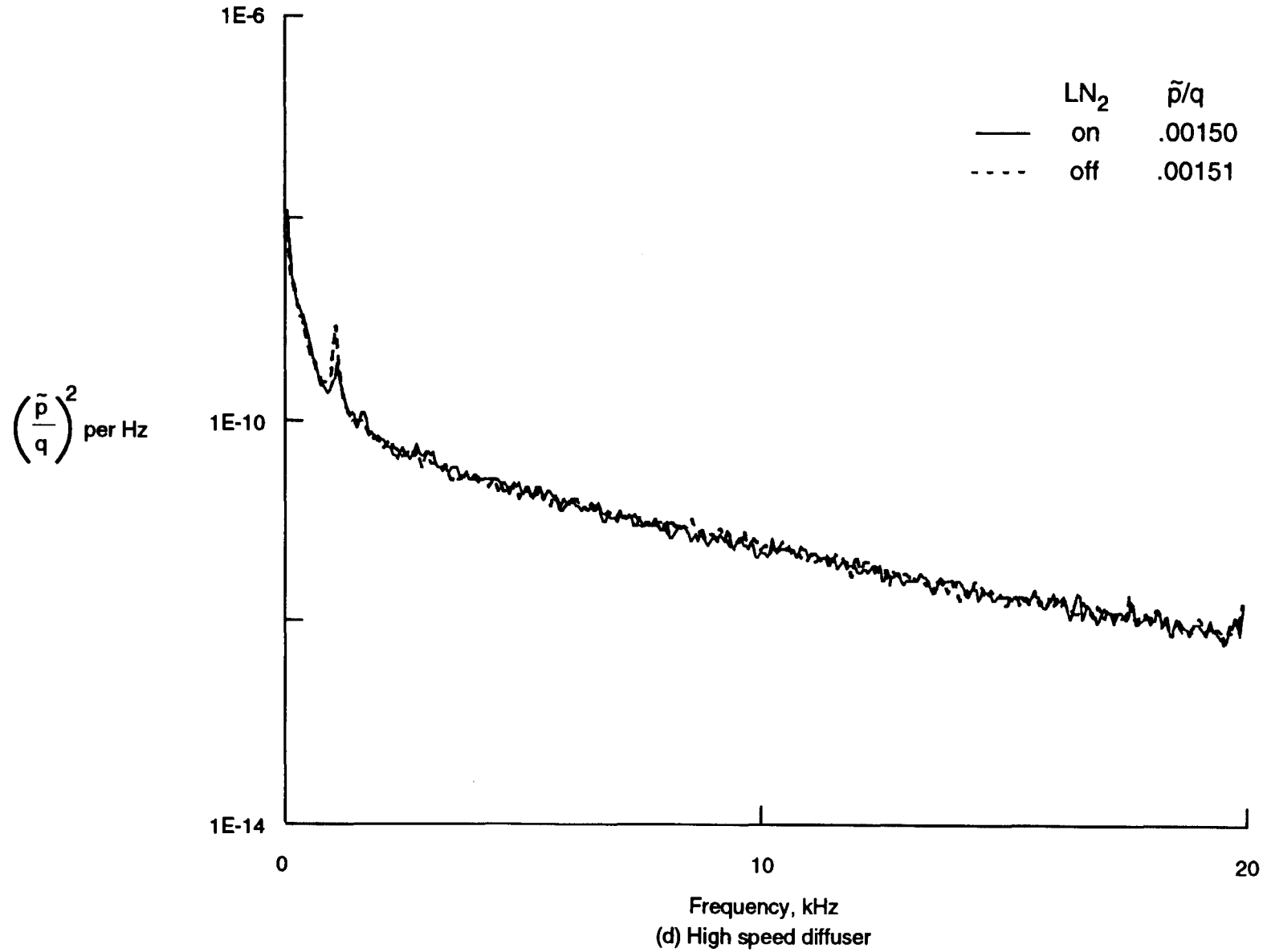

Figure 53. Concluded.

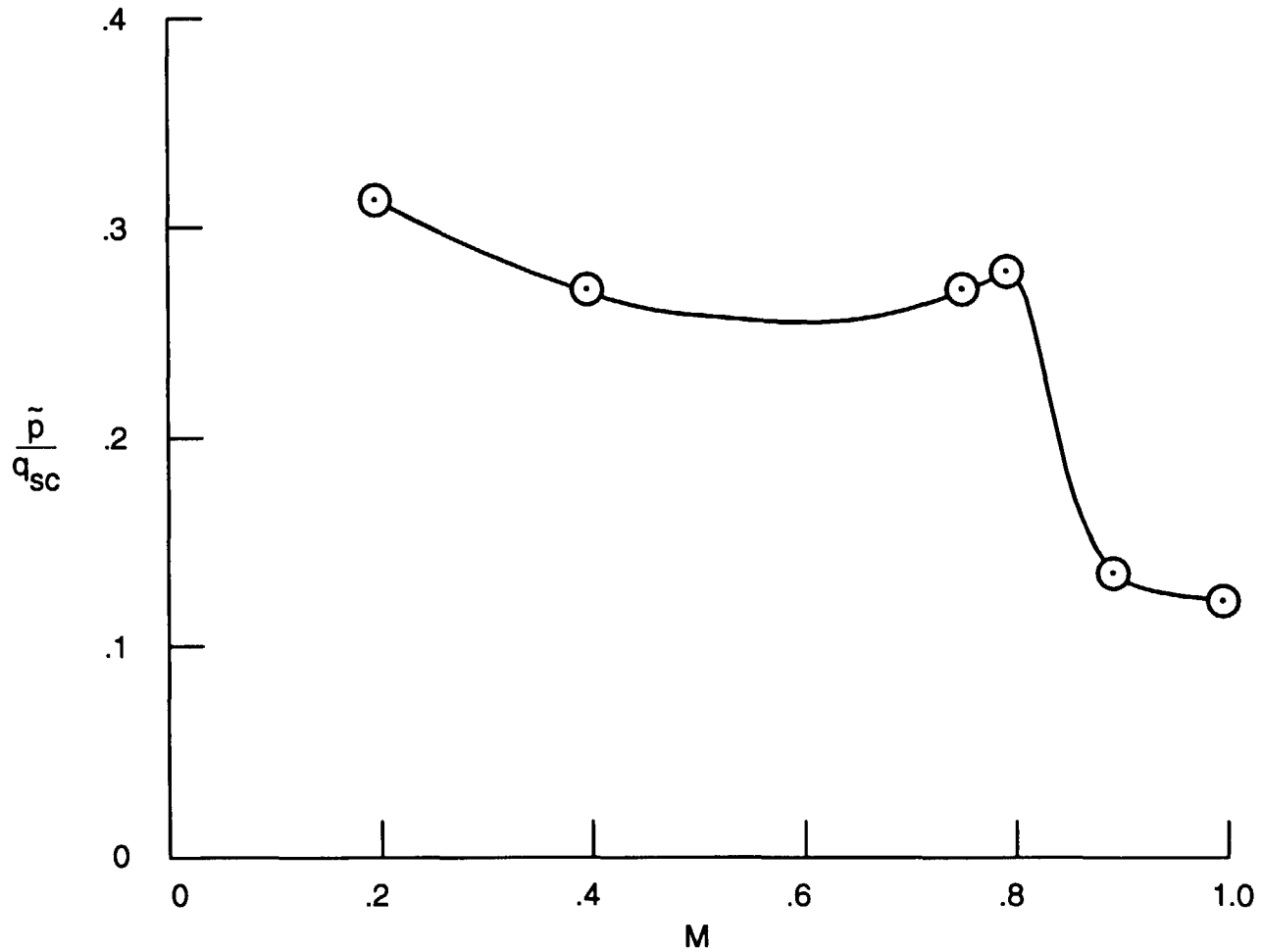

Figure 54. Fluctuating pressure coefficient in settling chamber for maximum Reynolds number boundary.

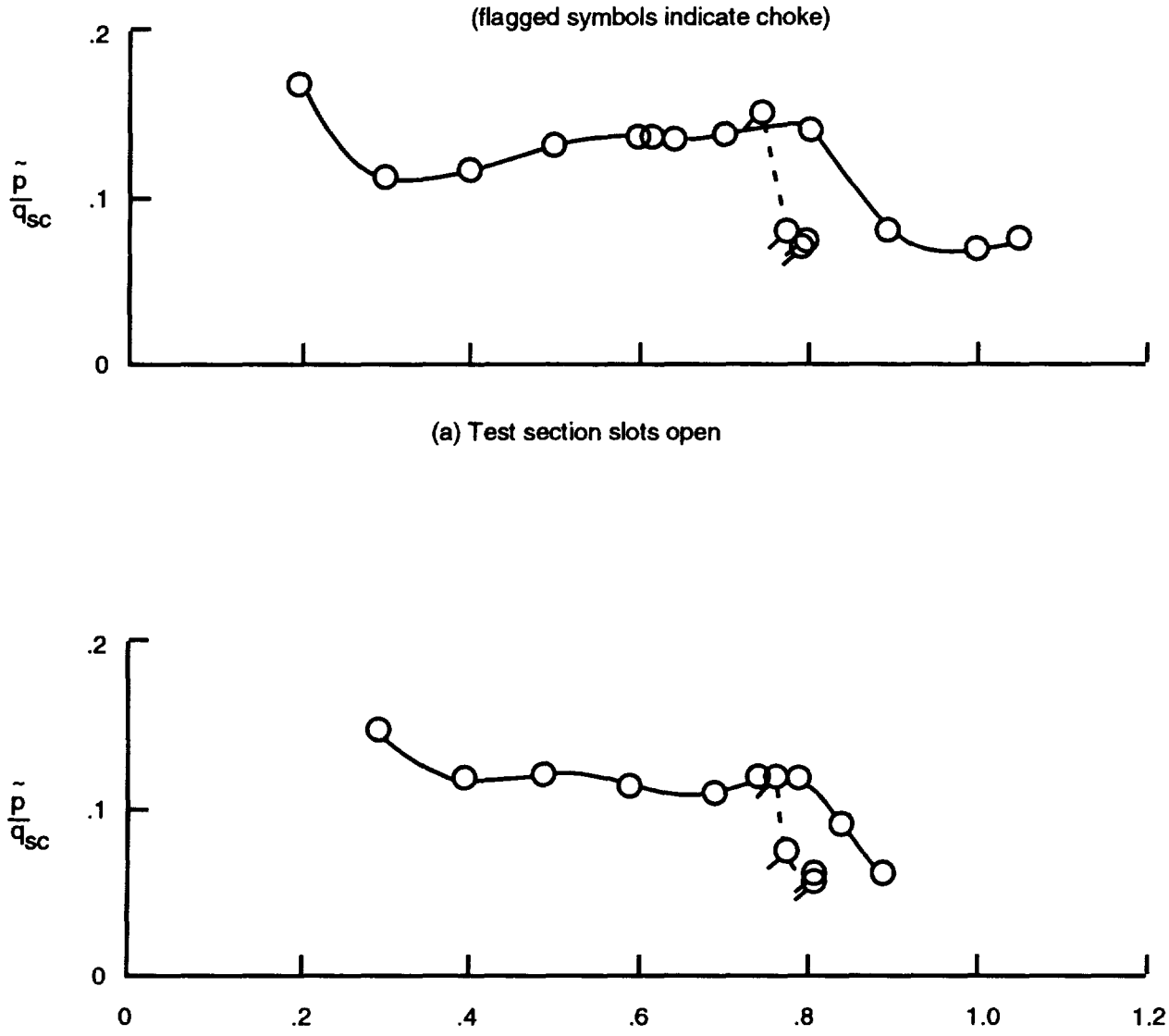

Figure 55. Fluctuating pressure coefficient in settling chamber for minimum Reynolds number boundary, air, choked and unchoked.

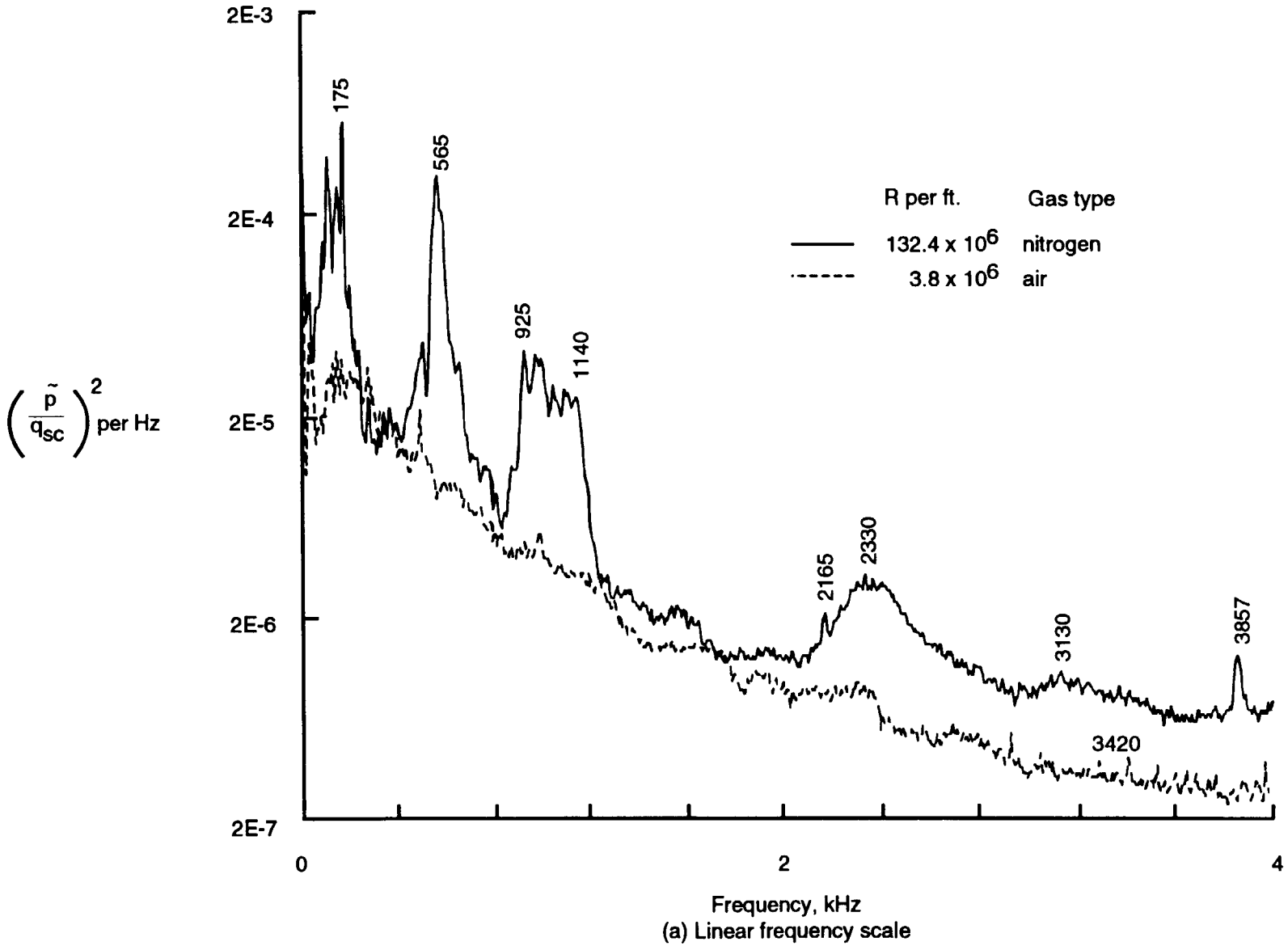

Figure 56. Power spectra of fluctuating pressure coefficient in settling chamber at M = 0.8 for minimum and maximum Reynolds number boundaries.

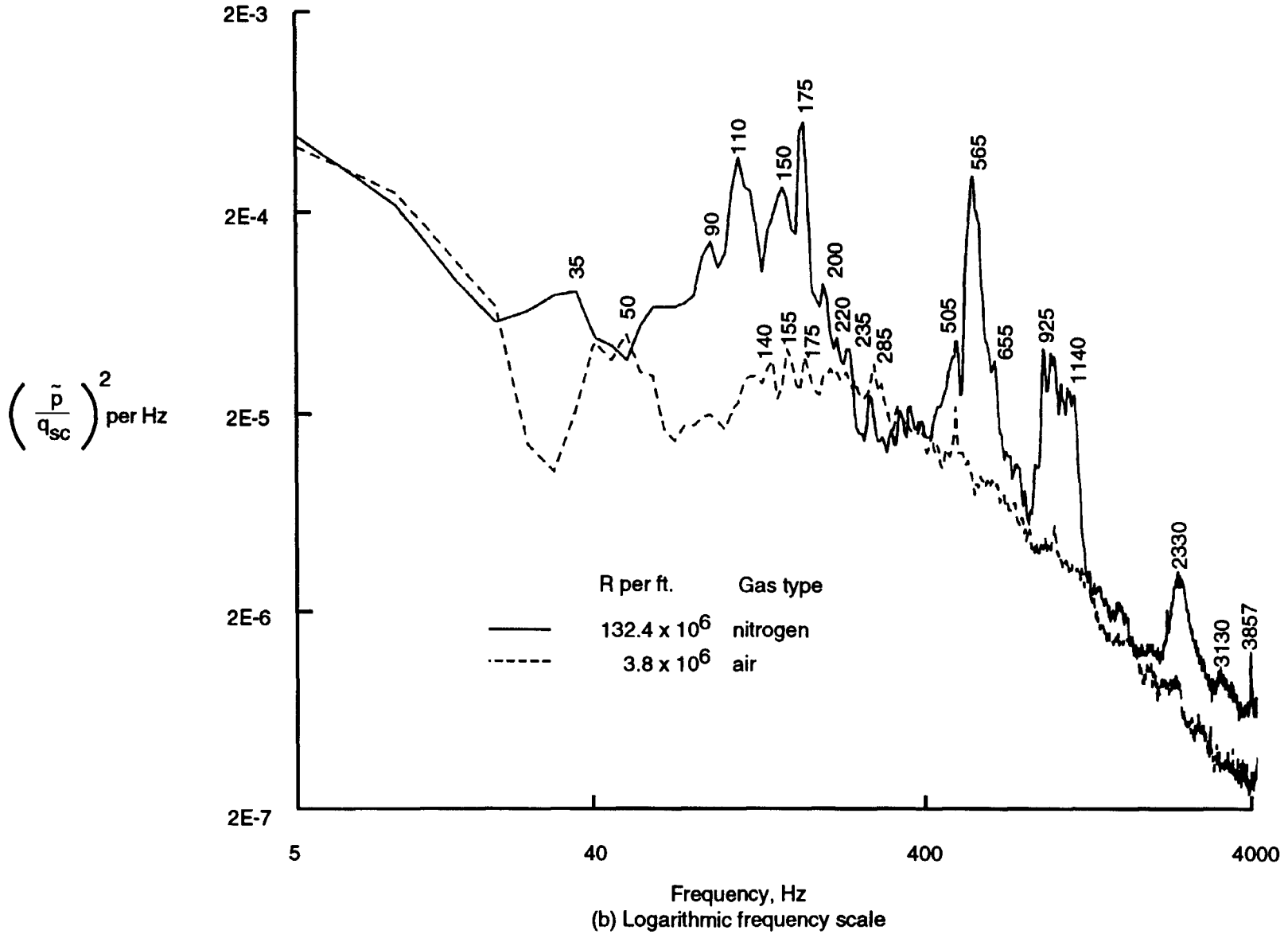

Figure 56. Concluded

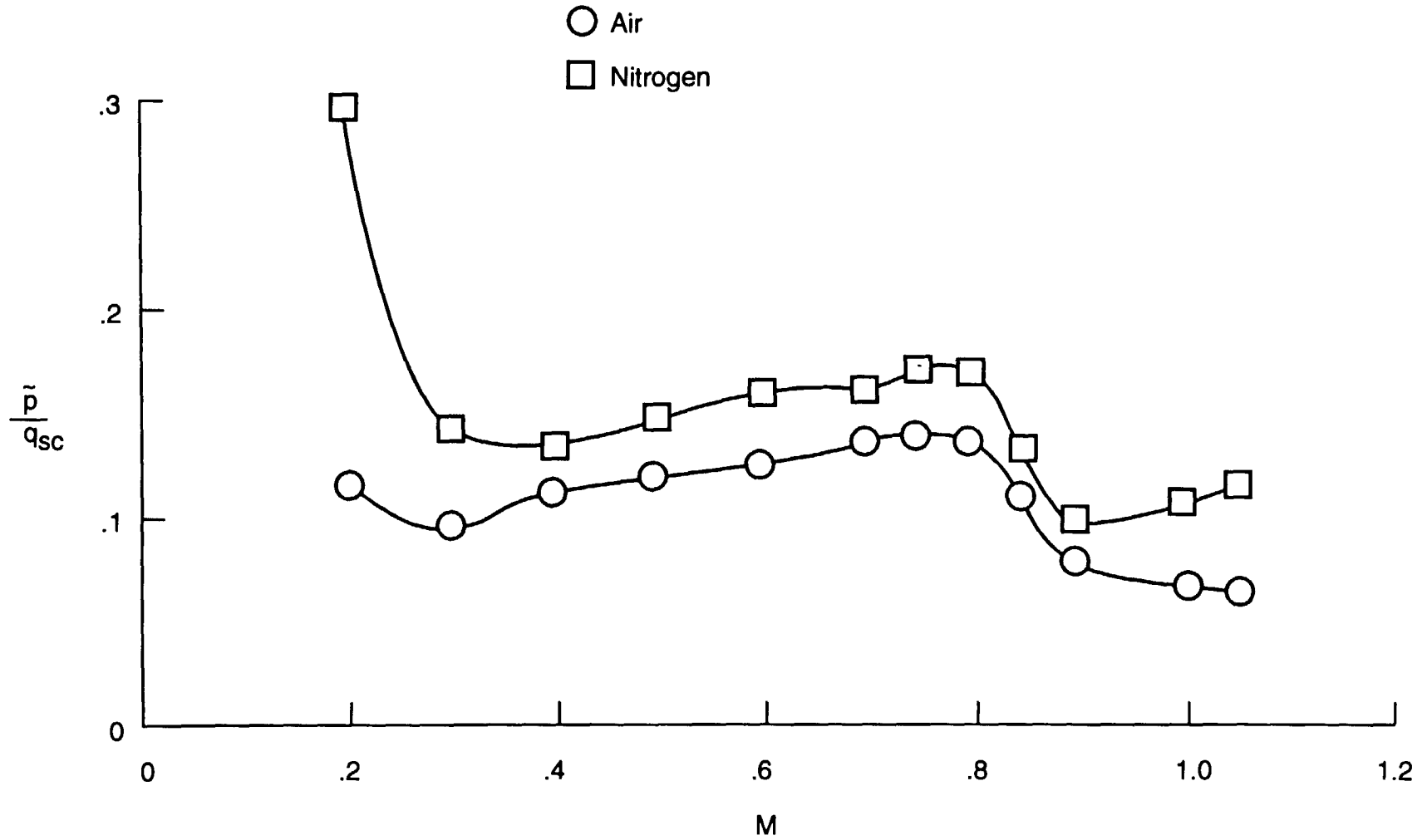

Figure 57. Fluctuating pressure coefficient in settling chamber at R = 6×10^6/ft, ambient temperature, comparison between air and nitrogen.

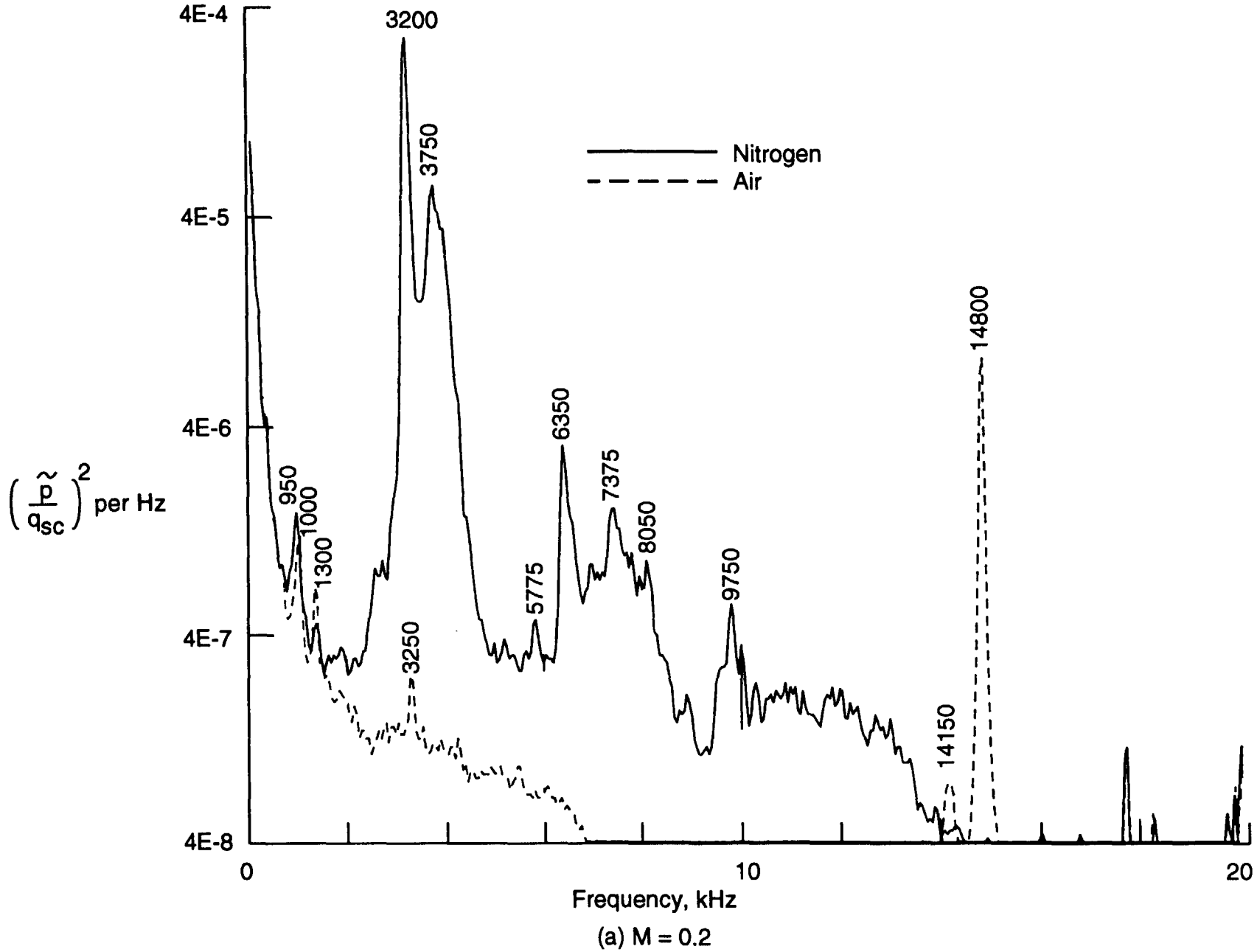

Figure 58. Power spectra of fluctuating pressure coefficient in settling chamber at R= 6 x 10^6/ft., ambient temperature, comparison between air and nitrogen.

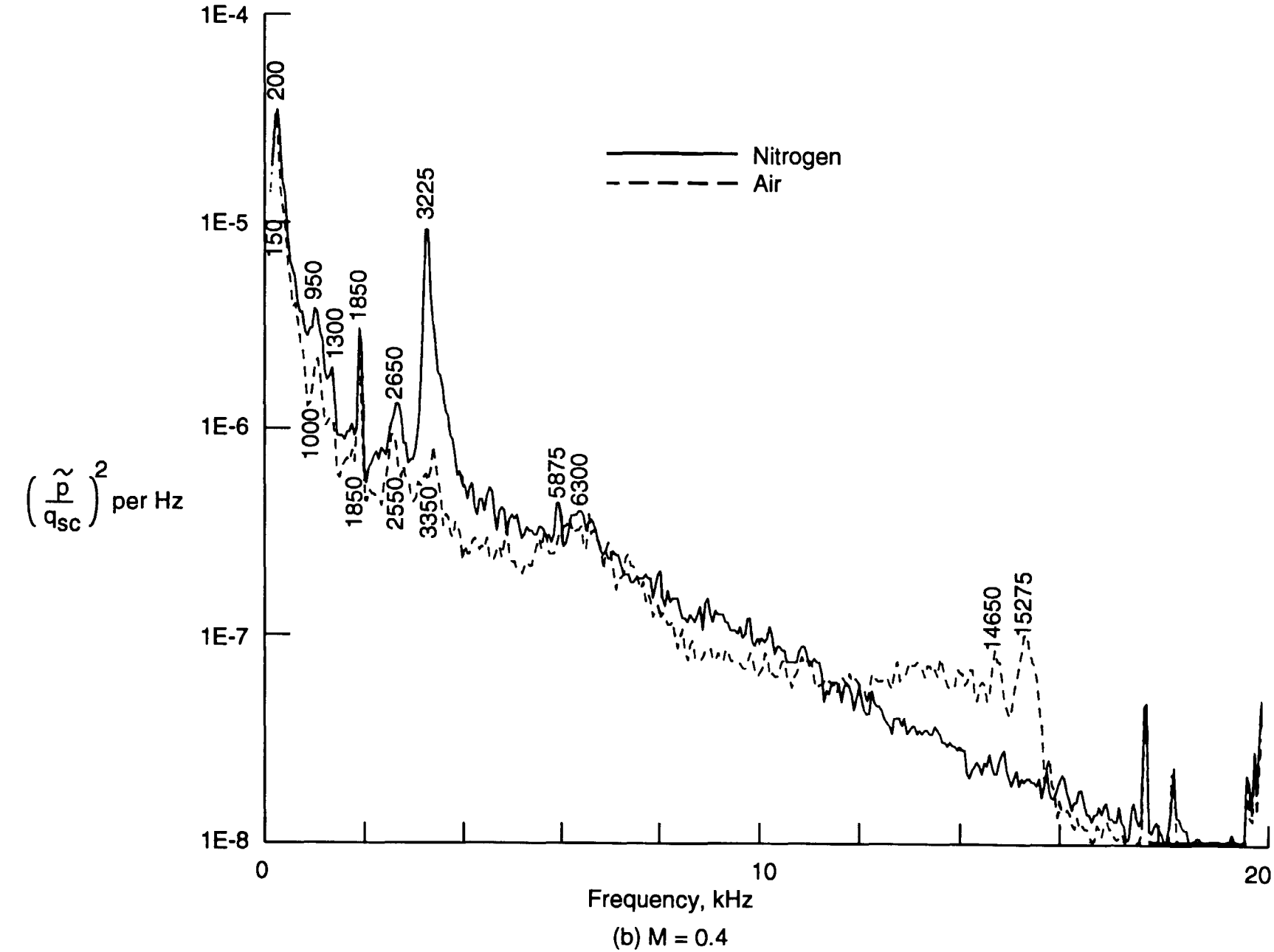

(b) M = 0.4

Figure 58. Continued

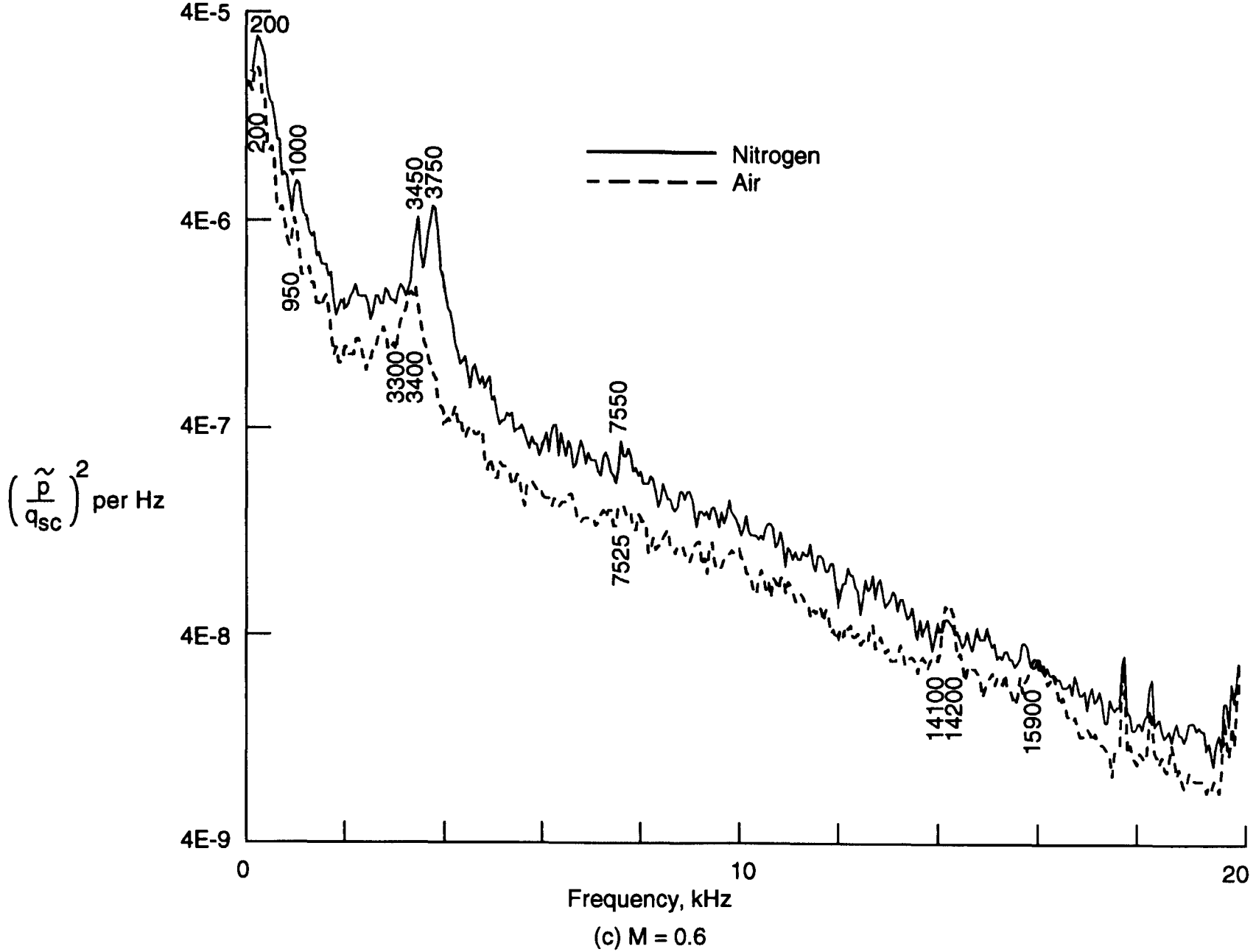

(c) M = 0.6

Figure 58. Continued

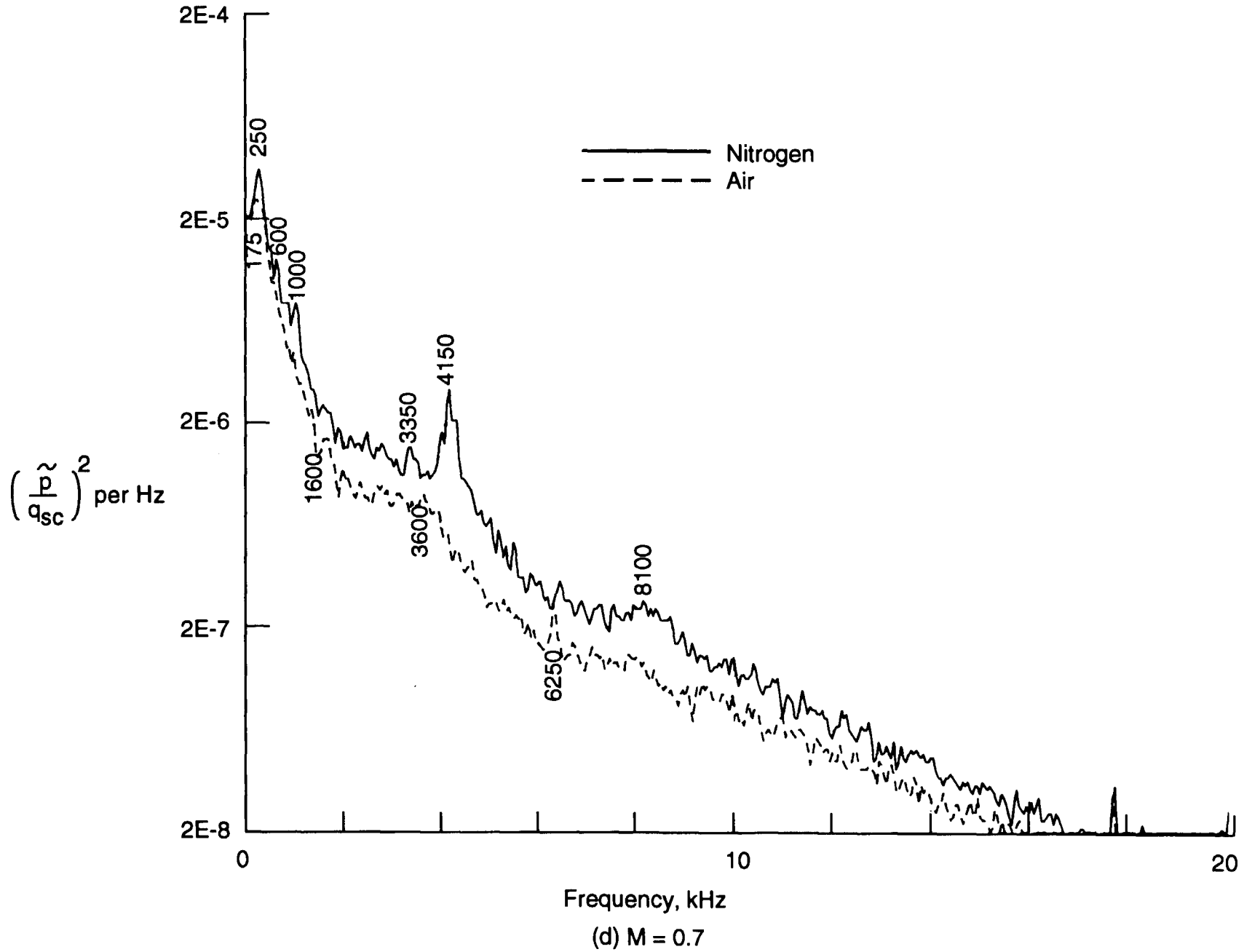

(d) M = 0.7

Figure 58. Continued

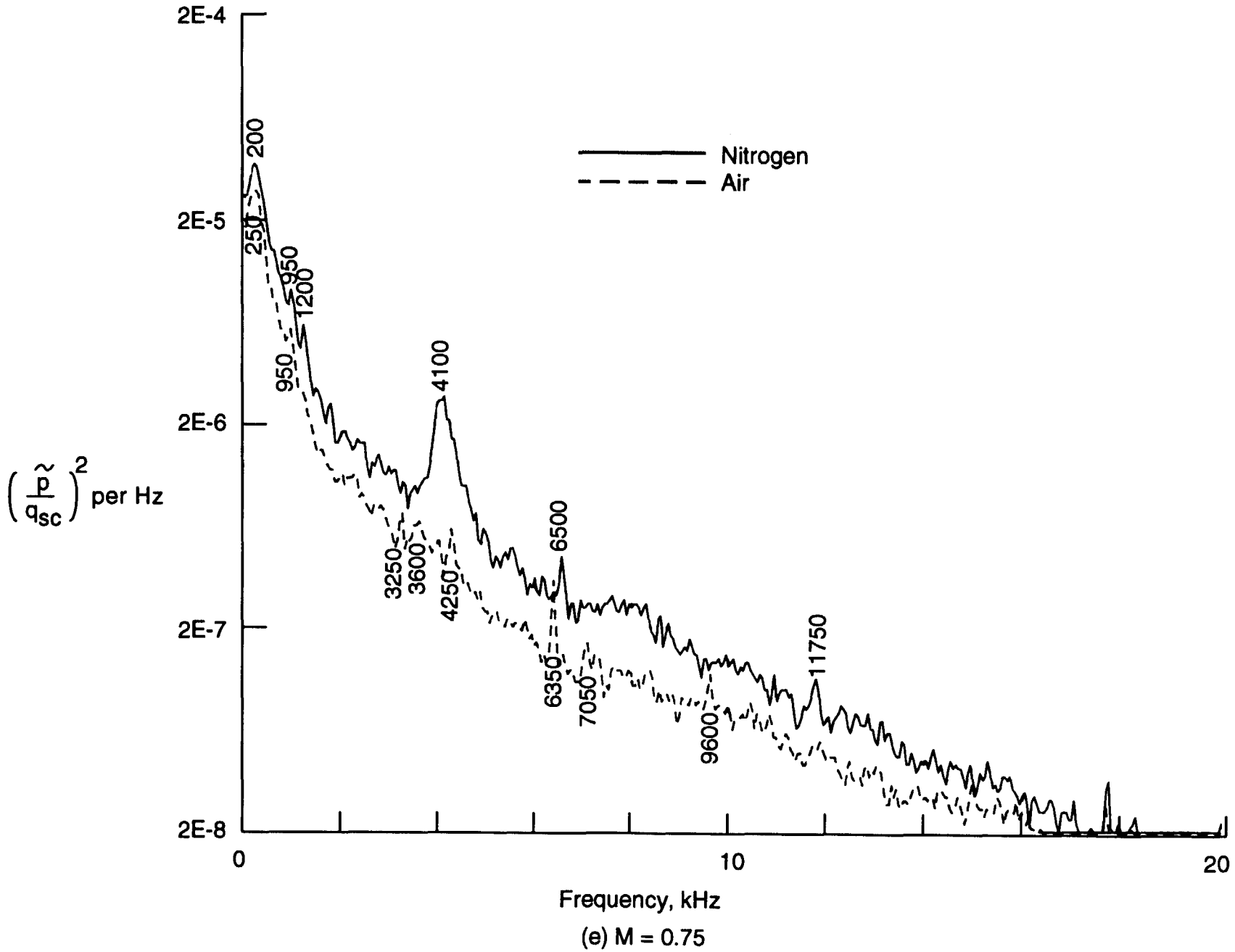

Figure 58. Continued

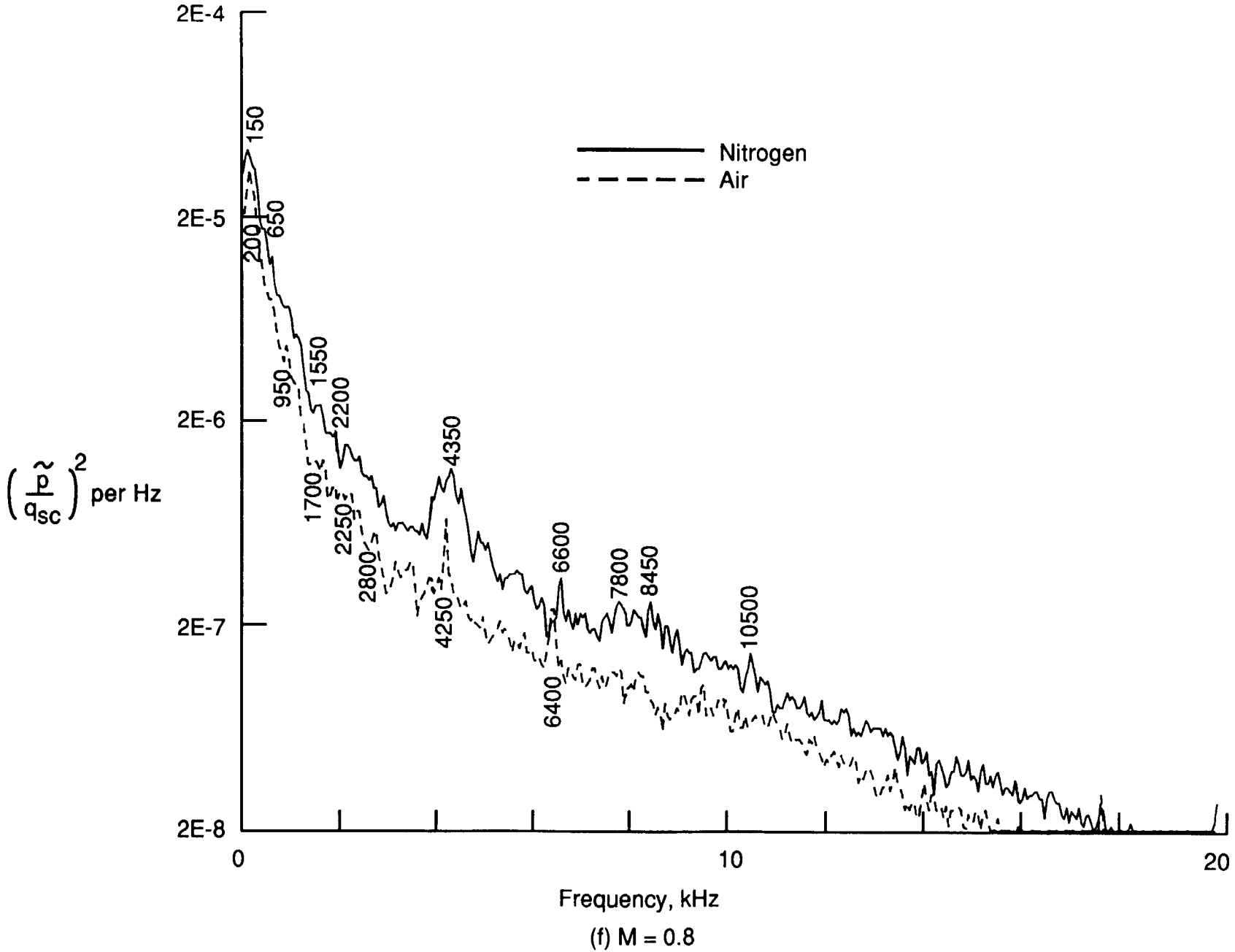

(f) M = 0.8

Figure 58. Continued

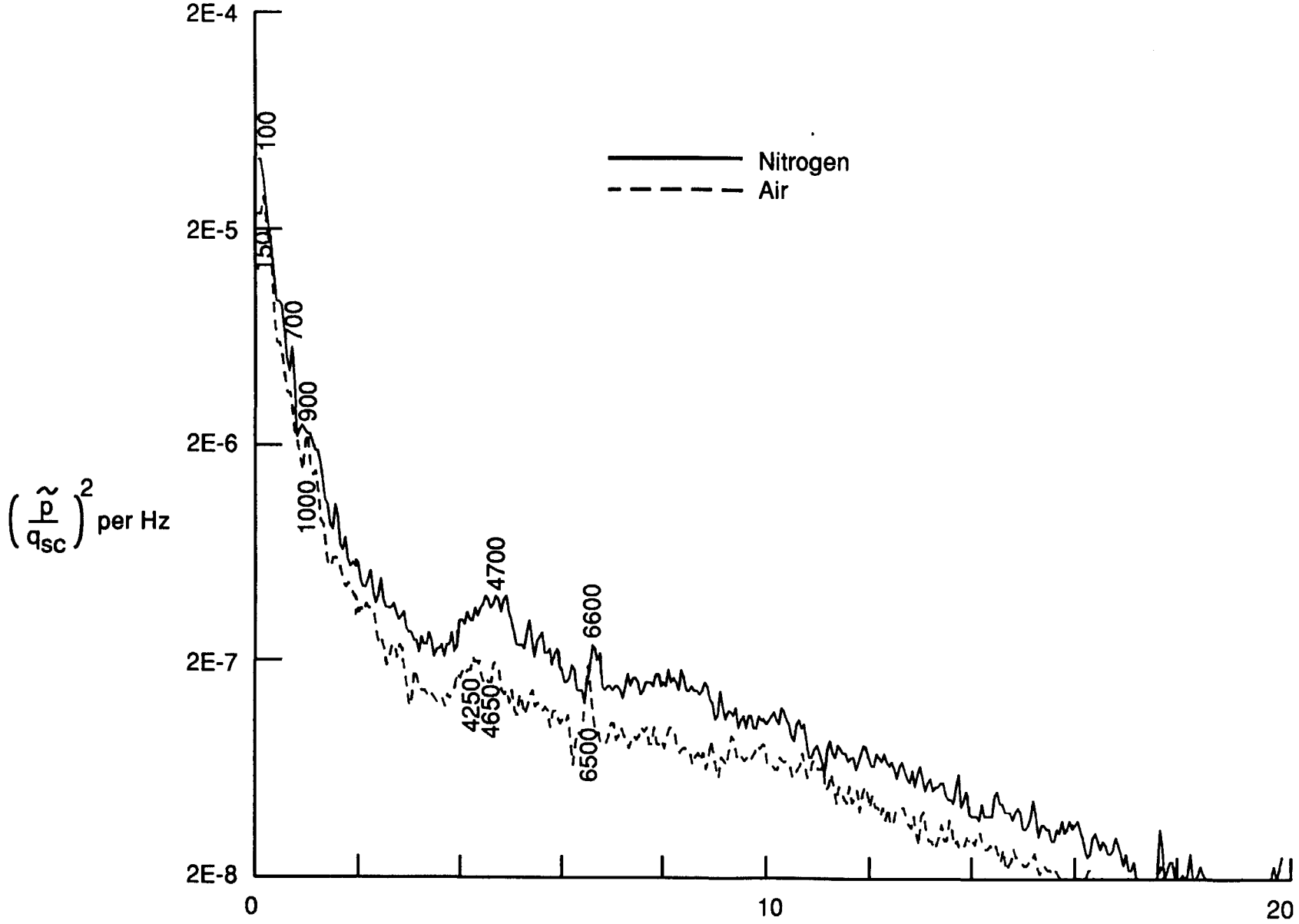

(g) M = 0.85

Figure 58. Continued

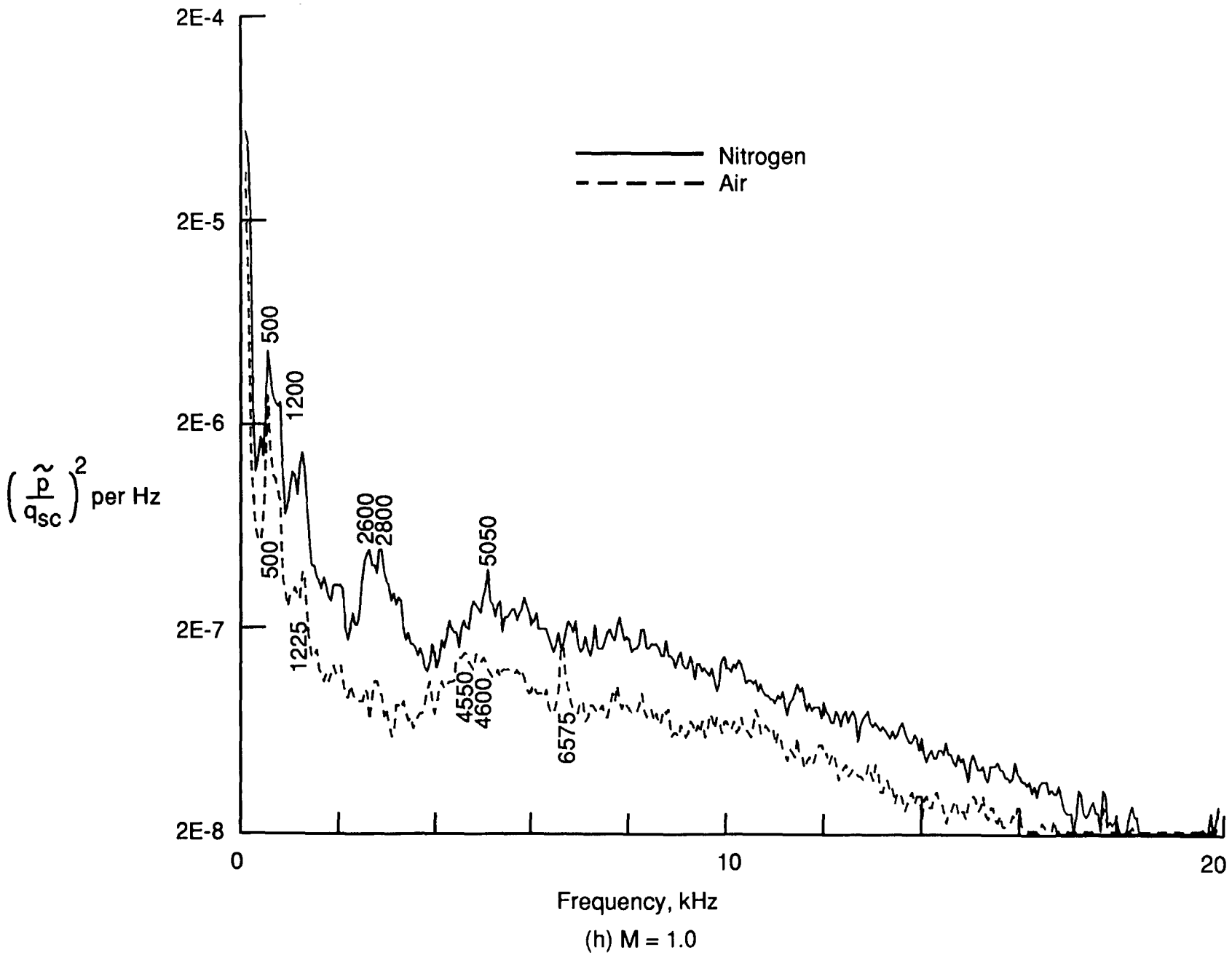

(h) M = 1.0

Figure 58. Continued

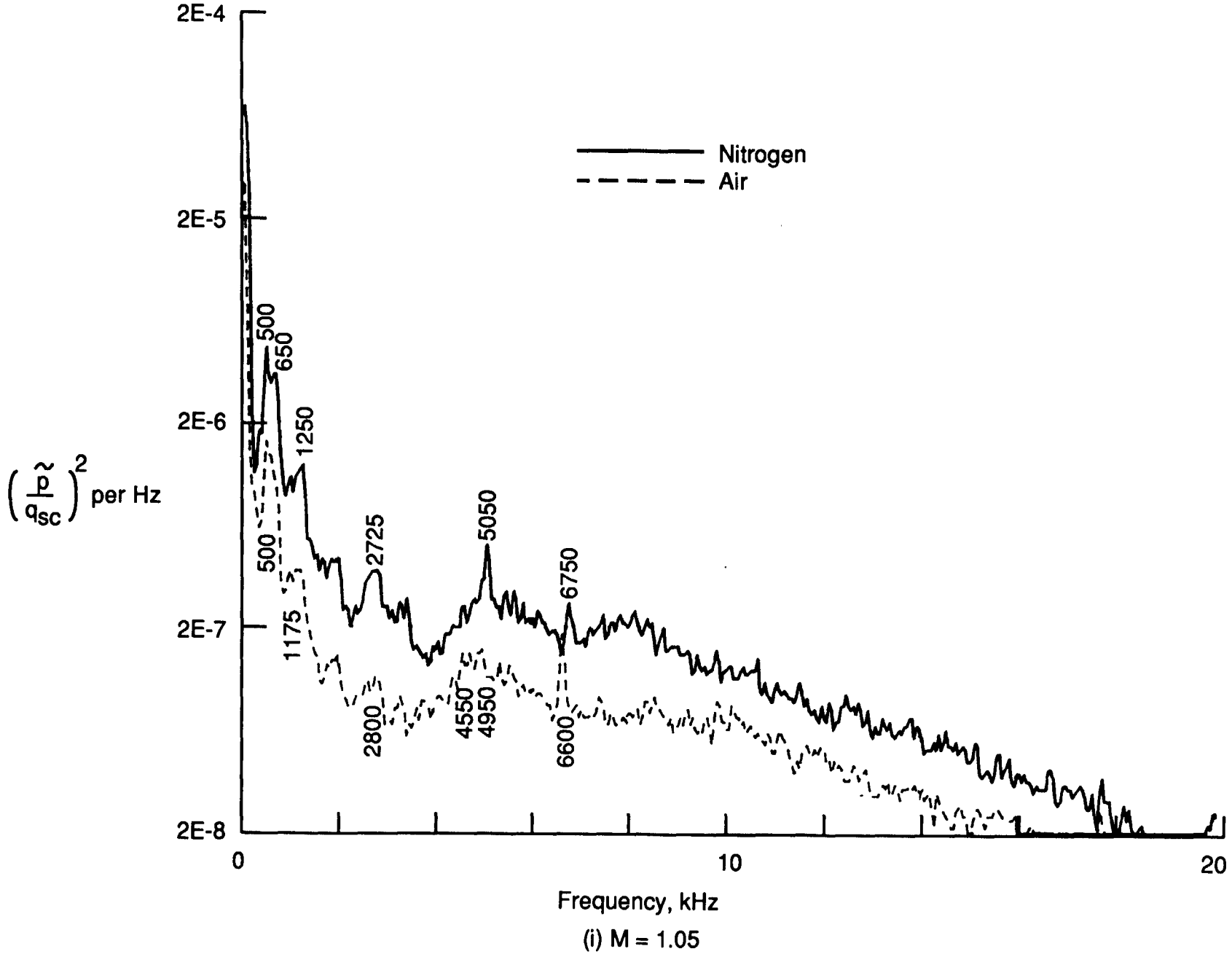

Figure 58. Concluded.

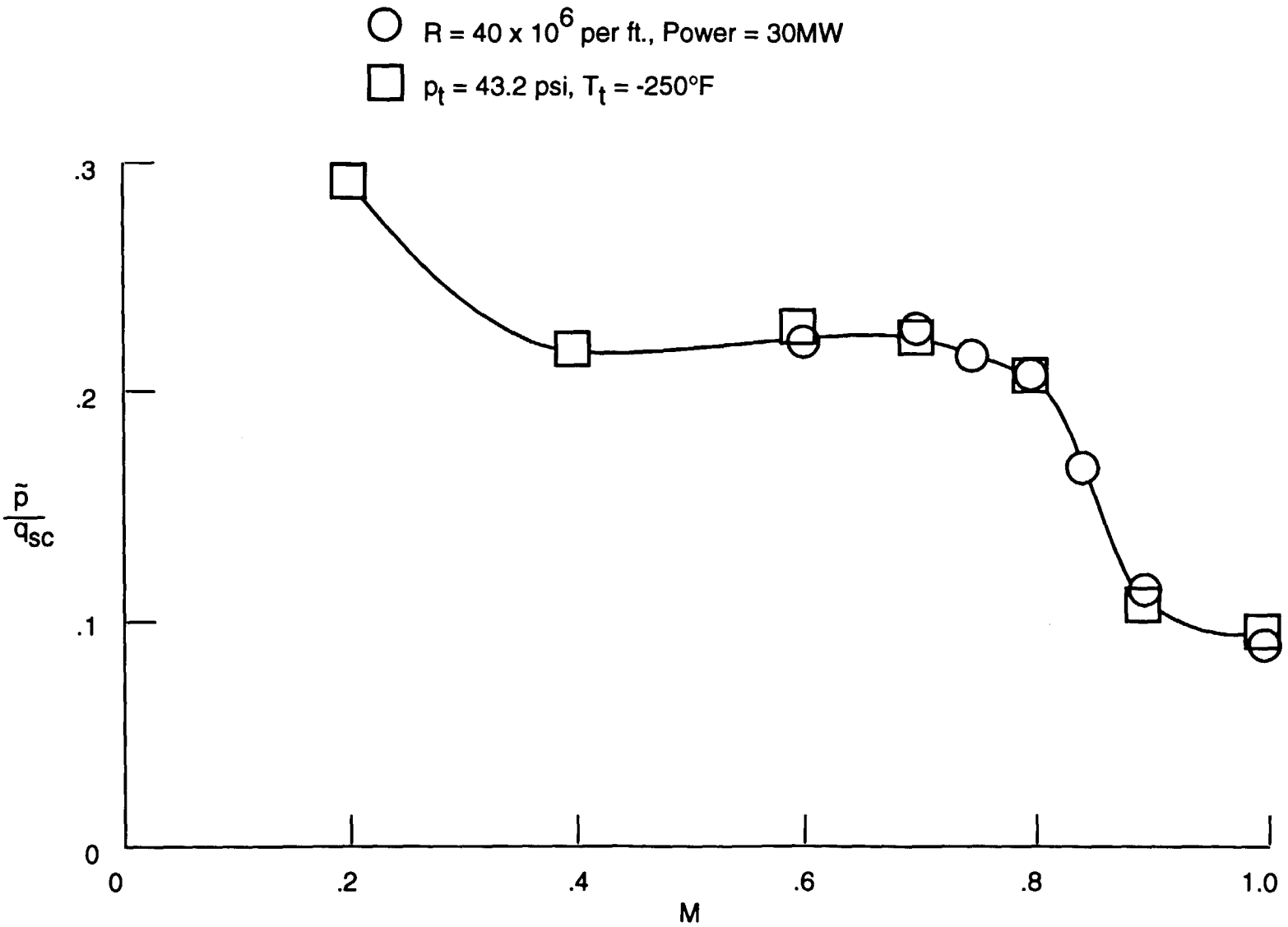

Figure 59. Fluctuating pressure coefficient in settling chamber as a function of test section Mach number, nitrogen mode.

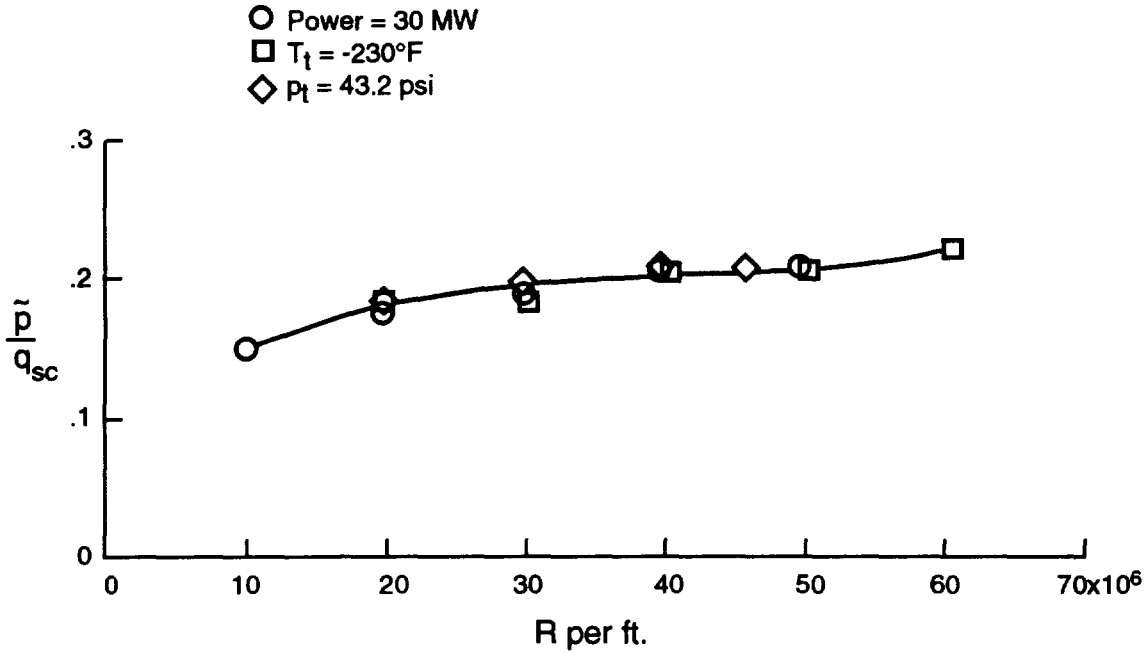

Figure 60. Fluctuating pressure coefficient in settling chamber as a function of test section Reynolds number at M = 0.8.

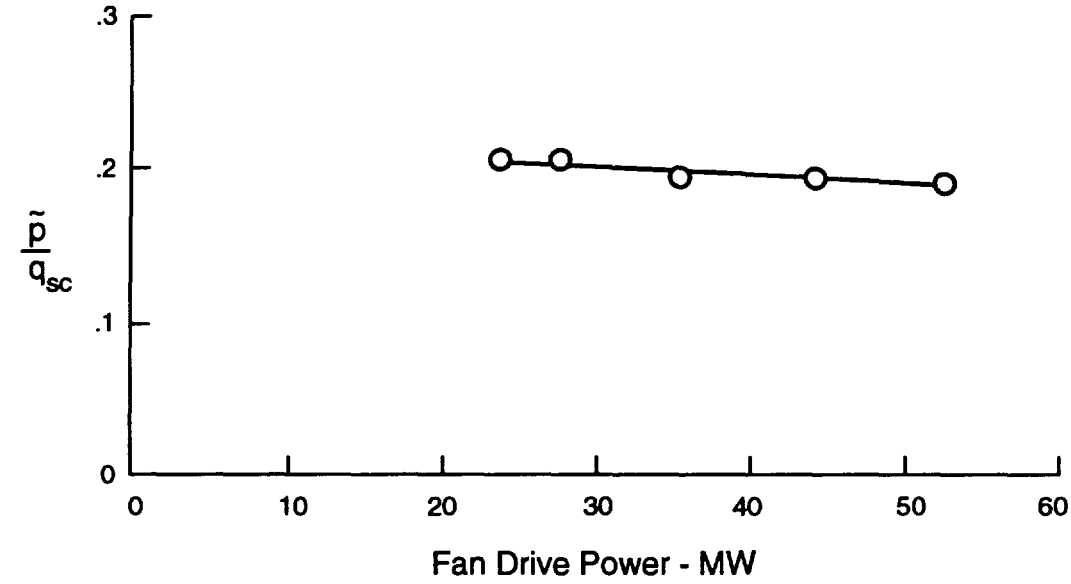

Figure 61. Fluctuating pressure coefficient in settling chamber for test section M = 0.8, R = 40x10⁶ per ft., effect of fan drive power.

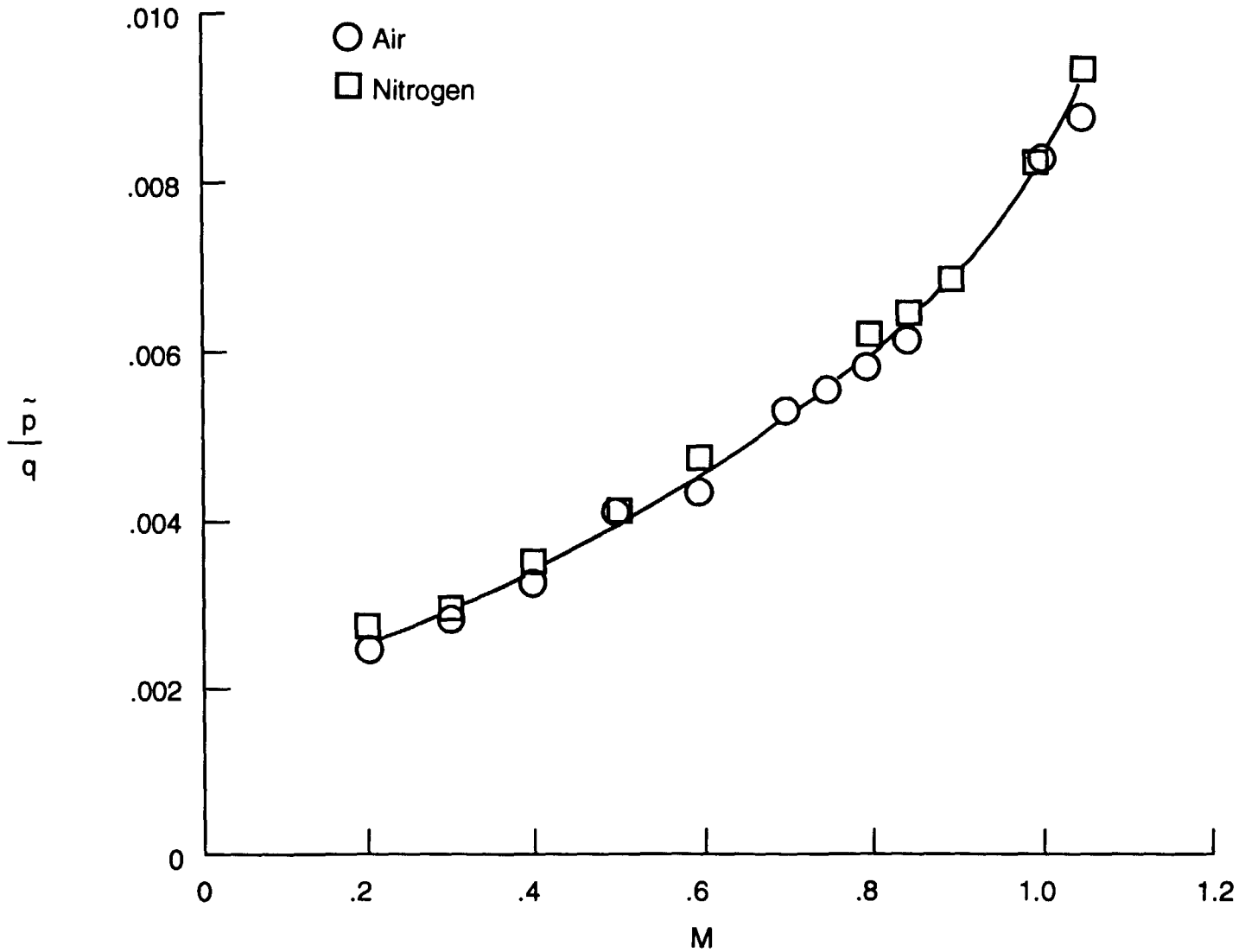

Figure 62. Fluctuating pressure coefficient in high speed diffuser as a function of test section Mach number for R = $6x10^6$ per ft., comparison of air and nitrogen at ambient temperature.

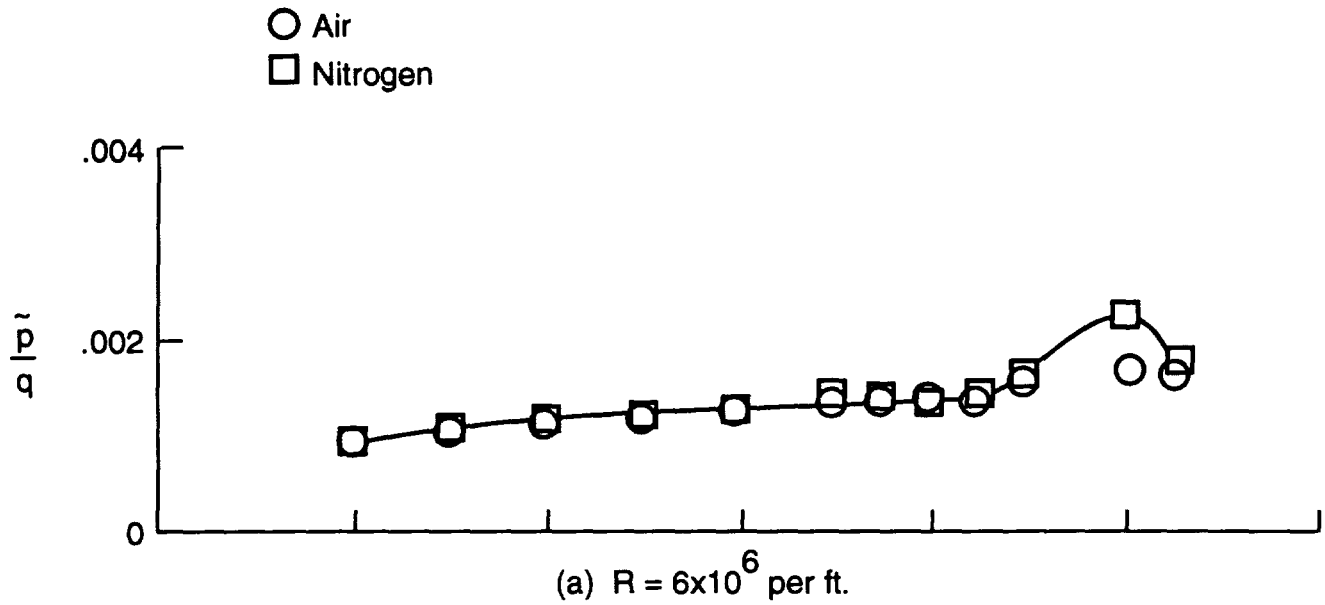

(a) R = 6×10^6 per ft.

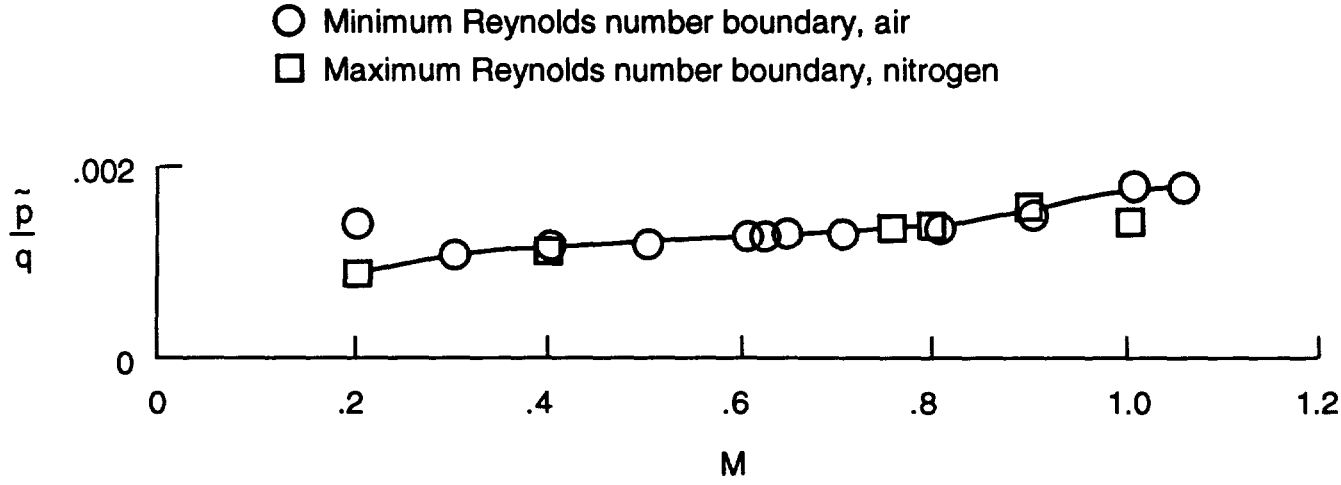

(b) Minimum and maximum Reynolds number boundary.

Figure 63. Fluctuating pressure coefficient in plenum.

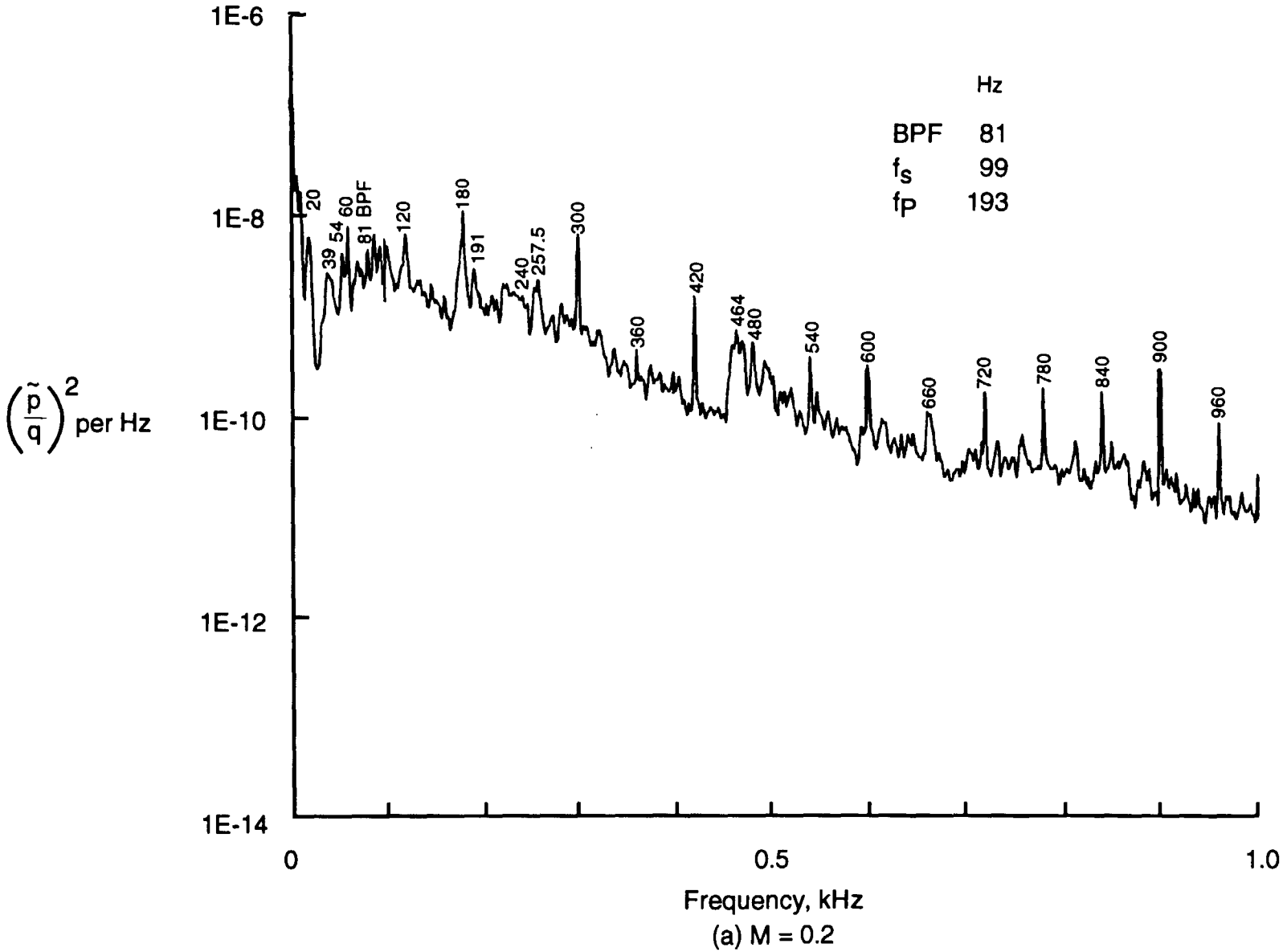

Figure 64. Power spectra of fluctuating pressure coefficient in plenum, minimum Reynolds number boundary, air.

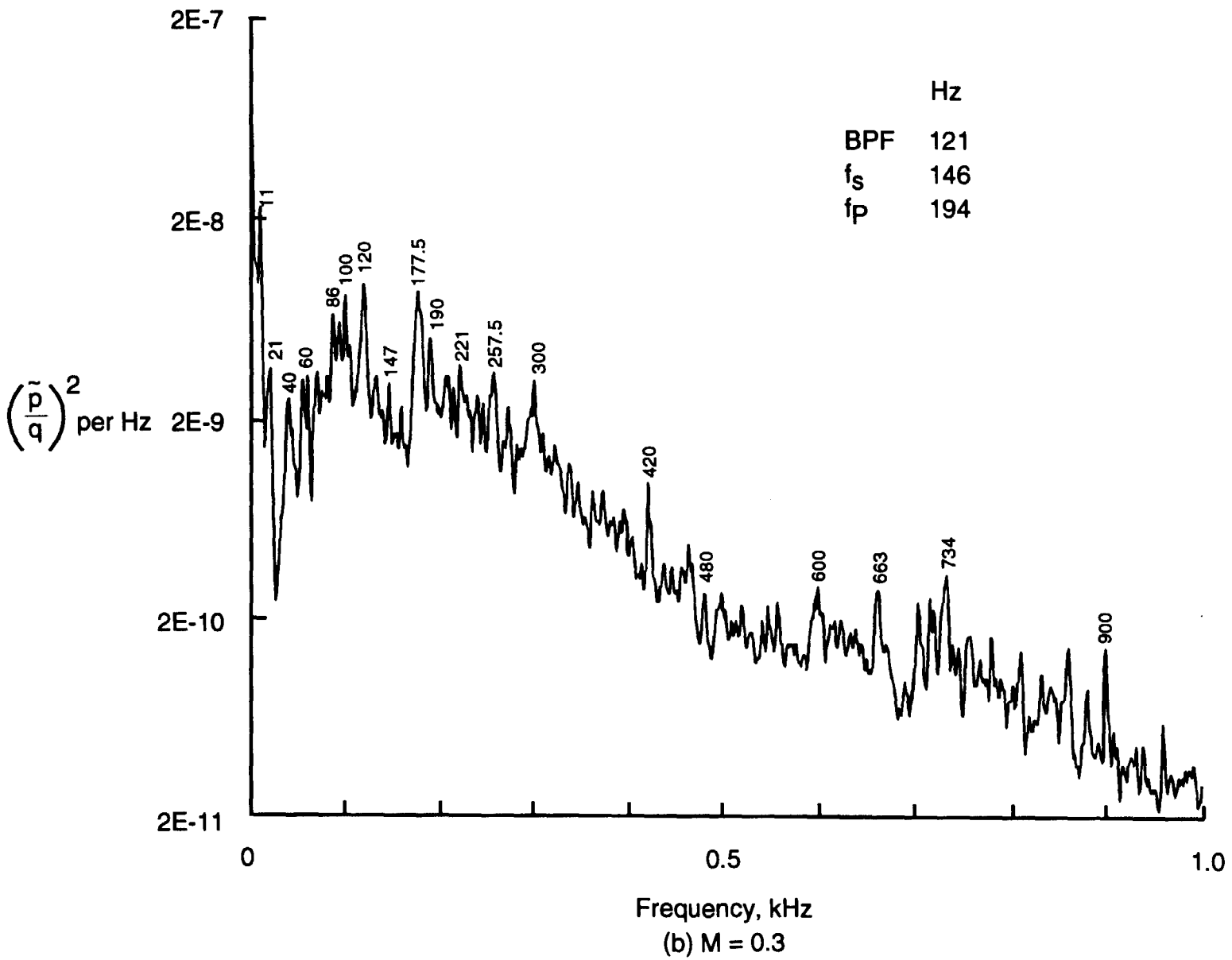

Figure 64. Continued

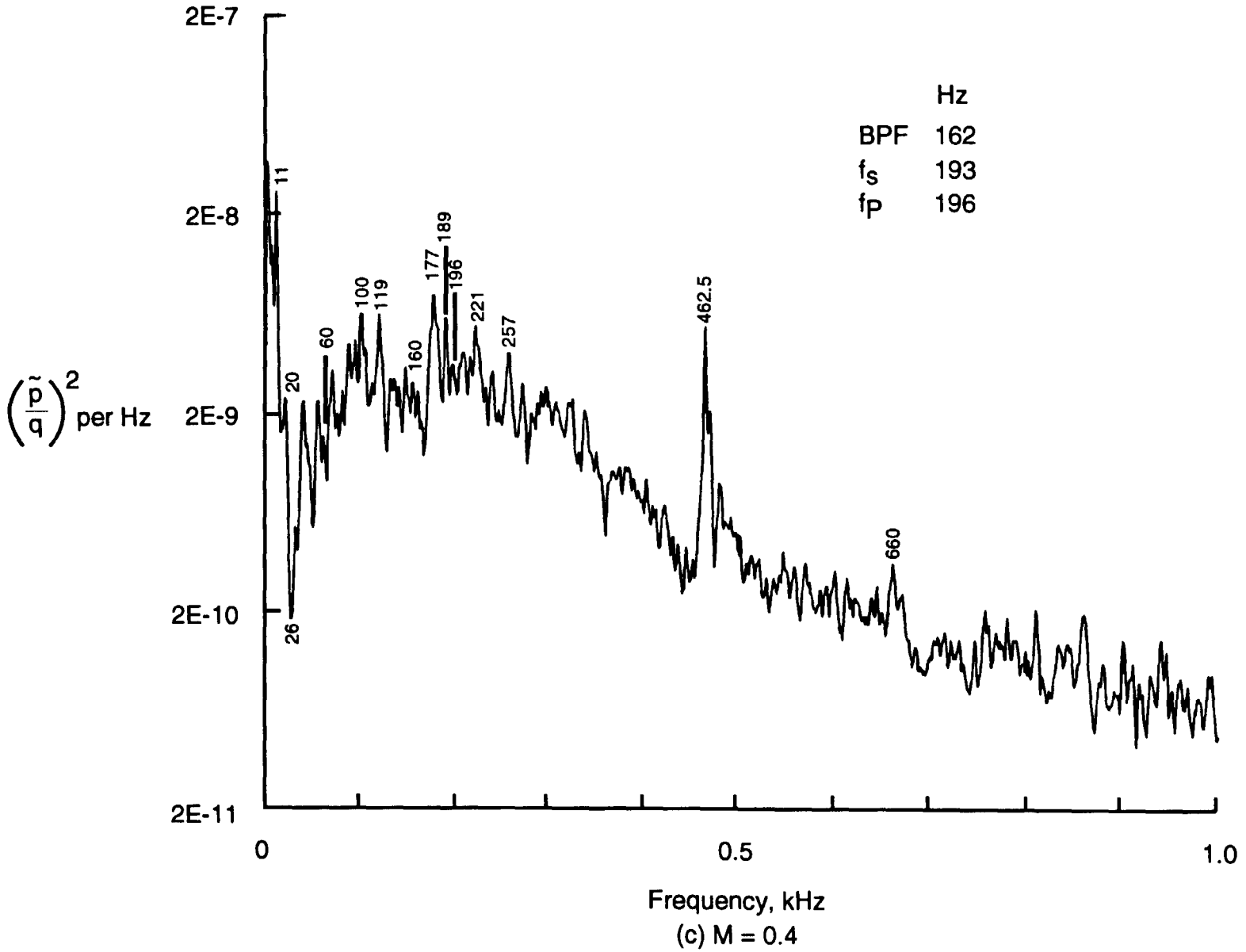

Figure 64. Continued

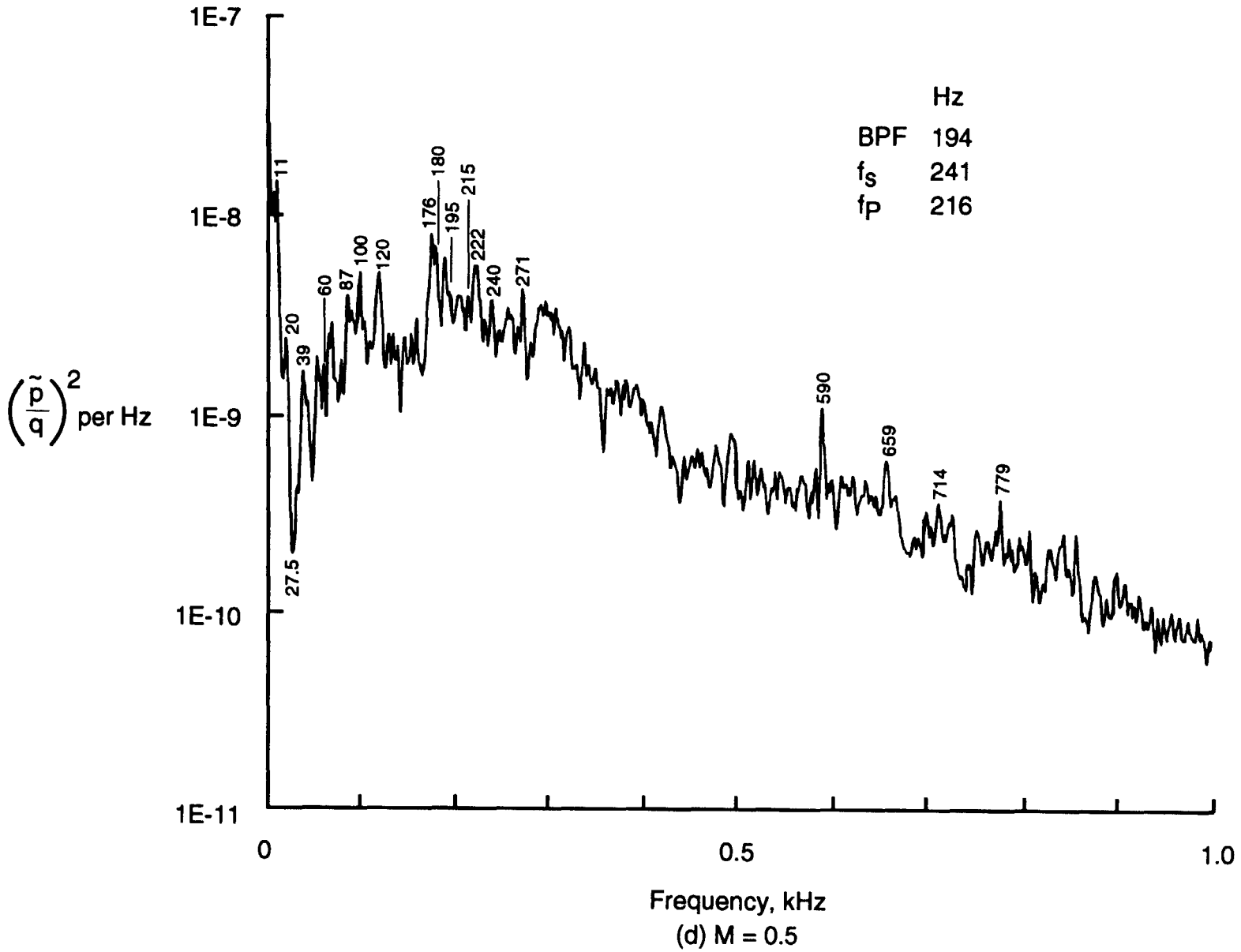

Figure 64. Continued

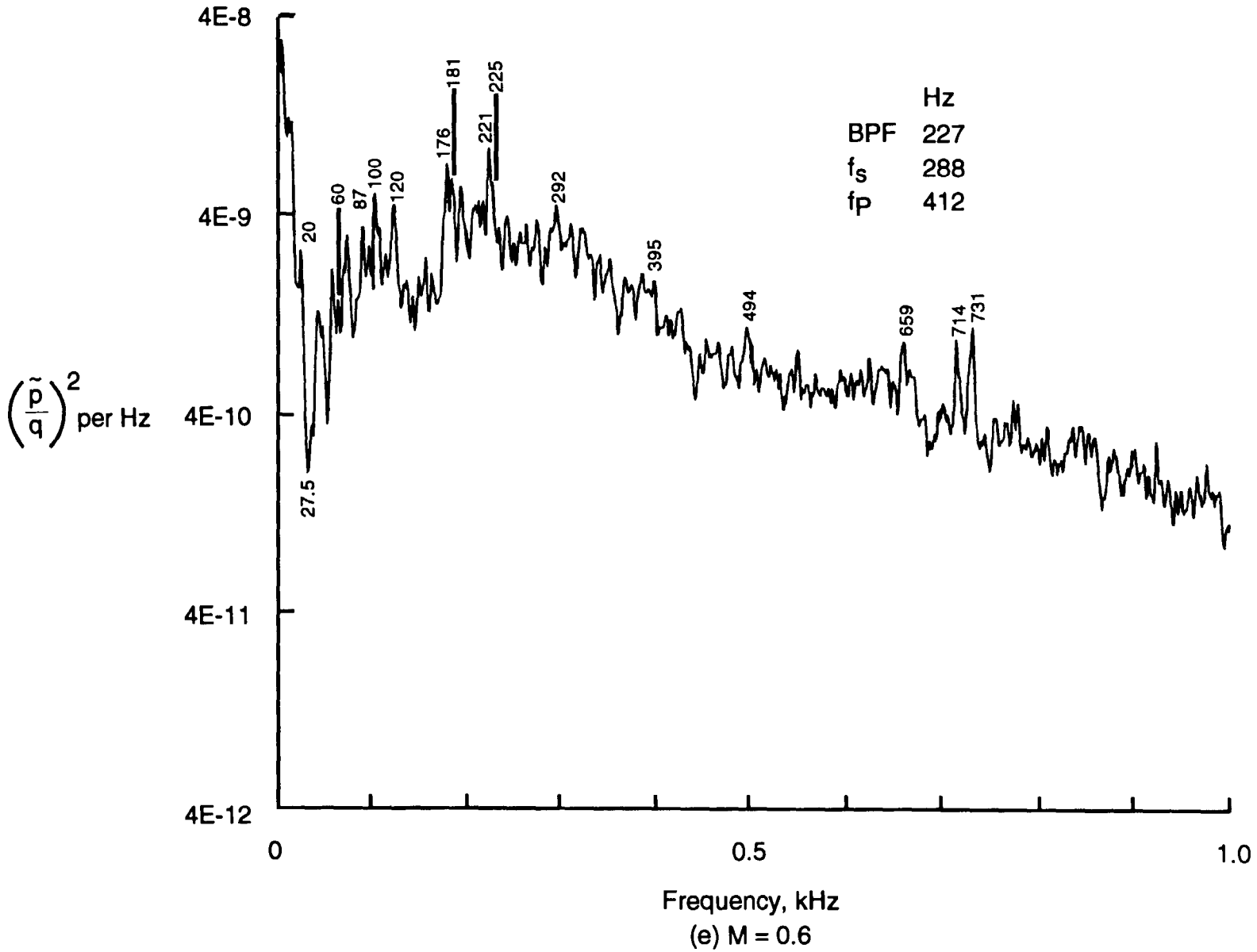

Figure 64. Continued

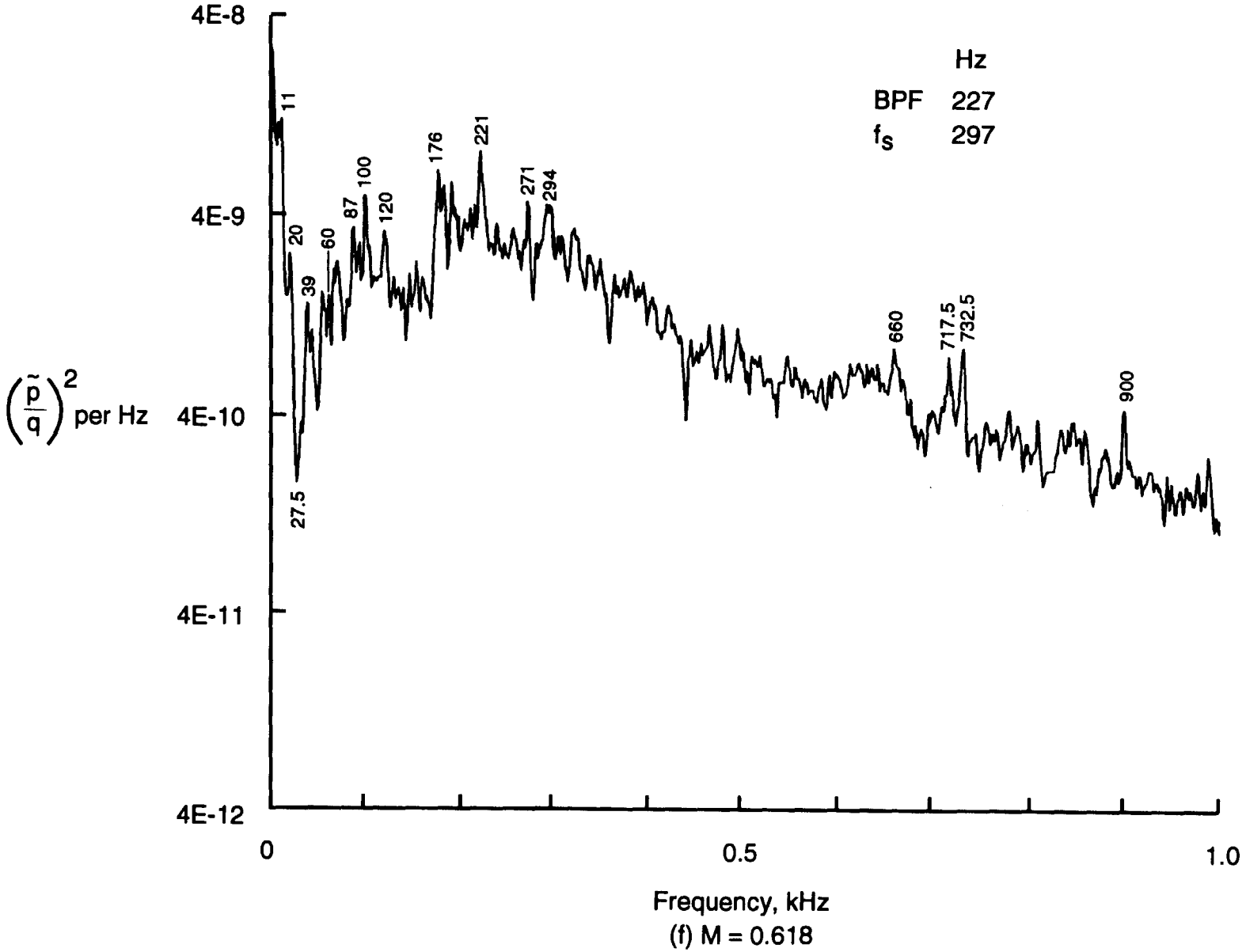

Figure 64. Continued

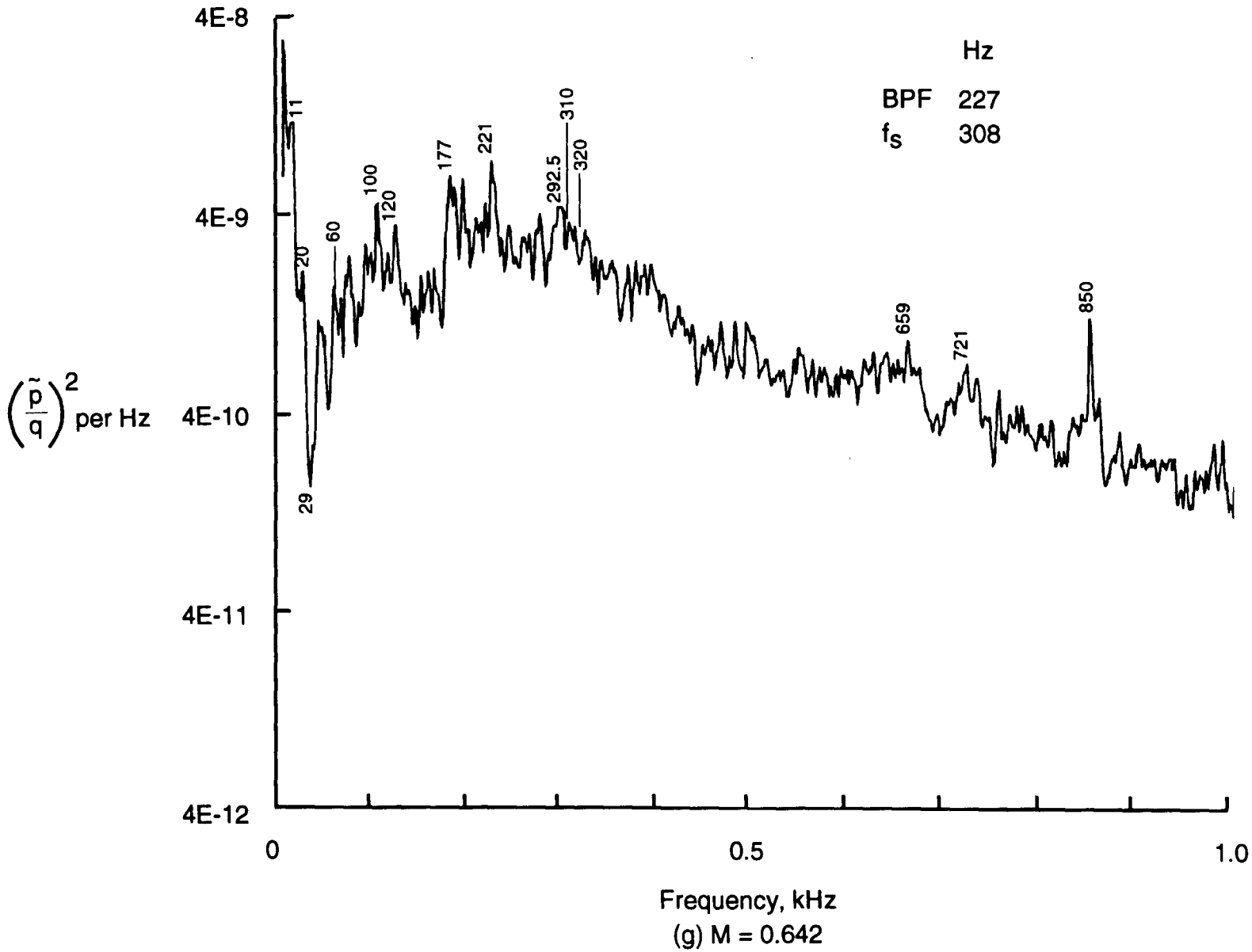

Figure 64. Concluded

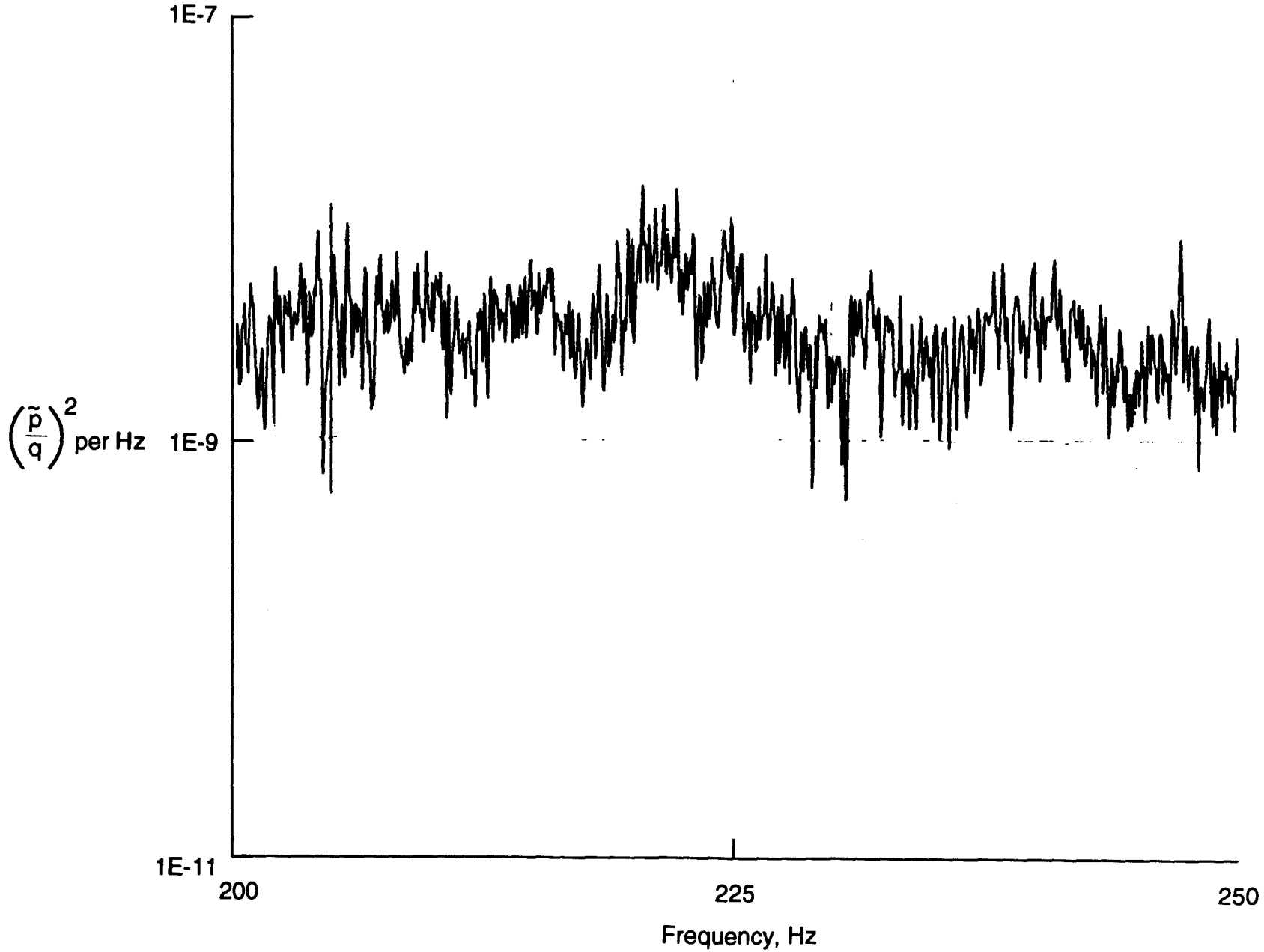

Figure 65. High frequency resolution power spectrum of fluctuating pressure coefficient in plenum M = 0.6, minimum Reynolds number boundary, air, BPF = 227 Hz.

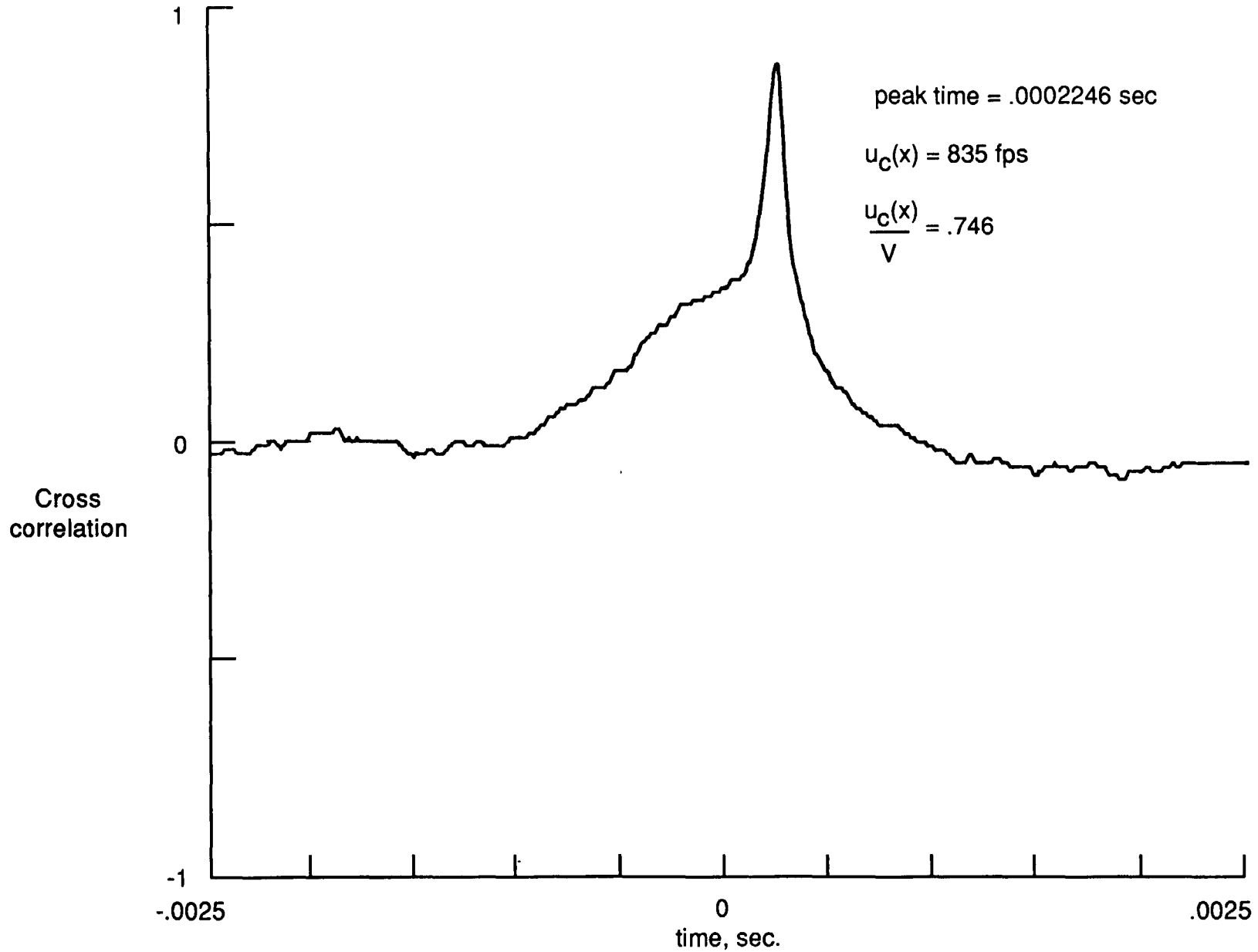

Figure 66. Cross correlation of adjacent pressure transducer signals on RHS test section sidewall, sta 13, M = 0.998, R = 6.1 x 10^6 /ft., nitrogen mode, ambient temperature, transducer separation distance 2.25 in.

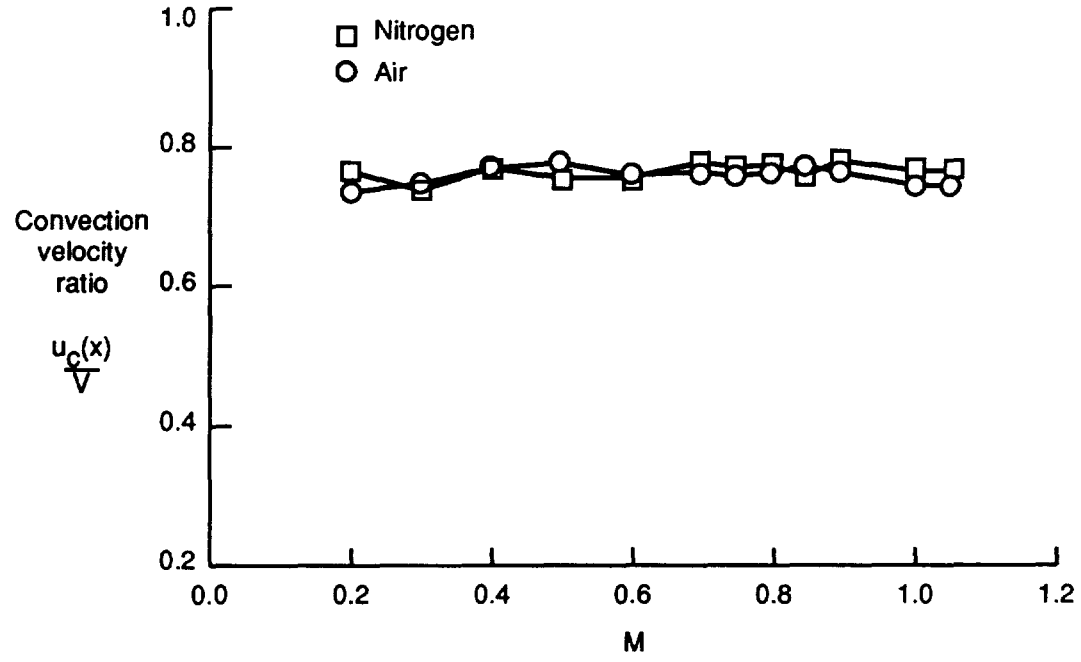

Figure 67. Convection velocity ratio on NTF RHS test section sidewall at sta 13, R = 6 x 10^6 per ft., ambient temperature, comparison of air and nitrogen.

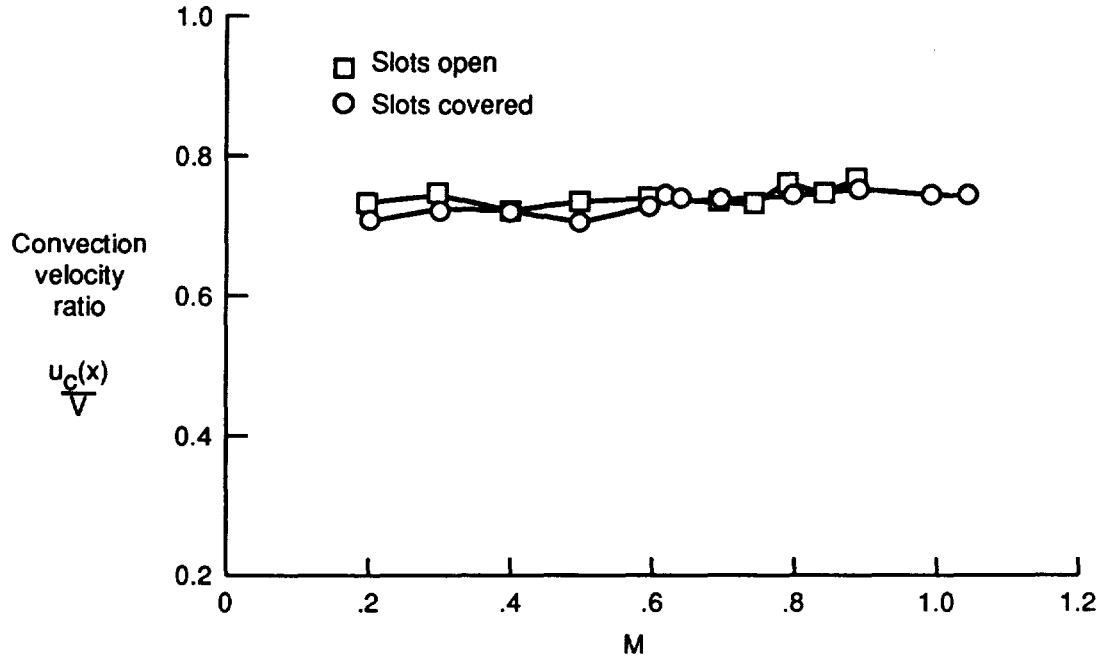

Figure 68. Convection velocity ratio on NTF RHS test section sidewall at sta 13, minimum Reynolds number boundary, air mode, ambient temperature, comparison of slots open and covered.

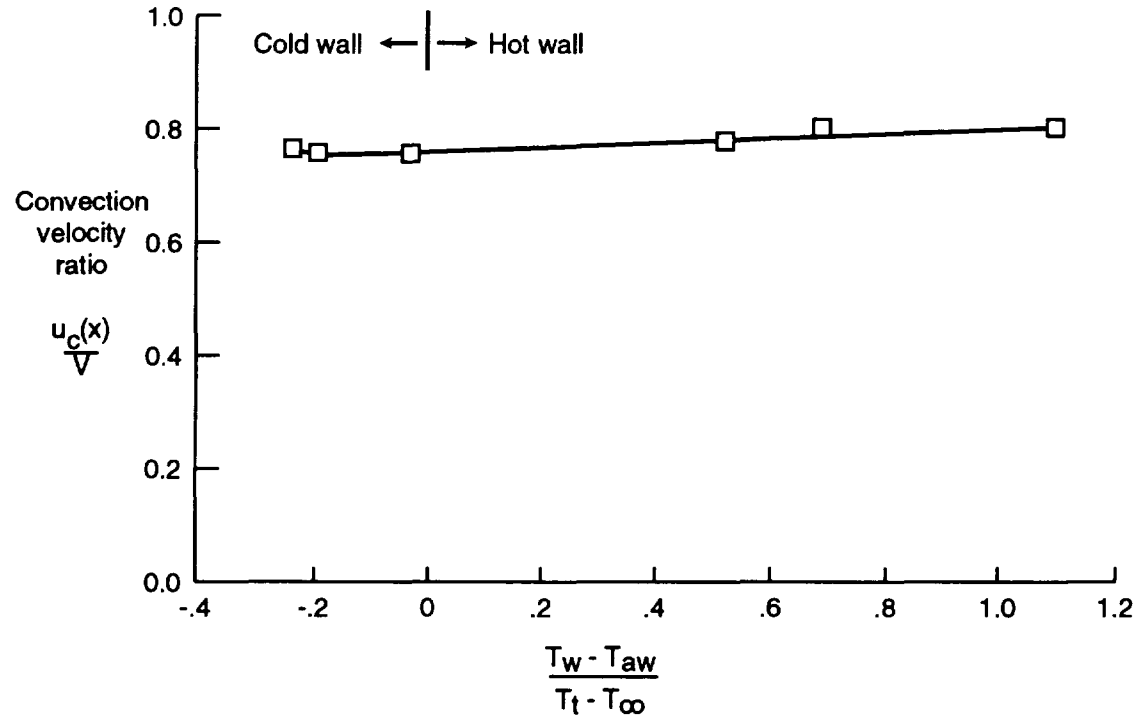

Figure 69. Convection velocity ratio on NTF test section sidewall at sta 13, M = 0.8, nitrogen mode, effect of hot wall versus cold wall.

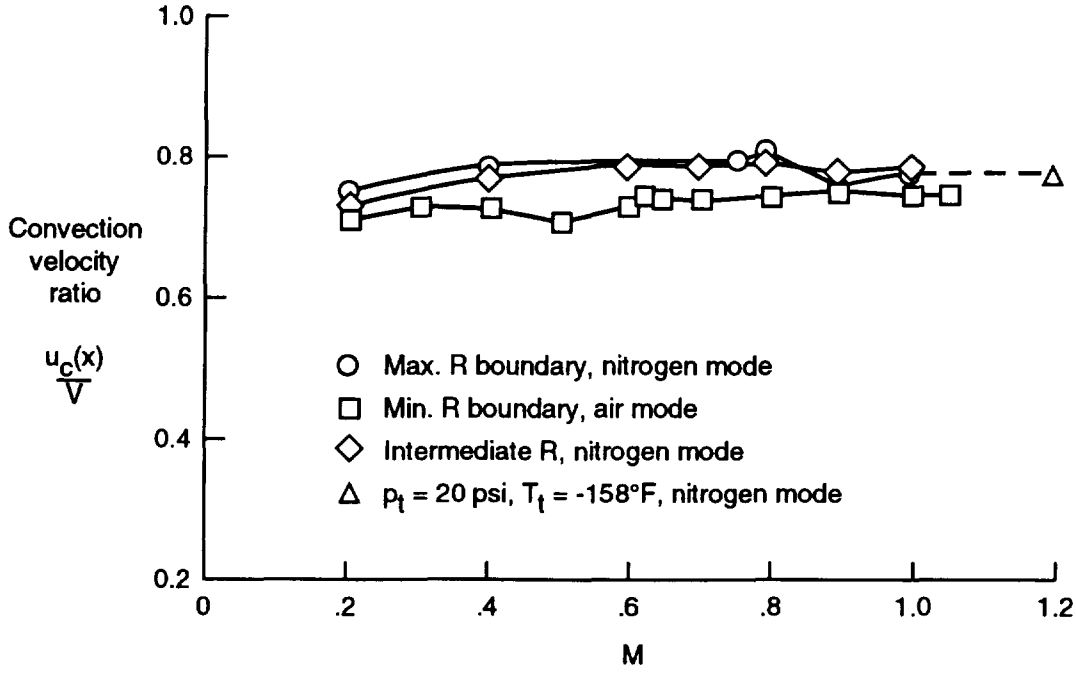

Figure 70. Convection velocity ratio on NTF test section sidewall at sta 13, effect of Reynolds number.

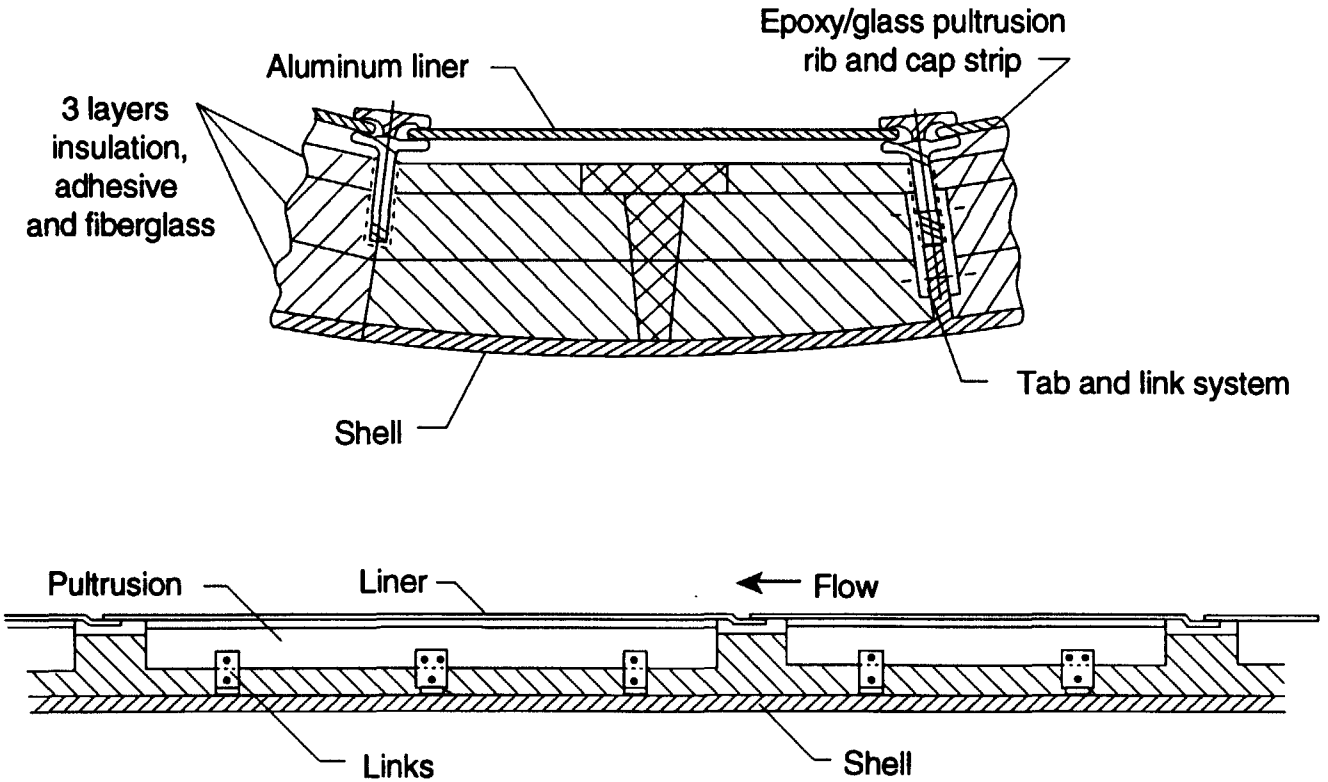

Figure A1. Sketch of thermal insulation and liner in NTF.

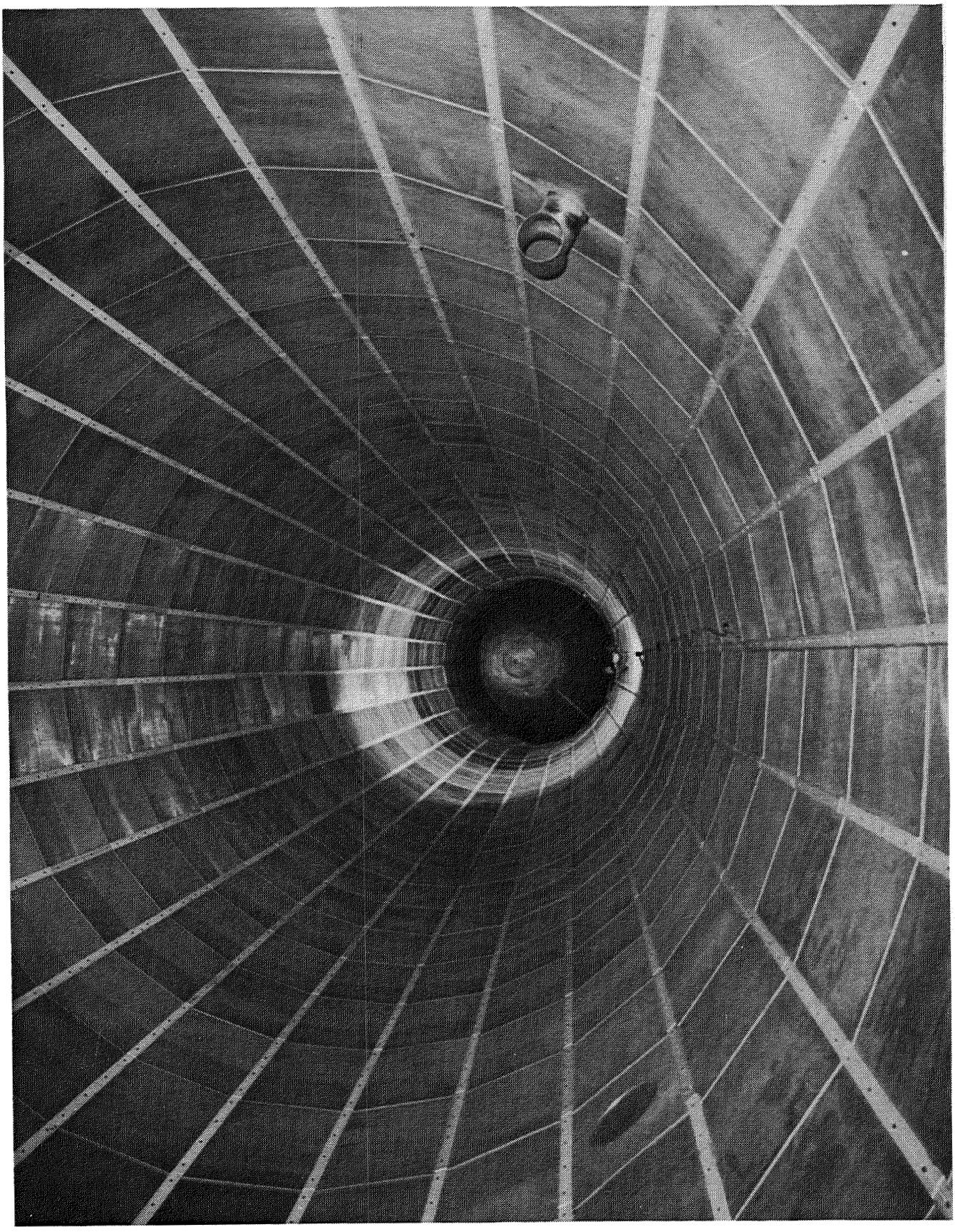

Figure A2. Photograph of the return leg of the NTF circuit showing aluminum liner plate flow-liner surface.

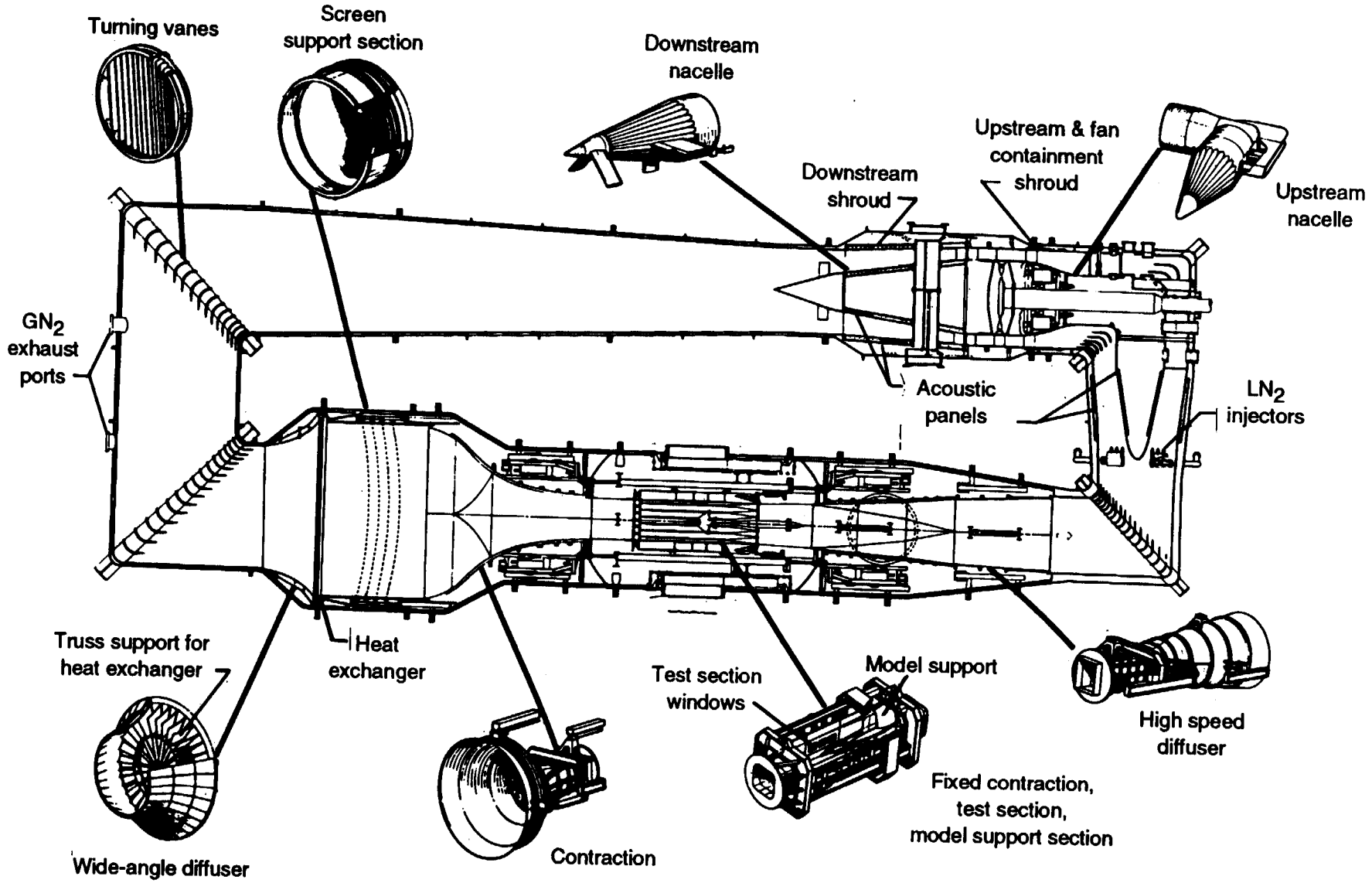

Figure A3. Principal components of NTF circuit.

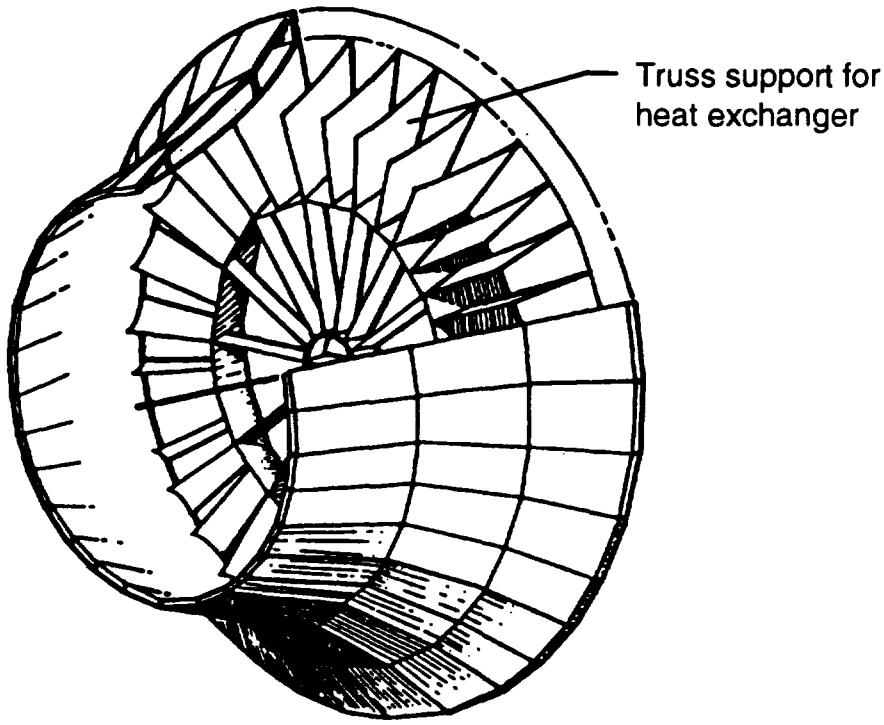

Figure A4. NTF wide-angle diffuser.

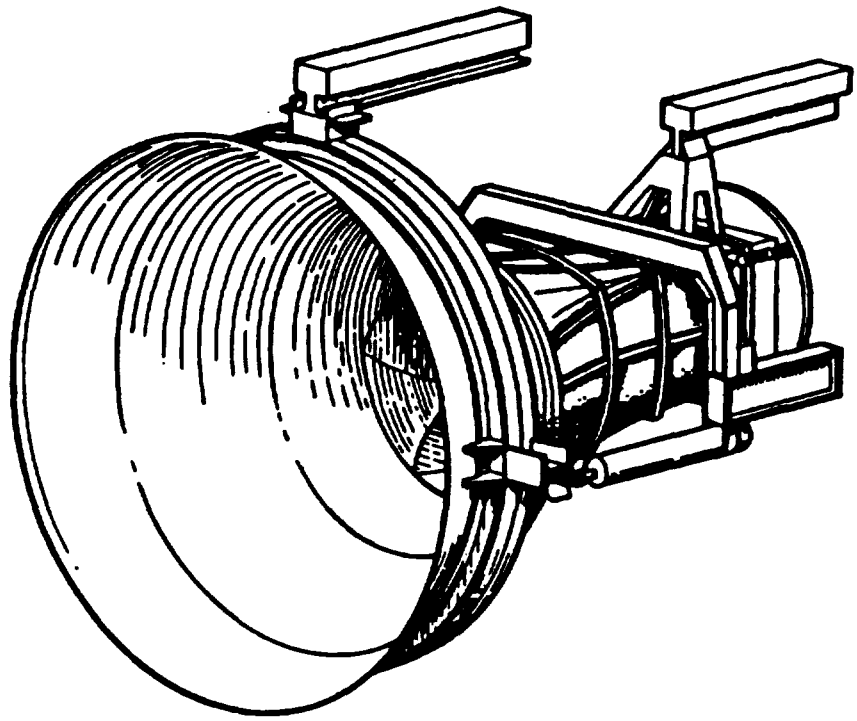

Figure A5. NTF Contraction section.

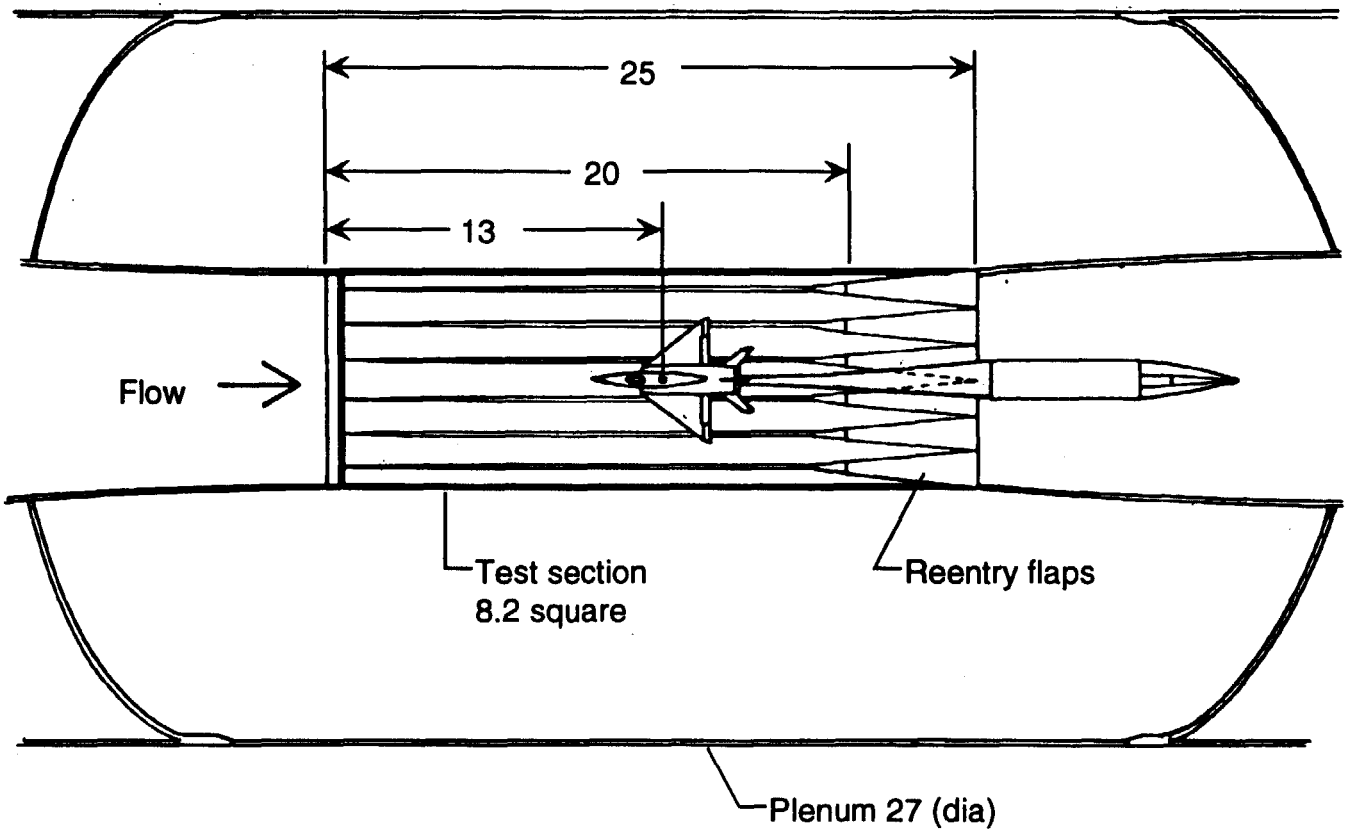

Figure A6. Planview of NTF test section (all dimensions in ft.).

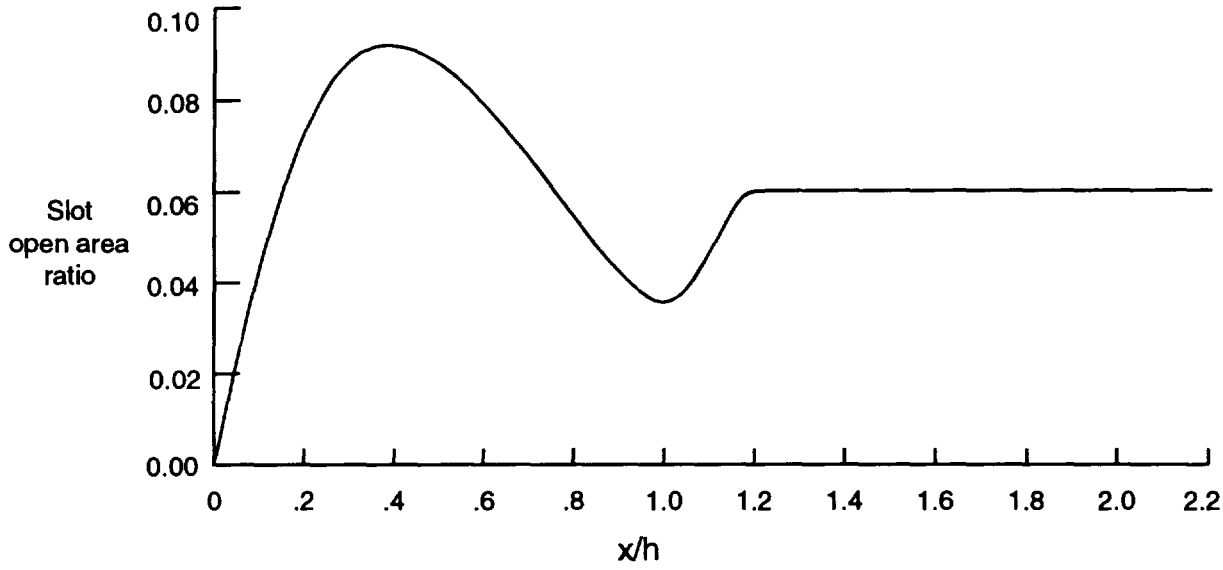

Figure A7. NTF slot shape for top and bottom walls.

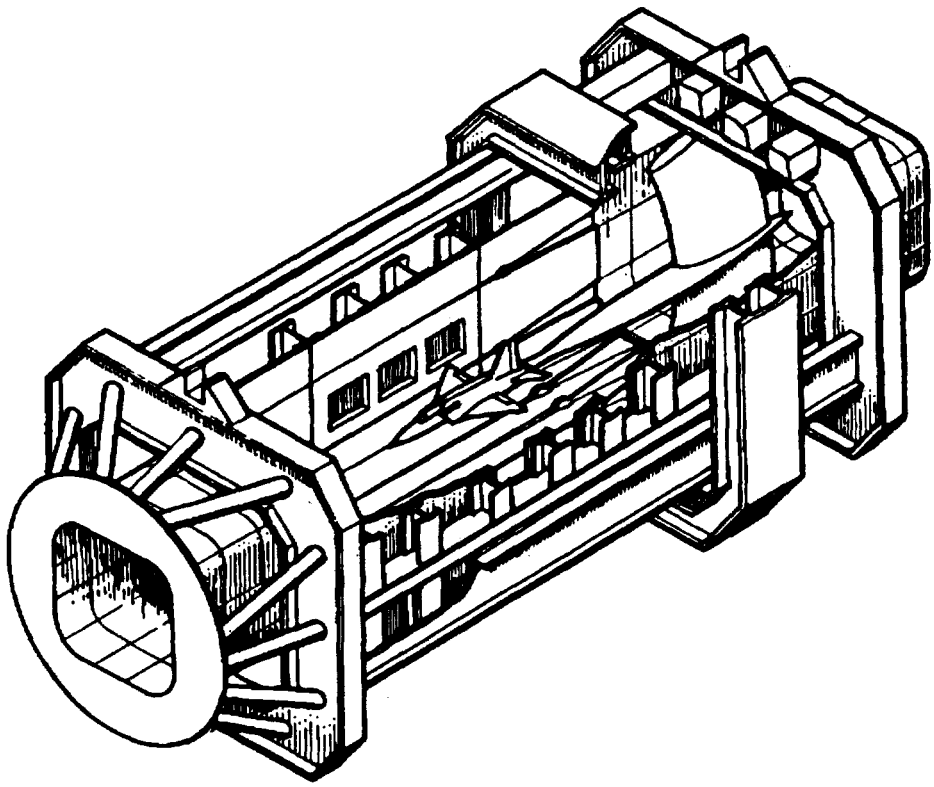

Figure A8. Sketch of NTF test section.

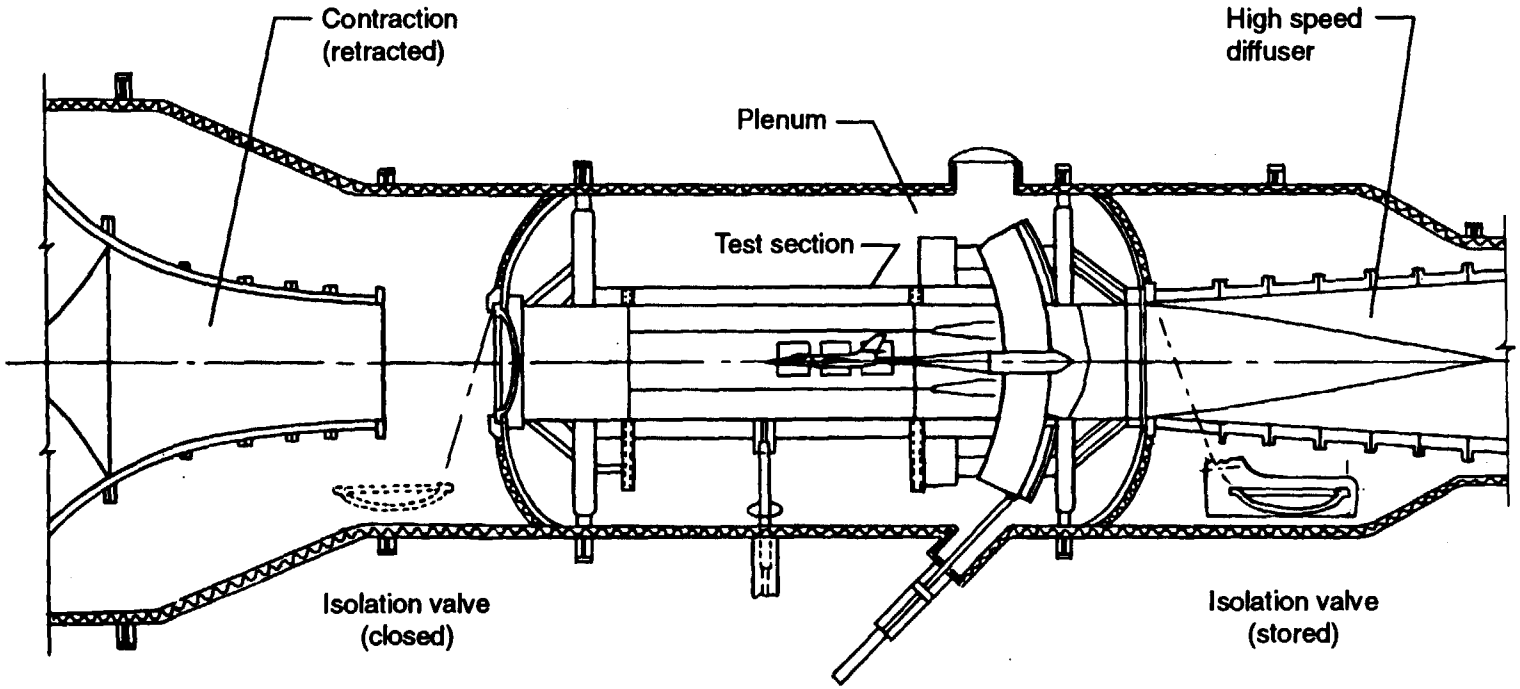

Figure A9. Elevation of NTF test section.

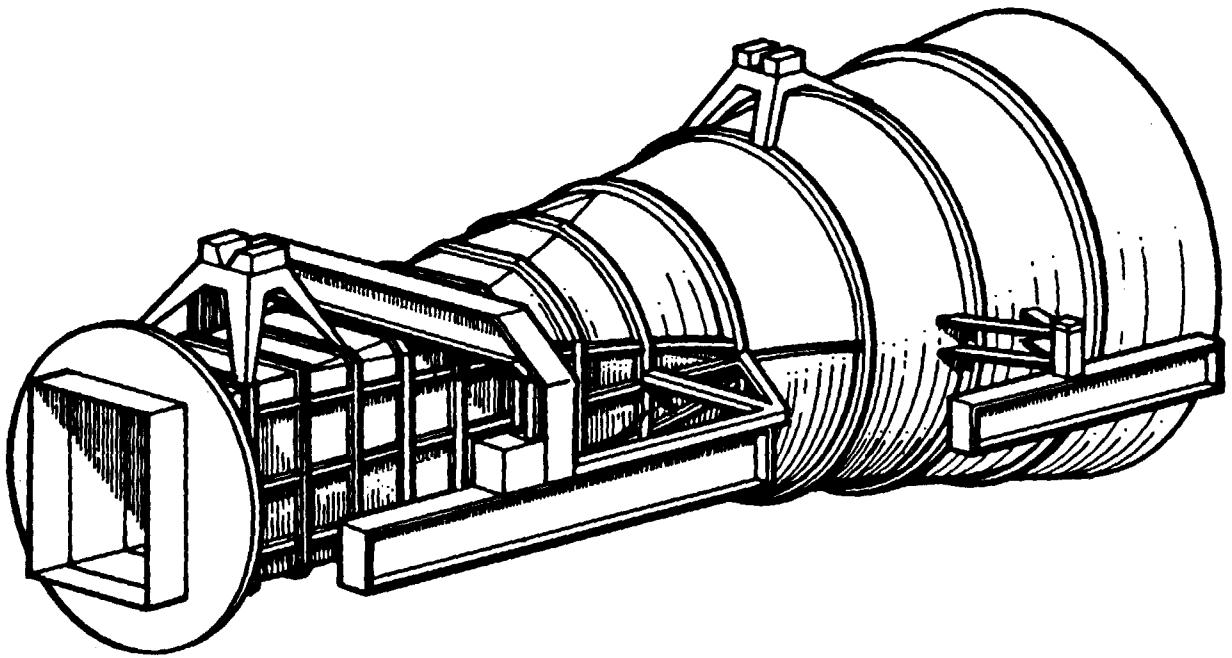

Figure A10. NTF high-speed diffuser.

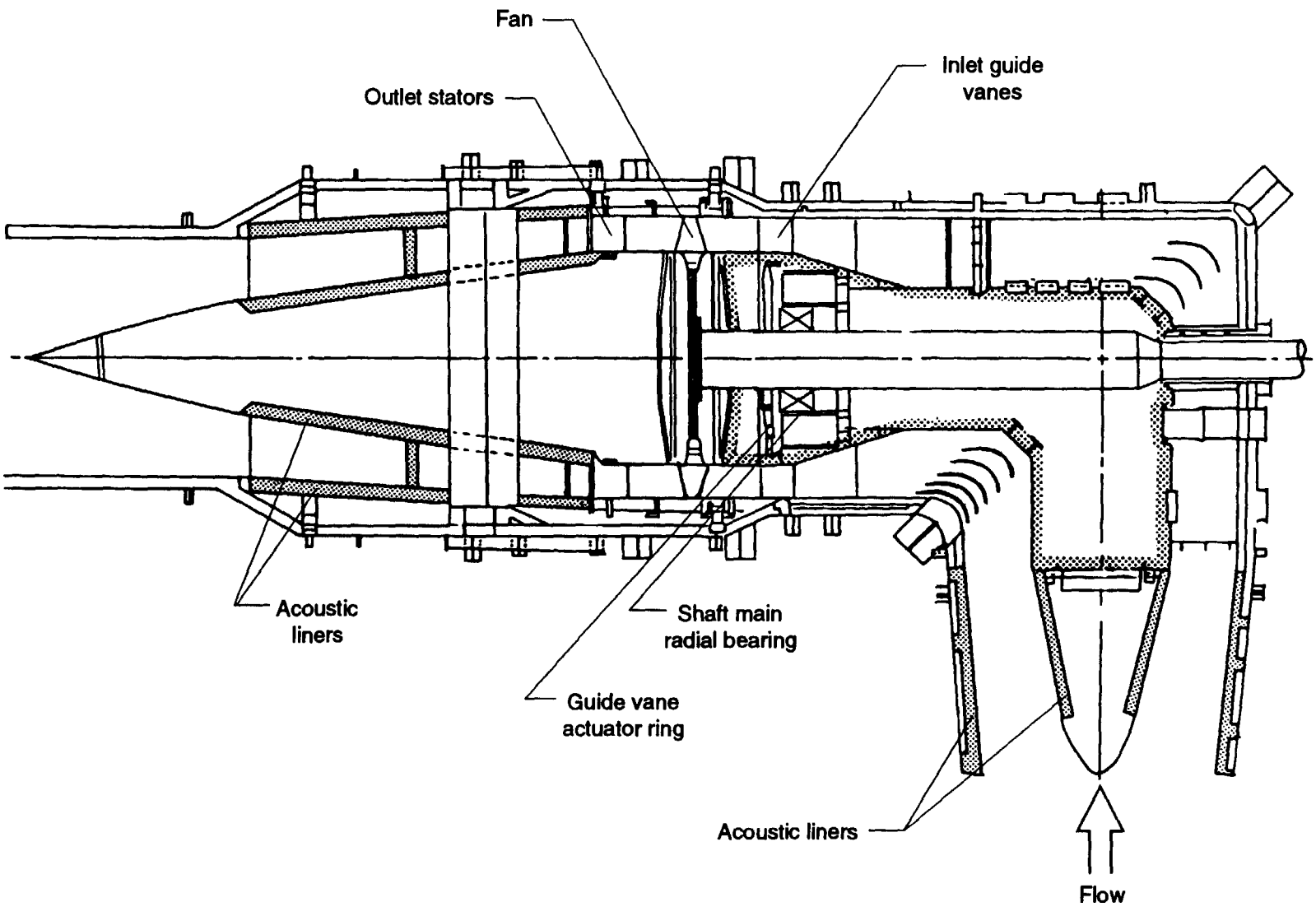

Figure A11. NTF fan section assembly.

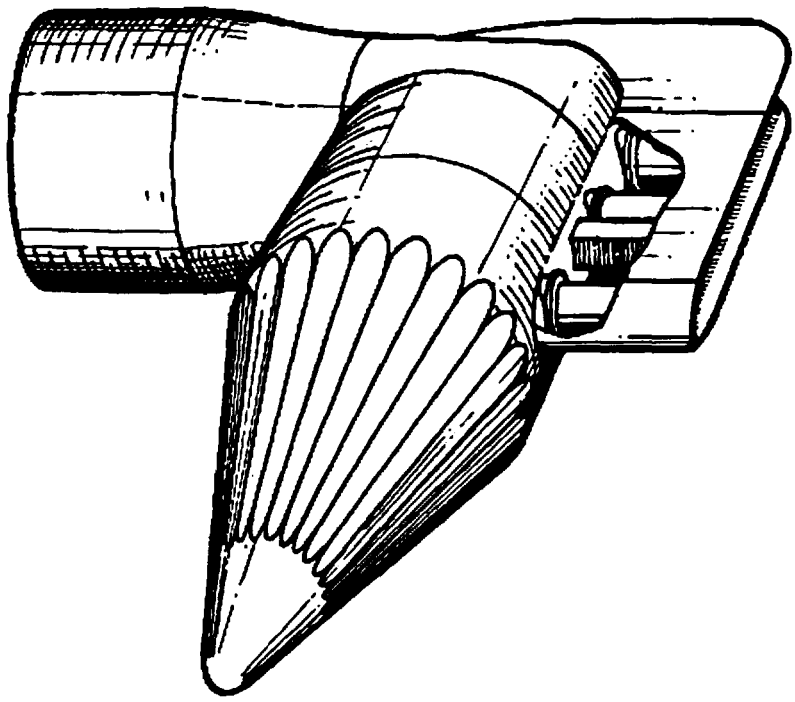

a. Nacelle nose cone.

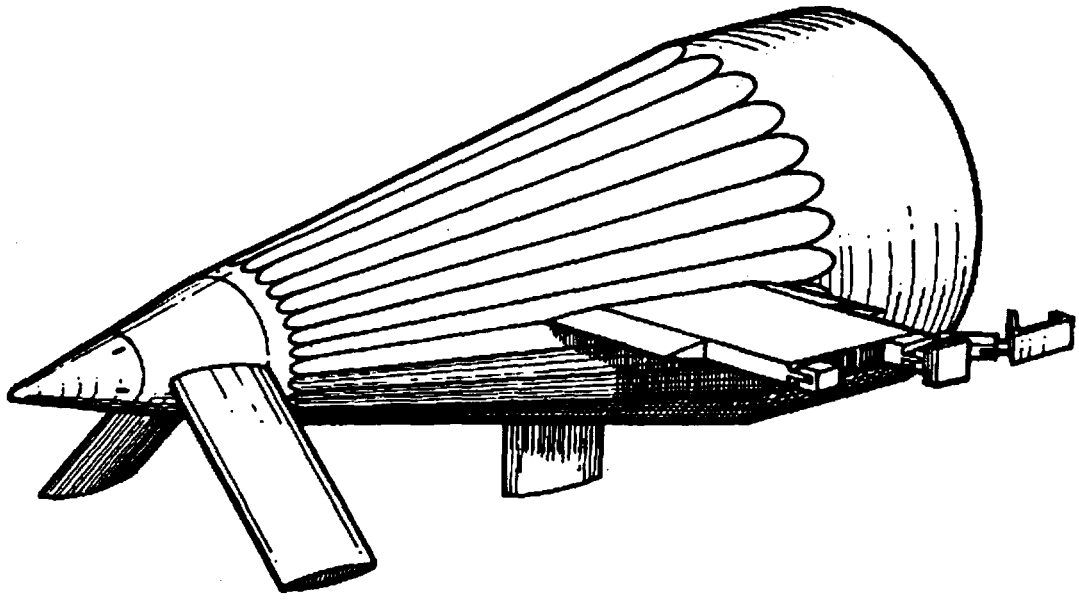

b. Nacelle tail cone.

Figure A12. NTF nacelle fairings showing artists' concept of flat acoustic liner panels.

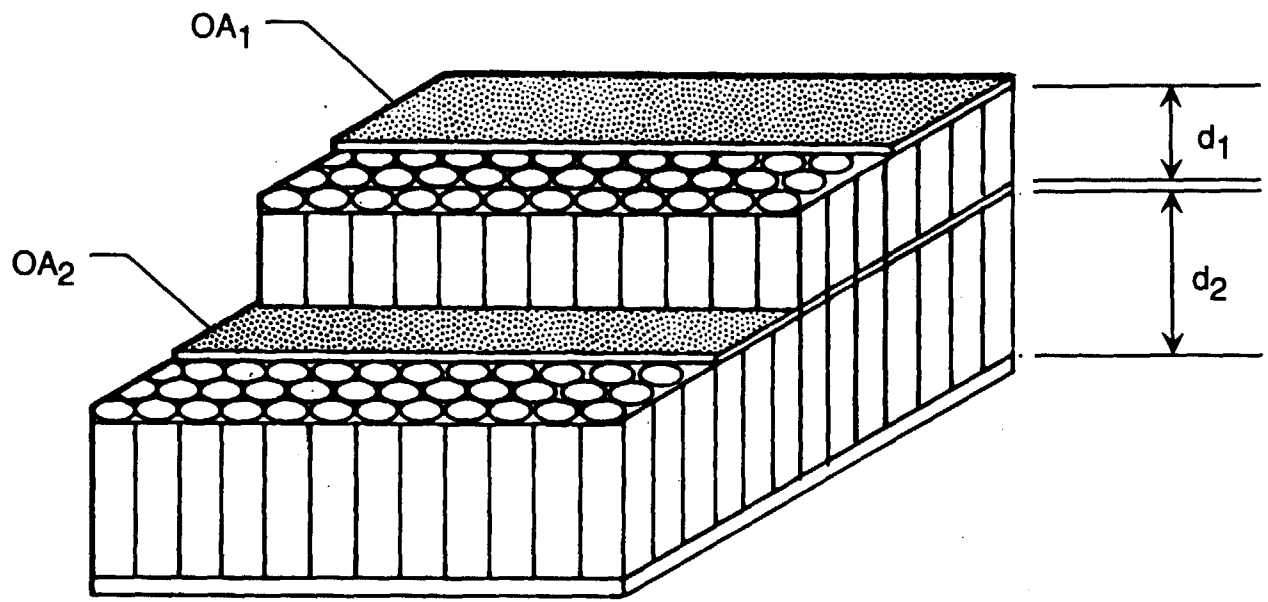

nacelle cone	open area (percent)		cavity depths (in)	
	OA_1	OA_2	d_1	d_2
nose	5.5	4.5	1.3	4.6
tail	5.5	4.5	2.5	7.5

Figure A13. NTF fan nacelle acoustic panel dual Helmholtz resonator concept.

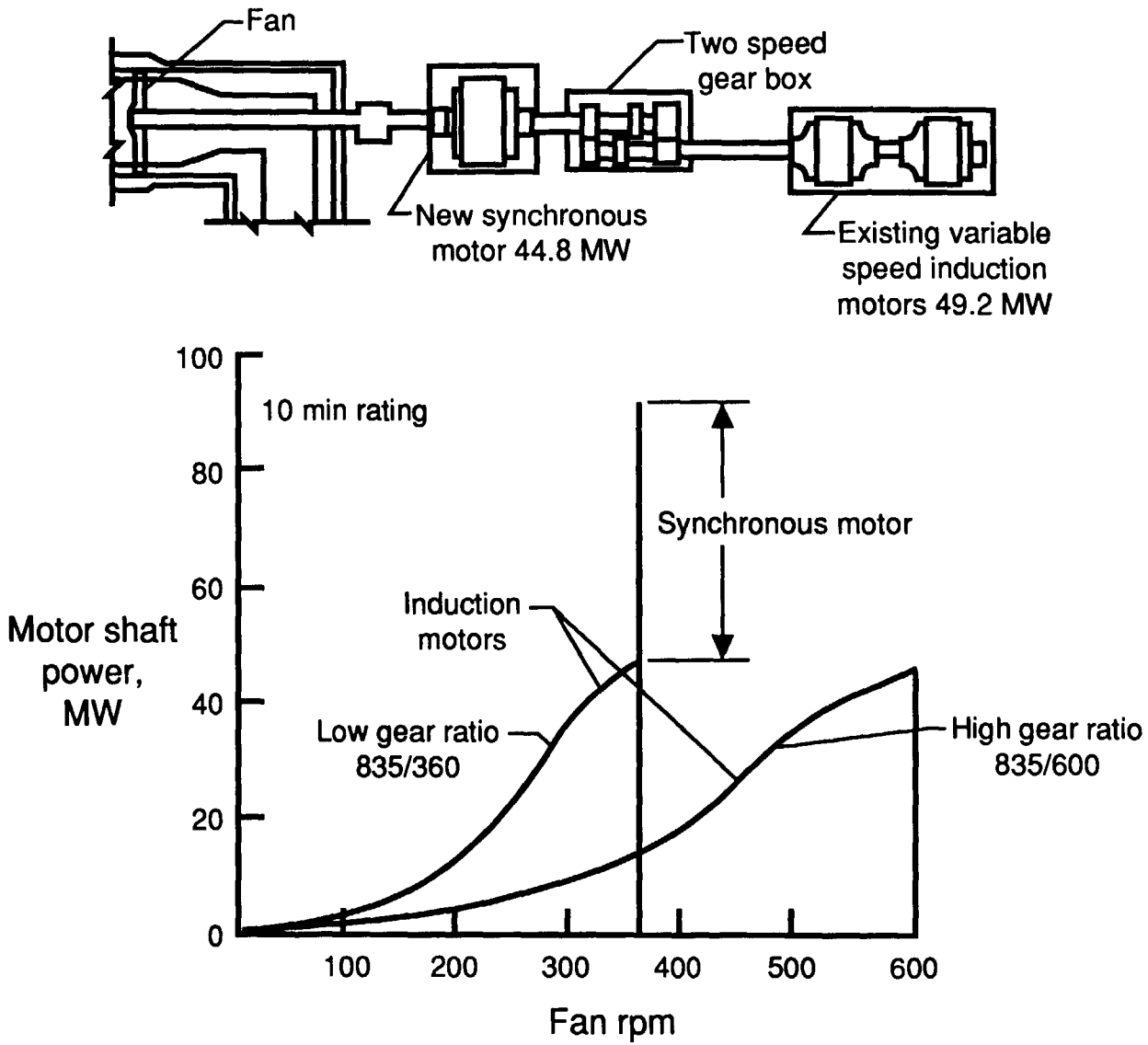

Figure A14. NTF drive system power.

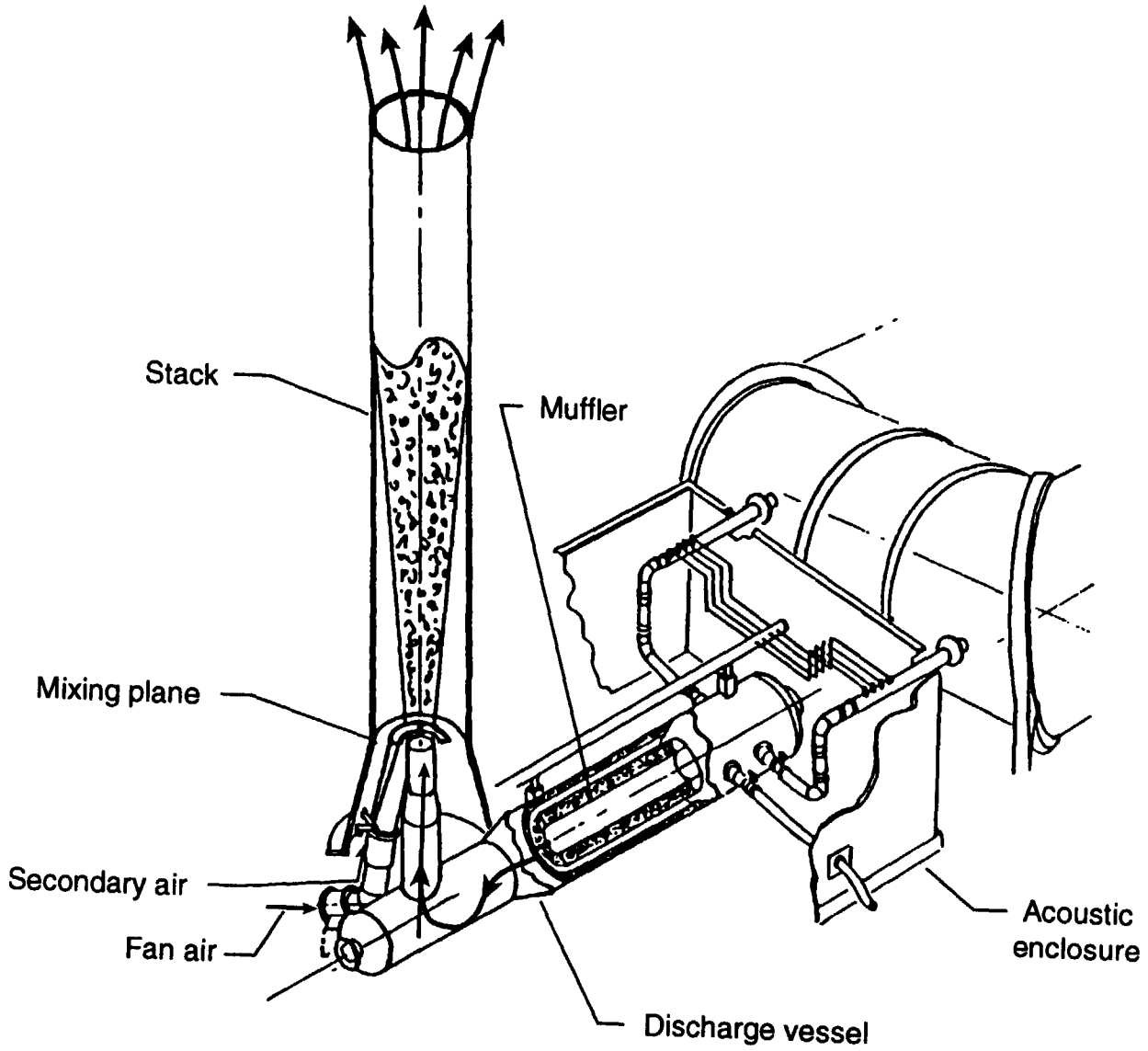

Figure A15. NTF exhaust muffler and vent stack.

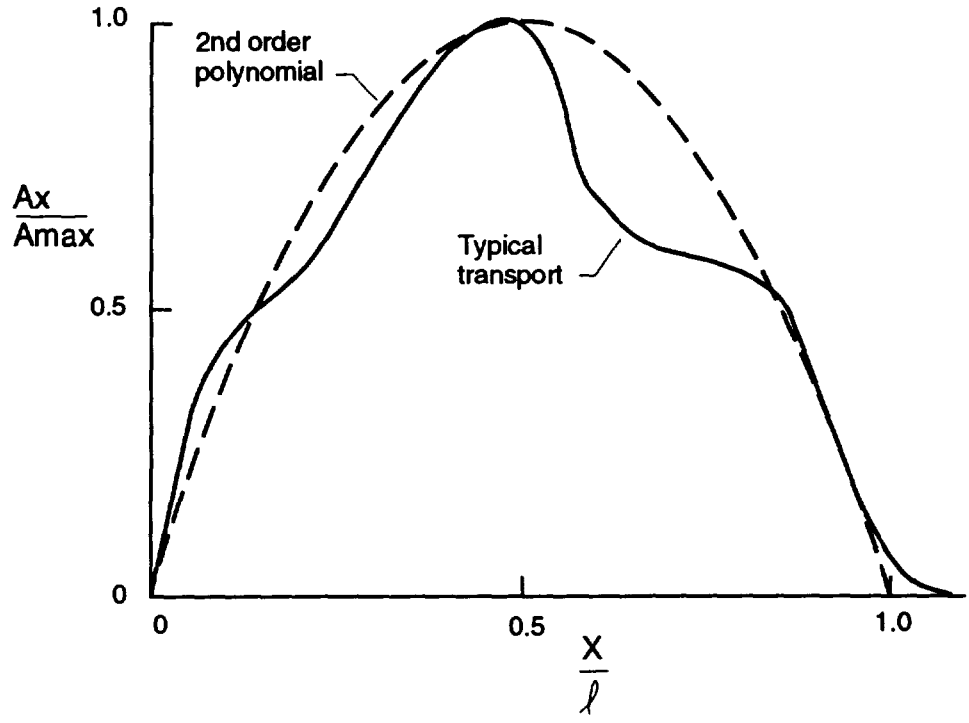

Figure B1. Cross-sectional area distribution for typical transport model

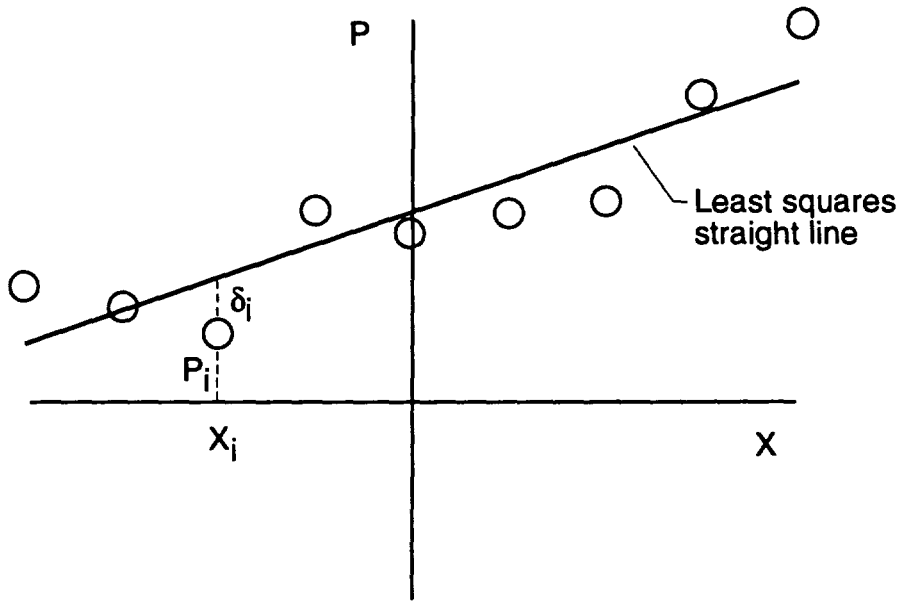

Figure C1 . Least squares straight line fit to points $P_1 ... P_n$.

Figure D1. Photograph of NTF test section showing centerline calibration probe with support cables.

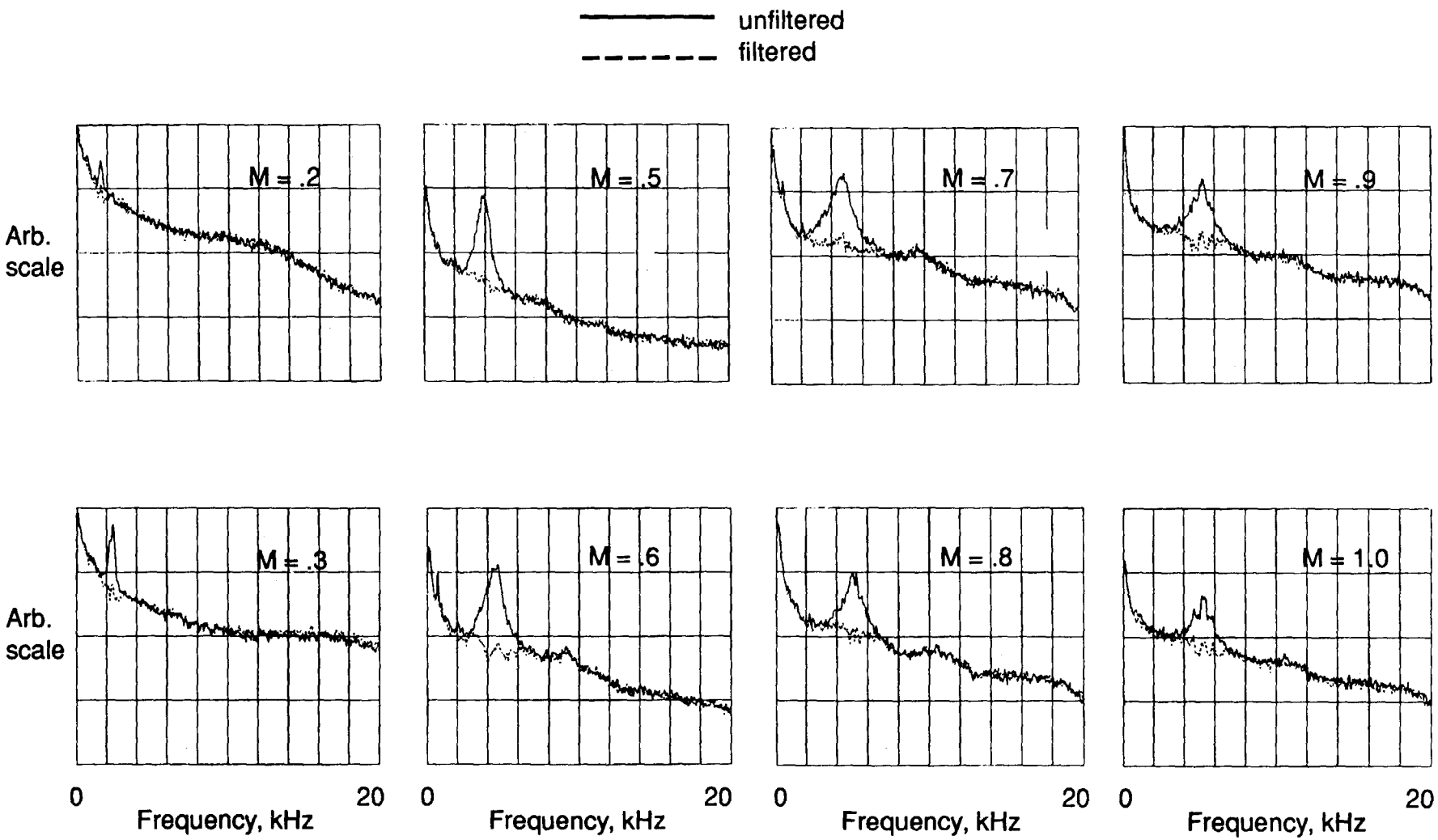

Figure D2. Power spectra obtained with the centerline calibration probe in the NTF test section, data are for the RHS test section wall at sta 13. (105 psi < p_t < 125 psi, T_t = -250°F)

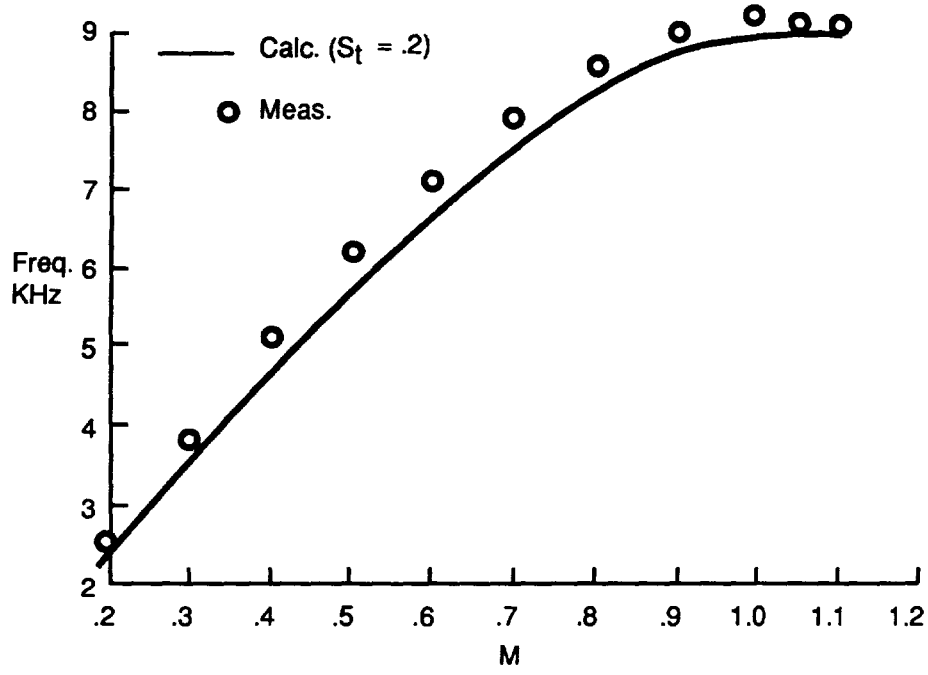

Figure D3. Calculated and experimental vortex shedding frequencies of centerline probe cables p_t = 17psi, T_t = 120°F, air mode).

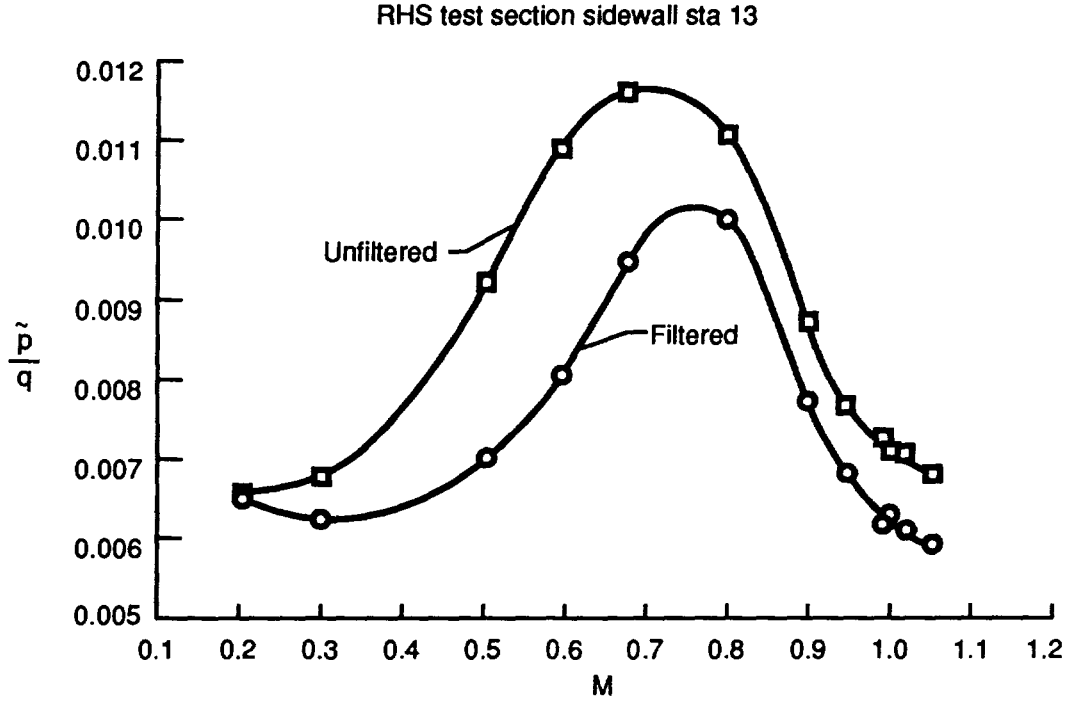

Figure D4. NTF fluctuating pressure coefficient showing effect of filtering of centerline calibration probe support cable vortex shedding frequency.

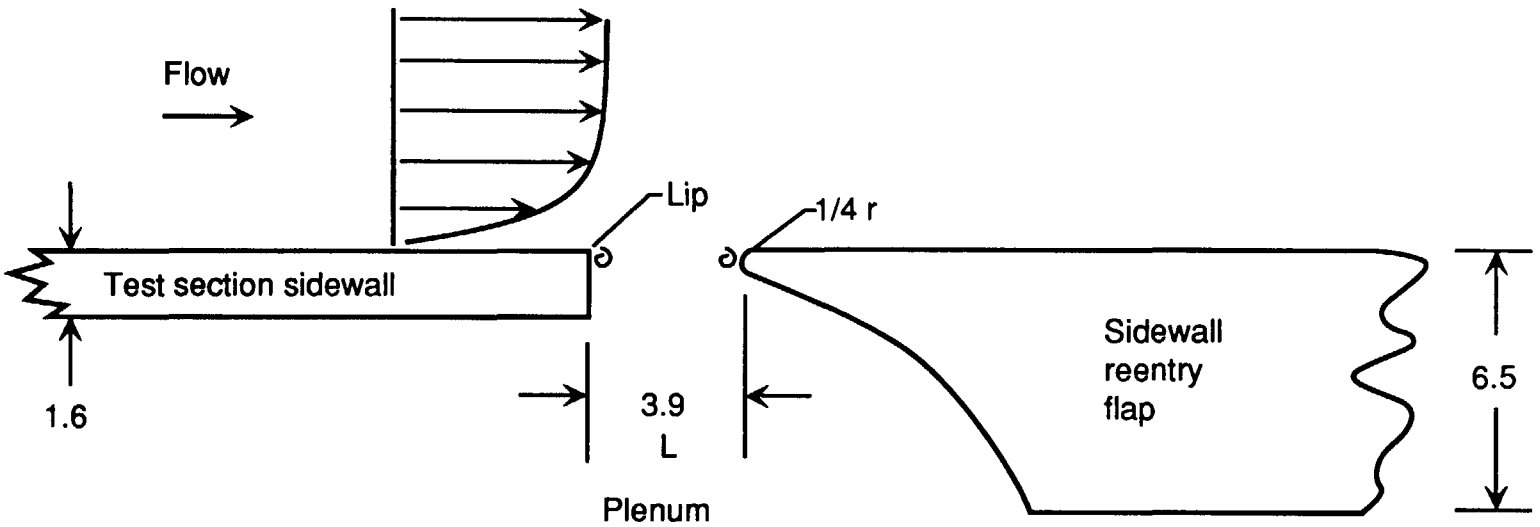

Figure E1. Sketch of gap profile between test section sidewall and reentry flap.
(all dimensions in inches)

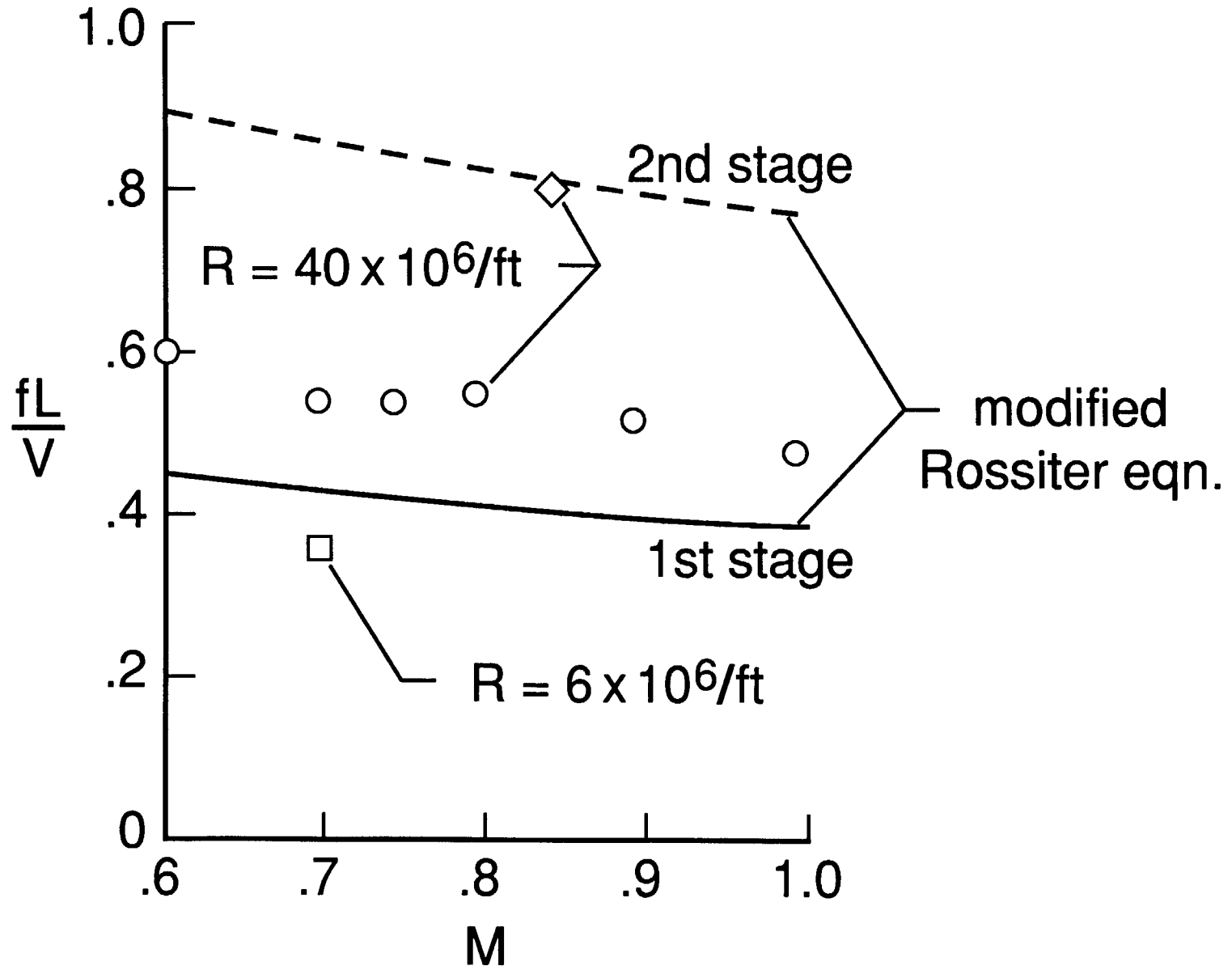

Figure E2. Comparison of measured reduced frequencies with free shear layer edge-tone reduced frequencies calculated using the modified Rossiter equation.